Development and Integration of Chemical Imaging Methods for Applications in Biomedical and Pharmaceutical Research

by

Elizabeth Claire Randall

A thesis submitted to the University of Birmingham for the degree of
DOCTOR OF PHILOSOPHY

PSIBS Doctoral Training Centre
School of Chemistry
University of Birmingham
B15 2TT

October 2016

Abstract

Visualisation of the spatial distribution of biomolecules in biological substrates by mass spectrometry or spectroscopic imaging techniques plays a major role in biomedical, clinical, and pharmaceutical research. The work presented in this thesis investigates the capabilities of three imaging techniques, liquid extraction surface analysis (LESA) mass spectrometry imaging (MSI), matrix assisted laser desorption ionisation (MALDI) MSI and stimulated Raman scattering (SRS) microscopy, and combinations thereof, for the analysis of biological samples. A method for combined LESA and MALDI analysis was developed and results provided high resolution imaging of multiple analyte classes (proteins, lipids and small molecule drugs) in thin tissue sections. Moreover, this method enabled fundamentals of LESA sampling to be probed. Similarly, SRS microscopy was used for the quantitative imaging of MALDI surface sampling effects and sample preparation, providing insight into fundamental processes of MALDI MS including ion yields obtained under different experimental and instrumental parameters. Multimodal SRS, LESA and MALDI imaging was executed on a single tissue sample revealing the complementarity between the three approaches, and enabling high resolution imaging with high sensitivity and specificity. Specific challenges for LESA were further explored, namely protein quantification, improved spatial resolution and alternative biological substrates. A quantitative LESA method based on the production of mimetic tissue models containing stable isotope-labelled proteins was developed. An alternative platform, comprising continuous flow sampling, the Flow-ProbeTM, with the potential to achieve higher spatial resolution both in discrete 'spot' and raster mode, was assessed. Finally, a LESA method for the direct analysis of proteins from live bacterial colonies growing in Petri dishes was developed.

Acknowledgements

Table of Contents

List of Figures

List of Tables

List of Abbreviations

MS – Mass spectrometry

MSI – Mass spectrometry imaging

MALDI – Matrix-assisted laser desorption/ionisation

CHCA – α-cyano-4-hydroxycinnamic acid

SA – sinapinic acid

DHB – 2,5-dihydroxybenzoic acid

PNA – *para*-nitroaniline

UV – ultra violet

DPSS – diode-pumped solid state

ESI – electrospray ionisation

TOF – time of flight

RF – radio frequency

FT-ICR – Fourier Transform ion cyclotron resonance

DESI – desorption electrospray ionisation

LMJ – liquid microjunction

LMJ-SSP – liquid microjunction surface sampling probe

LESA – liquid extraction surface analysis

DBS – dried blood spot

HPLC-MS – high performance liquid chromatography mass spectrometry

CRS – coherent Raman scattering

CARS – coherent anti-Stokes Raman scattering

SRG – stimulated Raman gain

SRL – stimulated Raman loss

SRS – stimulated Raman scattering

IR – infra red

TPA – two-photon absorption

SEM – scanning electron microscopy

NMR – nuclear magnetic resonance

UV-Vis – ultra violet-visible

LC-MS – liquid chromatography mass spectrometry

WBA – whole body autoradiography

QWBA – quantitative whole body autoradiography

Chapter 1

Introduction

1.1 Theory of Mass Spectrometry

A mass spectrometer is made up of three main parts; an ionisation source which produces ions from the sample, a mass analyser which separates ions according to mass to charge ratio (m/z) and a detector which measures the number and m/z of ions. From this information a chart indicating the number of ions detected with each m/z can be produced – this is known as a mass spectrum.[1]

1.1.1 Ionisation

Ionisation can be achieved via numerous methods. Traditional ionisation methods such as electron impact and chemical ionisation focussed on ionisation in the gas phase through collisions with charged particles. These methods were unsuitable for large biomolecules due to extensive fragmentation and degradation during transition to the gas phase.[2] In the 1980s two new methods of ionisation were developed which made possible the ionisation and analysis of proteins and other macromolecules such as oligonucleotides and complex carbohydrates. Matrix assisted laser desorption ionisation (MALDI) mass spectrometry was first introduced in 1987 by Karas *et al.*[3] and electrospray ionisation (ESI) followed two years later in a report by Fenn *et al.*[4]

1.1.1.1 MALDI Ionisation

MALDI MS involves dissolving the sample in a solution of matrix material, commonly an organic acid, which has a high molar absorptivity in the ultra-violet or infra-red range. As the carrier solvent evaporates, the matrix and analyte co-crystallise to form a 'solid solution' structure with analyte molecules embedded throughout, see Figure 1.1. The sample may then be introduced to the ion source of the mass spectrometer. Under vacuum conditions, an ultraviolet or infrared laser is used to irradiate the sample with short pulses, causing a build-up of energy within the matrix. This heat causes localised sublimation of the matrix and analyte into a plume of particulate matter in which reactions may occur to produce singly charged analyte and matrix ions.[3,5,6] Several ionisation models have been proposed although the exact mechanism by which this process occurs remains somewhat debated.[7-9]

Ionisation by MALDI is now generally accepted to be a two-step process involving initial or primary ionisation before ion-molecule interactions occur in the ablation plume, known as secondary processes. The two most popular models of primary ionisation are the cluster model and the pooling model.[9] The cluster model suggests that ions are pre-formed during matrix/analyte preparation and remain after crystallisation. Ions are therefore contained in clusters of matrix molecules ablated from the solid surface. Evaporation of molecules in the cluster may then release the ion. Alternatively charge may need to migrate from matrix to analyte in order to form analyte ions.[7-9] The pooling model differs in that it suggests ions are formed after laser irradiation and are not pre-formed during sample preparation. Pooling is the redistribution of electronic excitation energy which can occur after initial photoexcitation of the matrix. If two neighbouring molecules are raised to the first excited singlet state (S_1) or a higher excited singlet state (S_n) they can interact due to waveform overlap. The pooling event

2

can generate either a higher excited singlet state or an ion. Other primary ionisation models have been suggested, such as direct multi-photon ionisation, excited state proton transfer and the polar fluid model, but no single model has been universally agreed upon.[9] Secondary processes occur after the initial desorption/ablation event and primary ions have been produced. There is a large excess of neutral matrix in the plume, so it can be assumed that ions within this plume will therefore undergo bimolecular collisions with neutral matrix molecules during expansion of the plume. The possible reactions leading from these interactions could be electron transfer, proton transfer and cation transfer.[9]

The 'soft' nature of MALDI desorption/ionisation means the method is suitable for the analysis of large biomolecules because they remain intact during desorption/ionisation. There are several advantages of using the 'matrix assisted' method over traditional laser desorption ionisation. Firstly there is no requirement to adjust the laser wavelength to the absorption frequency of each analyte. Secondly, analytes of high molecular weight (~300,000 Da) can be detected because the ionisation/desorption process is independent of analyte molecular weight. Finally, due to the ratio of matrix to analyte ions in the sample being very high, the probability of forming sample clusters is decreased, thus increasing the chance of observing the molecular ion peak.[1,3,7]
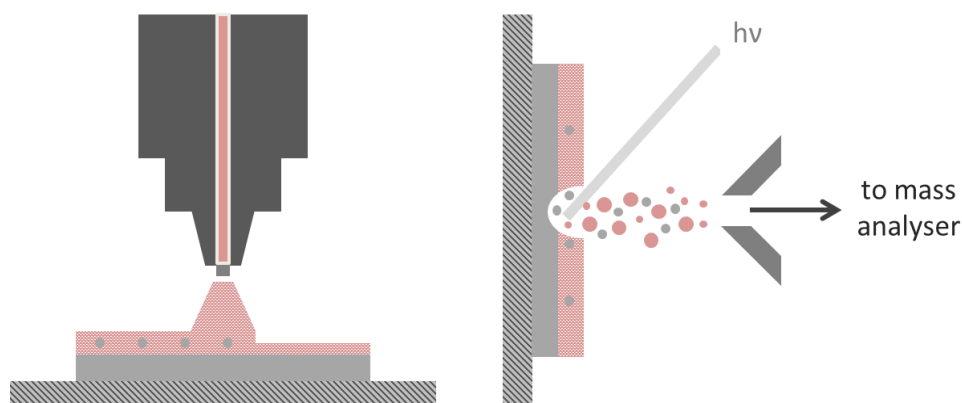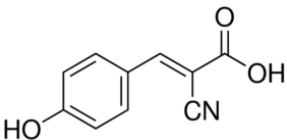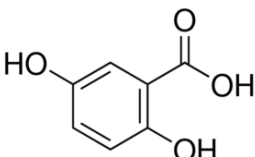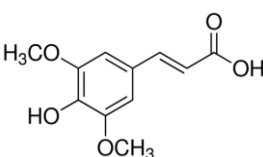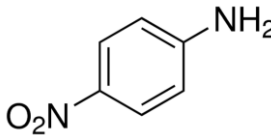
Figure 1.1 Illustration of MALDI MS sample preparation and ionisation: sample is coated with a solution of matrix compound which forms a co-crystalline structure with analyte molecules embedded throughout. Upon irradiation with a laser desoption/ionisation of matrix and analyte occurs. Ions are directed towards the mass spectrometer via ion lenses.

1.1.1.1.1 Matrix compounds

The choice of matrix compound can affect the sensitivity and the type and number of analytes detected in a MALDI analysis.[10] Different matrix compounds can be used to selectively analyse a particular class of analyte. Cinnamic and benzoic acid derivatives were quickly identified as useful MALDI matrices for the analysis of proteins.[7,11] The majority of reports centre on a small group of acidic organic compounds such as α-cyano-4-hydroxycinnamic acid (CHCA), sinapinic acid (SA) and dihydroxybenzoic acid (DHB), which have all been widely reported for the analysis of proteins, peptides and lipids.[10,12-14] A number of basic matrices such as anilines have also been suggested; *para*-nitroaniline (PNA) has been used for the analysis of lipids using instruments operating at intermediate pressure.[15] A list of the matrix compounds used in this work is given in Table 1.1. The quality of a given analysis is dependent upon a number of matrix-dependent factors such as: physicochemical properties of the matrix which

determine co-crystallisation with analyte, co-desorption upon irradiation and efficiency of ionisation.[12] The number of different instrumental set-ups available further complicates matrix assessment because different lasers operate at different repetition rates and have different wavelengths. The wavelength required for maximum absorption of laser energy is dependent on the UV absorption profile of the matrix compound which is determined by chemical structure and is therefore different for every matrix. Investigations into the ideal matrix and optimum preparation for different applications are ongoing.

Table 1.1 A list of matrix compounds used in this work and their associated analytes.

Matrix compound	Molecular structure	Analyte types
CHCA		Peptides and proteins[16] Lipids[10]
DHB		Peptides and proteins[11] lipids[17] Polymers[18]
SA		Peptides and proteins[16]
PNA		Lipids[15,19]

1.1.1.1.2 Matrix deposition methods

In addition to the choice of matrix compound, the method of matrix/analyte preparation can also critically affect MALDI analysis. In imaging experiments successful preparation must incorporate deposition of sufficient quantities of matrix, minimisation of matrix crystal sizes, sufficient extraction of analyte and minimal delocalisation of analytes. The matrix is typically dissolved in a mixture of organic/aqueous solvent and applied to the surface using a microspotter,[20] electrospray,[21] airbrush[10] or robotic spray device, such as the TM-Sprayer produced by HTX Technologies and used in this work. Alternatively the matrix can be applied without the use of a carrier solvent by sublimation.[22] It has been suggested that this decreases the probability that analytes will dissolve in the solvent and spread away from their original location – hence preserving sample integrity. The small crystals typically produced by this method are also a benefit when high resolution imaging is desired.[22] A possible drawback to solvent-free matrix deposition is poorer extraction efficiency resulting in lower sensitivity.

1.1.1.1.3 Laser types

In the past, MALDI MS has commonly been performed with a Nitrogen laser operating at a frequency of 20 Hz and a wavelength of 337 nm. This wavelength was ideal for many matrix compounds but the low repetition rate was unsuitable for high-throughput MALDI imaging applications.[19] Diode-pumped solid state (DPSS) lasers, such as the Nd:YAG and the Nd:YVO$_4$ are now commonly used in commercial MALDI instruments and were used in this work. The frequency tripled Nd:YAG and Nd:YVO$_4$ can operate at high repetition rates up to 20 KHz. This is ideal for high throughput raster mode imaging in which the energy from the laser must be delivered to the sample surface more quickly in order to obtain sufficient ion yields on a shorter timescale.[19]

These lasers have a wavelength of 355 nm which is also suitable for use in combination with the matrices listed above.

1.1.1.2 Electrospray ionisation

Electrospray ionisation involves three stages: production of charged droplets, droplet shrinkage and the production of gas-phase ions. A sample dissolved in solution is passed through a capillary held at high voltage, the tip of which is located close to a planar counter electrode, see Figure 1.2. Ions typically enter the mass spectrometer through an orifice in the counter electrode. The high electric field which is imposed partially penetrates the liquid inside the capillary. For simplicity, only the production of positive ions, in which a positive capillary potential is applied, will be discussed here. At the tip of the capillary, the liquid forms a meniscus where positive charge accumulates as a result of the movement of negative charge towards the capillary and positive charge to the liquid surface. The accumulation of positive charge destabilises the surface which is drawn downfield such that the liquid forms a cone shape, known as the Taylor cone. At sufficiently high electric field the cone is not stable and a liquid filament is drawn out, as illustrated in Figure 1.2. The filament becomes destabilised the further away from the cone it is and eventually breaks to form droplets. There is an excess of positive charge within these droplets.[1,4,23,24]
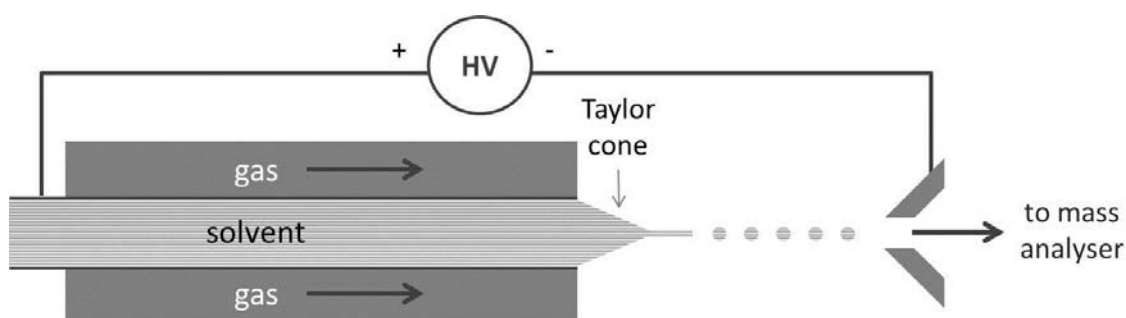
Figure 1.2 Illustration of electrospray ionisation, the sample is dissolved in a solvent and passed through a capillary held at either positive or negative potential. At the end of the capillary the liquid surface is drawn downfield into a cone shape known as the Taylor cone, this is further drawn into a long filament which eventually breaks up into droplets. Ions are released from the droplets and enter the mass analyser.

The droplets shrink by evaporation of solvent ions and at some point they come close to the Rayleigh limit. At this point the charge in the droplet becomes sufficient to overcome the surface tension that holds the droplet together and fission can occur. The parent droplet oscillates and emits a tail of smaller offspring droplets in a manner similar to the disruption of the Taylor cone. This was observed by Gomez and Tang who imaged charged droplets undergoing fission.[25]

There are two mechanisms which have been suggested for the formation of gas-phase ions from charged droplets: the first was first described by Dole in 1968 and involves the formation of very small droplets which contain only one ion.[26] This is known as the charged residue model; evaporation of solvent from the tiny droplet converts the charged droplet to a single gas phase analyte ion.[23] The other model was suggested by Iribarne and Thomson,[27] and is known as the ion evaporation model. This mechanism involves small but very highly charged droplets which do not undergo fission but emit gas-phase ions.
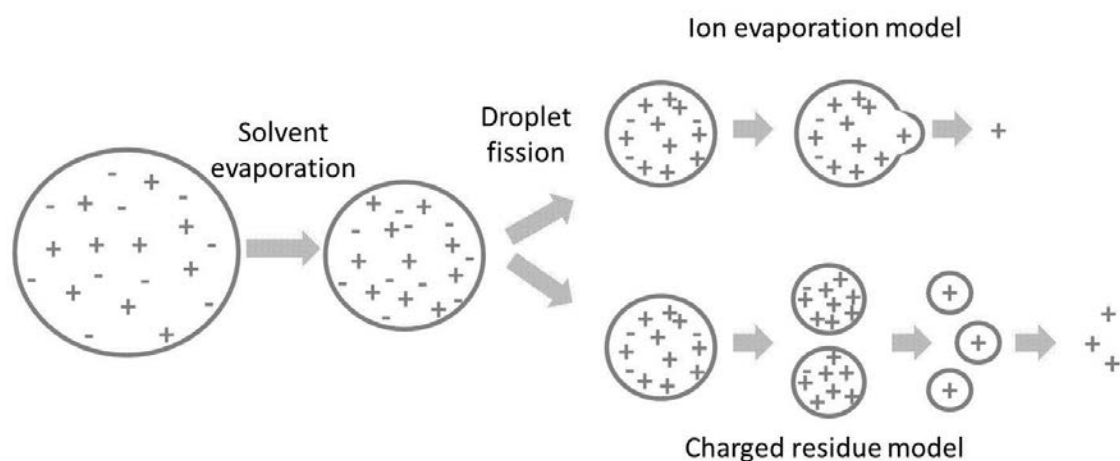
Figure 1.3 Models of electrospray ionisation: ions can be released from charged droplets either by the ion evaporation model or the charged residue model.

As previously mentioned, it is possible to generate multiply charged macromolecules such as proteins via ESI. A model suggested by Fenn[28] postulates that polyprotonated protein species are contained within droplets and due to Brownian motion some portion of the protein may approach the droplet surface. If a charged residue approaches the surface then this charge replaces a charge on the droplet surface. Thermal activation could provide the energy for the charged residue to move outside the droplet. An elastic oscillation of the droplet could then facilitate uneven fission of the droplet in which the protein and a very small amount of solvent are released to form a highly charged droplet.[23,28]

1.1.2 Mass Analysis

Once gas-phase ions have been produced from the sample, a mass analyser is required to separate ions of different mass to charge ratio. The type of mass analyser required depends on the sample, ionisation source and type of analysis required; hence numerous mass analysers and combinations of mass analysers exist. Broadly, a mass analyser uses electric and or magnetic fields to separate ions based on differences in their behaviour

within the field. Commonly used mass analysers include the quadrupole, time-of-flight (TOF), linear ion trap and the Orbitrap.

1.1.2.1 Linear Ion Trap

Ion traps are devices which use electric fields to trap ions either in two (linear ion trap) or three (3D Ion trap) dimensions. The linear ion trap consists of four rods held at a potential and ending in lenses which reflect ions back and forth, see Figure 1.4. Ions enter the device along the z-axis and oscillate along the x,y plane due to application of an RF field. Ions are confined by the electric field at either end of the trap and are reflected between the two ends. As a result an ion cloud forms inside the trap and these ions can be mass selectively ejected. Ions are typically ejected axially through openings cut into two opposite rods by applying AC voltages between rods in the ion trap and the exit lenses. Linear ion traps can be used as stand-alone mass spectrometers by ejection of ions towards a detector, or can be combined in hybrid instruments in order to isolate ions of particular *m/z,* perform tandem mass spectrometry and study ion-molecule chemistry.[1,29] An instrument employing an ion trap in combination with an orbitrap mass analyser – the Thermo Fisher Orbitrap Velos and Orbitrap Elite - was used in this work.
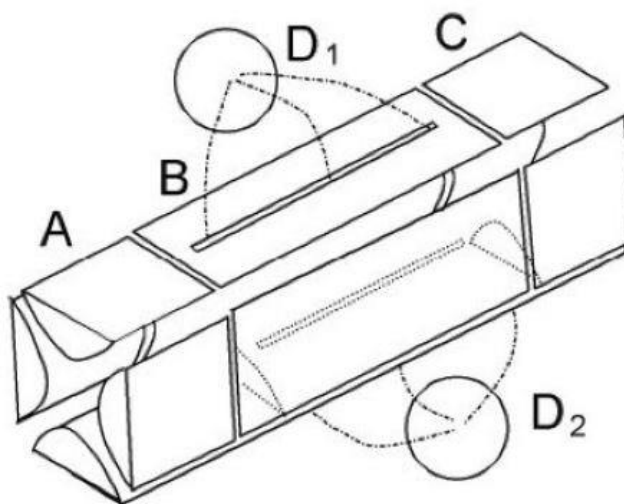
Figure 1.4. The linear ion trap: four parallel rods held at a potential with two end lenses which reflect ions back and forth trapping ions in cloud within the rods. Slits in two opposite rods allow for ejection of ions towards another mass analyser or a detector. Reproduced with permission from [1].

1.1.2.2 Quadrupole

The quadrupole mass analyser consists of four parallel conductive rods held at alternating potentials, see Figure 1.5. The potential applied to the rods is described by equation 1.1, where U is the direct potential, V is the zero to peak amplitude of the RF voltage and ω is the angular frequency in radians per second.[1]

$$\Phi_0 = U - V cos\omega t$$

1.1

The application of voltages to these rods creates an oscillating electric field into which ions are accelerated. Ions are subject to accelerations along x and y axes as a result of forces induced by the electric field. The trajectory of ions through this field is determined by their m/z ratio so by adjusting the strength of these fields and the applied RF potential, ions of a particular m/z can be selectively transmitted. Ions of differing

11

m/z will have an unstable path and will be deflected towards one of the rods and will not reach the detector. Quadrupole mass analysers are often used as ion guides to direct and focus ion beams towards a second mass analyser, owing to their low mass resolution when used independently.[1] Quadrupoles can be used in conjunction with other quadrupoles (for example in a triple quadrupole instrument) or with a time-of-flight mass analyser in a QqTOF instrument, such as the one used in this work.
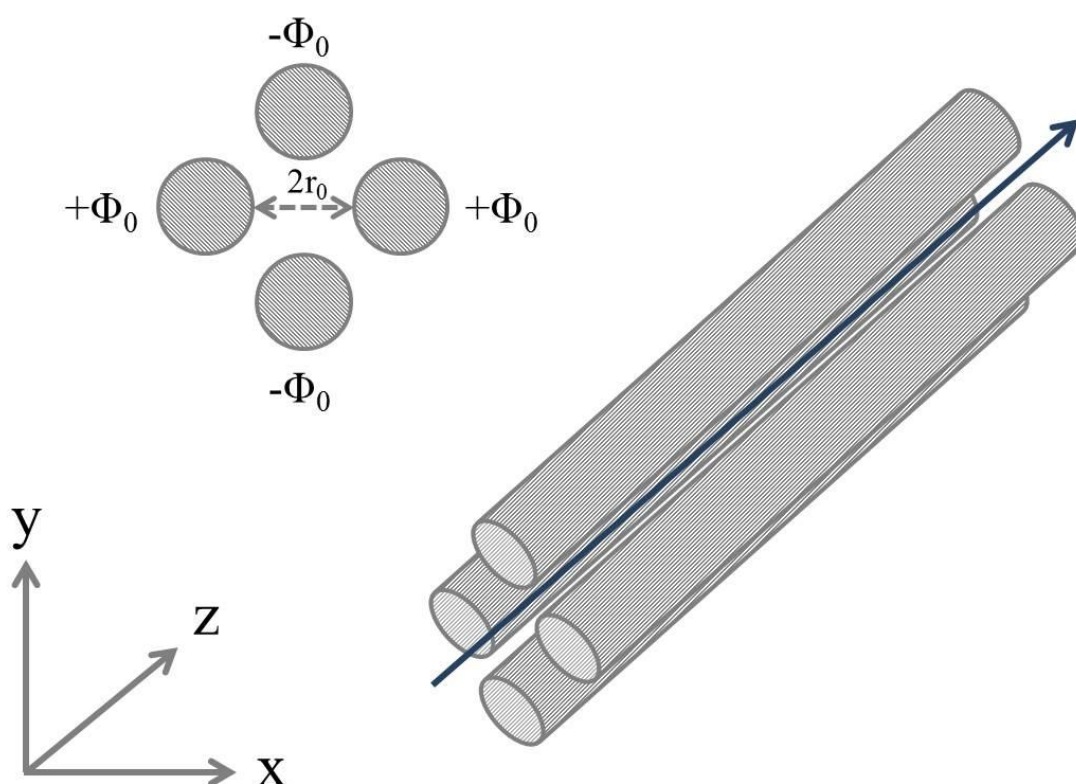
Figure 1.5 Schematic of the quadrupole mass analyser, ions enter the quadrupole along the z-axis and are subjected to the electric field imposed by the rods held at either positive or negative potential.

1.1.2.3 Time of Flight

Time of flight mass analysers separate ions based on their velocity which is dependent on their *m/z*. Ions are accelerated into the mass analyser by the difference in potential

between an electrode and an extraction grid. Ions acquire the same kinetic energy during this process and therefore their velocity will be related to their *m/z* ratio, see Equation 1.2. In this equation, which describes time taken, *t*, for an ion of given *m/z* ratio to reach the detector, *L* is the distance ions travel to the detector and V_s is the initial acceleration potential.[1]

$$t^2 = \frac{m}{z}\left(\frac{L^2}{2eV_s}\right)$$

1.2

Ions enter a field-free region known as the flight tube, where they separate according to velocity. A detector is located at the other end of the flight tube; *m/z* is subsequently measured by recording the time taken for ions to reach the detector. TOF mass analysers are generally associated with high transmission efficiency and therefore provide good sensitivity. Additionally, analysis time is short and upper mass limit of ions is high (>1,000,000 Th). The mass resolution achieved by TOF analysis is however poor (typically 5000 at *m/z* 1000). This can be somewhat improved through the use of a reflectron or ion mirror placed at one end of the flight tube, see Figure 1.6. Ions of the same *m/z* enter the reflectron with a kinetic spread and ions with larger kinetic energies will penetrate further into the ion mirror. Lower energy ions will therefore be reflected at an earlier timepoint thereby minimising the temporal spread of ions and improving mass resolution. Tandem instruments such as the QqTOF allow one to observe the fragmentation of ions by selecting and fragmenting ions in two sequential quadrupoles before scanning the resulting fragment ions in the TOF.[1]
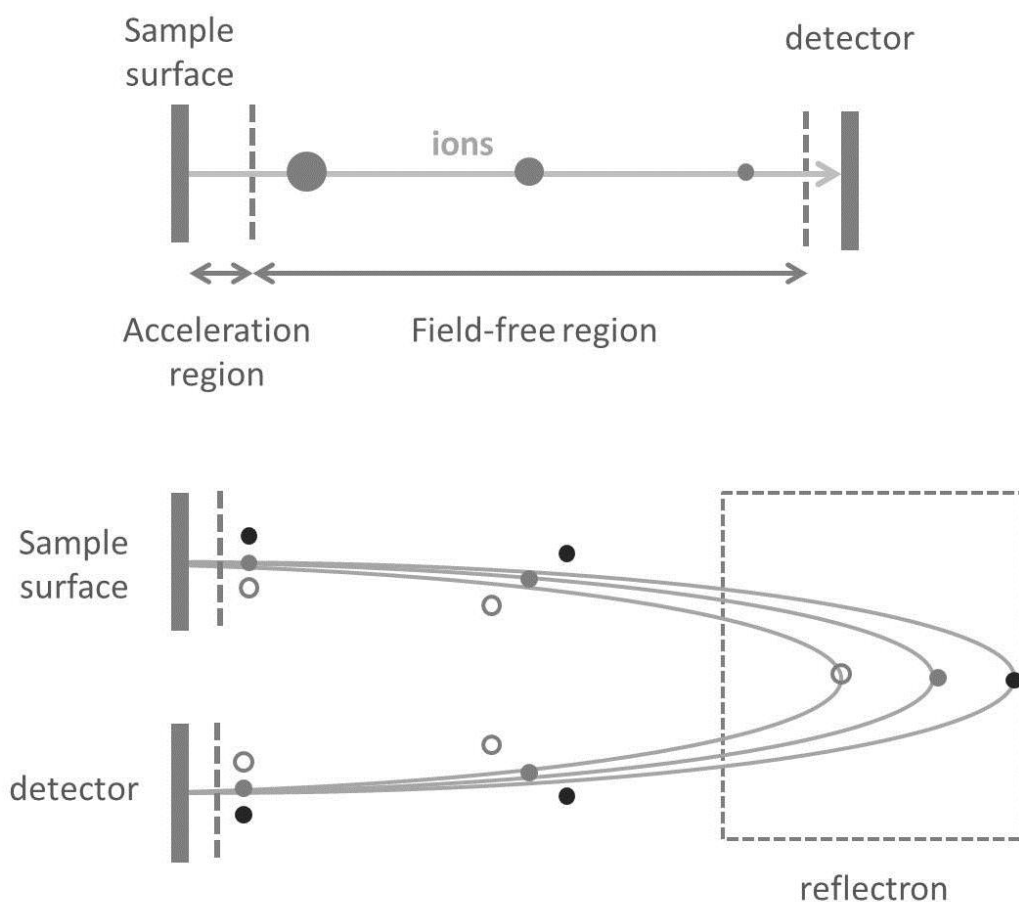
Figure 1.6 Principles of the TOF mass analyser which measures the time taken for ions of different *m/z* to reach the detector and the reflectron which can be used to improve mass resolution when using a TOF.

1.1.2.4 Orbitrap

The Orbitrap is a relatively new mass analyser, developed by Makarov and first introduced in 2000.[30,31] Branded as a smaller, cheaper and more energy efficient alternative to the high mass accuracy analysis provided by Fourier Transform-Ion Cyclotron Resonance (FT-ICR) mass spectrometry, the Orbitrap mass analyser has since been reported for the analysis of numerous analytes including proteins, peptides, oligosaccharides and glycoproteins. The high mass accuracy, mass resolving power and dynamic range of the Orbitrap make it the ideal choice for many types of analytical

experiment.[31] Ions are injected into the space between two electrodes: an inner 'spindle' which is surrounded by an outer barrel-shaped electrode, see Figure 1.7. A voltage is applied to the inner electrode while the outer is held at ground potential. Injected ions rotate around the inner electrode and oscillate along the z-axis. The frequency of ions oscillating in this dimension is related to the m/z ratio of ions via equation 1.3.[1]

$$\omega = \sqrt{\left(\frac{z}{m}\right)k}$$

1.3

Where k is field curvature and ω is frequency. Current is induced in the electrodes by oscillating ions and is measured, converted to frequency via the Fourier Transform and calibrated to m/z.[1]
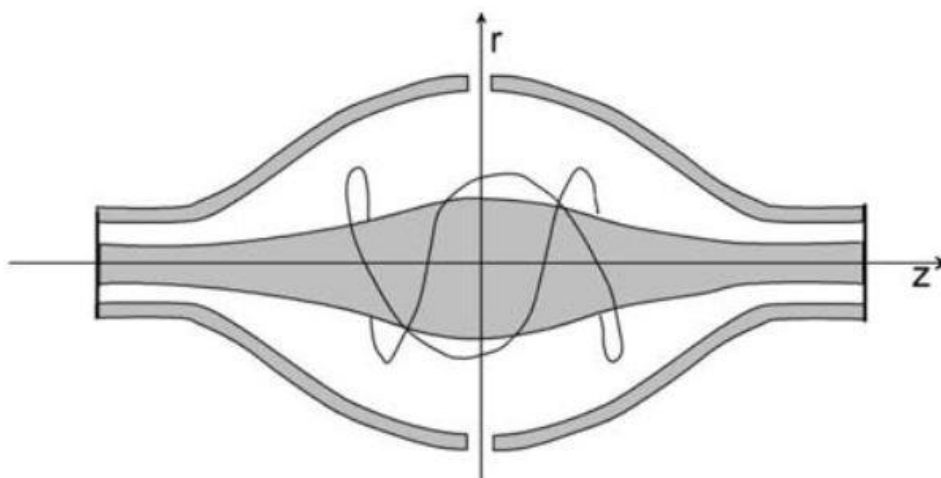
Figure 1.7 The Orbitrap mass analyser, ions are injected into the space between two electrodes where they oscillate along the z-axis with a frequency related to their m/z, reproduced with permission from [1].

1.1.3 Ion detection

Ions which pass through the mass analyser must be detected and a signal produced which is proportional to their abundance. Commonly, ions are detected using an electron multiplier in which a current is induced via collisions with accelerated incoming ions.[1] In the case of the Orbitrap mass analyser no such detector is required because the signal is generated by induction of current by oscillating ions, as described above.[31]

Mass spectrometry has proved a useful analytical tool and the advent of ion sources which could produce ions from large biomolecules was a turning point. The detection of such species with retention of spatial information was similarly important, and has enabled mass spectrometry imaging of thin tissue sections, whole body sections, bacterial colonies and plants.[21,32-50] There are numerous ways in which ions can be produced for MSI and some of these methods will be discussed in more detail in the following section.

1.2 Mass Spectrometry Imaging Methods

1.2.1 Matrix Assisted Laser Desorption-Ionisation Mass Spectrometry Imaging

Mass spectrometry imaging is made possible through sampling discrete spots or raster lines across a surface and the collection of mass spectra from each location. The intensity of a particular *m/z* species may then be mapped across the area by corresponding pixel intensity with spectral intensity for each pixel to produce an image.

Since its inception numerous applications of MALDI MSI have been developed for both biological and synthetic species and sample types.[18,51-53] MALDI MSI has been reported for thin tissue sections including whole body sections,[34,39,54] with the detection of peptides, proteins, lipids, oligonucleotides and drugs and associated metabolites

reported.[5,32,33,40,55-57] Clinical and pharmaceutical applications of such methods include the delineation of tumour margins via detection of characteristic proteomic and lipidomic signatures.[37,38,58] This has clinical implications for classification and diagnosis of tumour type,[36,59] which can greatly affect patient treatment and prognosis. There are also implications for the field of drug discovery and preclinical research because the localisation of a drug in tissues of a preclinical model could be mapped with respect to the exact location of the tumour. Whilst much work has focussed on applications in oncology, MALDI MSI is not limited to this and imaging of other types of tissue for research into other diseases has also been done. These include the imaging of peptides and proteins from brain sections of a Parkinson's disease model, which found a number of differences in expression profiles between disease and wild-type samples.[60] A number of recent reviews have discussed the use of MALDI MSI in clinical applications.[61-63]

The capabilities of MALDI MSI have been improved through development of sources employing high repetition rate lasers which allow high-throughput analysis.[15,64] Faster acquisition times will be essential as spatial resolution of images improves and larger quantities of data are acquired. Spatial resolution in MALDI MSI is typically limited by the diameter of the laser beam size. Pixel sizes of <20 μm can be routinely accessed by commercial instruments which is sufficient to distinguish between most tissue anatomies although imaging of organelles within single cells remains beyond the capabilities of MALDI.[65] A method known as oversampling is commonly employed in MALDI MSI, in which the sample stage is scanned continuously beneath the laser beam and relies on complete ablation of matrix at each location has allowed pixel sizes smaller than the laser beam diameter to be accessed.[66] Further improvements have been enabled through employing 'transmission geometry' in which a laser beam irradiates the

sample from behind therefore exhibiting a smaller beam diameter[67] and the atmospheric pressure MALDI source developed by Spengler in which the laser optics are positioned close to the sample and ions are collected via an opening in the optics themselves.[68] The drive towards higher spatial resolution in MALDI comes at the cost of sensitivity: the smaller the area irradiated per pixel the lower the desorption/ionisation yield. Therefore the requirements for individual experiments must be considered in advance.

Another area of significant interest is the development of quantitative MALDI MSI methods. The ability to analyse not only what is there but how much is there is of particular importance in the field of pharmaceutical research. Barriers to absolute quantification using MALDI include poor understanding of ion suppression, analyte extraction, extraction efficiency, ionisation efficiency and ion stability.[65,69,70] Ion suppression, or the competition for charge, during ionisation of a complex biological sample is common to many types of mass spectrometry analysis,[71] however the addition of a matrix compound during MALDI further complicates this issue. Heterogeneity in tissue samples can result in changing ion suppression effects across a single tissue section which can be amplified during matrix application due to sample composition-dependent changes in crystal size and morphology.[65] Several methods incorporating the use of internal standards to correct for these effects have been reported.[72-75] Such standards can be deposited directly onto the tissue or placed on the substrate prior to tissue sectioning which has been demonstrated to provide improved linearity.[76] One problem with this method is differences in extraction efficiency between compounds which have been dosed *in vivo* and spiked standards. Methods in which tissue homogenate is mixed with a standard prior to freezing in a mould and sectioning have been suggested as more appropriate because both extraction efficiency and ion

suppression can be accounted for. Such methods have been reported for the quantification of pharmaceuticals in tissue.[73]

A steady increase in the number and variety of applications employing MALDI MSI technology has increased the pressure for robust methods. Improvements in the publication and uptake of standardised, validated methods will be essential for routine clinical and biomedical analysis.[77] It is common for different research groups to optimise analytical methods for their own individual applications. Various stages of sample preparation and data acquisition can be adjusted for optimal analysis including: tissue thickness, tissue washing, matrix choice, matrix application and instrumental parameters.[65] Initiatives such as European COST Action BM1104 are working to improve guidelines around best practice by comparison and sharing of methods and techniques used in different laboratories.[78] The introduction of an open access file format and conversion software have also opened possibilities for sharing data between laboratories; allowing data acquired using different instruments to be viewed and analysed.[79,80]

Whilst highly successful MALDI MSI methods exist for the high resolution imaging of biological tissue, the fundamental requirement for the addition of a matrix compound raises the question of how useful and truly 'untargeted' MALDI MSI can be. Alternative ionisation methods in which the sample can be analysed with little or no preparation under ambient conditions could provide a more truthful analysis and provide a route towards more robust quantification of targets in tissue.

1.2.2 Desorption Electrospray Ionisation Mass Spectrometry

Desorption electrospray ionisation (DESI) mass spectrometry imaging was first described in 2004 by Takats *et al.*[81] The technique allows for desorption of gas-phase ions from a surface of interest at ambient pressure from the sample in its native

environment. DESI analysis involves directing an electrospray ionisation source at the surface of interest, see Figure 1.8. Charged droplets impacting on the surface desorb soluble species from the sample before entering the mass spectrometer via a carefully positioned heated inlet.
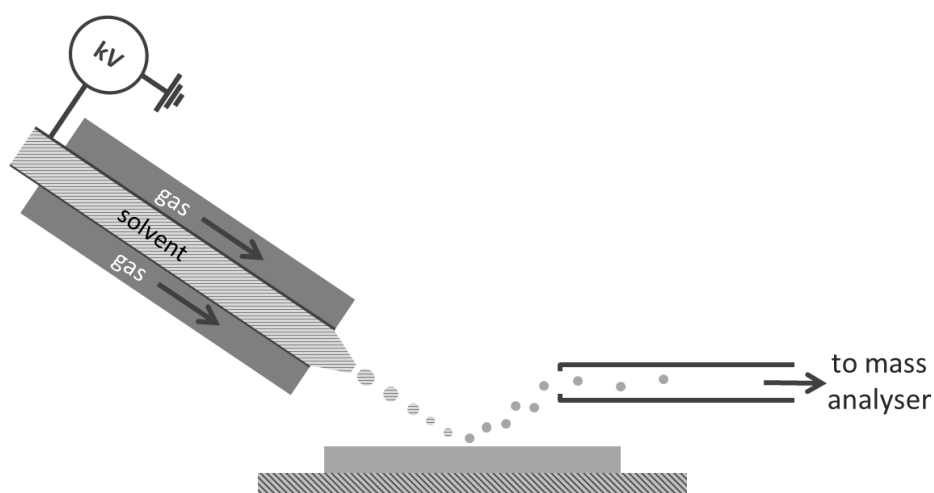
Figure 1.8 Illustration of desorption electrospray ionisation mass spectrometry. An electrospray ionisation source is directed towards a surface where analytes can dissolve into the electrospray droplets which are collected by an extended inlet.

Over the last 10 years methods have been developed for DESI interrogation of a range of biomaterials including thin tissue sections, bacterial biofilms and polymers.[41,45,82-89] DESI mass spectrometry has been used to image the distribution of drugs and lipids in rat brain, lung, kidney and testis[83], neurotransmitters in porcine and rabbit adrenal glands[90] and a variety of lipids in human prostate cancer[91], human liver adenocarcinoma[84] and various human brain tumours.[92] DESI has also been reported for mapping the exchange of metabolites between *Bacillus subtilis* and *Streptomyces coelicolor*[45] and identification of a range of bacterial species from colonies in petri dishes.[93]

Several studies aiming to optimise and characterise the capabilities of DESI have been reported. Takats *et al* set out the optimal DESI experimental parameters including

sample-to-inlet distance, electrospray parameters and angles between electrospray tip, inlet and sample surface.[81] Further to this, in 2008 Kertesz *et al* described an investigation into considerations of scanning and surface alignment.[94] Green *et al* used a model sample consisting of a thin uniform film of Rhodamine B deposited on glass, to further optimise sampling geometry on a sample of uniform composition. [95,96] The spatial resolution of DESI is determined by the 'erosion diameter' of the sprayer; DESI sprayer geometry, solvent system, flow rate and sheath gas pressure all have a direct effect on erosion diameter.[96] Recently Abbassi-Ghadi *et al* demonstrated that through the use of optimal DESI spray and geometry parameters, highly reproducible spectral profiles from a complex, biologically relevant sample could be obtained.[97] Typical pixel sizes accessible by DESI MSI are in the region 50-250 μm.[98]

1.2.3 Liquid-based surface sampling Mass Spectrometry

1.2.3.1 Liquid extraction surface analysis

Liquid based surface sampling was first described in 2002 in a report by Van Berkel.[99] In that work, the sampling probe consisted of two capillaries, one inside the other, in which solvent is delivered to the surface via the outer capillary and aspirated away through the inner capillary towards an ESI source. The solvent forms an interface between the sample surface and the probe tip which is known as the liquid micro-junction (LMJ). Soluble analytes dissolve into the liquid which is aspirated away and introduced to the mass spectrometer via electrospray ionisation. The method was originally used to sample compounds separated on the surface of TLC plates. In this experimental set-up, solvent was delivered to the surface continuously; this was termed the liquid microjunction surface sampling probe (LMJ-SSP).[100] Coupling of the LMJ-SSP to a mass spectrometer allowed for the analysis of various small molecules such as dyes[99] and drugs and their metabolites from tissue samples.[101] The concept of sampling

a surface by a wall-less liquid microjunction was commercialised by Advion Biosciences who incorporated the technology into their Triversa NanoMate nano-electrospray platform.[100] This platform did not operate with a continuous flow of solvent but instead used disposable conductive pipette tips which performed both extraction and electrospray, see Figure 1.9. This method was termed liquid extraction surface analysis (LESA).

Due to a combination of increased surface area sampled and improved extraction efficiency, LESA offers improved sensitivity over other ambient surface sampling techniques such as DESI. In addition, LESA has been successfully used in the extraction of intact protein species directly from biological samples such as tissue sections and dried blood spots (DBS).[102-109]
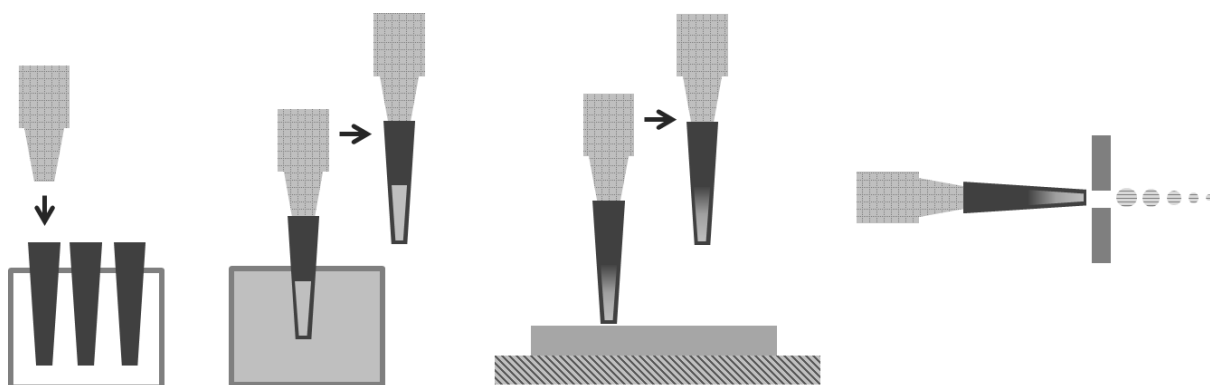
Figure 1.9 Schematic illustration of liquid extraction surface analysis. A conductive pipette tip is collected by the robotic arm. A portion of solvent is aspirated and the tip relocates to the user-defined location on the surface. The solvent is dispensed on the surface whilst maintaining contact with the pipette tip. Soluble analytes dissolve into the solvent which is then re-aspirated and introduced to the mass spectrometer via electrospray ionisation.

The study of proteins in biological systems is of great interest to the research community due to their ubiquity and the important roles they play in many processes.

Edwards *et al* reported the identification of a number of haemoglobin variants from neonatal blood samples, which are responsible for various haemoglobinopathies.[104] Schey *et al* describe the extraction and subsequent identification of proteins from a range of tissue types including mouse liver and kidney, and bovine ocular lens.[110] Intact protein ions can be identified via 'top-down' proteomics experiments in which the ion of interest is fragmented and a mass spectrum of the resulting fragment ions is acquired. Fragment masses can then be searched against a known proteome database. Top-down identification provides several advantages over the more established 'bottom-up' method, in which proteins in a sample are enzymatically digested into peptides before the sample enters the mass spectrometer.[111] Common problems with bottom-up methods include information loss, incorrect assignment of peptides and loss of peptides containing post-translational modifications.[111] Whilst these issues are somewhat overcome through top-down methods, database searching software for top-down methods frequently mis-assign fragments and require improvement before top-down methods can be applied reliably.

LESA also offers opportunities for further sample manipulation due to the decoupling of desorption/ionisation events. There have been several reports of coupling of LESA to HPLC-MS for improved separation, detection and identification of protein species.[103,109,112] The additional potential for introduction of derivatisation compounds or internal standards makes LESA an attractive technique. Whilst LESA-MS does provide spatial information, its capabilities as an imaging technique are limited due to the area of sample covered per pixel.

1.2.4 Flow-probe mass spectrometry

The LMJ-SSP system which incorporates a continuous flow of solvent, a smaller probe diameter and the potential for raster sampling could provide a different route towards

improved spatial resolution for liquid-based methods. The Flow-probe (see Figure 1.10), which was based on the LMJ-SSP developed by Van Berkel *et al.* was recently commercialised by Prosolia.[49,113] Flow-probe mass spectrometry has been demonstrated in the analysis of lipids, drugs and metabolites.[49,114-117] Van Berkel and Kertesz demonstrated the detection of multiply charged ions by Flow-probe mass spectrometry, however the resolution of the mass spectrometer was insufficient to identify the ions.[113]

Imaging by the Flow-probe can be performed in spot-mode analysis in which the probe does not move while the LMJ is in contact with the surface. The probe analyses discrete locations across the surface and an image is reconstructed by relating ion intensity to pixel location. Tissue imaging with a pixel size of ~600 μm was reported by ElNaggar *et al.* and Prideaux *et al.*[114,115] This level of spatial resolution was sufficient to establish the distribution of drugs within diseased lung tissue. It may also be possible to perform imaging in a continuous raster mode which could allow for further improvement of spatial resolution; a question which will be investigated in this thesis.
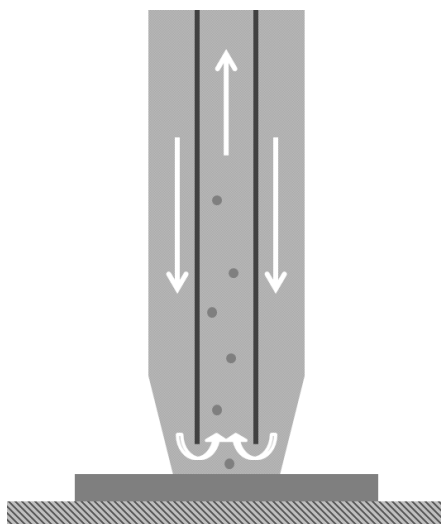
Figure 1.10 Schematic diagram illustrating surface sampling via continuous flow. Solvent is delivered to the surface via a capillary at a user defined flow rate. Soluble analytes dissolve into the solvent before the solution is aspirated away from the surface

via an inner capillary. This solution is introduced to the mass spectrometer via electrospray ionisation.

1.3 Raman Spectroscopy

The Raman effect was first described in 1928[118] and is a commonplace tool in chemistry laboratories for the analysis of reaction products, assessment of purity and confirmation of chemical identification. A sample is irradiated with an intense monochromatic (usually visible) light source. Most incident photons undergo elastic collisions in which the energy of the photon remains unchanged, however a small number undergo inelastic collisions with sample molecules resulting in a change in rotational or vibrational energy of the molecule. After the molecule absorbs energy from a photon, the molecule is raised to a higher, unstable energy state (known as the virtual excited state) and quickly returns to a lower energy state. If a molecule is initially in the ground state and after absorption returns to the ground state the overall energy remains constant. This is known as Rayleigh scattering. If however the molecule returns to an excited state then the energy of the molecules is increased by $+\Delta E_m$ or the difference between the ground and excited state, see Figure 1.11. Alternatively the molecule could exist in the excited state prior to absorption of photon energy. If after promotion to the virtual excited state the molecule returns to the ground state the overall energy of the molecule has changed by $-\Delta E_m$. A change in the energy of the incident photon can be detected and recorded in a spectrum known as the Raman spectrum. An increase in energy is detected as a band known as the Stokes shift and a decrease is known as the anti-Stokes shift. Due to the fact that more molecules exist in the ground state than the excited, the Stokes band has a higher spectral intensity.[119,120]
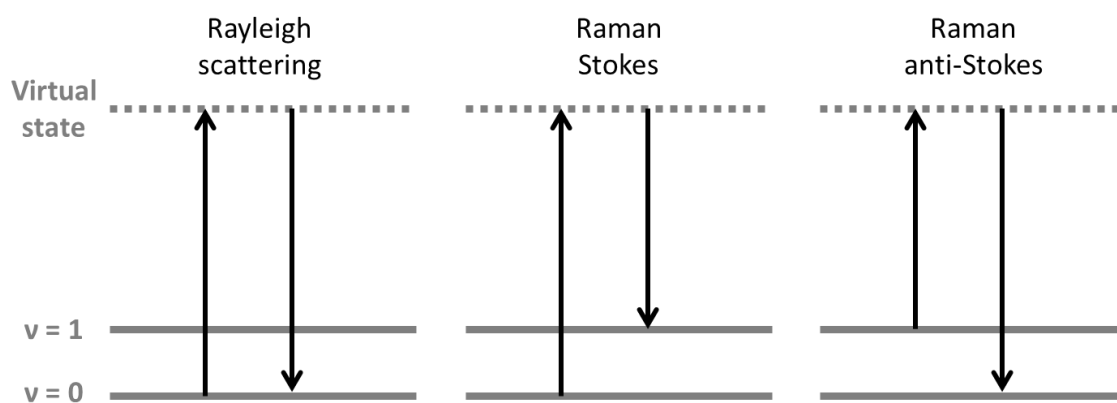
Figure 1.11 Energy level diagram illustrating Raman and Rayleigh scattering.

A relatively low number of photons go through the Raman scattering process, around 1 in 10^8, which accounts for the low sensitivity of techniques relying on spontaneous Raman scattering. Raman microscopy of biological samples can be achieved via scanning of the irradiating laser across a surface, but the long integration times required for sufficient signal to be acquired severely limit the use of Raman microscopy in biology.[121] Advances in laser technology and instrumentation have allowed new and more sensitive techniques to be developed – which still exploit the fundamental principles of Raman scattering.[122,123]

1.3.1 Theory of Coherent Raman Scattering

It is possible to obtain stronger molecular vibrational signals using a phenomenon known as coherent Raman scattering (CRS). CRS processes occur when two spatially and temporally matched excitation fields are incident upon a sample.[123] When the frequency difference between these two fields is resonant with a Raman active vibration, four major processes occur: coherent anti-Stokes Raman scattering (CARS) at two new frequencies, stimulated Raman gain (SRG) and stimulated Raman loss (SRL), see Figure 1.12.[124] The two latter processes are known as stimulated Raman scattering (SRS). If excitation fields are scanned across a sample and the corresponding changes in

energy are detected, molecular vibrations from different chemical components of the sample can be mapped as an image. This is known as either CARS or SRS microscopy.[125] SRS microscopy offers several advantages over CARS; firstly, there is no non-resonant contribution to the SRS signal which results in a linear relationship between intensity and concentration. Secondly, SRS produces signals identical to a spontaneous Raman spectrum which simplifies interpretation.[124] These features enable quantitative chemical imaging. The near-IR radiation used for SRS is ideal for biological samples because it causes minimal damage. This non-destructive feature of SRS means it can be used to take measurements *in vivo* and is a step towards *in situ, real-time*, quantitative measurements of biological systems.[123,126-132]
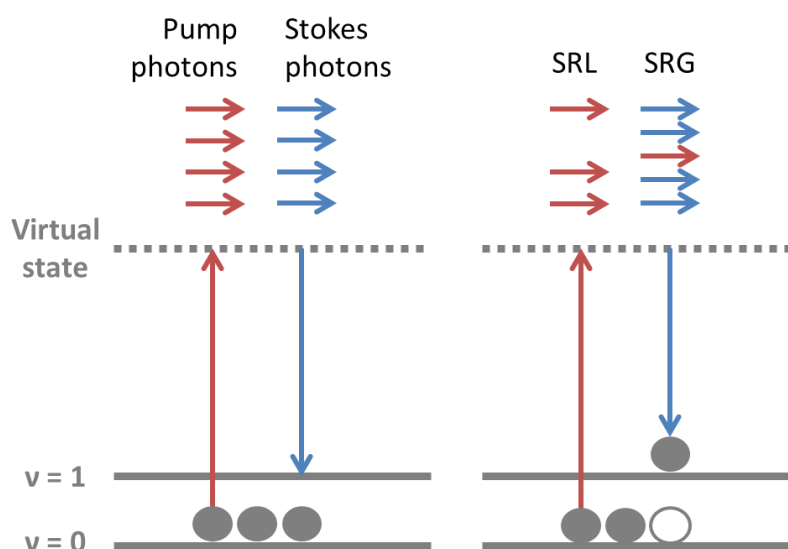
Figure 1.12 Energy level diagram depicting the stimulated Raman scattering process.

1.3.2 Stimulated Raman Scattering Microscopy

A number of applications of SRS microscopy have been reported. Biological analytes which have been imaged by SRS include drugs, water, lipids, proteins, nucleic acids and DNA.[123,126-129,131,133,134] Fast acquisition rates enable near video speed imaging which makes possible the monitoring of processes in real time.[126,131,133] In 2010, Saar *et al*.

demonstrated the real time *in vivo* imaging of water, lipids and proteins in skin and mapped the penetration of topically applied drug compounds.[126] The quantitative nature of SRS has been taken advantage of by Fu *et al.* who determined the concentration of melamine, polystyrene beads and PMMA in a mixed system[127] and also the concentration of a drug in biological cells.[128]
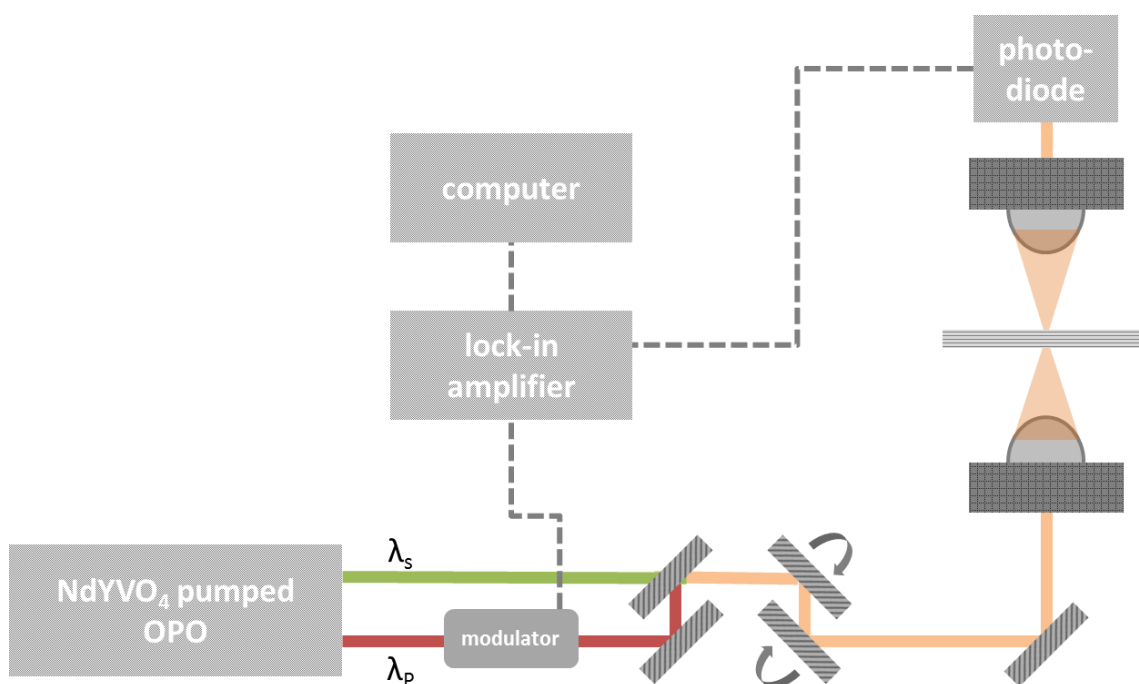
Figure 1.13 Illustration of the custom-built SRS microscope used in this work: two overlapping laser beams are generated by the Nd:YVO₄ laser and the laser pumped optical parametric oscillator (OPO). The pump beam is modulated at 80 KHz in order to distinguish the SRS signal from laser noise. A series of lenses and scanning mirrors direct the excitation beam towards the sample. Light exiting the sample is collected via the condenser lens onto a photo-diode which is connected to a lock-in amplifier which is tuned to the signal at 80 KHz.

One of the main drawbacks of SRS is its non-specific nature. SRS signals are produced by probing chemical bond vibrations which may be common to multiple species – for example C-H bonds are common to all lipids, so it is only possible to image 'lipids' in

general. This becomes increasingly problematic when imaging complex biological systems. It is difficult to isolate peaks which are unique to a single chemical compound, so attempting to image for example a drug in tissue is very difficult. Judicious choice of compounds can somewhat mitigate this problem (for example some Raman active modes such as nitrile and carbonyl appear in the biologically 'silent' region of the spectrum) but this approach has limited applicability. Another problem is caused by other absorption phenomena interfering with SRS signal, such as two-photon absorption (TPA). This commonly occurs in compounds which are highly absorbing of UV energy, such as haemoglobin and chlorophyll.[127,135,136] Such interference results in a non-linear intensity dependence with concentration – and hence measurements would no longer be quantitative. This thesis presents the use of SRS microscopy as a complementary tool in combined mass spectrometry imaging experiments and an assessment of its use as a quantitative technique.

1.4 Multimodal methods

There are numerous reports in the literature of different chemical imaging modalities being combined on the same sample - so called 'multimodal' imaging.[137-140] Several reasons exist for pursuing such methods; firstly, it could be possible to use one imaging method to understand how another method caused changes to the sample and therefore infer qualitative/quantitative information about sampling effects. For example optical microscopy is frequently used following MALDI analysis to provide information about irradiated regions and pixel size. This enables better characterisation and metrology of the technique. The perhaps most widely reported reason for employing multimodal methods is to simply combine the advantages of each individual technique and use them to provide complementary information from a single sample. The importance of executing multimodal MSI workflows on the same or adjacent tissue sections has been

recognised in studies seeking to combine mass spectrometry techniques, these will be discussed in more detail in the following sections.

1.4.1 Combined methods to study fundamental processes

There have been various reports of different imaging methods being combined with a second technique in order to probe fundamental processes involved. Several groups have used this approach to study the MALDI desorption/ionisation process. Fournier *et al.* imaged various matrix crystals after laser irradiation using white light microscopy and scanning electron microscopy (SEM) to assess any resulting morphology changes.[141] This method is a quick and simple way to visually assess irradiation effects, however provides no chemical or quantitative information. Tarzi *et al.* reported various chemical analyses including UV-Vis absorption spectroscopy and H[1]-NMR of thermally treated matrix compounds.[142] This allowed for the identification of thermal decomposition products of matrices but measurements were not carried out *in situ,* or on samples analysed directly by MALDI. Leisner and co-workers used an in-source, time-resolved imaging system to capture images of the desorption/ionisation process and allow for the elucidation of plume dynamics for two different laser pulse durations.[143] Photoacoustic measurements were used by Soltwisch *et al.* to study ejection yields under different laser wavelength and fluence conditions.[144] This provided a measure of quantitation of in-source events and allowed ionisation yields to be calculated because the amount of material removed from the surface relative to the number of ions detected could be measured. As yet, no method combining the ability to quantitatively measure changes to the sample surface and simultaneously image surface morphology has been reported.

Combined methods have also been demonstrated by various groups who have sought to better understand MALDI sample preparation by imaging the distribution of analytes

within single matrix crystals. The incorporation of peptides and proteins has been imaged using confocal laser scanning microscopy,[145,146] field emission scanning electron microscopy,[147] and time of flight secondary ion mass spectrometry.[148,149]

1.4.2 Combined methods for enhanced analysis

Through combining techniques such as MALDI and LESA, it is possible to maximise the advantages of each and use them in complement. Several examples of such an approach exist in the literature, MALDI MSI and LESA MS have been used on adjacent tissue sections to study drug absorption into skin; LESA MS was used as a verification step to complement the MALDI MSI data.[150] Quanico and co-workers used a MALDI MSI-guided approach to identify regions of anatomical interest. These regions of an adjacent section were then analysed by LESA coupled to LC-MS for improved sensitivity, resulting in more complete identification of proteins.[151] Griffiths *et al.* used MALDI MSI and LESA MS to demonstrate that a sample preparation technique for improved lipid analysis yielded similar results when two different ionisation methods were employed.[13] The potential for inclusion of internal standards in LESA extraction solvents was exploited by Tomlinson *et al.* who used LESA coupled to nano-electrospray ionisation and LC-MS to investigate ion suppression effects in MALDI.[152] Swales and co-workers demonstrated the complementary capabilities of various MSI techniques including MALDI MSI and LESA MS. They employed each on adjacent sections of organs from cassette- and discrete-dosed animals and compared their ability to detect four different target compounds.[153] It is important to note that each of these methods have employed MALDI MSI and LESA MS on adjacent sections which are therefore non-identical. This increases the challenge when attempting to correlate, compare or combine the data acquired with each technique. Additionally, this would be impossible in situations where no adjacent section is available.

Repeat analysis of a single tissue section was reported by Steven *et al.*[10] and Garrett *et al.*,[154] who demonstrated that multiple MALDI MSI datasets could be acquired from a single sample, either by taking advantage of remaining matrix after initial analysis or by addition of a tissue wash and re-application of matrix. These results show that re-analysis of tissue samples is an avenue towards obtaining complementary data. The importance of executing multimodal MSI workflows on the same tissue section has been recognised in studies seeking to combine other mass spectrometry techniques. Eberlin *et al.* reported a method for combining desorption electrospray ionisation (DESI) MSI for lipid imaging, MALDI MSI for protein imaging and H&E staining for morphological information on the same tissue section.[86] Eijkel and co-workers performed MALDI MSI and SIMS imaging on the same tissue section and outlined a workflow for correlating these datasets.[155]

1.5 Quantification by MALDI MSI

The development of methods which can be used to provide quantitative mass spectrometry images have been the focus of much research. Techniques which could provide quantitative data could also be used in combination with methods more traditionally used for non-quantitative imaging. During pharmaceutical preclinical studies it is necessary to establish absolute quantities of drugs and their metabolites within tissues of dosed animals.[69] Whole body autoradiography (WBA) or quantitative whole body autoradiography (QWBA) is the current preferred method for obtaining such information.[134,156,157] The technique involves tagging the drug compound with a radiolabel which may be imaged to determine the location of the drug. The advantages of this method are that it is highly sensitive and can be made quantitative by the use of a calibration radiation source; however it is limited by a lack of specificity. These data only measure the radiolabel and not the drug itself therefore it gives no indication as to

whether the drug has been metabolised. Furthermore, any metabolites which do not contain the radiolabel cannot be imaged so accumulation of such metabolites in an organ or tissue could be missed. Additionally, the process of tagging the compound of interest can be expensive and time consuming and could potentially alter the properties of the drug itself.[69] One of the biggest advantages of mass spectrometry is its label-free nature. Anything present in a sample which can be ionised will be present in the spectrum; there is no requirement for *a priori* knowledge. A single MSI experiment could in theory yield the distribution of a drug, its metabolites and colocalised endogenous species which could be a biomarker of disease progression, toxicology or therapeutic effect.[69]

Whilst MSI provides several advantages over traditional methods, ion suppression effects and variation in tissue extraction efficiencies present problems when using MSI as a quantitative technique. SRS microscopy, as a non-destructive technique whose signals are linear in concentration, could be used to quantify targets in tissue. This information could then be used to validate relative concentration distributions detected using mass spectrometry. This could help lead to a better understanding of ion suppression effects observed during mass spectrometry of complex samples and could aid validation of current 'quantitative' mass spectrometry methods.

1.6 Sample types used in this work

Methods in this thesis were developed using a variety of sample types. Tissue from control animals was used for initial optimisation studies. Mouse and rat brain thin tissue sections are widely used in MSI method development studies due to their abundance of lipid and protein species which are readily analysed by techniques such as MALDI and DESI. In addition rodent brain is small enough to image full sections relatively quickly

and contains easily defined anatomical features which have been well characterised by projects such as the Allen Brain Atlas.[158]

In addition to control rodent tissue, methods were further developed using drug-dosed tissue to demonstrate how such methods could be of use in pharmaceutical research. Thin tissue sections from various organs from a rat which had been cassette-dosed with four different drug compounds were used. Cassette dosing involves careful selection of drug compounds and simultaneous dosing for higher throughput screening of physiochemical and pharmacokinetic properties. The potential presence of four different drug compounds in tissues provides a good platform from which to assess the relative sensitivities of the different techniques studied.

Whilst many MSI techniques have been developed for tissue imaging purposes, another significant area of research is MSI analysis of microbial samples. For the period 2013-2016, the World Economic Forum has listed the rise of antibiotic- resistant bacteria as one of the greatest threats to human health globally.[159-162] Addressing this complex problem requires a better understanding of basic microbial functions such as intercellular communication and biofilm formation, pathways to resistance and a large-scale search for novel therapeutic compounds or anti-microbial substances. Methods for the fast and accurate chemical analysis of microbes and their metabolites could aid in all three facets of this work.[41,43,45,159] Ambient mass spectrometry techniques are ideal for the analysis of bacterial colonies because they can directly sample living colonies growing in petri dishes.[44,163] Mass spectrometry imaging of bacterial colonies has allowed for the mapping of metabolites and could aid in elucidation of pathways and processes, many of which remain poorly understood.[41] Diverse classes of analytes including lipids, peptides, and metabolites have been detected from bacterial colonies

by ambient MS techniques such as DESI, nano-DESI, LESA and the Flow-probe.[45,48,49,87,164]

1.7 Project aims

This thesis presents the development of methods to provide insight into the metrology of MALDI MSI and liquid surface-sampling methods alongside SRS microscopy. Additionally, methods for acquiring enhanced information from biological samples have been developed. Practical considerations for combination of the techniques are presented, such as suitable sample substrate and sample preparation methods. Analysis of the same complex, biological sample type and also of specially designed and prepared calibration references on each instrument has provided novel information pertaining to their capabilities in terms of spatial resolution, chemical identification and sensitivity. The specific aims of this project are:

- To combine MALDI and LESA MSI on the same tissue section and evaluate the individual capabilities of each technique in terms of spatial resolution, relative sensitivity and breadth of molecular classes analysed. This work is presented in Chapter 3.

- To use SRS microscopy to image MALDI sampling effects on model samples which will be designed and prepared in this work. The removal of material under different experimental parameters will be measured. This work is presented in Chapter 4.

- To assess how suitable a multimodal MALDI, LESA and SRS method for tissue imaging would be and characterize any associated problems. This work is presented in Chapter 5.

- To develop a LESA MS method for the quantification of intact proteins from tissue and assess the capabilities and scope of such as method. This work is presented in Chapter 6.

- To develop methods for the analysis of proteins in tissue using the Flow-probe and compare such methods with more established LESA methods. This work is presented in Chapter 7.

- To develop methods for the analysis and imaging of proteins from microbiological samples using LESA MS. This work is presented in Chapter 8.

Chapter 2

Materials and Methods

Materials

Ethanol, methanol, dimethylformamide, acetonitrile and formic acid were purchased from Fisher Scientific (Leicestershire, UK). Trifluoroacetic acid was purchased from Acros Organics. α-cyano-4-hydroxycinnamic acid (α-CHCA), *para*-nitroaniline (PNA), dihydroxybenzoic acid (DHB), sinapinic acid (SA) and picolinic acid (PA) matrices were purchased from Sigma Aldrich (Gillingham, UK) and glass slides from Thermo Scientific. Ubiquitin protein standard and stable-isotope labelled ubiquitin (98% atom 13-C and 15-N) were purchased from Sigma Aldrich (Gillingham, UK). Fresh frozen mouse brain tissue was provided by Prof. Steve Watson at the University of Birmingham. Cassette-dosed rat tissues, control rat tissues and drug compounds were provided by Dr Richard Goodwin at AstraZeneca.

Methods

2.1.1 Sample preparation

2.1.1.1 Tissue preparation

A cassette-dosed rat was euthanized 2 hours post oral administration (of moxifloxacin, olanzapine, erlotinib and terfenadine at 25, 10, 10 and 25 mg/kg respectively). Tissues were snap-frozen and stored at -80°C until required. Rat organs were sectioned at a thickness of 14 μm and thaw mounted on either glass slides (for MALDI and LESA) or

glass coverslips (for SRS). Coverslips were turned face-down onto a glass slide and sealed with nail varnish to protect the sample from objective lens immersion oil. Control mouse brain tissue was sectioned (Leica CM 1850 Cryostat, Milton Keynes, UK) at 10 μm thickness and thaw-mounted onto glass slides. Mimetic tissue models were sectioned at 14 μm and thaw-mounted onto glass slides.

2.1.1.2 Tissue preparation for MALDI MS analysis

Tissue sections were coated with CHCA or PNA matrix (5 mg/mL in 80% MeOH, 0.1% TFA) using a TM-Sprayer (HTX Technologies, LLC). Matrix was sprayed with a flow rate 0.115 mL/min and track speed of 1333 mm/min. The capillary temperature was 90 °C and the spacing between tracks was 3 mm. A total of 8 spray cycles were used to deposit matrix.

2.1.1.3 Model sample preparation

Model samples for analysis by MALDI and SRS were prepared using a TM-Sprayer (HTX Technologies, LLC). Thin films of various drug and matrix compounds were deposited on glass coverslips (thickness 170 μm).

2.1.1.4 Preparation of bacterial samples

A strain of *Escherichia coli K-12* was inoculated onto solid LBA medium (LB 20 g L^{-1} Agar 20 g L^{-1}) in 6 cm diameter petri dishes. The smaller size of petri dish allows it to fit inside the sample tray of the Advion TriVersa NanoMate system. Bacteria were incubated at 21 °C for 3 days before storing in the dark at 4°C or were allowed to grow at room temperature on the bench and were stored at room temperature (~20 °C). The solvent system for surface sampling/electrospray ionisation consisted of acetonitrile (J.T. Baker, The Netherlands) and water (J.T. Baker, The Netherlands) (39.6:59.4) with 1% formic acid (Sigma-Aldrich Company Ltd., Dorset, U.K.).

2.1.2 Analytical Techniques

2.1.2.1 Liquid extraction surface analysis

Surface sampling was performed using a TriVersa Nanomate chip-based electrospray device (Advion, Ithaca, NY). The electrospray device was coupled to a Thermo Fisher Orbitrap Velos (Thermo Fisher Scientific, Bremen, Germany) instrument. The robotic system was controlled through LESA Points and ChipSoft 8.3.3 software. The sample was mounted in the LESA universal adaptor plate and scanned using an Epson flatbed scanner. The scanned image was imported into LESA Points and the sampling locations were defined. Sampling locations were selected with an x,y spacing of 1mm, covering the whole tissue section. For contact LESA the z coordinate was set to a height 0 mm relative to the sample surface. For 'non-contact' LESA experiments, the pipette tip descended to a height ~0.2 mm above the surface of the sample. The solvent system for extraction and electrospray was methanol, water and formic acid (69.3:29.7:1). The robotic arm collected a conductive pipet tip and aspirated 0.7 µL of solvent from the reservoir. The arm relocated to the x,y coordinates specified by LESA Points software. The pipette tip descended to the predetermined height (see above) and dispensed 0.5 µL solvent. The liquid microjunction was maintained for 4 seconds before re-aspiration. Each sample was delivered for 1 minute via the Triversa Nanomate with a gas pressure of 0.3 psi and a tip voltage of 1.4 kV. Positive ion mass spectra were acquired in full scan mode (*m/z* 150-2000) at a resolution of 100 000 at *m/z* 400. The Automatic Gain Control was turned off and the injection time fixed at 100 ms. Each scan was comprised of 5 coadded microscans.

2.1.2.2 MALDI mass spectrometry imaging

MALDI MS imaging was carried out on a QSTAR XL QqTOF mass spectrometer (AB Sciex). An Elforlight (Daventry, UK) Nd:YAG laser with λ=355 nm was coupled to the

MALDI source via a 100 μm diameter fibre (OZ Optics Ltd) and was operated at a frequency of 1 kHz. The fluence at the sample surface was ~120 J m^{-2}. The sampling raster speed was 0.2 mm/s. Data were acquired in positive ion mode with a pixel size of 100 x 100 μm or 50 x 50 μm.

2.1.2.3 DESI MS analysis mouse brain tissue

Mouse brain tissue was sampled using a Prosolia DESI source coupled to a Thermo Fisher Orbitrap Velos (Thermo Fisher Scientific, Bremen, Germany) instrument. The solvent system used was 1:1 dimethylformamide:acetonitrile, delivered with flow rate of 1 μL/min and a nebulising gas pressure of 175 psi. The electrospray voltage was 5 KV and the inlet capillary temperature was set to 300°C. Raster speed was set to 88.88 μm/sec, which corresponded to a pixel size of 200 μm in the x-dimension. Positive ion mass spectra were acquired in full scan mode (*m/z* 650 - 1000) at a resolution of 100 000 at *m/z* 400. The Automatic Gain Control was turned off and the injection time fixed at 500 ms. Each scan was comprised of 1 single microscan. Optical images were acquired after DESI analysis. The section and an adjacent control section were then prepared and analysed by MALDI mass spectrometry imaging under the same conditions outlined above.

2.1.2.4 SRS microscopy

SRS images were acquired using a custom-built system operated with an Nd:YVO$_4$ laser and a tunable OPO. This involves two collinear laser beams focussed to a single focal point; the Stokes beam has a wavelength of 1064 nm, the Pump beam can be tuned between 790-950 nm. The resulting signal was detected by a lock-in amplifier. The Stokes beam was modulated at high frequency (80 MHz) in order to distinguish SRS from low frequency laser noise. A series of scanning mirrors direct the beam at the

sample and scan in x,y and z dimensions to produce 3-dimensional image stacks. Sample regions were selected by white light microscopy prior to SRS. Integration times were optimised for each individual sample/analyte.

2.1.2.5 UV-Vis absorption spectroscopy

UV-Vis absorption spectra of matrices were acquired using a Lambda 850 (PerkinElmer) spectrometer.

2.1.2.6 Hematoxylin and Eosin Staining

H&E staining was performed by Epistem according to standard protocols.

2.1.2.7 Optical Microscopy

Optical microscopy was performed on a Pathscan Enabler IV slide scanner and an Olympus CX40 microscope fitted with 5, 10 or 20x magnification objective lenses.

2.1.3 Image Generation

2.1.3.1 LESA

A separate RAW file was generated for each LESA experiment (corresponding to a single pixel), consisting of multiple scans. Data were converted from RAW to mzML using msconvert as part of ProteoWizard.[165] The mean spectrum within a single mzML file (for each pixel) was calculated and output to a new mzML file, resulting in a spectrum per pixel. These were combined, along with the spectra locations, into an imzML file using imzMLConverter to produce an MS image. [80]

2.1.3.2 MALDI

WIFF files generated by the QSTAR XL QqTOF mass spectrometer were converted to mzML files using MS Data Converter (AB Sciex). One mzML file was produced per

raster line of the image. These were converted to a single imzML file using imzMLConverter.[80]

2.1.4 Data analysis

2.1.4.1 Multivariate analysis

Image files (imzML) were viewed and processed using in house software, running in MATLAB (R2014b). Memory efficient PCA and k-means ($k = 7$) were applied as described by Race *et al.*[166] with the smoothing step in the preprocessing workflow modified to dual-pass Savitzky-Golay (window size of 11).

PC1 and PC2 score images were used in combination to generate a binary mask for isolating the on tissue spectra. MALDI MSI on tissue spectra were further reduced by selecting peaks from the total spectrum using a gradient based method,[166] using the modified preprocessing workflow described above. NMF ($k = 25$. MATLAB) and t-SNE[167] were applied to the reduced data.

Chapter 3

MALDI and LESA Mass Spectrometry

Imaging of Biological Tissue

Work presented in this chapter was published in the following paper: Randall, E. C.; Race, A. M.; Cooper, H. J.; Bunch, J. *Analytical Chemistry* **2016**, 88, 8433-8440. This is included in Appendix 1.

3.1 Overview

Reports of LESA MS imaging in the literature have so far focussed on the detection of single classes of analytes.[153] This chapter presents the optimisation and combination of MALDI and LESA MSI for sensitive analysis and high spatial resolution imaging of drugs, lipids and proteins in tissue. The method could be suitable for use in pre-clinical pharmaceutical studies in which the distribution of drugs alongside endogenous molecules is desired.

In this work MALDI MSI was used to image post-LESA analyte distribution in tissue and indicated how LESA sampling had altered the sample composition. Therefore in addition to demonstrating the complementary use of LESA and MALDI, this experiment provided insight into aspects of LESA sampling such as the area of tissue surveyed and variation and spatial precision of sampling. Previously this has only been assessed using optical images. A number of multivariate analysis techniques were applied to the MALDI MSI data to determine spectral and spatial changes to the sample which

occurred as a result of LESA sampling. This analysis indicated how MALDI spectra change as a result of LESA sampling. Practical considerations for combining MALDI and LESA on the same sample, e.g., the optimal order for sampling are also discussed. A further ambient mass spectrometry technique, DESI, which is more traditionally used for tissue imaging was also assessed by the combined MALDI method and results were compared with those from LESA.

3.2 Experimental

3.2.1 Tissue sample preparation

Tissue was prepared as described in section 2.2.1. One section of mouse brain was spotted with 4 x 0.1 µL of 2 mM solutions of erlotinib, propranolol and verapamil. The section which was destined for imaging by LESA-MS was spiked with 0.3 µL 200 nM erlotinib solution (80/20 methanol/water).

3.2.2 Optimisation of MALDI MS analysis of drug compounds

Solutions of nine different drug compounds (erlotinib, propranolol, verapamil, imatinib, amiodarone, retinoic acid, tiotropium bromide, neratinib and moxifloxacin) were made up to a final concentration of 2 mM in 80:20 methanol:water solvent. Matrix solutions (α-CHCA, PNA, DHB, SA and PA) were made up to a final concentration of 50 mM in 80:20 methanol:water solvent with 0.1% trifluoroacetic acid modifier. Stainless steel MALDI target plates were spotted with 0.3 µL of each drug/matrix combination, 3 repeats of each combination were deposited. MALDI data were acquired in positive ion mode with 1 second accumulation time and 5 scans coadded per spectrum. The average ion intensity across 3 repeats was plotted for the $[M+H]^+$ ion of each drug compound. MS/MS spectra of erlotinib were acquired between *m/z* 50 and 410 via fragmentation in the collision cell with a normalised collision energy of 35%.

3.2.3 Liquid extraction surface analysis

LESA sampling was performed as described in section 2.2.4. A grid of 108 sampling locations was selected with an x,y spacing of 1mm, covering a single mouse brain tissue section.

3.2.4 MALDI mass spectrometry imaging

The tissue section which had been imaged by LESA MS and a control section placed adjacent on the slide were coated with CHCA matrix as described in section 2.2.2. MALDI data were acquired as described in section 2.2.5, with a pixel size of 100 x 100 μm. In a repeat experiment the same data were acquired from a replicate sample with a pixel size of 50 x 50 μm.

3.2.5 DESI MS analysis mouse brain tissue
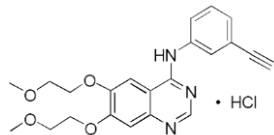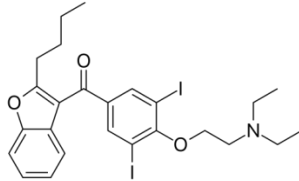
A section of mouse brain tissue was imaged using the DESI method described in section 2.2.6. This section, along with a control section placed adjacent on the slide was coated with CHCA matrix as described in section 2.2.2. MALDI data were subsequently acquired as described in section 2.2.5, in positive ion mode with a pixel size of 100 x 100 μm.

3.3 Results and Discussion

3.3.1 Selection of suitable pharmaceutical compound

A study was conducted to select a suitable drug compound which could be used in combined MALDI and LESA experiments. A list of possible compounds was identified from the literature, see Table 3.1. The suitability of these drugs for use in Raman spectroscopy and SRS microscopy was also considered, this will be discussed in more detail in Chapter 4.

Table 3.1 List of drug compounds identified from the literature as used in chemical imaging experiments.

Drug compound	Molecular structure	Drug target/use	Reference of use in chemical imaging
Erlotinib		Tyrosine kinase inhibitor, used to treat certain types of cancer.	− SRS microscopy of colon cancer cells [168] − MALDI MSI [169,170]
Amiodarone		Antiarrhythmic used in treatment of cardiac dysrhythmias.	− Raman spectroscopy[171] − SIMS imaging[172]

Drug compound	Molecular structure	Drug target/use	Reference of use in chemical imaging
Moxifloxacin		Antibacterial agent	− MALDI MSI[173] − Raman spectroscopy[174]
Retinoic acid		Used as a topical formulation in treatment of various skin conditions	− MALDI MSI (as matrix)[175] − SRS microscopy[123]
Tiotropium bromide		Anticholinergic bronchodilator	− MALDI MSI[176-178]
Imatinib		Tyrosine-kinase inhibitor	− Atmospheric pressure MALDI MSI[179] − SRS microscopy[128]
Propranolol		Beta blocker	− LESA MS[112] − DESI MS[180] − MALDI MSI[75]
Verapamil		Calcium channel blocker used to treat	− Laser ablation electrospray (LAESI) MS[181]

Drug compound	Molecular structure	Drug target/use	Reference of use in chemical imaging
		hypertension.	

Analysis of each compound listed in Table 3.1 was performed by MALDI mass spectrometry with a selection of matrix compounds commonly used for the analysis of drugs and tissue.[10,15,182-187] Droplets of each drug and matrix solution were deposited on MALDI target plates. Both the total number of moles of each drug deposited and the molar ratio of analyte:matrix were kept constant for each combination. Average ion intensity detected for the protonated species of each drug (n=3) is plotted in Figure 3.1. Erlotinib was found to exhibit the highest ion intensity with almost every matrix compound; in addition ions of erlotinib were detected in the absence of a matrix. Erlotinib, in addition to propranolol and verapamil, were identified as suitable candidates for further study. Interestingly the lowest ion yields were obtained for experiments using retinoic acid which is contrary to its reported use as a matrix compound.[175] An example MALDI mass spectrum (acquired using CHCA) is presented in Figure 3.2. CID of parent ions detected with m/z 394.2 confirmed the detection of erlotinib, with characteristic fragment ions[170] detected at m/z 336.1 and 278.8, see Figure 3.2.
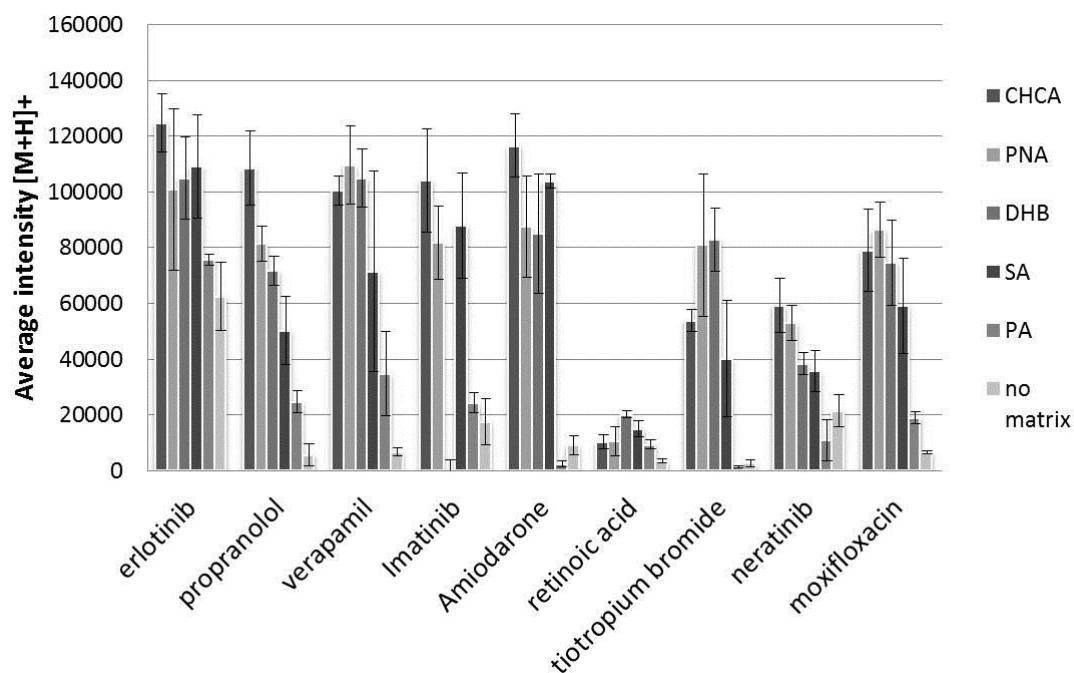
Figure 3.1 MALDI mass spectrometry analysis of selected drug compounds in combination with a variety of matrices, each data point represents the average of three repeats, errorbars represent ±1 standard deviation.
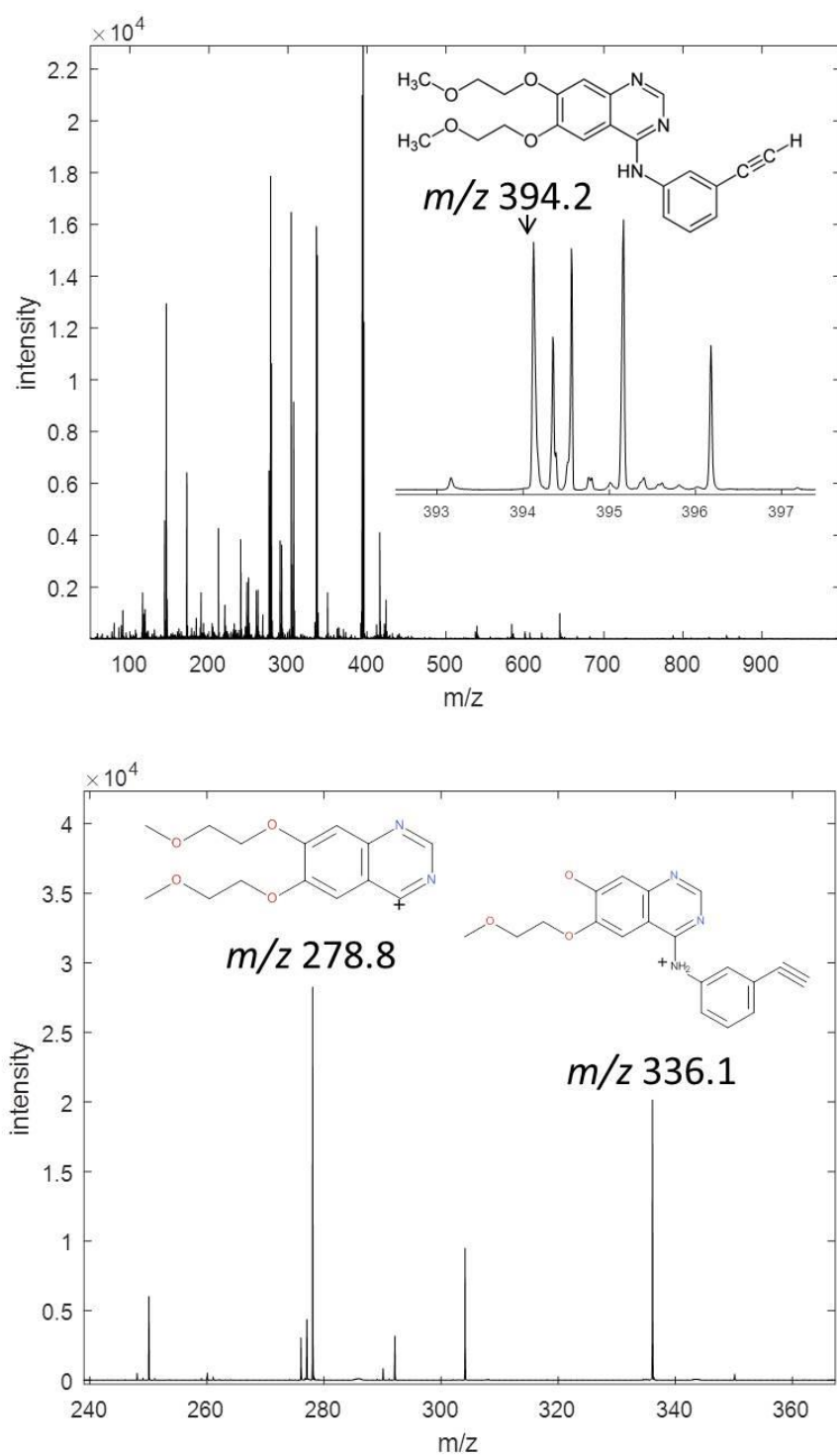
Figure 3.2 Top: MALDI mass spectrum acquired from sample of erlotinib in combination with CHCA, ions with m/z 394.2 correspond to [M+H]+ ions of erlotinib. Bottom: MS/MS spectrum of parent ions with m/z 394.2, major fragment ions were detected with m/z 278.8 and 336.1 confirming the detection of erlotinib.

The three drug compounds identified as suitable for MALDI analysis were then used in a further experiment to establish whether they could be detected in a complex biological mixture. Erlotinib, propranolol and verapamil were spotted onto sections of mouse brain tissue; the tissue was coated with α-CHCA matrix and imaged using MALDI MSI, see Figure 3.3. Both erlotinib and verapamil were detected as the protonated species as well as the potassium adduct, due to large amounts of potassium and sodium in biological tissue. No ions were detected with *m/z* corresponding to ions of propranolol.
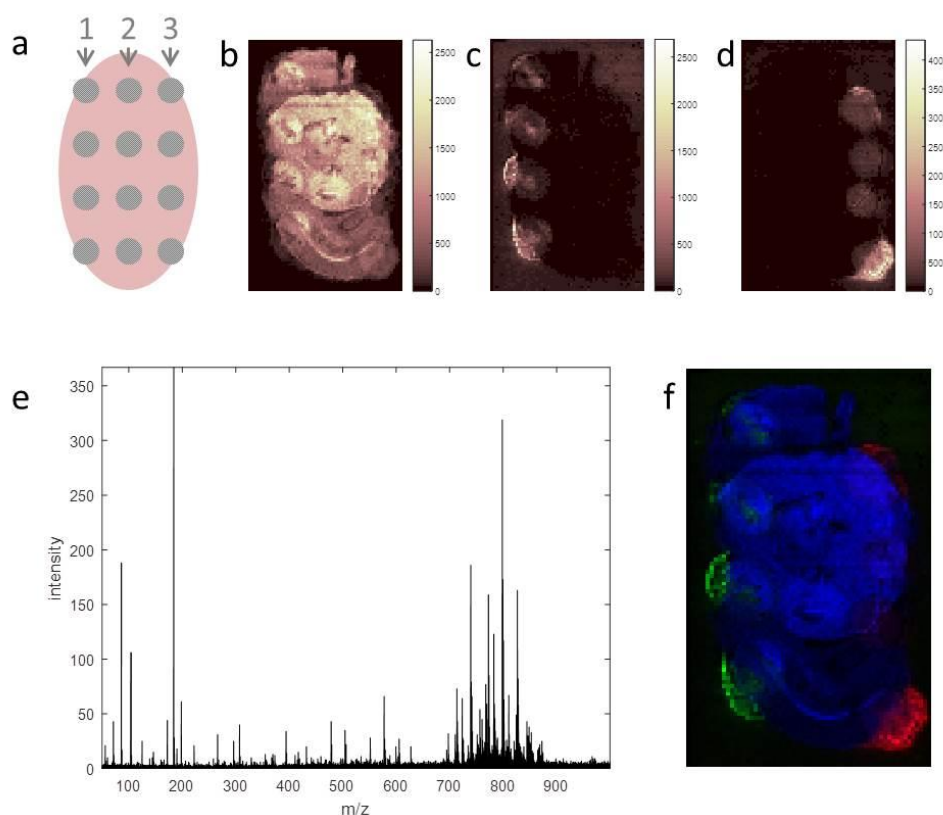
Figure 3.3 MALDI MS imaging of drug compounds in mouse brain tissue: a) diagram of location of spiked drug compounds 1) erlotinib, 2) propranolol, 3) moxifloxacin, 4 spots of each compound were deposited, b) ion intensity map of ions with *m/z* 826.6 tentatively assigned as [M+K]$^+$ phosphatidylcholine lipid (PC 36:1), c) ion intensity map of ions detected at *m/z* 432.2 assigned as [M+K]$^+$ ions of erlotinib, d) ion intensity map of ions with *m/z* 493.4 assigned as [M+K]$^+$ ions of verapamil, e) example single

pixel spectrum acquired from tissue region spiked with erlotinib, the majority of ions detected in the region *m/z* 700 – 850 are lipid ions, f) overlay of ions in b,c and d.

3.3.2 Optimisation of LESA MS analysis of mouse brain tissue

Erlotinib was selected as a potentially useful compound due to successful detection by MALDI from tissue and its reported usefulness in SRS microscopy studies.[128] A further sample of mouse brain tissue was spiked with erlotinib for analysis by LESA mass spectrometry. An example LESA mass spectrum from drug spiked tissue is displayed in Figure 3.4. These data demonstrate for the first time that multiple analyte classes can be detected and analysed simultaneously by LESA MS. Erlotinib, heme, a variety of PC lipids and ubiquitin were all detected in a single extraction/electrospray event.
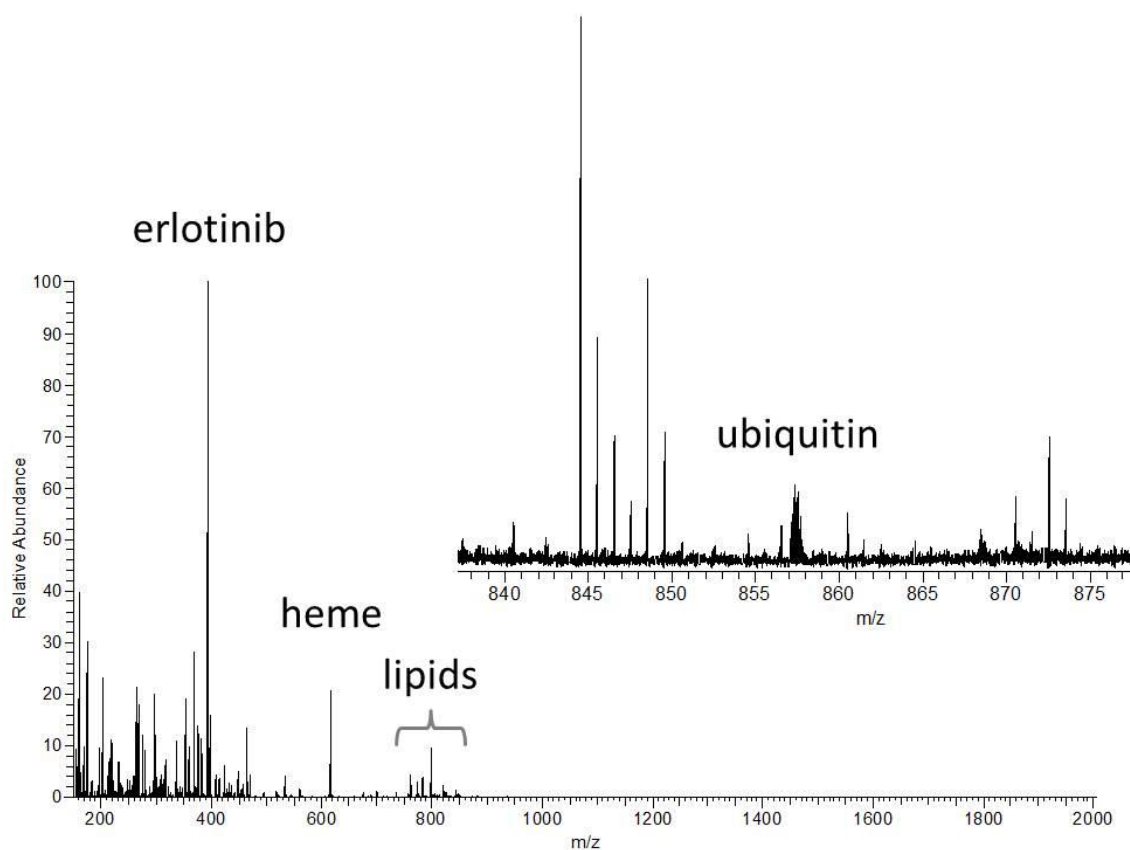
Figure 3.4. Example LESA mass spectrum acquired from erlotinib spiked mouse brain tissue. Erlotinib was detected as the [M+H]$^+$ ion at *m/z* 394.1779, heme was detected at

m/z 616.1797, ions in the range *m/z* 700-900 are tentatively assigned as various PC lipids and ubiquitin was detected in a variety of charge states including (+10) shown inset at *m/z* 857.3751.

3.3.3 Optimisation of MALDI sample preparation

Sample preparation is a critical stage in MALDI MSI analysis and can have a large effect on results and experimental success. The choice of matrix application method is of particular interest for mass spectrometry imaging due to the balance which must be struck between efficient analyte extraction and preservation of analyte location. Solvent-free matrix application – often achieved by sublimation – can provide images with high spatial resolution and good retention of spatial integrity.[186] However in pharmaceutical studies sensitivity is often critical and molecules of low abundance such as drugs might not be successfully extracted via solvent-free matrix application methods. In this work a TM-Sprayer (HTX Technologies, LLC) was used for matrix application. This system deposits user-defined quantities of matrix onto the surface via a heated nebuliser. The 'wetness' of the spray can be controlled via spray temperature, proportion of organic solvent composition, speed of spray travel and flow rate. Each of these parameters was used at its maximum recommended value in order to provide as dry a deposition as possible (i.e. high temperature, high organic solvent composition, maximum speed of travel and minimum flow rate). A sample of mouse brain tissue was coated using this method and optical images were taken after each cycle of coating – up to a final number of 8 cycles, see Figure 3.5. Visual analysis of these images suggests that complete coverage is achieved after 5/6 cycles of this deposition method. A slight change in crystal morphology at the edge of the tissue suggests that some residue from the tissue has been incorporated into matrix crystals beyond the tissue boundary. This region extends ~30 μm from the tissue edge. After one cycle of matrix deposition

53

crystals have an approximate diameter of 10 μm. The morphology of crystals formed on glass and tissue is very different. CHCA on glass forms small regular individual crystals whereas individual crystals on tissue are not clearly discernible. An important point of note is that crystals are smaller than the 50/100 μm pixels used for MALDI imaging experiments. If crystals are larger than the laser spot size or pixel size it cannot be assumed that the spatial location of analytes within tissue has been maintained.
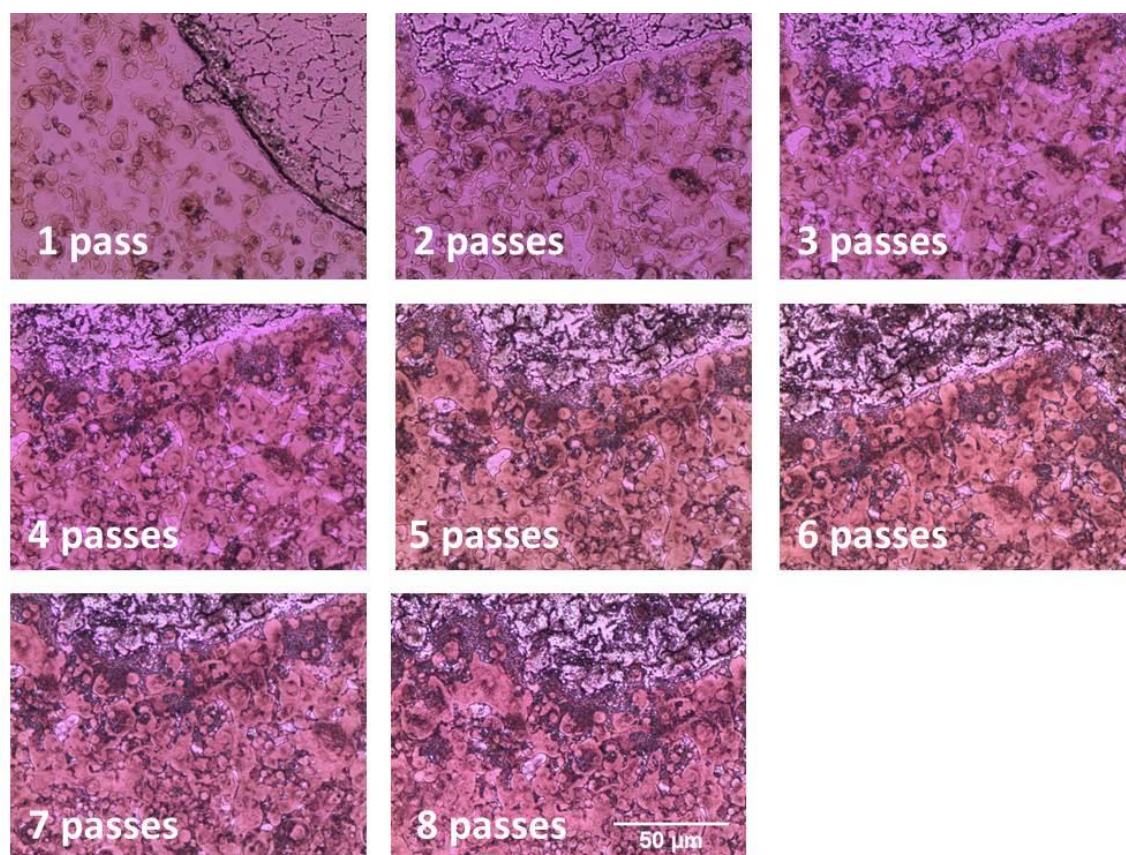
Figure 3.5 Optical images of mouse brain tissue after deposition of subsequent cycles or 'passes' of matrix. All images are presented on the same scale.

Visual analysis of tissue images provides an indication of crystal sizes and surface coverage but only mass spectrometry analysis can provide information about efficiency of analyte extraction. The sample prepared with increasing amounts of matrix was analysed by MALDI MSI to assess the number of ions detected under different sample

preparation methods, see Figure 3.6. A number ion images are presented in Figure 3.6; including various ions identified as PC lipids and characteristic fragment ions including the phosphatidylcholine headgroup detected with *m/z* 184.1. It is clear from these images that larger amounts of matrix result in higher numbers of ions detected but also a larger degree of lipid delocalization.
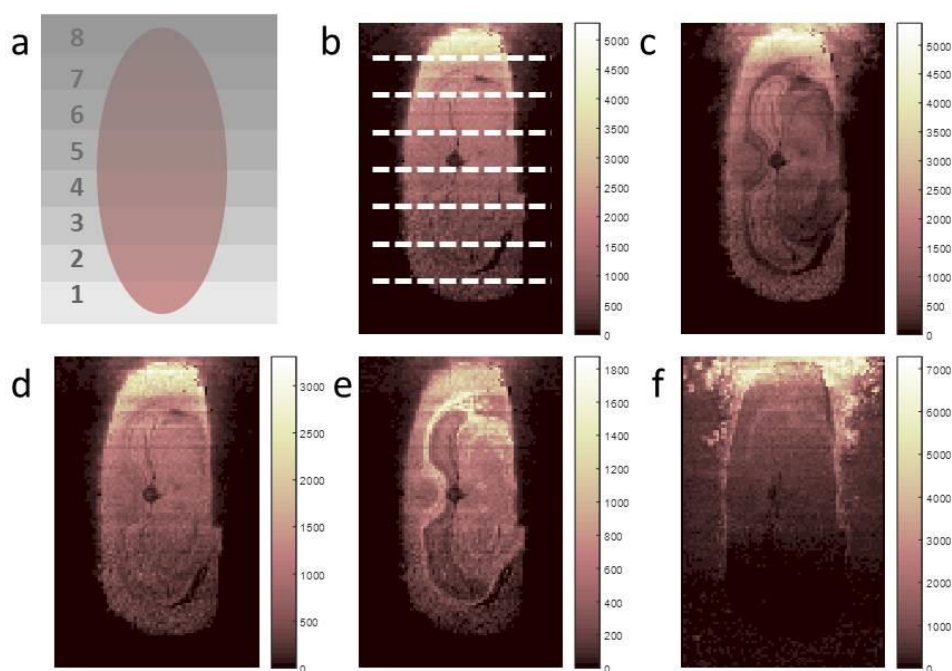
Figure 3.6 MALDI MS images of various lipids after application of different amounts of matrix, a) illustration of sample, numbers indicate no. cycles of matrix deposition, b-f) ion intensity maps of ions with m/z 798.6, 772.6, 739.6, 826.6 and 184.1. Increased ion intensity towards the top of these images demonstrates how increased amounts of matrix aid desorption/ionisation yields. Increased ion intensity in the background towards the top also suggests delocalisation of analytes occurs after repeated deposition cycles.

3.3.4 Combined LESA and MALDI MS imaging experimental design

A workflow was designed to investigate the combined use of LESA and MALDI MS imaging on the same tissue sample. In order to establish a suitable order of techniques, serial sections of mouse brain tissue were subject to LESA then MALDI or MALDI then LESA analysis as outlined in Figure 3.7. A third serial section was used as a morphological reference to which any apparent changes in tissue structure could be compared. The mouse brain was spiked with erlotinib prior to analysis in order to assess the capabilities of each technique with respect to how useful each would be in pharmaceutical distribution studies.
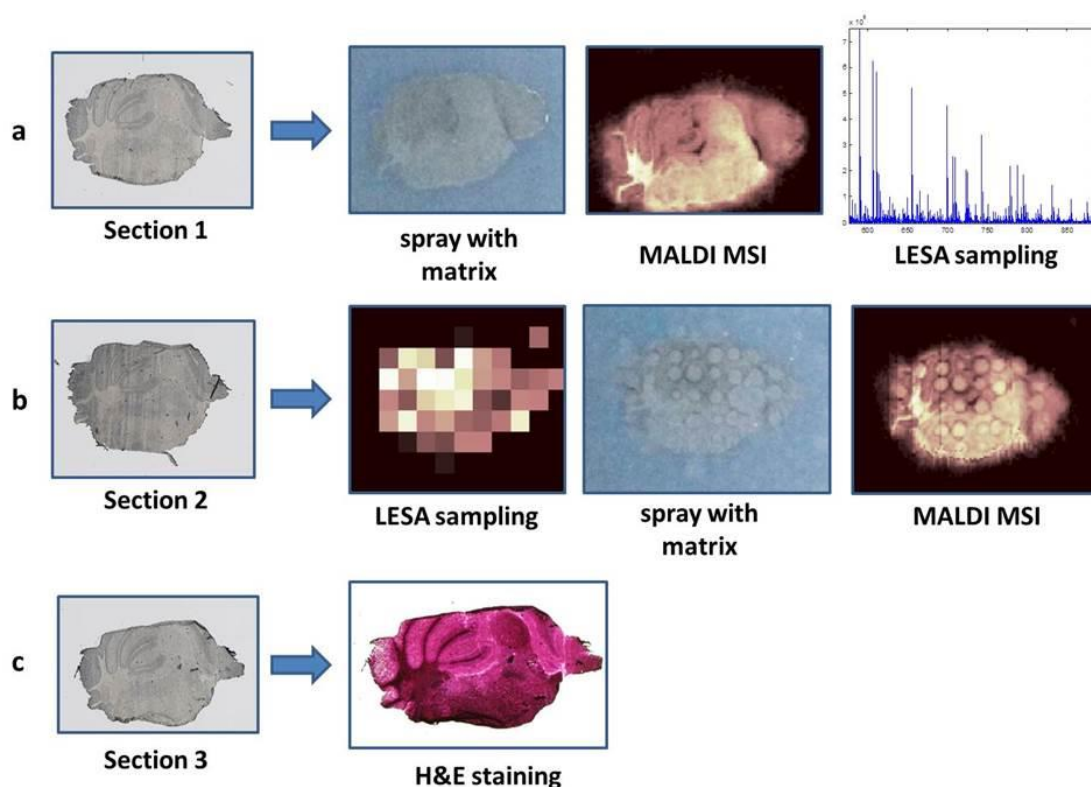
Figure 3.7 Illustration of combined method: 3 serial sections each underwent a different workflow.

3.3.5 Combined LESA and MALDI MS imaging of drug in mouse brain tissue: LESA MS Imaging

An automated surface sampling routine was defined and implemented using the TriVersa Nanomate. The locations selected for LESA sampling are illustrated in Figure 3.8. Full scan mass spectra were obtained from each sample location (for example, see Figure 3.8). This approach demonstrates how LESA-MS is able to detect multiple classes of analyte in a single extraction/electrospray event. Peaks in the m/z range 700-900 correspond to various phosphatidylcholine (PC) lipid ions, preferentially detected as the protonated species. Ions detected with m/z 734.5708, 760.5870 and 782.5703 are tentatively assigned as protonated molecules of (PC) 32:0 (Δppm = 1.9), (PC) 34:1 (Δppm = 2.5), and (PC) 36:4 (Δppm = 1.2), respectively. Multiply charged protein ions predominantly appear in the m/z range 600 – 1200. Ions centred at m/z 857.5714 (charge state +10) are tentatively assigned as ubiquitin (Δppm = 2.1), which has previously been detected from mouse brain tissue using LESA MS.[110] Other protein ions (unidentified) were detected with charge states ranging between +7 and +22. The tissue was spiked with 0.3 µL of 200 nM erlotinib solution. Taking into account the area over which the droplet spread, it is estimated that approximately 4.8 femtomoles erlotinib was present per 0.4 mm^2 (the approximate area covered by a single contact LESA extraction, more discussion to follow). The drug was detected in every LESA spectrum sampled from this region. Example LESA MS images are displayed in Figure 3.8, indicating the different distributions of PC 32:0, ubiquitin, haem and erlotinib, across the tissue section. In this work it was found that a LESA solvent system comprising 70% MeOH, 1% formic acid is suitable for the simultaneous analysis of singly charged small molecules, multiply charged protein species and the drug compound erlotinib, which was detected with m/z 394.1773 corresponding to $[M+H]^+$ ions.
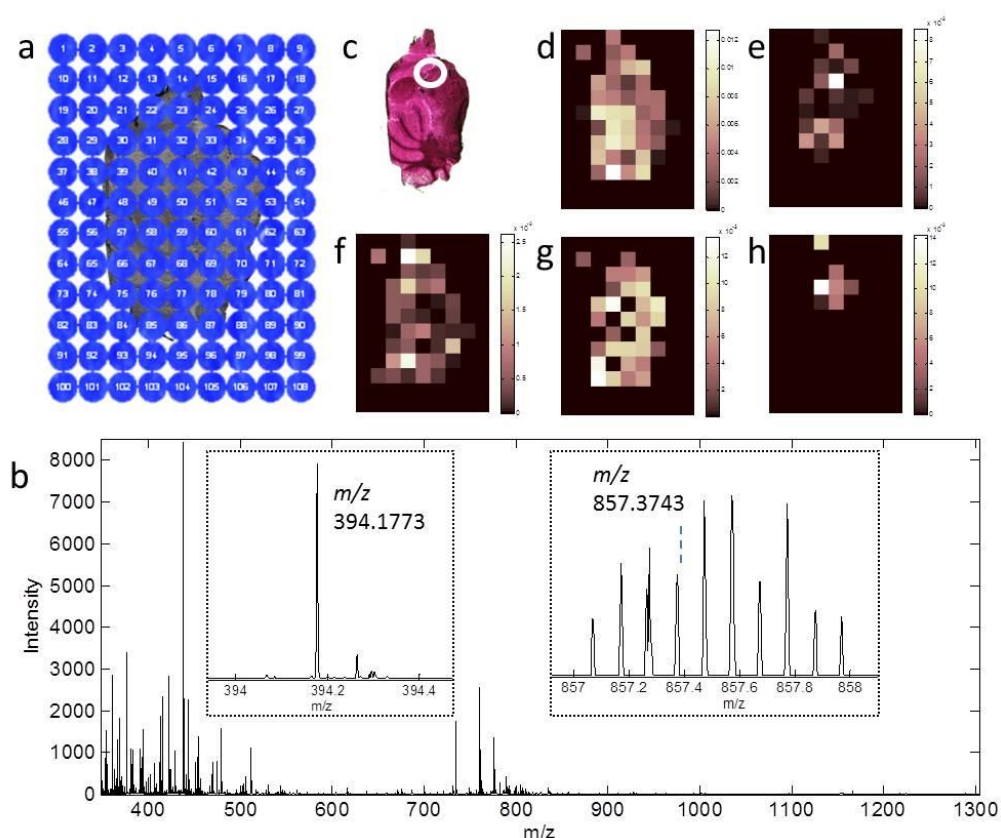
Figure 3.8 LESA MS of mouse brain tissue: a) locations selected for LESA sampling, b) example full scan LESA mass spectrum, peaks with *m/z* in the range 700 – 900 correspond to lipid ions, enlargements of peaks corresponding to erlotinib (m/z 394.1773) and ubiquitin (m/z 857.3743) are shown inset, c) circle indicates location selected for erlotinib deposition, covering both grey and white matter as indicated using H&E stained reference, d) LESA MS image of ions with *m/z* 184.0739 corresponding to the phosphotidylcholine lipid headgroup, e) LESA MS image of ions with *m/z* 760.5870 corresponding to [M+H]⁺ ions of PC 34:1, f) LESA MS image of ions with *m/z* 616.1782 corresponding to haem, g) LESA MS image of ions with *m/z* 857.3743 corresponding to ubiquitin (+10 charge state), h) LESA MS image of ions with *m/z* 394.1773 corresponding to [M+H]⁺ ions of erlotinib.

3.3.6 Investigations into 'contact' LESA sampling

The spacing between LESA sampling locations was defined as 1mm; the minimum distance permitted by LESA Points software. The sampling routine used to acquire this dataset was modified to minimise solvent spreading and allow for greater sampling precision; the method will be referred to as 'contact' LESA. A more detailed discussion about the development of the contact method is presented in Chapter 8, and was published in Analytical Chemistry.[108] The method involves bringing the sampling pipette into contact with the sample surface prior to solvent dispensation and an assumption that the solvent is entirely contained within the pipette tip during sampling – 'plugged' by the sample itself. Optical images of the tissue section after 'non-contact' (in which only the solvent was allowed to come into contact with the surface and all other sampling parameters remained the same) and 'contact' LESA demonstrate a decrease in relative size of area sampled (spot diameter decreased from ~1158 μm to ~690 μm), Figure 3.9. These images also highlight un-sampled regions of tissue which result from sample spacing of 1 mm and sampling diameter of less than 1 mm. Reliability of sampling was found to be improved using contact LESA because there was no requirement for formation of a stable liquid microjunction. Sampling precision was also found to be improved using contact LESA; the pipette tip walls prevent solvent droplet spreading to the same extent observed during normal LESA sampling, although some spreading beyond the expected contact area of the pipette tip is still observed.
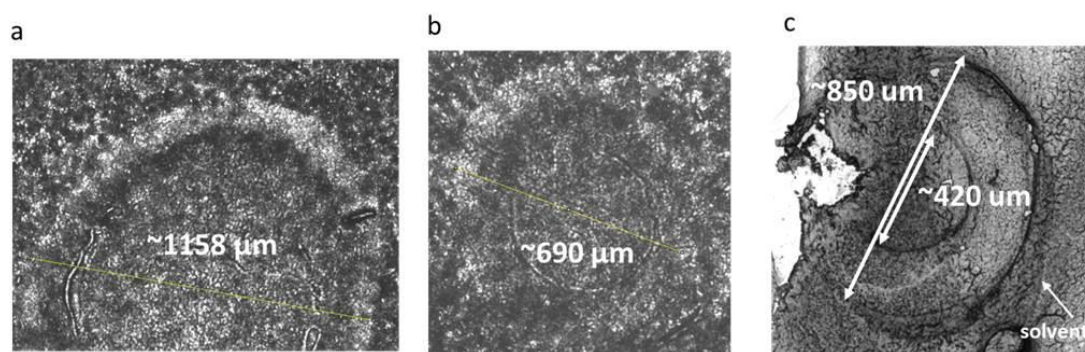
Figure 3.9 Optical images of tissue after LESA sampling: a) optical image of LESA sampled region using normal LESA sampling allowing only the solvent to come into contact with the sample surface, the sampled region was measured using imageJ and the diameter was found to be ~1158 µm, b) optical image of LESA sampled region using contact LESA sampling, the diameter of area sampled is measured to be ~690 µm, c) optical image taken after contact LESA sampling in which the pipette tip exerted a larger force of the tissue, the inner and outer diameter of the pipette tip can now be seen. It appears that the solvent spread ~150 um beyond the outer edge of the pipette.

3.3.7 Combined LESA and MALDI MS imaging of drug in mouse brain tissue: Post-LESA MALDI MS Imaging

After the sample had been imaged by LESA MS, both this section and a serial section placed adjacent on the slide were coated with matrix and imaged using MALDI MS. There were several reasons for doing this: to provide higher resolution tissue images which complement the LESA MS data, to establish whether performing LESA prior to MALDI in a multimodal workflow is feasible (i.e., to determine whether MALDI image integrity is maintained) and to ascertain whether higher resolution MALDI MS images can be used to better understand LESA sampling. The adjacent tissue section served as a control and allowed changes induced by LESA sampling to be assessed.
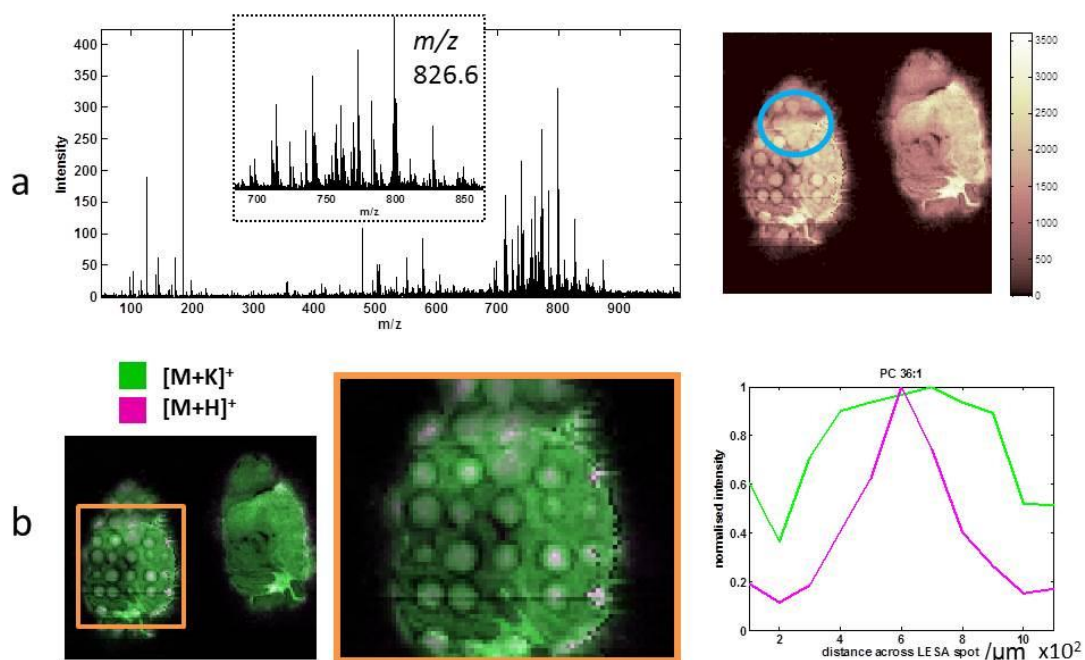
Figure 3.10 MALDI MS imaging of tissue after LESA sampling: a) (left) example single pixel spectrum, peaks in the m/z range 700 – 900 correspond to lipid ions, (right) MALDI MS image of ions with m/z 826.6, tentatively assigned as [M+K]+ ions of PC 36:1, blue circle indicates region spiked with erlotinib solution, b) (left) overlaid MALDI MS ion images of protonated and potassium adduct of PC 36:1, (right) overlaid intensity line profiles across centre of one LESA sampled region, plot in pink corresponds to [M+H]+ ion intensity which peaks sharply towards the centre of the spot, plot in green corresponds to [M+K]+ ions which are more homogeneously distributed across the spot.

The MALDI MSI method was optimised for lipid analysis; an example single pixel spectrum from the tissue section which had not been sampled by LESA is displayed in Figure 3.10. A number of lipid species were detected in the *m/z* range 600-900, an example ion image (tentatively assigned as PC 36:1) can also be seen in Figure 3.10. The lipids were preferentially detected as the potassium adduct. Ions detected at *m/z*s corresponding to the sodium adduct and protonated molecule were also observed but

with a lower intensity. In these images it is possible to see the regions which were sampled by LESA. These features are generally classified by a region of higher ion intensity surrounded by a dark ring in which very few ions were detected. These features were not observed in the control image. It would appear that LESA sampling acts as a localised tissue wash, enhancing lipid detection via the extraction of analyte to the tissue surface and extraction and washing of salts resulting in a concentration gradient – highest at the edge of the spot. The region of tissue which was spiked with erlotinib solution appears as a similar although larger feature in the image. This supports the theory that analyte extraction, rather than mitigation of suppression effects, is responsible for the observed intensity increase because the spiked solution was allowed to remain on the tissue and therefore didn't remove any dissolved species. To further probe the distribution of lipid species across the LESA sampled area, a composite ion image of the protonated and potassiated molecules of PC 36:1 was generated, and intensity line profiles across a single LESA spot were plotted, see Figure 3.10. It was found that $[M+H]^+$ ions were preferentially detected towards the centre of the LESA sampled area, whereas $[M+K]^+$ ions were more abundant towards the outside or homogeneously distributed across the spot. This behaviour was also observed for a number of other lipid species. Accumulation of salt at the outer perimeter could also be responsible for the 'dark ring' observed in MALDI MS lipid images; matrix crystals exhibit different morphology when formed from solution containing different proportions of salts.[13]
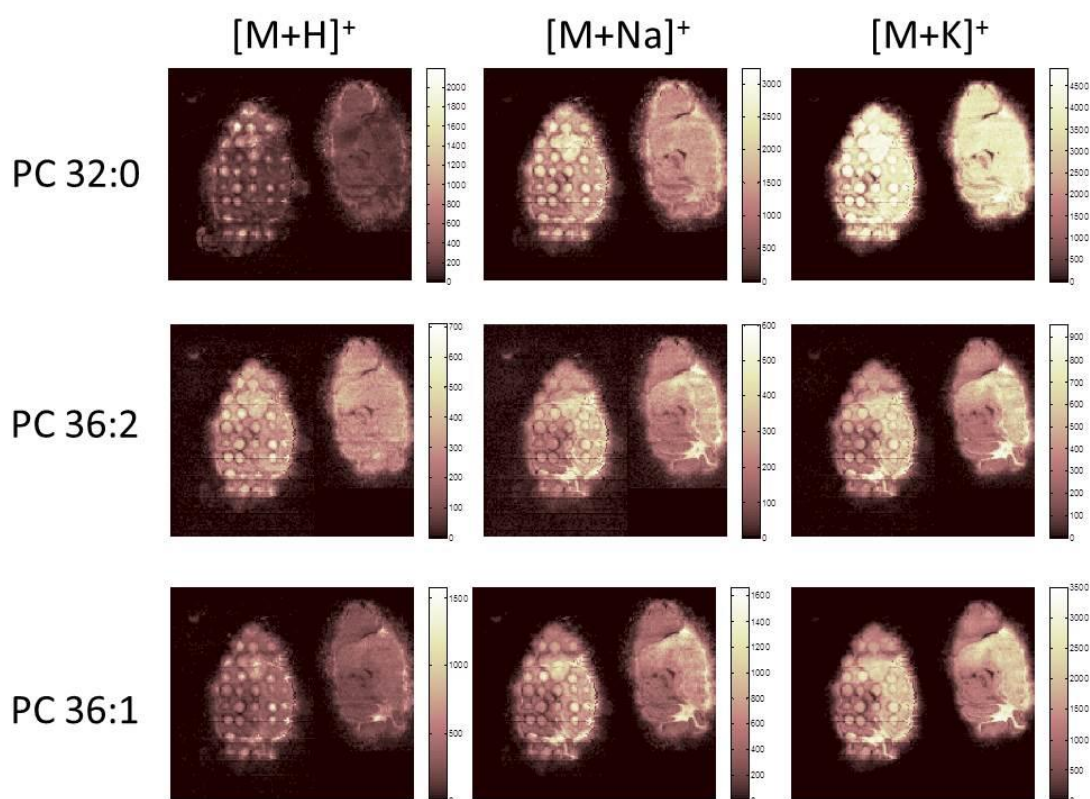
Figure 3.11 Example lipid ion images of protonated, potassium and sodium adducts for three PC lipid species, demonstrating the effect of LESA sampling on the distribution of multiple lipid species and adducts.

Optical images of a LESA-sampled tissue section before and after coating with matrix are displayed in Figure 3.12. The regions sampled by LESA appear as darker regions compared to un-sampled tissue; a circular imprint can be observed in the middle of this region which results from the pipette tip coming into contact with the tissue. A larger, more irregular dark region surrounds this mark which suggests the solvent spread further than the confines of the pipette tip.
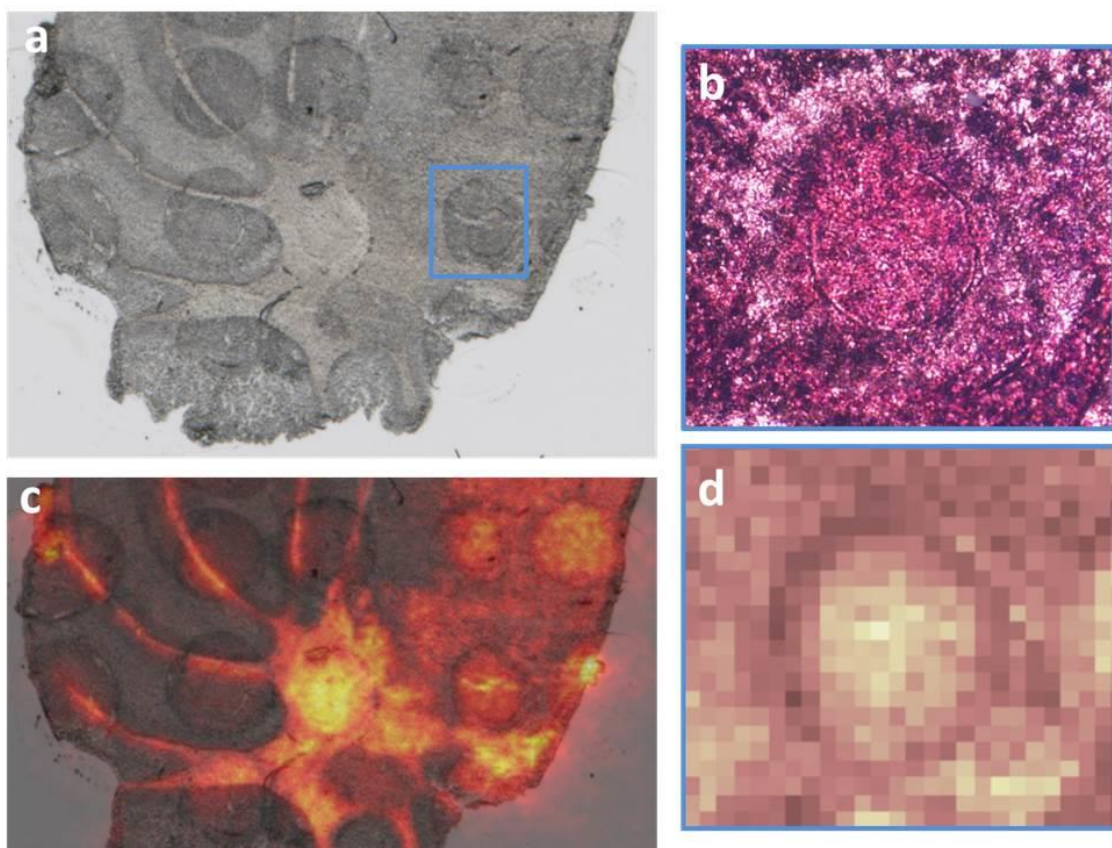
Figure 3.12 a) Optical image of tissue section after LESA MS, darker regions indicate solvent contact with tissue, smaller circle in middle of dark region is caused by imprint of pipette tip, b) optical image of LESA sampled region after coating with CHCA matrix, lighter region at perimeter of LESA spot indicates thinner crystal layer, c) overlaid MALDI MS image of ions with m/z 826.6 and optical image, d) enlargement of MALDI MS image of ions with m/z 826.6 to show same LESA sampled region as displayed in (b), dark region in ion image corresponds with thinner region of matrix crystals in optical image.

The image displayed in Figure 3.12 demonstrates the size and distribution of CHCA crystals on the tissue surface after matrix coating. A region of sparse, thin crystals can be seen around the outer edges which correspond with the dark region of the ion image displayed in Figure 3.12; suggesting changes to matrix morphology resulting in poor

analyte inclusion and subsequent ablation/ionisation are responsible for low ion counts from this region. An example MALDI MS image (*m/z* 826.6) overlaid with the optical image demonstrates that regions of higher intensity in the ion image correspond with darker regions observed in the optical image, see Figure 3.12.

MALDI MS ion images reveal details about locations, size and variation of LESA sampled areas. Previous work has relied on optical images alone to provide this information, whereas this method provides mass spectral data which verifies visual changes to the tissue correspond with spectral changes indicative of solvent contact. Additionally, delocalisation and other changes in analyte distribution within the sampled area (which appears as a homogeneous area in the optical image) can be visualised using MALDI MSI. Two MALDI MSI datasets were obtained from tissue sampled by LESA, with pixel sizes of 100 and 50 μm respectively. Whilst no further features could be observed with the increased image detail afforded by 50 μm pixels, the outer limits of the sampled region could be more accurately defined. As such, MALDI MS images with 50 μm pixels were used to determine the size of regions sampled by LESA. The average area sampled per contact LESA spot is 0.41 mm^2. Differences in size of these areas is caused either by differing degrees of solvent spreading during sampling or differing volumes of residual solvent left on the tissue after LESA sampling, or some combination of both. The distance between these areas in x and y dimensions varies considerably, as indicated by images in Figure 3.12. In order to maximise the total surface sampled by LESA in an imaging experiment, individual samples should be taken next to each other with as small a gap between them as possible but without overlapping (this would result in oversampling which although common practice in MALDI MSI, is inappropriate for LESA MS because signal can be acquired multiple times from the same location). The spacing required between points for maximum coverage using contact LESA would be

~700 μm, providing sampling spatial precision was accurate. However, MALDI MSI images reveal that inter-sample distances (measured from centre to centre) vary between 0.8 and 1.3 mm. Improved positional accuracy of the sampling robot is required to improve LESA MS as an imaging technique.

An experiment in which contact LESA was performed without any solvent confirmed that solvent washing effects and not compression or damage of the tissue during contact were responsible for the observed intensity changes in MALDI images, Figure 3.13.
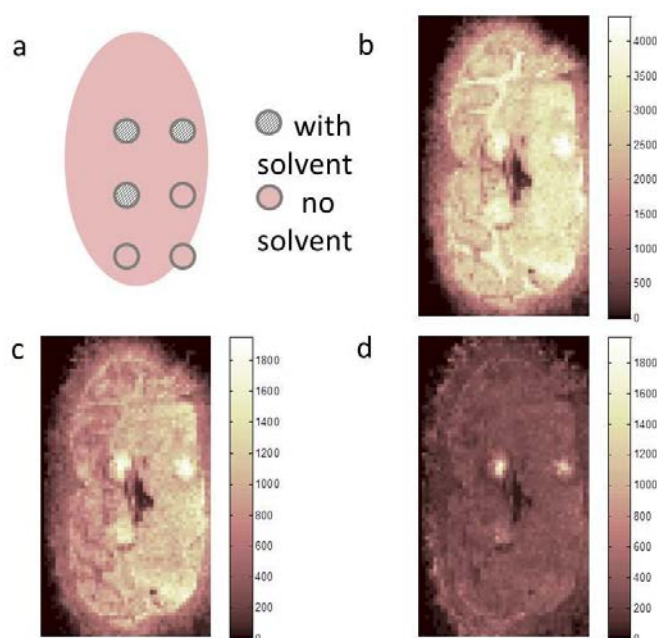
Figure 3.13 Results after performing LESA with and without solvent: a) locations selected for sampling, b-d) example lipid ion images, b) *m/z* 798, c) *m/z* 782, d) *m/z* 760. Increases/decreases in ion intensity in LESA sampled regions are only observed when solvent is used, therefore it is unlikely that these changes are caused by compression or damage of the tissue during contact.

3.3.8 Multivariate analysis of MALDI MSI data

In order to fully assess changes between the LESA-sampled section and serial control it is necessary to consider variation of multiple ions simultaneously. This also aids in interpretation of MALDI data obtained after LESA sampling. A number of multivariate analysis techniques were applied to the data in an attempt to uncover other trends. Principal component analysis (PCA) score images are displayed in Figure 3.14. The score image of PC1 indicates that the largest source of variance in the dataset is the difference between tissue and background. PC5 indicates variance between LESA sampled areas and background tissue. PC6 identifies LESA sampling regions on areas of white matter but not grey matter. The latter is interesting because it suggests that changes associated with LESA sampling do not appear uniformly across the tissue. This has implications for any sample preparation procedures which undergo a wash step because it implies that inhomogeneous washing occurs across the tissue and therefore false contrast could be introduced in ion images. Thresholded PCA score images were used as a mask to segment the background from the tissue for further multivariate analysis. k-means clustering (K=7) was applied to the PCA-reduced dataset to identify pixels with similar spectral profiles and label them with a randomly assigned colour. k-means clustering successfully separated the different brain anatomies and LESA sampled regions on white and grey brain tissue. The results from this analysis are easy to interpret and demonstrate agreement with individual lipid ion images. Two clusters are identified which are unique to the LESA-sampled tissue section and are labelled red and pale blue in Figure 3.14. Clustering, with the parameters used, does separate the outer perimeter of these regions into a unique cluster. In general, k-means clustering provides no visual indication of how spectrally similar the identified clusters are. t-Distributed stochastic neighbour embedding (t-SNE) is a dimensionality reduction technique which

has been used in MSI for visualisation of complex datasets.[188] The colour of each pixel is related to its location in the reduced space, thus providing a visual indication of how similar two pixels are spectrally. When applied to this dataset, t-SNE reveals very similar results for control tissue and unsampled regions of section sampled by LESA. The regions sampled by LESA appear significantly different to the unsampled regions, with slight differences observable depending on whether the sampled region was grey or white matter, see Figure 3.14. Although this data visualisation approach is useful in identifying regions of spectral similarity and gradients of change affected by LESA sampling, no spectral information about the different regions is provided and therefore it is hard to identify which spectral features have contributed. Non-negative matrix factorisation (NMF) decomposes the data into a set of unique spatial distributions and associated spectral profiles. NMF applied to this dataset identifies a number of spatial distributions arising from LESA sampling. The image in Figure 3.14 identifies a distribution corresponding to white matter in the tissue sections. Major *m/z* values contributing to this distribution are 798 and 826, which are tentatively assigned as the potassium adducts of PC 32:0 and PC 36:1 respectively – i.e. the most abundant lipid species detected from mouse brain tissue. The image in Figure 3.14 identifies regions at the centre of the LESA sampled regions; examination of individual ion images revealed that protonated molecules of lipids were detected with higher intensity here. Peaks with *m/z* 760 and 788 (tentatively assigned as protonated molecules of PC 32:0 and PC 36:1 respectively) are identified by NMF as major contributors to this distribution, supporting conclusions drawn from manual analysis.
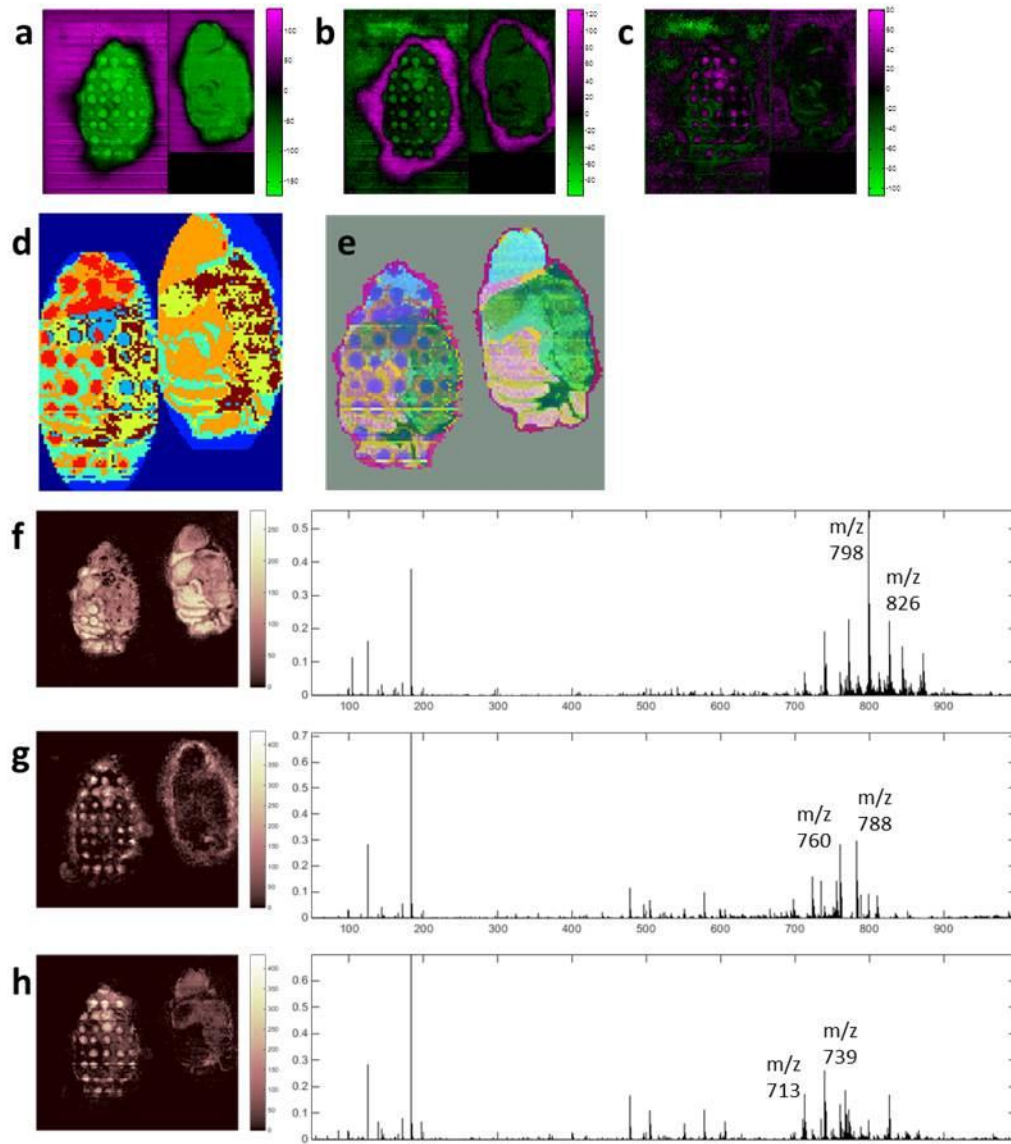
Figure 3.14 Results from multivariate analysis: a-c) score images of principal components 1, 5 and 6 respectively, principal component 1 indicates that the greatest variance is between tissue and background, principal component 5 indicates variance between LESA sampled areas and the rest of the tissue, principal component 6 indicates that LESA sampled regions on white matter are more different from the original tissue type than those from grey matter, d) k-means clustering (k=7) on masked image to remove background, the same clusters corresponding to anatomical features within the tissue are found in both LESA sampled tissue and the control section indicating that LESA only induced localised changes, these are identified as different clusters in grey

and white matter, further clusters identify the outer perimeter of LESA sampled regions, e) t-SNE reveals the same clusters identifying different tissue anatomies in LESA sampled tissue and control tissue, LESA sampled regions are assigned different clusters depending on the original type of tissue however these are more similar to each other than the original type of tissue, the region where the drug was spiked is also similar to the LESA sampled regions but more similar to the original tissue type presumably because the solvent was not removed from the tissue and therefore didn't deplete the tissue in the same way, f) examples of three factors identified by NMF, their spatial distributions and contributing spectral components.

3.3.9 Investigation into normalization strategies for MALDI MSI data

It was found that features introduced into some MALDI MS ion images can be largely removed via total intensity normalisation, see Figure 3.15. For other ion images this normalisation strategy is less successful, see Figure 3.15. This is to be expected based on asserted changes to distribution of lipid adducts. An understanding of MALDI mass spectral changes associated with LESA sampling could help inform more sophisticated and appropriate normalisation methods – for example, factors identified by NMF could be used to correct for changes in intensity and distribution.
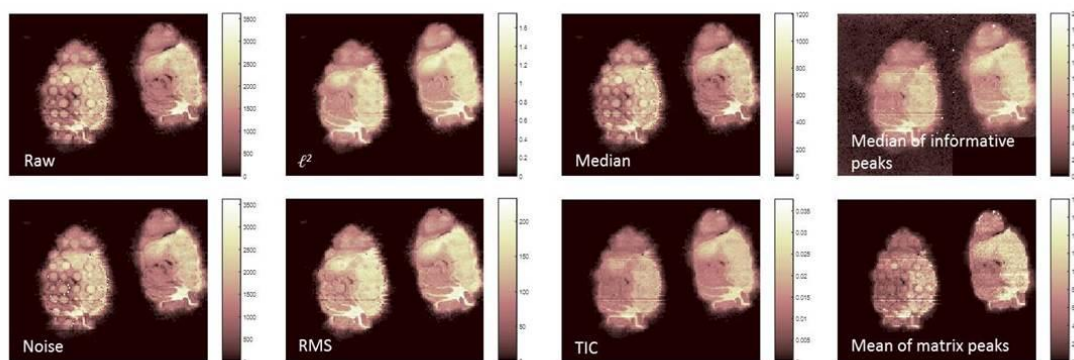
Figure 3.15 MALDI MS image of ions with m/z 826.6 before and after normalisation using various different strategies as indicated.

3.3.10 Combined LESA and MALDI MS imaging of drug in mouse brain tissue: Post-MALDI LESA MS sampling

In order to determine the ideal order of techniques in a multimodal workflow, the control section imaged by MALDI MS was subjected to LESA MS. The same sampling and mass spectrometry parameters were used as before. Full scan mass spectra were obtained from discrete locations across the tissue section. It was found that the low *m/z* range (150-500) was dominated by peaks corresponding to matrix ions and matrix ion clusters. The *m/z* range was adjusted to 500-2000 to account for this. Localised washing of the tissue with ethanol/water (50/50 v/v) via LESA sampling (to remove matrix) prior to sampling with the usual methanol solvent was found to slightly reduce spectral complexity and increased the intensity with which some lipids were detected, but had little effect on the number and type of lipid species observed, see Figure 3.16. All of the most abundant lipid species detected by LESA MS prior to MALDI MS were detected post-MALDI MS, again predominantly as $[M+H]^+$ ions. This observation is surprising, the addition of matrix is expected to introduce additional salts to the sample. It was found that no multiply charged protein ions were detected in LESA mass spectra in the

71

presence of matrix. Washing the tissue with ethanol or methanol and reducing the acid content of the solvent system did not enable protein desorption/ionisation.
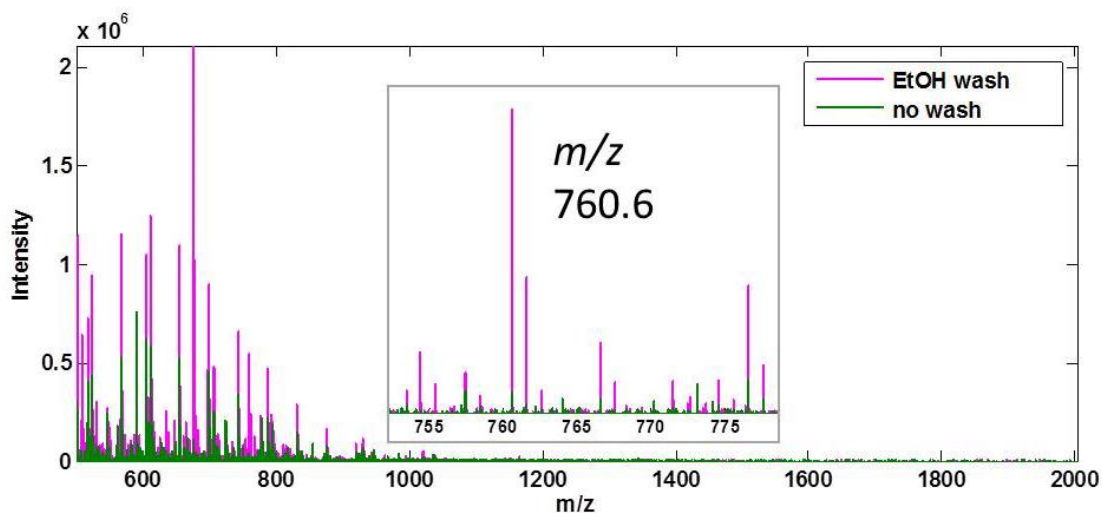
Figure 3.16 Example LESA mass spectrum from tissue analysed by MALDI MS before and after washing tissue with ethanol. Lipid ion intensity is improved after the wash step, no protein ions were detected from this sample.

3.3.11 MALDI MSI analysis of DESI sampled tissue

The combined method was extended to investigate a different ambient MSI technique. DESI MSI is a commonly used mass spectrometry imaging technique which benefits from operation under ambient conditions in addition to good spatial resolution. An experiment in which MALDI MS was performed on tissue which had been previously analysed by DESI was designed. MALDI MS images of various lipids are displayed in Figure 3.17. No significant enhancement of lipid ions in regions analysed by DESI is observed. This suggests that DESI extraction is not as efficient as LESA and could be responsible for the lower sensitivity of DESI and the inability to detect larger species.
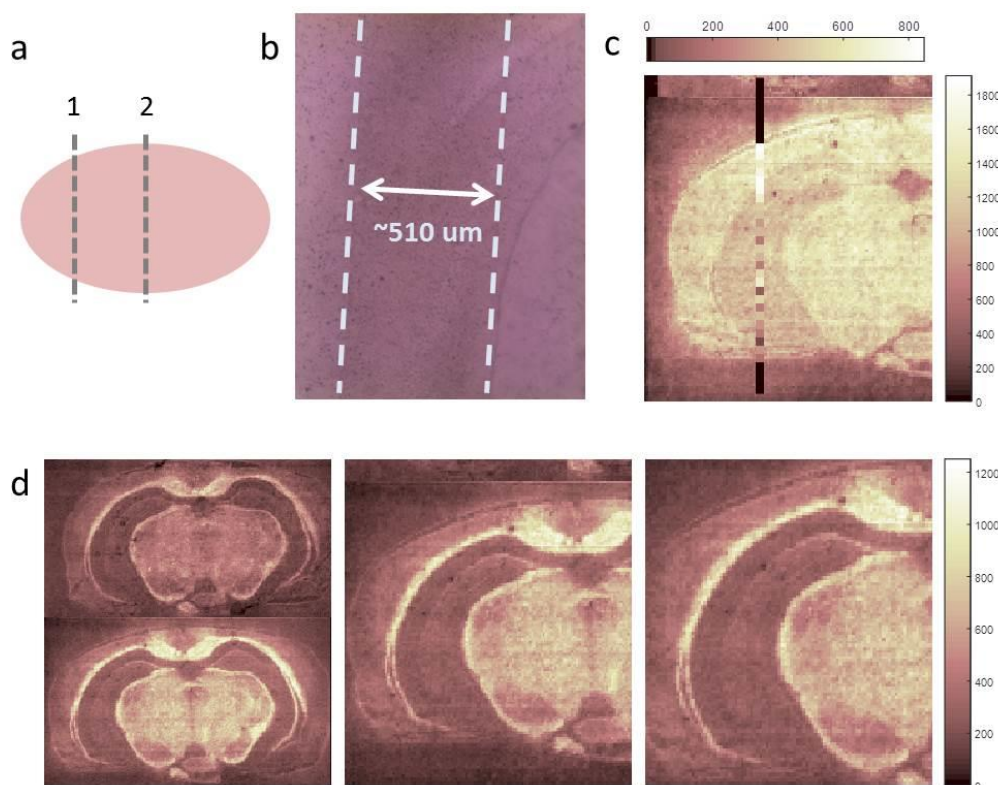
Figure 3.17 MALDI MS imaging of DESI sampled tissue: a) location of DESI sampled areas, b) optical image of tissue after DESI sampling, lateral resolution was measured as approximately 510 μm, c) MALDI MS image of ions with *m/z* 798.6 overlaid with single line ion image acquired by DESI MS (also *m/z* 798.6), d) MALDI MS image of ions with *m/z* 826.6 at various magnifications, no obvious delocalisation or enhancement of intensity by DESI is observed.

3.4 Conclusions

A combined workflow is presented which exploits the advantages of LESA and MALDI MSI and additionally provides insight into aspects of ambient surface sampling. For the first time LESA has been used for the detection of a drug compound, lipids and proteins simultaneously. MALDI provided high spatial resolution images which detailed the exact locations sampled by LESA allowing for the registration of data from both. This has important implications for pharmaceutical research; high resolution MALDI images

can be used to detail exactly where drug, lipid and protein signals originated from. Several multivariate techniques were employed to assess changes to distribution induced by LESA. Future implementations of MALDI MSI after LESA analysis could assess different washing protocols, or how the same wash affects different regions of tissue. This could also be used to assess improvements or changes made to the automated LESA sampling routines described here, for example to determine the spacing of sampled areas and ensure that no oversampling had occurred. LESA MS is somewhat limited as an imaging technique by the poor spatial resolution it affords, however there are opportunities for further decreasing pixel size via contact LESA and smaller sampling pipette tips. As the technique improves in terms of sampling precision and repeatability, combining with MALDI will become an even more attractive option. The potential for inclusion of standards by LESA is also attractive, and provides possible routes towards quantitative analysis. The combined LESA-MALDI MSI workflow could then be applied to drug in tissue studies which could provide quantitative analysis of drug/lipid/protein via LESA and a higher spatial resolution reference in MALDI MS images.

Chapter 4

SRS Microscopy of MALDI Sample

Preparation and Sampling Effects

4.1 Overview

In the previous chapter it was demonstrated that MALDI MS ion images of LESA sampled tissue can provide information about LESA sampling effects. The work presented in this chapter uses a similar approach to investigate how a higher resolution, quantitative imaging technique could be used to provide insight into MALDI sample preparation and sampling effects. Various aspects of MALDI sampling remain unclear; better understanding of ionisation processes, the behaviour of different matrices and combinations of matrix and laser parameters are of primary importance for successful analytical applications of the technique.[189] Insight into these parameters could lead to optimum analysis in terms of improved limits of detection for a wider variety of analytes and could be instrumental in the drive towards higher-throughput analysis.[10] SRS microscopy has been used for a number of successful imaging applications in biology and has been demonstrated as a quantitative technique.[123,126-129] This chapter presents an investigation into the use of SRS microscopy for imaging and quantification of samples analysed by MALDI MS. The preparation of model samples of analyte and matrix compounds deposited on glass, and assessment of their use in fundamental MALDI MS studies is also discussed.

4.2 Experimental

4.2.1 Preparation of model samples

4.2.1.1 PNA sample for calibration:

Thin films of PNA were deposited on glass coverslips. A solution of PNA (5 mg/mL in 80:20 MeOH:H_2O) was sprayed at a flow rate of 0.115 mL/min, track speed of 1333 mm/min, track spacing of 3 mm and a spray nozzle temperature of 90°C. One cycle of this deposition method was applied before a mask was used to cover a 5mm portion of the slide. Another cycle was applied and the mask was moved 5 mm after each subsequent cycle. The coverslip was turned face down onto a glass slide and sealed at the edges with nail varnish to protect the sample from the objective lens immersion oil.

4.2.1.2 Fluence response study:

For the study into fluence response combined thin films of PNA and erlotinib were prepared on glass coverslips using the TM-Sprayer method described in section 2.2.1.1. The total amount of erlotinib deposited was 0.42 μg/mm^2, total PNA was 1.15 μg/mm^2.

4.2.1.3 Repetition rate response study:

Thin films of erlotinib and PNA and erlotinib and SA were prepared on glass coverslips using the TM-Sprayer method described in section 2.2.1.1. The molar ratio of analyte:matrix was fixed at 1:100 for both samples and the total amount of analyte was also fixed. The total amount of erlotinib deposited on each sample was 0.184 μg/mm^2, total PNA was 6.46 μg/mm^2, and SA was 10.5 μg/mm^2.

4.2.2 Spontaneous Raman spectroscopy

Spontaneous Raman spectra of matrix compounds were acquired using a custom built system. Samples were irradiated using a frequency doubled Nd:YAG laser (λ=532.5

nm) the integration time was optimised for each matrix compound: CHCA: 10 s, SA: 10 s, DHB 20 s. The spontaneous Raman spectrum from erlotinib was acquired using a Renishaw instrument, the sample was irradiated at 633 nm with a 30 second integration time.

4.2.3 SRS microscopy of PNA calibration sample

SRS images were acquired as described in section 2.2.2.4. 3 regions of 75 x 75 μm were selected and a stack of 10 images spanning 10 μm in the z-dimension was acquired for each region. The pump beam was tuned to 1110 cm^{-1} and an integration time of 0.1 ms was found to give sufficient image contrast. The total summed intensity in each image region was calculated along with the mean image intensity over 3 regions. To produce the calibration curve, mean image intensity was plotted against number of molecules deposited as calculated from the TM-Sprayer method. Linear regression analysis was performed on these data.

4.2.4 MALDI MS for fluence response study

A thin film of erlotinib and PNA described above was fixed into the MALDI plate holder and placed in the ion source. A frequency tripled Nd:YAG (355 nm) laser was coupled to the source via a 100 μm core fibre, the laser was triggered by a function generator (TTi – TG2000 20 MHz DDS) at a frequency of 1 KHz. The energy delivered per pulse was controlled by a variable attenuator (Motorized Watt Pilot; Altechna, Lithuania) and measured using a pyroelectric sensor (PD10-C, Ophir Photonics). Laser beam spot size was calculated by measurement of the fluorescent region of an irradiated sample of CHCA. The stage raster speed was also held constant at 0.2 mm/second. Data were acquired in the positive ion mode in the *m/z* range 50 - 1000. Single line raster

images were acquired at a range of laser fluences (34.22, 61.58, 89.45, 117.51, 145.34, 173.92, 201.80 and 229.60 J m^{-2}) with a lateral resolution of 100 μm.

4.2.5 SRS microscopy for fluence response study

The sample described above was removed from the mass spectrometer and turned face-down on a glass slide and sealed with nail varnish. SRS images were acquired from 3 regions of each irradiated region and one non-irradiated region. For each image region (50 x 50 μm, 10 images spanning 10 μm in the z-dimension) 2 sets of images were acquired, one tuned to the resonance frequency of PNA (1110 cm^{-1}) and one to erlotinib (2110 cm^{-1}). The total summed intensity in each image region for each compound was calculated along with the mean image intensity over 3 regions.

4.2.6 MALDI analysis for repetition rate response study

Thin films of erlotinib and PNA or SA were fixed into the MALDI plate holder and placed in the ion source. An Nd:YVO$_4$ (355 nm) laser was coupled to the source via a 100 μm core fibre, the laser was triggered by a function generator (TTi – TG2000 20 MHz DDS) at frequencies of 1-6 KHz. The energy delivered per pulse was kept constant across all repetition rates and was controlled by a variable attenuator (Motorized Watt Pilot; Altechna, Lithuania). The stage raster speed was also held constant at 0.2 mm/second. Data were acquired in the positive ion mode in the *m/z* range 50 - 1000. Single line raster images were acquired for each repetition rate (1,2,3,4,5,6 KHz) on each sample with a lateral resolution of 100 μm.

4.2.7 SRS microscopy for repetition rate response study

Samples were removed from the mass spectrometer and turned face-down on a glass slide and sealed with nail varnish. SRS images were acquired from 3 regions of each irradiated region and one non-irradiated region of each sample. For each image region

(50 x 50 µm, 10 images spanning 10 µm in the z-dimension) 2 sets of images were acquired, one tuned to the resonance frequency of PNA (1110 cm^{-1}) or SA (1644 cm^{-1}) and erlotinib (2110 cm^{-1}). The total summed intensity in each image region for each compound was calculated along with the mean image intensity over 3 regions.

4.2.8 Spontaneous Raman spectroscopic imaging

Spontaneous Raman mapping of erlotinib/SA irradiated thin film was performed using a custom built system. Samples were irradiated using a frequency doubled Nd:YAG laser (λ=532.5 nm), the integration time was 5 seconds per pixel and the pixel size was 1 µm. The total image region covered an area of 40 x 128 µm.

4.2.9 SRS imaging of matrix-coated tissue

Mouse brain tissue was coated with DHB as described in section 2.2.1.2. SRS microscopy was performed at the resonance frequency corresponding to lipid species (2860 cm^{-1}). Images regions of 30 x 30 µm were selected and 10 images spanning 10 µm in the z-dimension were acquired. An integration time of 2ms per pixel was used. 3-dimensional image reconstructions were performed in imageJ.

4.3 Results and Discussion

4.3.1.1 Equivalence of SRS with spontaneous Raman spectroscopy

Single channel SRS images of a thin film of PNA were acquired over a range of Raman shifts (1200-1400 cm^{-1}). The average image intensity was calculated and plotted against Raman shift, see Figure 4.1. This trace demonstrates the same peak shape as the spontaneous Raman spectrum acquired from another sample of PNA and thus

demonstrates that resonance frequencies for SRS interrogation can be determined by examination of spontaneous Raman spectra.
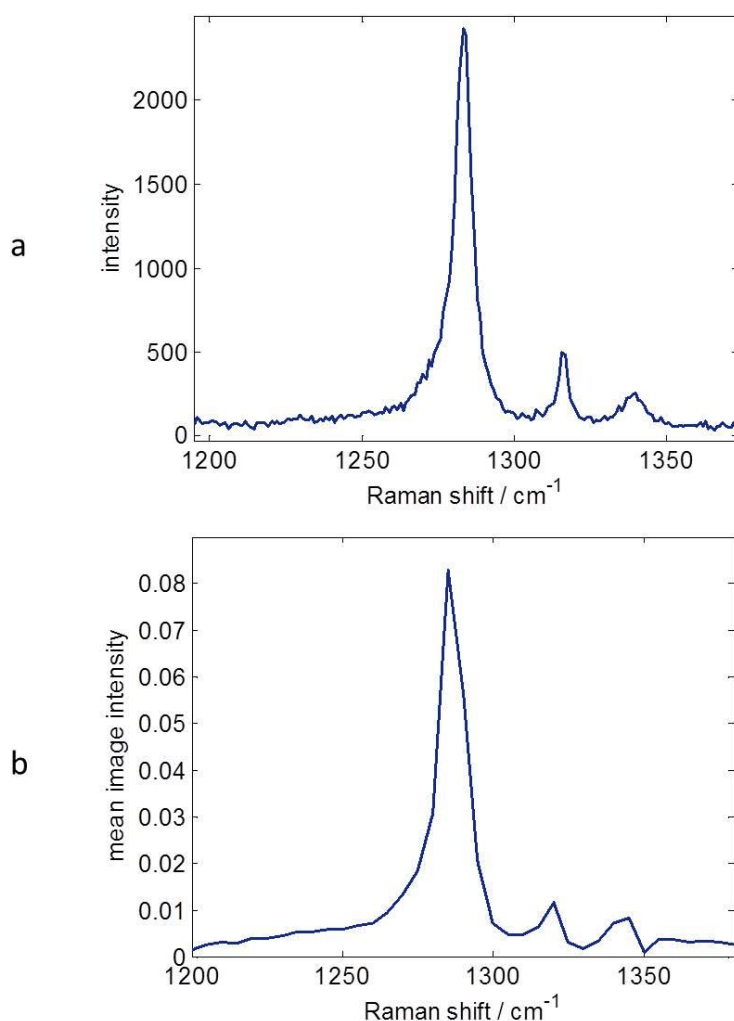
Figure 4.1 a) spontaneous Raman spectrum of PNA, b) SRS 'spectrum' of PNA acquired by calculation of mean image intensity over a selected range of wavenumbers.

4.3.1.2 Developing a model sample

In order to perform combined MALDI and SRS analysis on the same sample it is important that analytes and matrices are compatible with both types of instrumentation. A survey of three commonly used matrix compounds was performed; spontaneous Raman spectra were acquired from CHCA, PNA and DHB, see Figure 4.2. Examination of these spectra revealed resonance frequencies which could then be probed by SRS.

Images of thin films of each matrix compound were acquired at one resonance frequency and one off-resonance frequency. As demonstrated by the images in Figure 4.2, strong off-resonance absorption was observed for CHCA. This would present a problem when imaging CHCA in combination with another analyte or tissue because it would be impossible to determine the molecular origin of the signal. A low intensity off-resonance signal was also observed for PNA. Only very weak signals were observed for DHB either on or off-resonance, suggesting that samples coated with DHB crystals could be imaged using SRS with confidence that no off-resonance absorption had occurred, however it would not be possible to image DHB crystals directly. It is possible that CHCA and PNA exhibit off-resonance absorption due to their strong absorption of UV radiation, which is of course why they are used in MALDI MS. The wavelength of the Stokes beam was 1064 nm and the pump beam was 840 nm (CHCA) and 868 nm (PNA). Both CHCA and PNA exhibit a strong absorption band in their UV-Vis absorption spectra at 350-450 nm,[190] therefore when irradiated at 800-900 nm it is possible that two-photon absorption occurs.
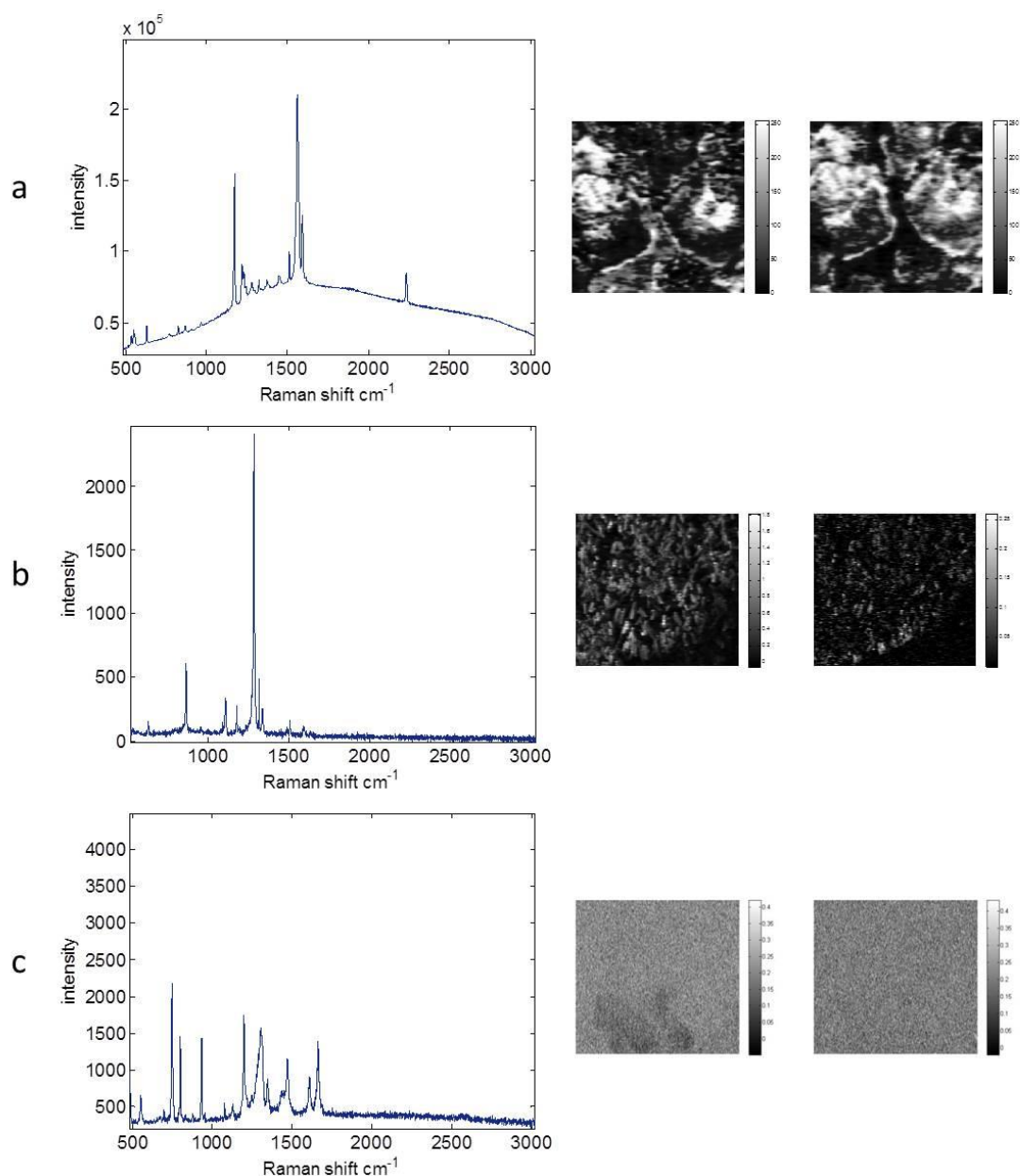
Figure 4.2 Spontaneous Raman spectroscopy and SRS microscopy of MALDI matrices, a) CHCA, SRS on-resonance (left image) 2235 cm^{-1}, off-resonance (right image) 2500 cm^{-1}, b) PNA, SRS on-resonance 1283 cm^{-1}, off-resonance 2115 cm^{-1}, c) DHB, SRS on-resonance 1665 cm^{-1}, off-resonance 2250 cm^{-1}.

To further probe the properties of PNA, SRS images of a PNA thin film were acquired at a range of Raman shifts which correspond to pump beam wavelengths of 800 – 905 nm, see Figure 4.3. For comparison, the equivalent region of the spontaneous Raman

spectrum of PNA is also displayed. There are no Raman bands in the 2500 – 3100 cm^{-1} region of the spontaneous spectrum however the SRS 'spectrum' shows increasing average image intensity with Raman shift. This increase in intensity corresponds with a decrease in pump beam wavelength. As the pump beam nears 800 nm PNA absorption increases. Considering the absorption profile of PNA, see Figure 4.3, these data support the hypothesis that two-photon absorption is responsible for off-resonance signal. Such properties have been reported for a number of chemical species such as chlorophyll and haemoglobin.[127,135,136] Whilst such absorption phenomena would clearly present a problem in the imaging of higher frequency resonances, it would still be possible to image resonance frequencies of PNA below 2500 cm^{-1} with confidence that no off-resonance absorption had occurred.
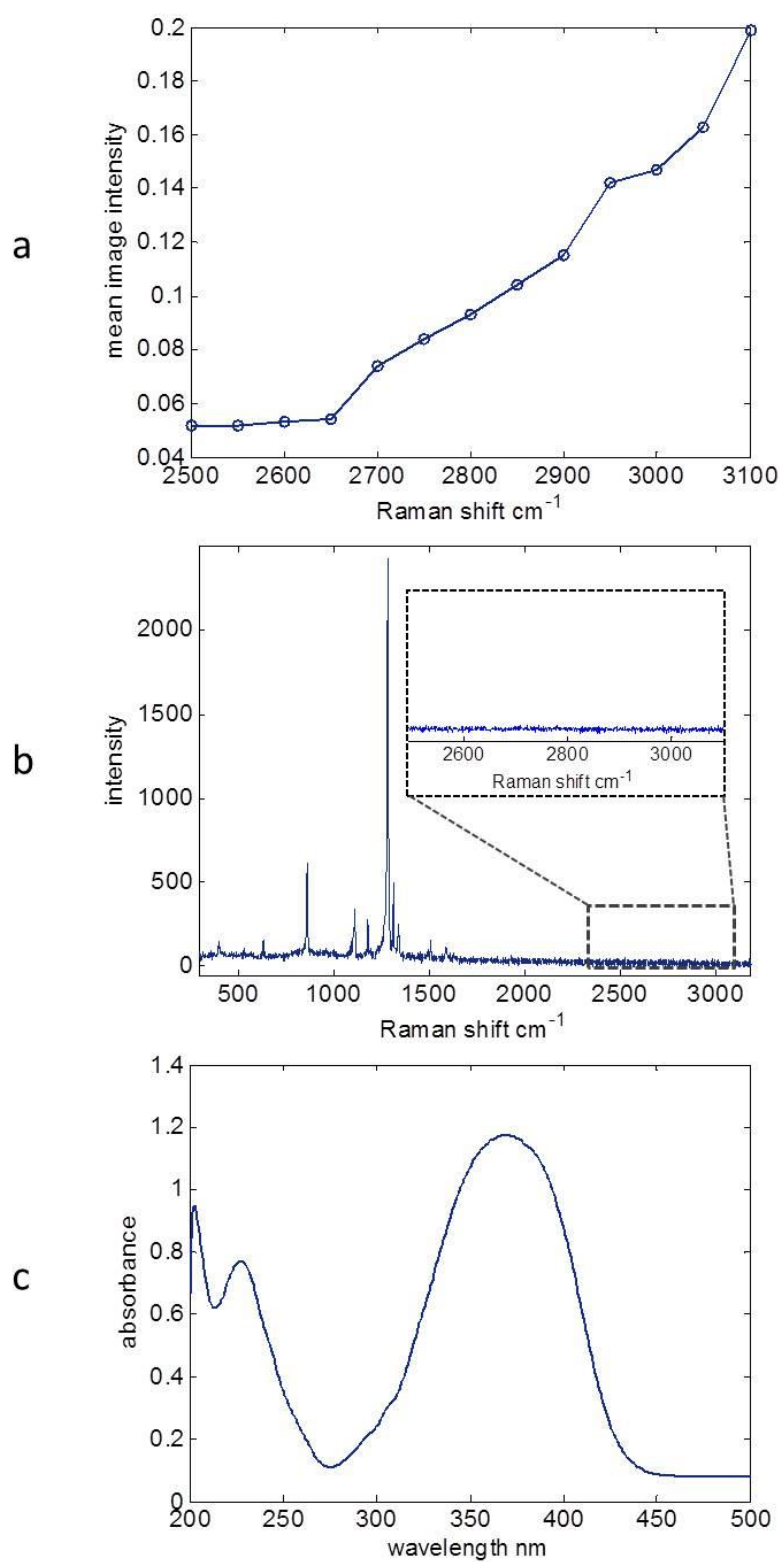
Figure 4.3 SRS microscopy of PNA thin film, a) SRS spectrum acquired by plotting the average image intensity measured at each Raman shift, b) spontaneous Raman spectrum PNA, c) UV-Vis absorption spectrum PNA.

The suitability of three matrices have now been assessed for use in model samples for combined MALDI and SRS studies, a suitable matrix compound has been identified and appropriate resonance frequencies have been established. In Chapter 3 the drug compound erlotinib was identified as a useful compound for MALDI MS imaging experiments. Erlotinib has been reported in a number of SRS microscopy studies and has been identified as particularly useful for bio-distribution studies due to the carbonyl group which exhibits a strong Raman active mode in the biologically silent region of the spectrum. This means that drug and endogenous biological species in the same sample can be imaged separately. SRS images were acquired from a thin film of erlotinib deposited on a glass slide, see Figure 4.4. SRS spectra surrounding two known resonance frequencies of erlotinib[168] were reconstructed by calculating the average image intensity at each Raman shift. This demonstrates that no off-resonance absorption phenomena occur during irradiation of erlotinib at these frequencies.
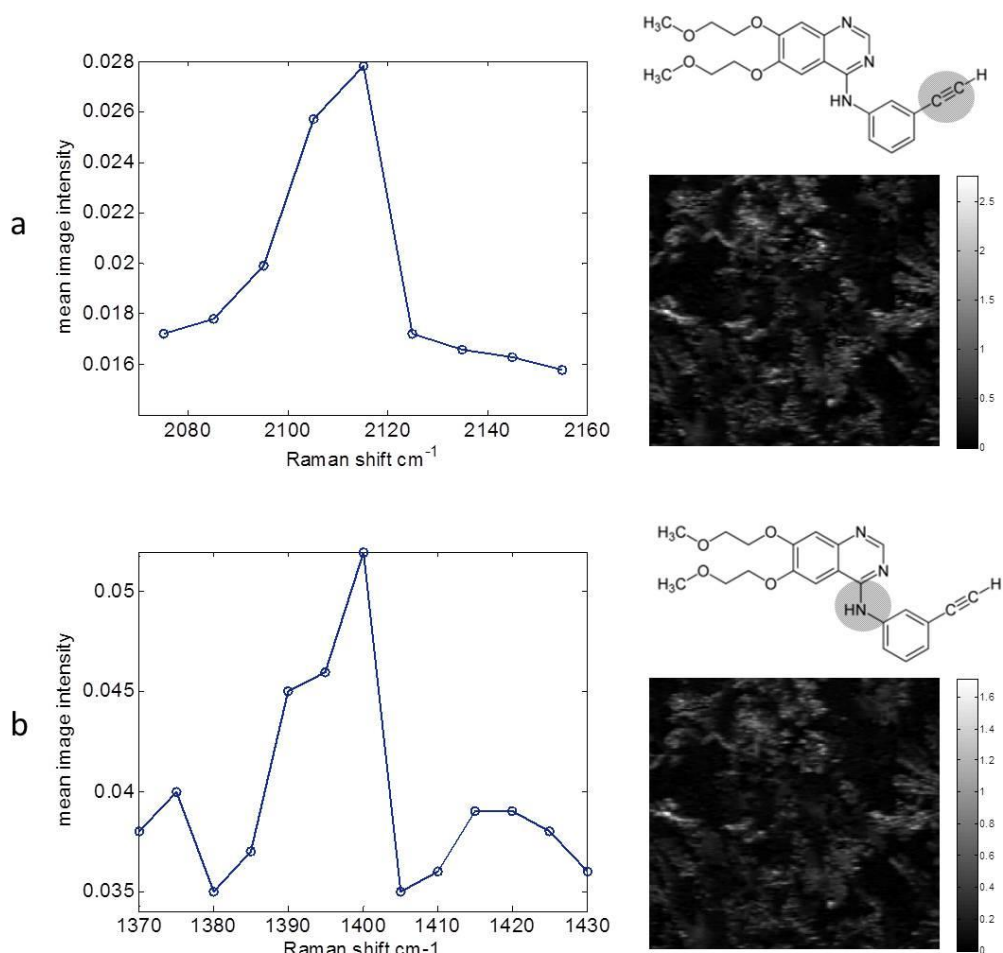
Figure 4.4 SRS images and spectra acquired from erlotinib thin film, a) resonance frequency around 2110 cm^{-1}, b) resonance frequency around 1395 cm^{-1}.

A model sample for combined MALDI and SRS studies requires matrix and analyte compounds which can be imaged separately by SRS within a dual-compound thin film. Therefore each compound must exhibit unique Raman signals which do not interfere with the other. Spontaneous Raman spectra from samples of erlotinib and PNA were acquired, see Figure 4.5. A suitable Raman shift for SRS imaging was identified for each compound and it was confirmed that neither compound would interfere with the other.
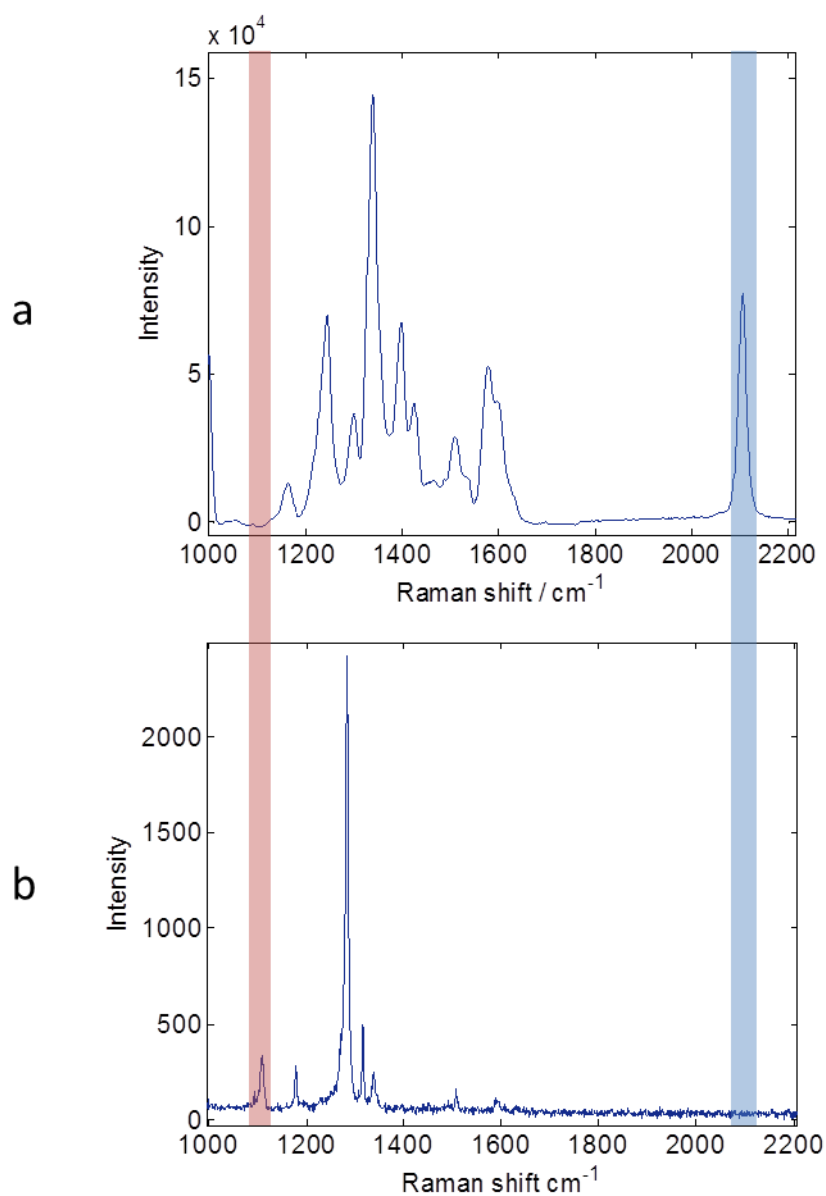
Figure 4.5 Spontaneous Raman spectra from: a) erlotinib and b) PNA. The red and blue lines indicate the Raman shifts selected for SRS imaging of each compound.

4.3.1.3 Quantitative SRS analysis of MALDI matrix compound

After careful optimisation and development of a suitable model sample for combined studies, several experiments were designed to investigate the use of SRS to probe MALDI MS sampling effects. SRS microscopy has been demonstrated to provide quantitative data.[127] An experiment was designed to establish whether SRS could quantitatively measure a sample of known composition. PNA matrix was deposited at a

range of concentrations on a glass coverslip, see Figure 4.6. SRS images of PNA (1110 cm^{-1}) at each concentration were acquired and average image intensity was plotted against number of molecules deposited. The number of molecules deposited was calculated via equation 4.1, where M_d is the mass of matrix deposited per unit area, NP is the number of passes or cycles of matrix deposition, C_m is concentration of matrix (mg/mL), F_m is the flow rate (μL/min), V is nozzle velocity (mm/min) and TS is track spacing (mm). Linear regression was performed and a line fitted to the data with an r^2 of 0.964. The variation observed in the data is likely to be due to inhomogeneity of the sample surface which can be observed in white light and SRS images of the sample. Reduced error could be acheived by depositing a more uniform layer of matrix, which would be difficult using a solvent spray based deposition technique. Sublimation of the matrix could provide a more homogeneous layer and smaller crystals, but determination of exact quantities deposited would be more complicated by this method. Alternatively, larger regions of the sample could be imaged and averaged, however the maximum field of view of the instrument used in this work was 80 x 80 μm and therefore numerous individual regions would have to be imaged separately which is a lengthy process.

$$M_d = \frac{NP * C_m * F_m}{V * TS}$$

4.1
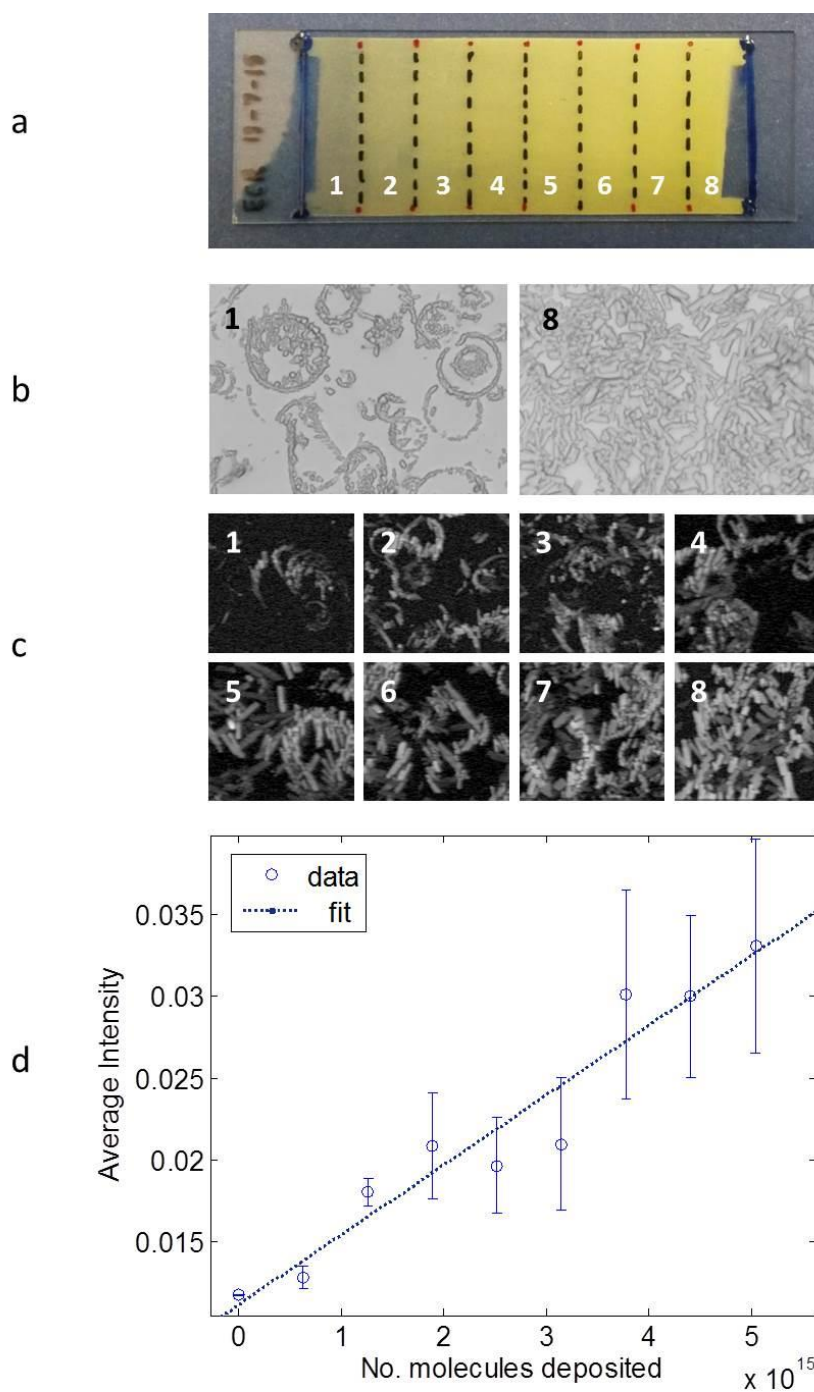
Figure 4.6 Quantitative analysis by SRS microscopy: a) preparation of calibration reference sample using TM-Sprayer, final concentrations of PNA: 0.14, 0.29, 0.43, 0.57, 0.72, 0.86, 1.01, 1.16 $\mu g/mm^2$, b) example white light images of the sample, rings of small crystals demonstrate how crystals have formed at the edges of droplets deposited on glass, c) example SRS images of PNA sample, each SRS images spans a

region of 75 x 75 µm, d) calibration curve, error bars represent ±1 standard deviation of the mean, $r^2 = 0.964$.

4.3.2 SRS analysis of MALDI sampling: fluence response study

SRS was demonstrated to produce a linear intensity response with concentration for a sample of known composition which suggests that the technique could be used to provide quantitative measurements from an unknown sample. An experiment was devised to study the response of an analyte/matrix system under varied laser fluence, see Figure 4.7. Known amounts of erlotinib and PNA were deposited on a glass coverslip and then subject to MALDI mass spectrometry using a laser operated at a range of fluences. Mass spectra were recorded for each fluence value, the sample was removed from the instrument and SRS images were acquired from irradiated and non-irradiated regions. The intensity difference observed in different irradiated regions could be equated to number of molecules removed because the total number of molecules originally deposited was known. The number of molecules removed via MALDI can be calculated by equation 4.2.

$$m_r = \frac{(I_0 - I_n)}{I_{max}} * m_d$$

4.2

Where m_r is no. molecules removed, I_0 is intensity measured from non-irradiated area, I_n is intensity measured from irradiated area, I_{max} is the maximum possible range of intensity values observed (I_0 minus background) and m_d is the number of molecules originally deposited.
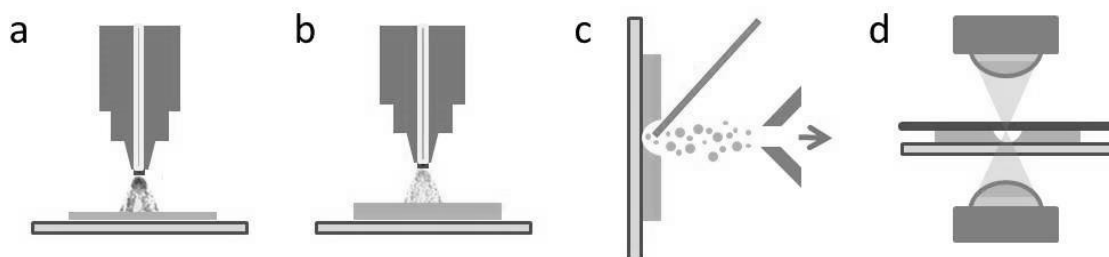
Figure 4.7 Schematic describing the use of SRS to measure MALDI sampling effects: a) deposition of analyte, b) deposition of matrix, c) acquisition of MALDI MS data, d) acquisition of SRS data.

The mass spectrometry results of this experiment are displayed in Figure 4.8. The boxplot of ion intensity vs fluence indicates a sigmoidal curve shape which has previously been reported for a variety of other analyte molecules.[144,191-194] There is a threshold energy above which detected ion intensity rapidly increases, this is typically reported to be between 20 and 1700 J/m^2.[191] The threshold for this system appears to be ~34 J/m^2 although more data points within this region would be required to give an accurate figure. The steep increase observed above threshold can be attributed to the rapid conversion of photons into heat which leads to particle ejection and hence ionisation.[195,196] A plateau in ion intensity can be observed at ~117 J/m^2. Steven *et al.* report an ionization threshold of ~24 and plateau at 72 J/m^2 for a thin film system of lipid standard and CHCA, the difference in these results can presumably be attributed to the different matrix and analyte compounds.[191]
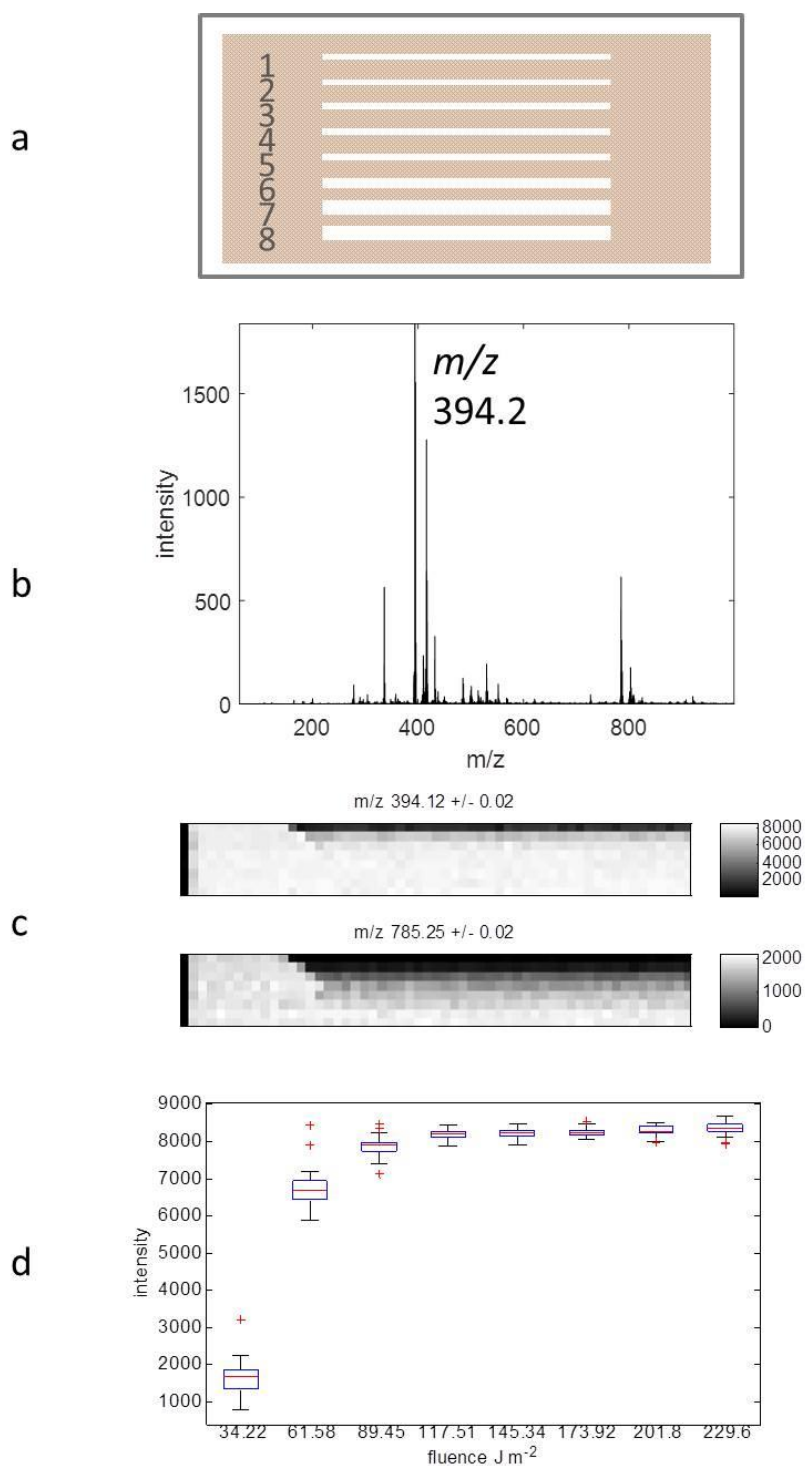
Figure 4.8 MALDI mass spectrometry results from fluence study: a) schematic of the sample, 1-8) fluence values of 34.22, 61.58, 89.45, 117.51, 145.34, 173.92, 201.80 and 229.60 J m^{-2} respectively, b) example single pixel spectrum acquired with a fluence of 34.22 J m^{-2}, c) example ion images of drug (*m/z* 394.2) and matrix cluster (*m/z* 785.2) a cluster ion was selected because the molecular ion was not detected, d) boxplot of

MALDI MS ion data for m/z 394.2, this indicates increasing ions detected with increasing laser fluence.

The sample was removed from the mass spectrometer and was imaged using SRS. Lasers were tuned to resonance frequencies of PNA and erlotinib in turn, three regions of each irradiated region were imaged at each frequency, see Figure 4.9 and Figure 4.10. The horizontal stripes which become obvious at fluence values ~89 J/m^2 are a result of uneven fluence distribution across the beam profile which has been well characterised.[64,192,193,197,198] The laser beam is coupled to the MALDI ion source via a patchcord fiber; the beam profile post-fiber has a characteristic 'speckle pattern'. This means there is variation in fluence across the area irradiated by the laser and some regions may be below the threshold fluence for desoption/ionisation. As the sample moves beneath the laser, unablated regions of material become stripes. At higher laser fluence ~230 J/m^2 the stripes disappear because the total energy delivered by the laser is high enough that even regions of lower fluence are above threshold. It is clear from these images that an increasing amount of material has been removed at higher laser fluence. This is in accordance with mass spectrometry data and suggests that larger numbers of ions are detected at higher laser fluence because more material has been ablated during desorption events. However the plateau in ions detected at ~120 J m^{-2} in the mass spectrometry data is not obvious in SRS images; it would appear that complete ablation of the sample occurs ~230 J m^{-2}. This suggests that there is a maximum detected ion intensity for this analyte/matrix combination which cannot be overcome by irradiating the sample with larger amounts of energy. It is most likely that detector saturation is responsible; the sensitivity of the detector is insufficient to detect any more ions even though they have been produced from the sample.
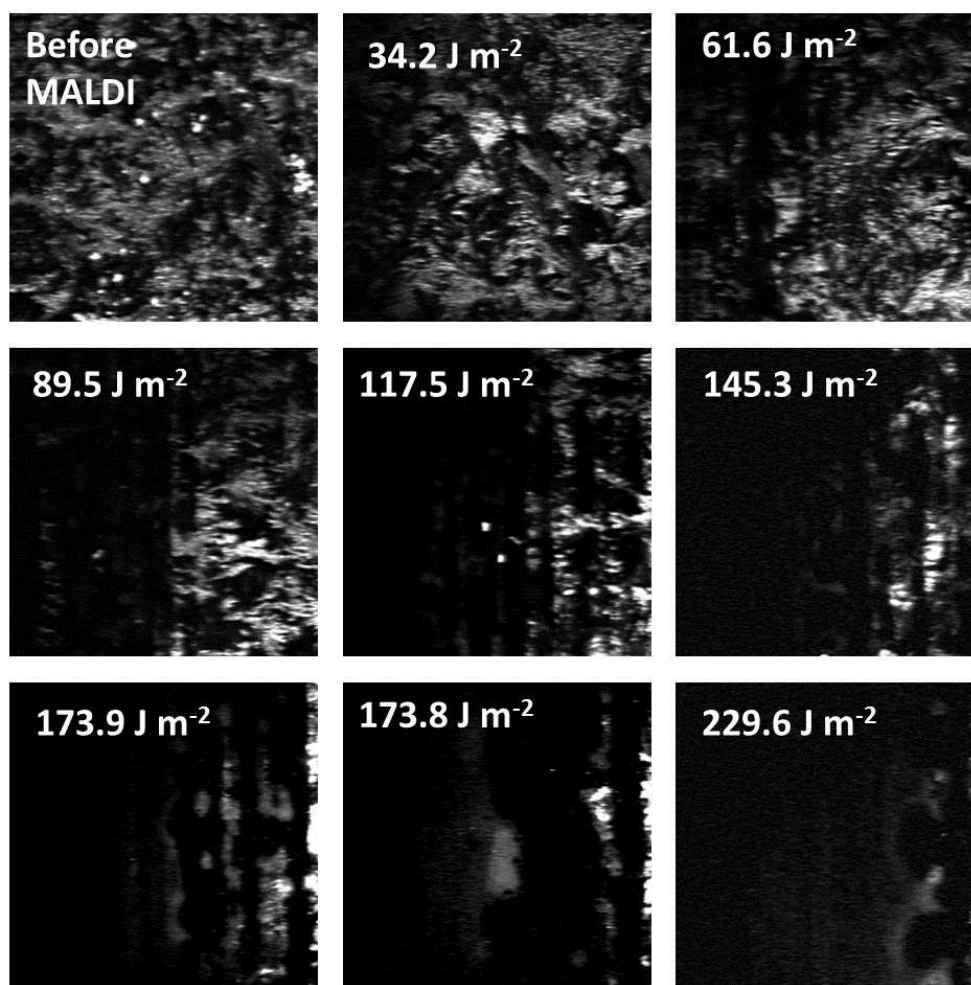
Figure 4.9 SRS images of PNA after MALDI analysis at a range of laser fluences.
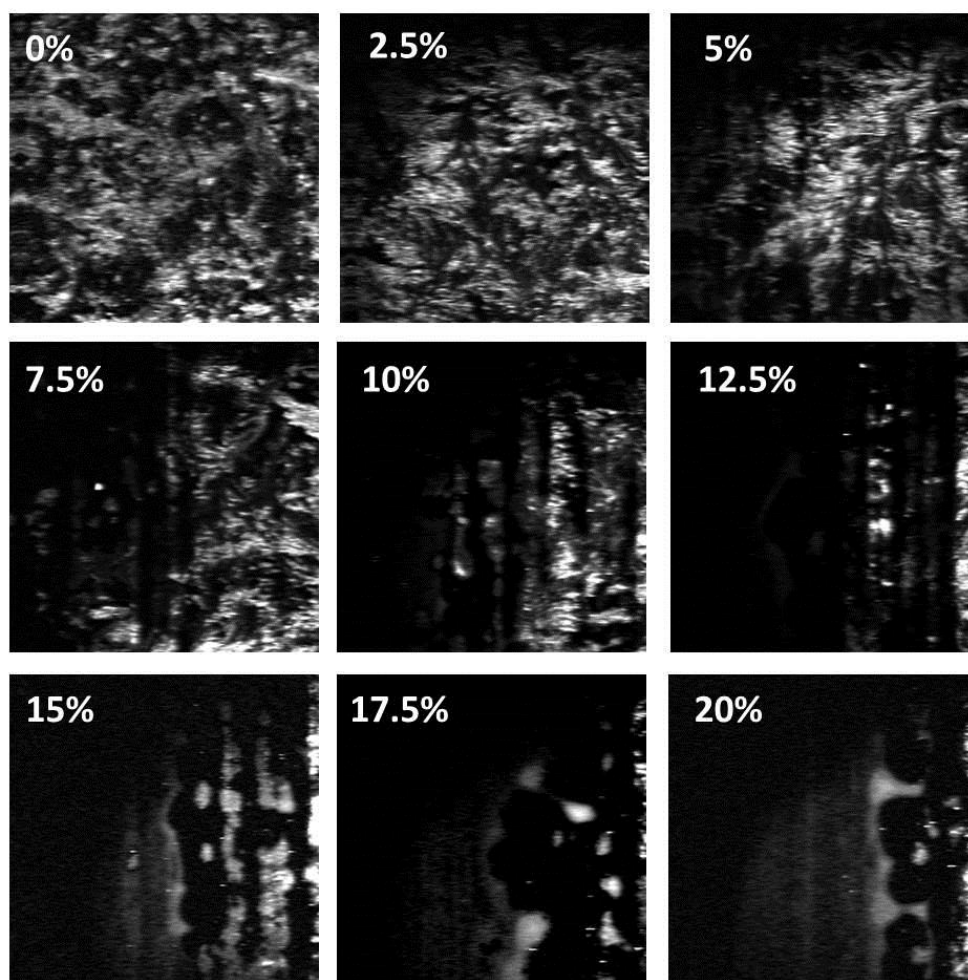
Figure 4.10 SRS images of erlotinib after MALDI analysis at a range of laser fluences.

It is possible to infer some information just by visual analysis of the SRS images, however quantitative data requires calculation of total intensity observed at each location and average intensities at each laser fluence value. The results from this analysis are displayed in Figure 4.11. Graphs demonstrating the number of ions detected by MS vs fluence and the number of molecules removed (as calculated from SRS images) are largely in agreement. Similar sigmoidal curve shapes are observed by each technique. The steep increase in erlotinib ion intensity observed by MS occurs at a threshold value of 34 J/m^2, however the steep increase in the number of molecules removed doesn't occur until a fluence of 80-90 J/m^2 is reached. This suggests that the increased ion intensity detected by MS is not a direct result of increased desorption.

Photoacoustic measurements have been used to measure ablation volumes during MALDI MS.[144,199] A report by Rohlfing *et al.* found that for a system of substance P (a protein) and glycerol matrix, significant ablation occurred at fluence below threshold.[199] Due to the number of data-points collected in this experiment it is difficult to determine whether similar levels of ablation occur below threshold, however at threshold the number of molecules removed from the surface is 1-1.5 x 10^{14}. Similar features were observed in the work described here and the photoacoustic measurements, such as the steeper gradient observed for ion intensity with fluence compared to that observed for material removed. Additionally the plateau in ion intensity occurs at lower fluence compared with material removed. This suggests that the method described in this work provides an accurate picture of desorption/ionisation events. The benefit of this method over photoacoustic measurements is the absolute quantification of molecules removed during ablation – this is the first report of a method with such capabilities.

The variation observed in SRS data could again be caused by inhomogeneity in the sample. The graph of ions detected vs number of molecules removed tells us the ionisation efficiency of this MALDI analysis which is 1-2 in 10^9. Ion yields are typically quoted in the literature between 1 in 10^3 - 10^4,[9] however it is possible that the method described in this thesis is the first capable of calculating an accurate value. An ionisation efficiency of 1 in 10^9 is less favourable than the picture painted in the literature but this could be due in part to detector inefficiencies. The important point to note is that this method can be used to quantitatively measure efficiencies and so performance under different experimental parameters may now be compared.
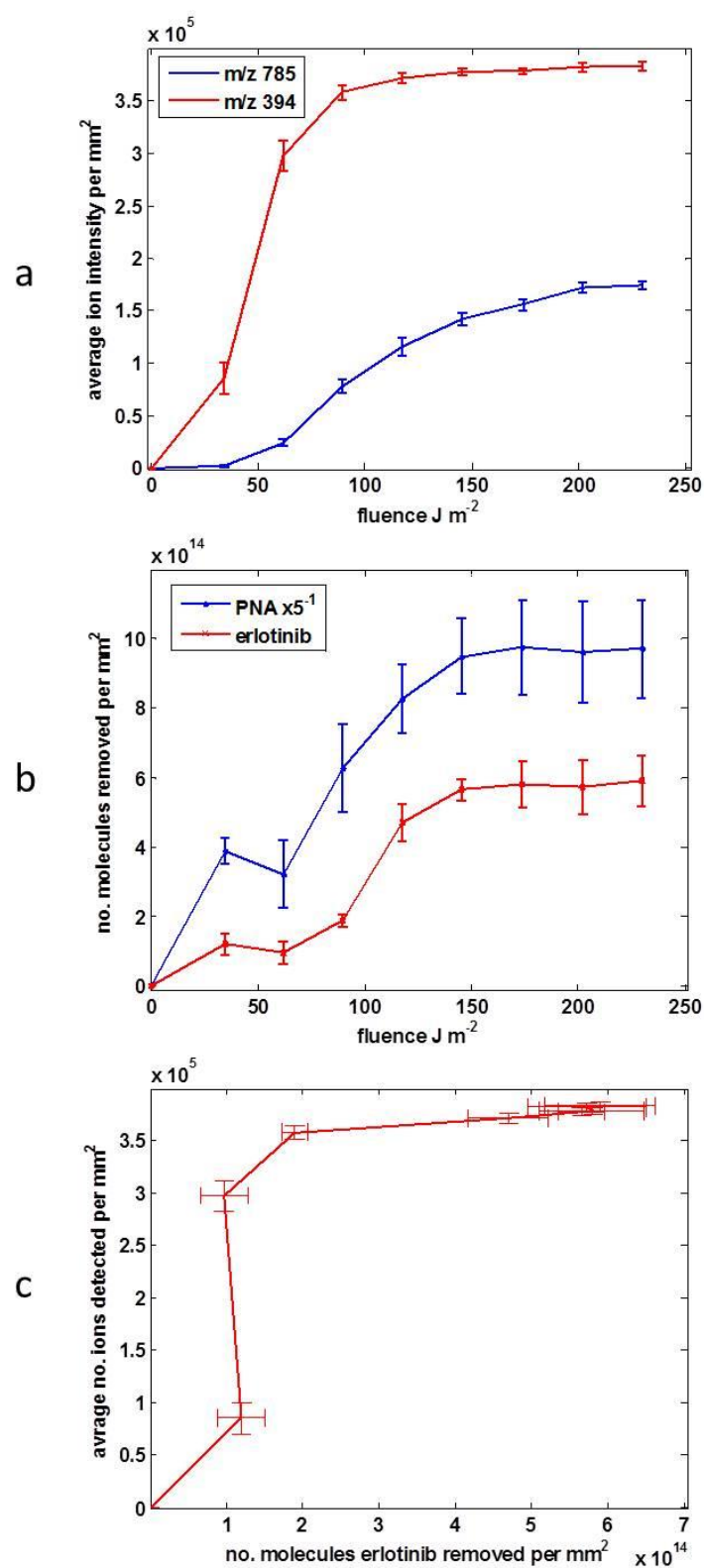
Figure 4.11 Results from SRS analysis of MALDI sample: a) ions detected vs fluence, b) molecules removed from surface vs fluence (as calculated from SRS data), c) number of ions detected vs number of molecules removed from the surface.

4.3.3 A quantitative study of the effects of laser repetition rate in MALDI MS

After demonstrating how SRS could be used to quantify MALDI surface sampling with respect to laser fluence, a further experiment was designed to use SRS to provide insight into the effects of laser repetition rate on desorption/ionisation. Laser repetition rates, or the number of laser shots delivered to the surface per unit time have been found to critically affect ionisation in MALDI.[19,141] Lasers capable of operating at high repetition rates are now commonly used in commercial MALDI MSI instruments and therefore the behaviour of different matrices at different repetition rates must be understood in order to optimise experiments.

Thin films of erlotinib and SA and PNA matrices were prepared. SA is a cinnamic acid derivative containing a carboxylic acid group which has been proposed to undergo photomodification effects under high laser repetition rate irradiation.[141,142,200] PNA is an aniline derivative which contains no such carboxylic group and can therefore be expected to exhibit different behaviour upon irradiation. The molar ratio of matrix to analyte and total amount of drug deposited were kept constant for each sample. Single line raster images were acquired from each sample at a range of different laser repetition rates (1-6 KHz). The average drug and matrix ion intensity detected at each repetition rate is displayed in Figure 4.12 and Figure 4.13. When PNA was used as matrix the average number of ions detected steadily increases with repetition rate and reaches a maximum at ~4 KHz, after which a slight decrease in ion intensity is observed. However when SA was used as the matrix, the inverse relationship was observed and fewer ions were detected as the repetition rate increased. This cannot be explained by increased levels of fragmentation at higher repetition rates because the same relationship is observed for major fragment ions of erlotinib, see Figure 4.13. This is counter-intuitive because the energy per laser pulse and raster speed were kept constant,

therefore the only thing changing is the number of laser shots delivered per area per unit time. This suggests that energy build up or heating within the matrix is causing decomposition in the sample which results in lower desorption yields.
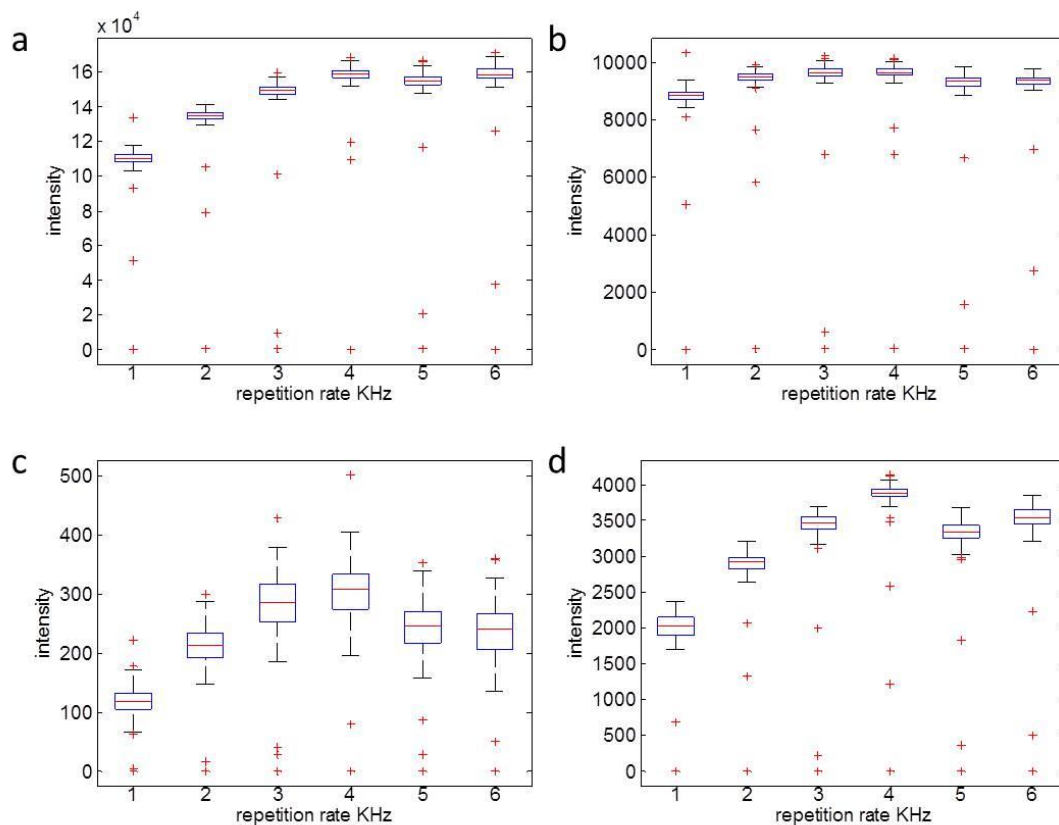
Figure 4.12 Boxplots of MALDI MS data acquired from PNA sample at different laser repetition rates: a) TIC, b) ions with *m/z* 394.2 corresponding to [M+H]$^{+}$ ions of erlotinib, c) ions with *m/z* 336.2 corresponding to the major fragment ion of erlotinib, d) ion with *m/z* 139.0 corresponding to [M+H]$^{+}$ ions of PNA.
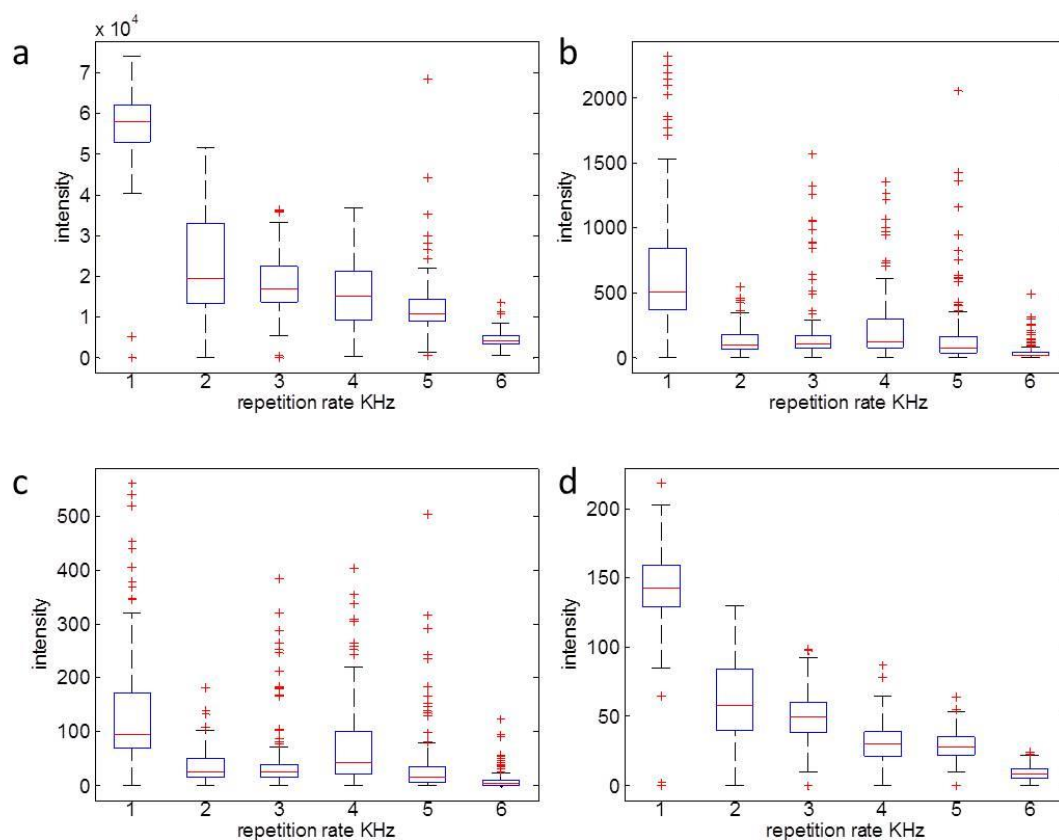
Figure 4.13 Boxplots of MALDI MS data acquired from SA sample at different laser repetition rates: a) TIC, b) ions with *m/z* 394.2 corresponding to [M+H]$^+$ ions of erlotinib, c) ions with *m/z* 336.2 corresponding to the major fragment ion of erlotinib, d) ion with *m/z* 225.1 corresponding to [M+H]$^+$ ions of SA.

Both samples were imaged using SRS after MALDI analysis to quantify the amounts of material removed under different conditions. Example white light and SRS images of each sample can be seen in Figure 4.14. Images of PNA reveal an intuitive relationship with repetition rate, in which more material is removed when larger numbers of laser shots are incident on the samples, which agrees with the MALDI data. Images of SA show that the largest amount of material is removed at a repetition rate of 1 KHz, under which conditions the largest number of ions is detected. At higher repetition rates SRS image intensity is similar to non-irradiated regions; however white light images reveal changes to surface morphology which look similar to those reported by Fournier *et*

al.[141] As previously mentioned, it has been postulated that photomodification of matrix molecules after repeated irradiation results in lower absorption efficiency and therefore lower desorption/ionisation yields. Cinnamic acids are known to undergo configurational changes in lattice structure upon irradiation with UV light.[201] The thermal stability of CHCA and SA were investigated by Tarzi *et al.* who proposed mechanisms for the decarboxylation and photo-dimerisation of cinnamic acids upon UV-irradiation.[142] By comparison of the number of ions detected in subsequent analyses using CHCA and an alternative non-carboxylate matrix compound (PNA) Steven *et al.* found additional evidence for such photomodifications.[10] SRS data acquired in this work provides further evidence that laser-induced changes to SA crystal morphology are responsible for decreased ion intensity at high repetition rates.
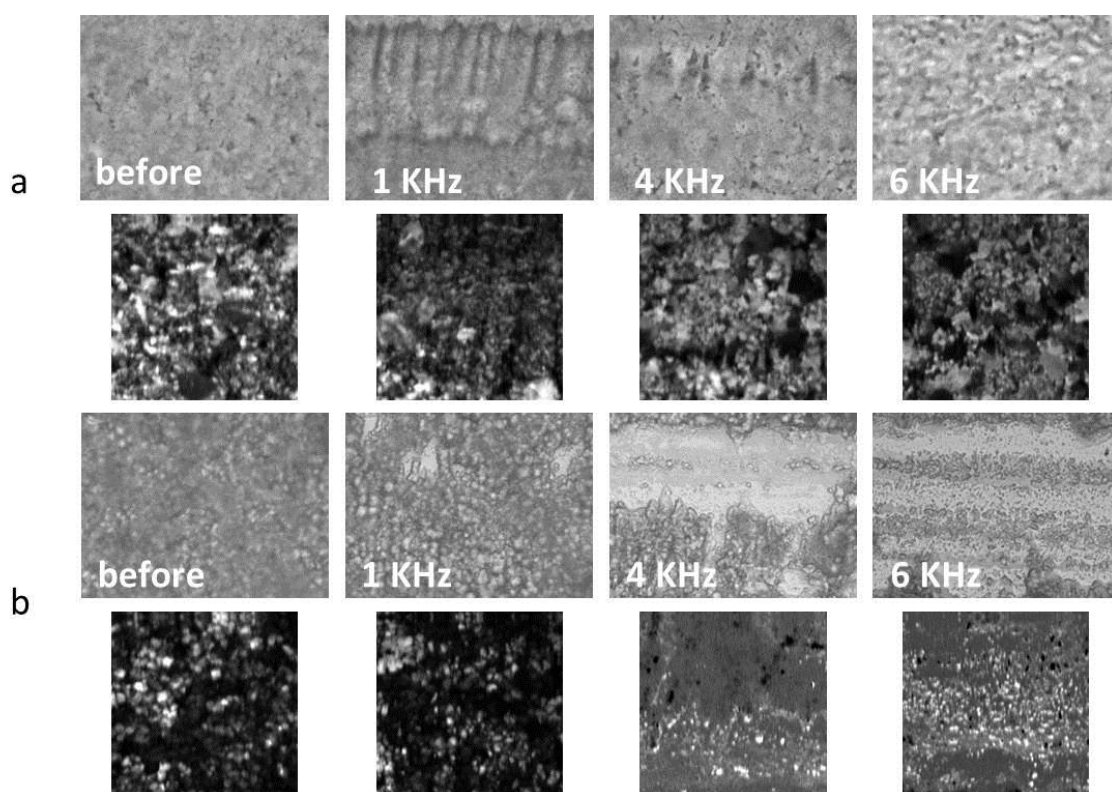
Figure 4.14 Example white light (top) and SRS (bottom) images from a) SA and b) PNA samples irradiated with different repetition rates.

In order to further probe changes in surface chemistry of the SA thin film, spontaneous Raman mapping of a small region of the irradiated sample was performed, see Figure 4.15. This imaging technique is much slower than SRS due to the inefficiency of the Raman scattering process, hence the small image region selected. The image region spans the edge of one irradiated region so that both irradiated and non-irradiated regions feature in the image. An example Raman spectrum from each region is presented in Figure 4.15. A number of subtle effects can be seen in these spectra, multivariate analysis was performed to further investigate these spectral changes.
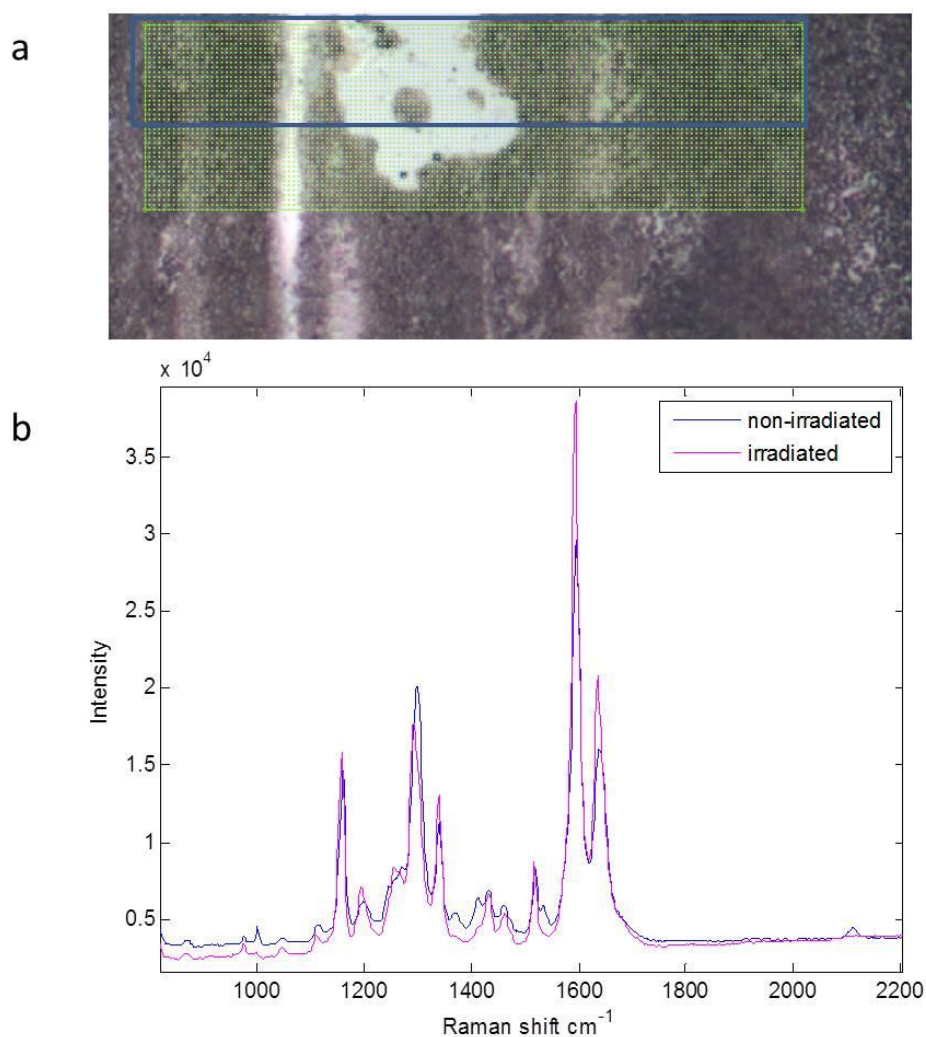
Figure 4.15 Spontaneous Raman spectroscopic imaging of irradiated erlotinib and SA sample, a) optical image of imaged region, b) example Raman spectra from irradiated and non-irradiated region.

Principal component analysis (PCA) was performed on the full dataset in order to identify the largest sources of variation within the image. Score images for principal components 2 and 3 are displayed in Figure 4.16. These images indicate that there is a large amount of variation between non-irradiated and irradiated material. Loadings plots for these principal components show the Raman bands which contribute to this variation. Two intense peaks at ~ 1600 cm^{-1} and 1650 cm^{-1} localised in the non-irradiated region, could be due to the C=C aliphatic stretching mode and C=O stretching

103

mode of the carboxyl group. These modes are known to decrease in intensity on formation of the dimer because the aliphatic C=C rearranges to form a cyclobutane ring and the C=O forms a hydrogen bond.[202] These modes are less intense in the irradiated region of the sample. This data supports the theory that photodimerisation of sinapinic acid occurs under higher repetition rate laser irradiation.
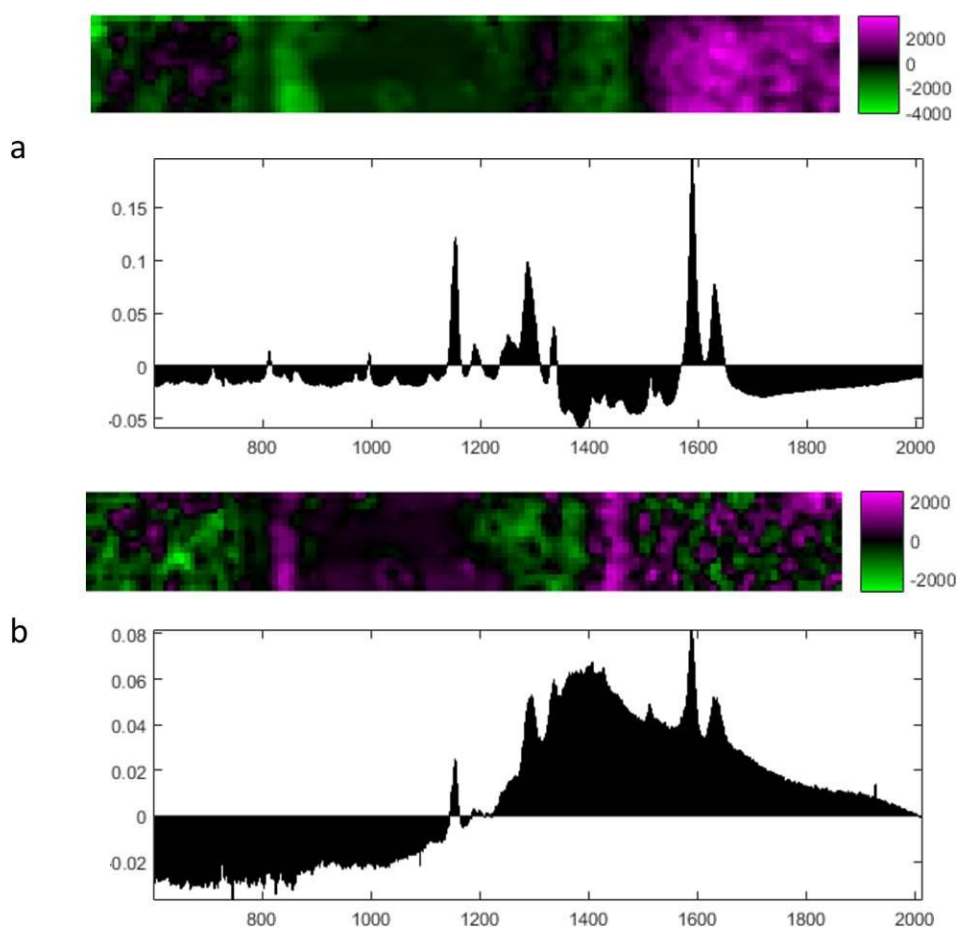
Figure 4.16 Principal component analysis of spontaneous Raman map of sinapinic acid sample, score images and loadings plot: a) principal component 2, b) principal component 3.

4.3.4 SRS imaging of MALDI sample preparation

In addition to quantifying MALDI surface sampling, SRS could be used to image sample preparation for optimisation purposes, for example to quantify analyte extraction and incorporation in matrix crystals. Matrix application is a critical step in the MALDI process; understanding of analyte distribution and extraction in matrix crystals could inform optimum sample preparation.

SRS image stacks were obtained from a thin film of erlotinib and PNA. 3-D reconstructions of these images are displayed in Figure 4.17. Images of the analyte and matrix have been overlaid so that the distribution of analyte in matrix crystals can be observed. It is apparent from these images that the two compounds are not completely co-localised. Erlotinib appears to be inhomogeneously distributed through matrix crystals; small green 'hotspots' of analyte can be seen within the larger purple crystals.
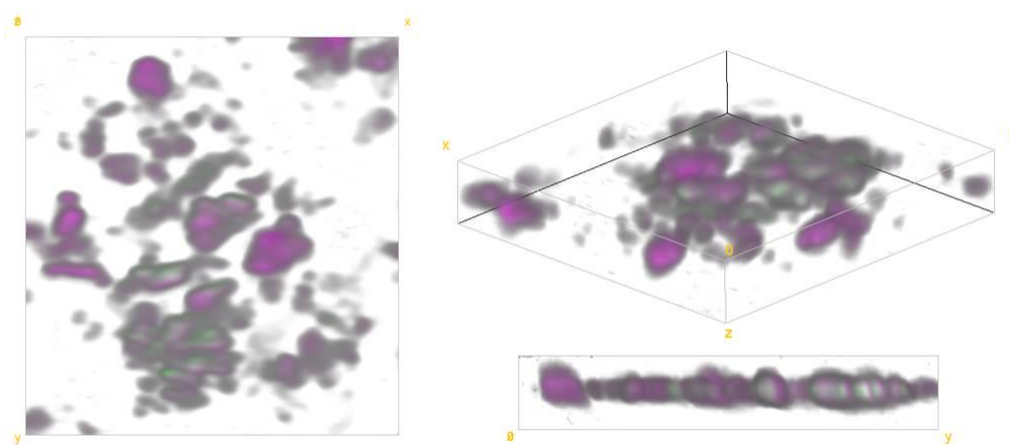
Figure 4.17 3-D reconstructions of SRS images of PNA (pink) and erlotinib (green).

To demonstrate how the technique could be used to assess sample preparation in biological studies, a further sample was prepared. A section of mouse brain tissue was coated with DHB matrix which was shown earlier to exhibit very weak SRS signals. This is important because it would be difficult to separate signals from the tissue and

any of the other matrices we have studied. It would therefore be difficult to image the analyte with confidence that the matrix had not contributed to the signal. SRS lasers were tuned to the resonance frequency of lipids and regions of tissue and matrix were selected for SRS imaging. 3-D reconstructions of image stacks were generated and are displayed in Figure 4.18. It can be seen that lipids are not homogeneously distributed throughout crystals but are localised in 'hotspots' which are similar to those seen in the simpler model system.
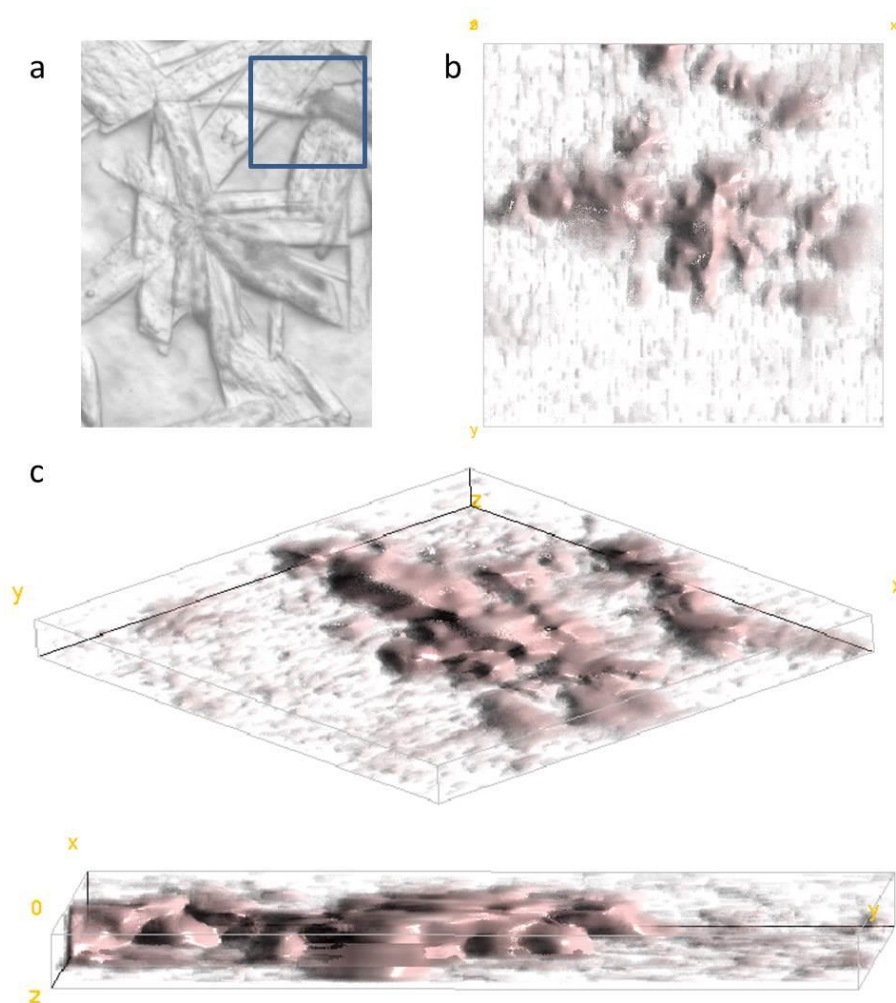
Figure 4.18 SRS imaging of lipids in mouse brain tissue and DHB crystals, a) white light image of imaged region of sample, b and c) 3-D reconstructions of SRS images of lipids.

4.4 Conclusions

This work has demonstrated for the first time how SRS can be used to visualise and quantify MALDI MS surface sampling under different laser conditions. Similar trends were seen to those reported by other techniques suggesting the data is reliable. The error associated with these measurements is likely due to inhomogeneity of the sample which would need to be addressed in order to make the method more accurate and repeatable. SRS imaging of MALDI sample preparation has for the first time been reported. The information such images provide could be crucial for the optimisation of sample preparation in MALDI. Several different matrix compounds were assessed for use in combined MALDI and SRS studies and PNA was identified as an ideal candidate. The absorption phenomena observed using CHCA and PNA at certain resonance frequencies present a problem in the future application of the method in more complicated and varied experimental set-ups.

Chapter 5

Multimodal Chemical Imaging of Biological Tissue: LESA, MALDI and SRS

5.1 Introduction

The previous two chapters have discussed the individual capabilities of LESA, MALDI and SRS. This chapter presents a combined 'multimodal' workflow in which the three techniques are executed on a single tissue section to provide complementary information and a more complete analysis of the sample. The ability to combine established imaging techniques could allow for the advantages of one method to overcome limitations in the other, for example limited spatial resolution. The highly specific nature of mass spectrometry data could be used to increase confidence in assignment of SRS data and the excellent spatial resolution of SRS images could be combined with mass spectral data for improved image resolution. Quantitative SRS could also be used to calculate absolute quantities of drug targets in dosed organisms. SRS, MALDI and LESA produce images over a length scale which spans 6 orders of magnitude. This scale of magnification is illustrated in Figure 5.1. If we take the example of imaging the Earth, these differences could be approximately equated to distinguishing between land and water (LESA), countries in Europe (MALDI) and navigating the streets of London (SRS). A single field of view in the SRS microscope is smaller than a typical single pixel in a MALDI imaging experiment. Primarily the 3

techniques will be used for absolute quantification of a drug compound, high resolution mass spectrometry images with good specificity and sensitive analysis of multiple drug compounds and classes of analyte simultaneously.

The sample used is this work was taken from an animal which had been cassette-dosed. This involves dosing several carefully selected drug compounds simultaneously for higher throughput screening of physiochemical and pharmacokinetic properties. Such an approach reduces the number of animals required which is an important step towards the 'three Rs' concept (reduce, refine, replace)[203] and has also been shown to reduce time and financial costs.[153,204,205] Such samples provide an ideal platform on which to test the relative sensitivity and versatility of LESA, MALDI and SRS.
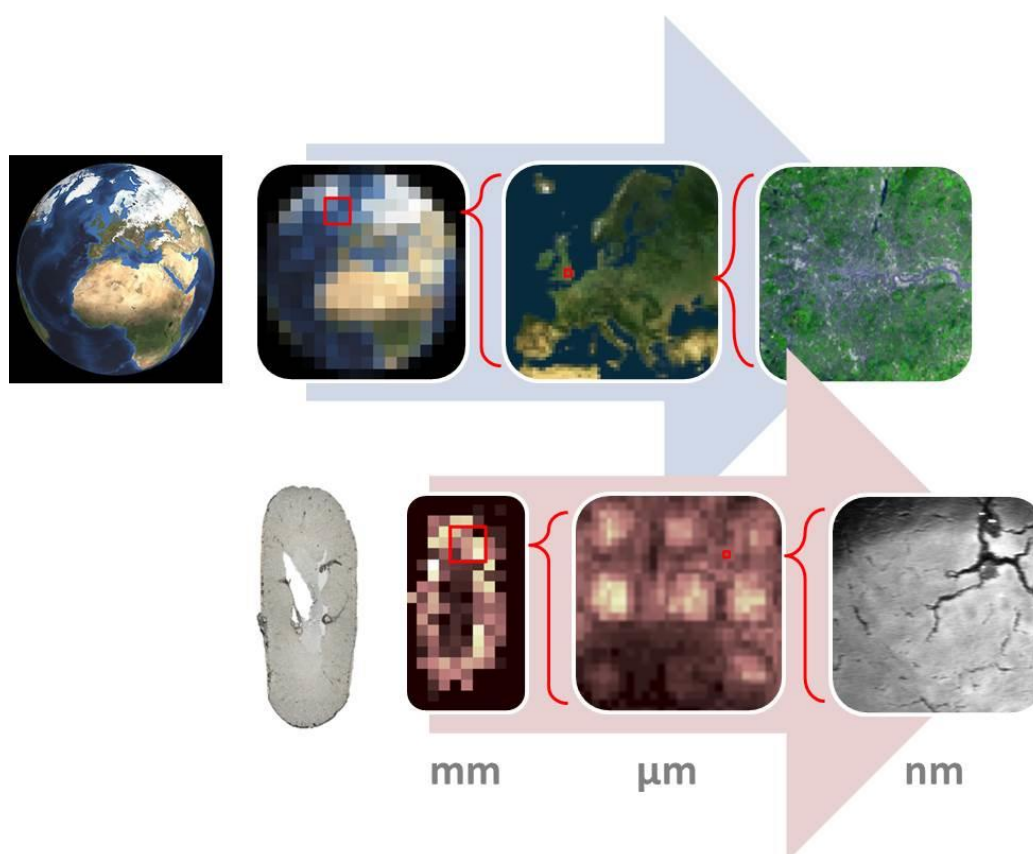
Figure 5.1 Illustration of relative length scales involved in LESA, MALDI and SRS imaging.

5.2 Experimental

5.2.1 Tissue sample preparation

Tissue from control and cassette-dosed animals was sectioned as described in section 2.2.1.1 and prepared for MALDI analysis as described in section 2.2.1.2 using CHCA as the matrix.

5.2.2 SRS microscopy of mouse brain tissue

SRS microscopy of mouse brain samples was performed as described in section 2.2.2.4. Lipids, proteins and water (2860, 2930 and 3253 cm^{-1} respectively) were imaged by adjusting the OPO. Regions of tissue were identified via white light images of the sample and 50 x 50 μm regions were selected for SRS imaging. Integration time of 3 ms per pixel was found to provide sufficient contrast within the imaged region, images of 256 x 256 pixels were acquired.

5.2.3 Preparation of erlotinib calibration sample

The calibration sample was prepared using a TM-Sprayer (HTX Technologies LLC). Known amounts of erlotinib were deposited on a glass coverslip to the following final concentrations: 0.197, 0.262, 0.328, 0.393, 0.458 μg/mm^2. The coverslip was sealed face-down onto a standard glass slide.

5.2.4 SRS microscopy of calibration sample

Three regions of each erlotinib concentration were selected and imaged by the SRS system. Image regions of 80 x 80 x 15 μm (15 images, separated by 1 μm in the z-dimension) were scanned with laser beams tuned to the nitrile group of erlotinib (2110 cm^{-1}). A pixel dwell time of 100 μs and laser power of 70 mW were used.

5.2.5 SRS microscopy of cassette-dosed tissues

Cassette-dosed tissues were imaged as described in section 2.2.2.4. Image regions of 80 x 80 x 15 μm (15 images, separated by 1 μm in the z-dimension) were scanned with laser beams tuned to the nitrile group of erlotinib (2110 cm^{-1}). A pixel dwell time of 100 μs and laser power of 70 mW were used.

5.2.6 LESA mass spectrometry imaging

Surface sampling of cassette-dosed kidney tissue was performed as described in section 2.2.2.1. A grid of 220 sampling locations was selected with an x,y spacing of 1mm.

5.2.7 MALDI mass spectrometry imaging

Kidney tissue which had been sampled by LESA MS was coated with CHCA matrix as described in section 2.2.1.2. MALDI MS imaging was performed as described in section 2.2.2.2. Data were acquired in positive ion mode with a pixel size of 100 x 100 μm.

5.3 Results and Discussion

5.3.1.1 SRS microscopy of mouse brain tissue

To demonstrate the capabilities of SRS microscopy in terms of tissue analysis, images of various species endogenous to brain tissue were acquired from a sample of mouse brain tissue, see Figure 5.2. Images reveal anatomical details of what appears to be a blood vessel containing red blood cells. Lipid images (2860 cm^{-1}) reveal circular features of ~8 μm diameter, which is approximately the size of a red blood cell and could therefore correspond to the phospholipid cell membrane. Images of water (3253 cm^{-1}) reveal an inverse intensity distribution as compared with the lipid image, the higher water intensity seen inside the blood vessel corresponds to the high water content of blood plasma. Protein images (2930 cm^{-1}) reveal a similar distribution to lipids; it is not possible to further discern cellular features in this particular region. Images acquired at an off-resonance frequency (2245 cm^{-1}) reveal no anatomical features and a low background signal, thus validating the SRS images acquired. The pixel sizes used in this study (~200 nm) are sufficient to reveal cellular and intracellular features.
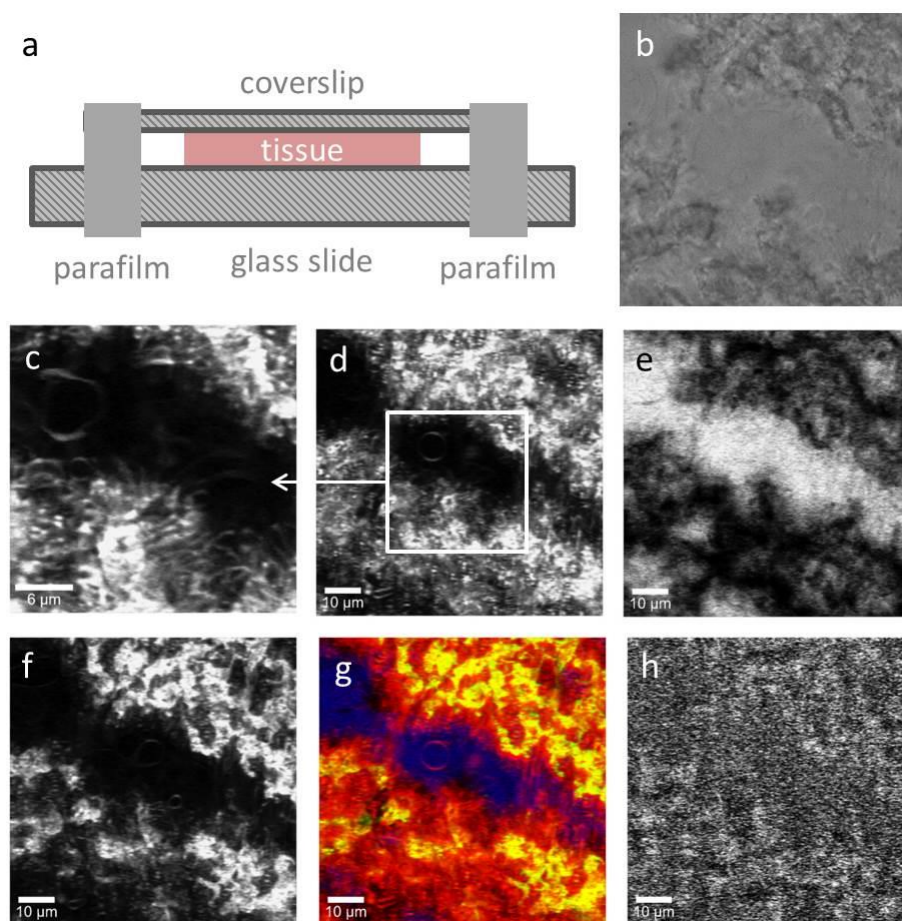
Figure 5.2 SRS microscopy of mouse brain tissue, a) sample set-up: tissue section was sandwiched between a glass coverslip and a microscope slide, b) white light image of tissue region imaged by SRS, c) SRS image of lipids (2860 cm^{-1}), d) lower magnification image of lipids in same region, e) SRS image of water (3253 cm^{-1}), f) SRS image of protein (2930 cm^{-1}), g) overlay of lipid (red), water (blue), and protein (yellow) images, h) SRS image acquired off-resonance (2245 cm^{-1}).

5.3.2 Cassette dosed tissue samples

Tissue sections from various organs of a rat dosed with erlotinib, terfenadine, olanzapine and moxifloxacin were analysed by SRS microscopy, LESA and MALDI mass spectrometry imaging. It was not previously known where each drug would accumulate within organs of the body. A survey of the different organs was performed to ascertain which organ would be most suitable for a multimodal imaging study. SRS images of lipids (2860 cm^{-1}), proteins (2930 cm^{-1}) and erlotinib (2111 cm^{-1}) were

113

acquired from each tissue type, see Figure 5.3. Of the dosed drug compounds, only erlotinib exhibits Raman bands outside of the biological 'fingerprint' region, therefore SRS images of this drug only were acquired. Images acquired at an off-resonance frequency (1800 cm^{-1}) are also displayed for comparison. Tissue structures can be observed in lipid and protein images from every tissue type. Hotspots of high intensity can be observed in images of kidney, liver and lung; these signals are likely to be due to two-photon absorption by haemoglobin[135] in blood because they appear in images at all resonance frequencies measured, including the off-resonance frequency in which no SRS should be observed.[127,136] Images of erlotinib demonstrate very low signal compared with lipid and protein which is to be expected due to its relative abundance. The only tissue type from which the observed signal from erlotinib seems significantly higher than the background noise is kidney. It was therefore concluded that kidney tissue would be the most suitable tissue type for a study in which SRS was used to quantify erlotinib in tissue.
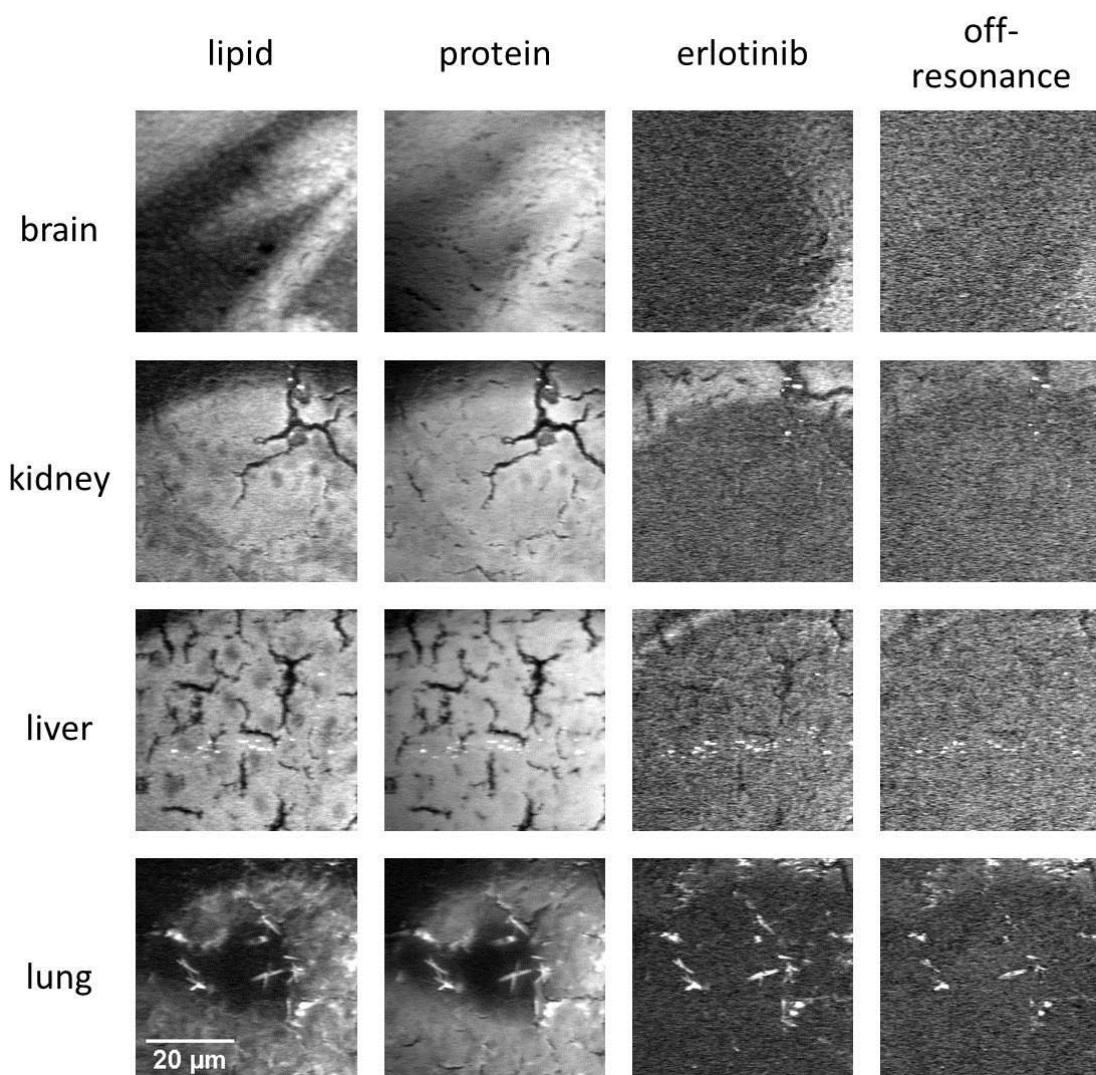
Figure 5.3 SRS images acquired from thin tissue sections of various organs taken from cassette-dosed rat, lipids (2860 cm^{-1}), proteins (2930 cm^{-1}), erlotinib (2111 cm^{-1}) and an off-resonant frequency (1800 cm^{-1}) were imaged.

A further set of samples from the dosed rat organs were subject to LESA MS. Example mass spectra acquired by LESA MS from each tissue type are displayed in Figure 5.4. This region of the mass spectrum demonstrates the different lipids preferentially detected from each tissue type and their relative abundances. Lipids were preferentially detected as the [M+H]$^{+}$ species in every tissue type. The most abundant lipid species detected from each tissue type are labelled in Figure 5.4. Lipids could be detected from

every tissue type studied, as could each of the dosed drug compounds. However multiply charged protein ions could only be detected from brain, kidney and lung (under these specific sampling conditions). Unidentified protein ions centered at *m/z* 993.70 (+5) and 828.25 (+6) were detected from brain, kidney and lung.
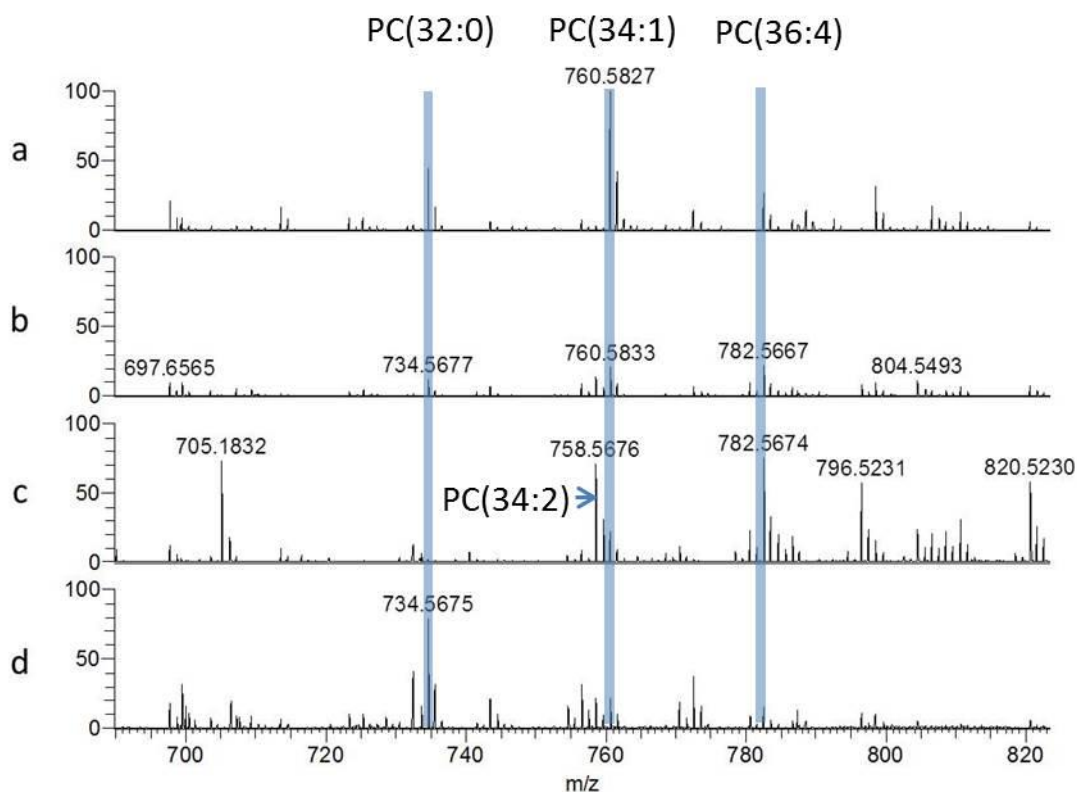
Figure 5.4 Example spectra acquired by LESA mass spectrometry analysis of various organs from cassette-dosed rat, a) brain, b) kidney, c) liver, d) lung.

LESA MS intensity profiles of each drug compound detected from each different tissue type are displayed in Figure 5.5. All four drug compounds were detected as the [M+H]$^+$ species and were detected from every tissue type using LESA MS. Particularly high relative abundances were noted for olanzapine and moxifloxacin from kidney tissue. This indicates that kidney would be a promising model tissue for a combined study. In addition, the anatomical features within rat kidney tissue (cortex and medulla) are of

sufficient size that contact-LESA pixel sizes could be capable of distinguishing the two tissue types.
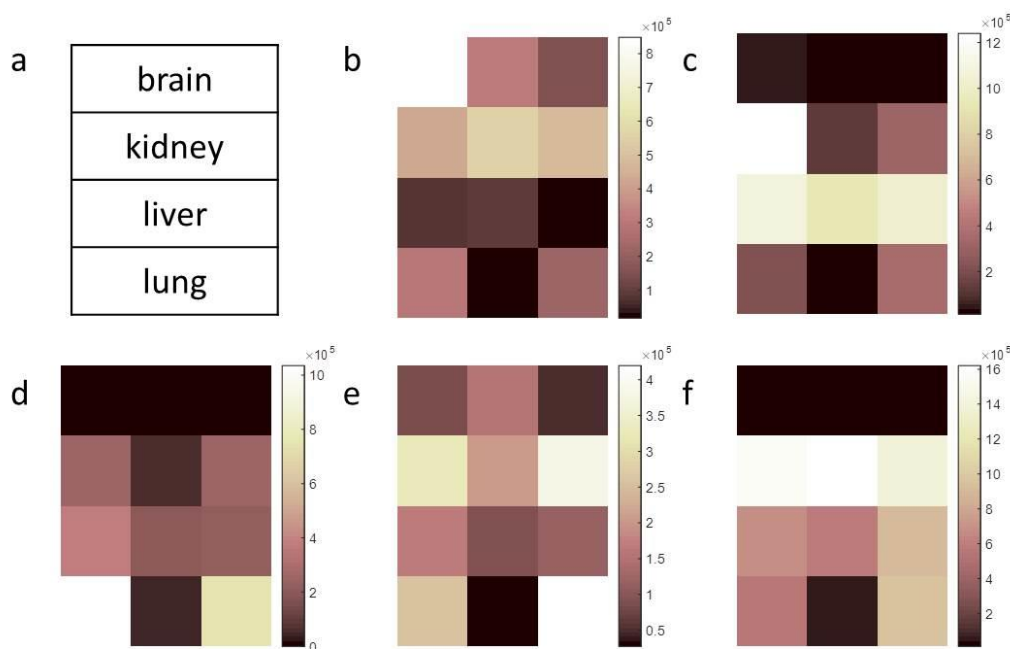
Figure 5.5 Intensity of cassette dosed drug compounds in various organs from cassette-dosed rat acquired over three repeats: b) ions detected with *m/z* 760.5827 (endogenous lipid for comparison), c) ions detected with *m/z* 394.1752 (erlotinib), d) ions detected with *m/z* 472.3197 (terfenadine), e) ions detected with *m/z* 313.1472 (olanzapine), f) ions detected with *m/z* 402.1813 (moxifloxacin).

A further set of organ sections was coated with CHCA matrix and imaged using MALDI MSI. Single pixel spectra from each tissue type are displayed in Figure 5.6. Good lipid signal intensity was observed from each tissue type. Lipids were predominantly detected as the potassium adduct. Interestingly, in the case of brain, liver and lung tissue, the most abundant lipid species detected were the $[M+K]^+$ species of the same lipid detected by LESA MS. This correlation suggests that the differences spectral abundance reflects true differences in abundance in the tissue and not ionisation or desorption efficiencies because different ionisation mechanisms occur in each

method. The methanol based solvent system was used both as LESA extraction system and matrix carrier during sample preparation for MALDI, therefore the result could be due to relative lipid solubilities in methanol/water.
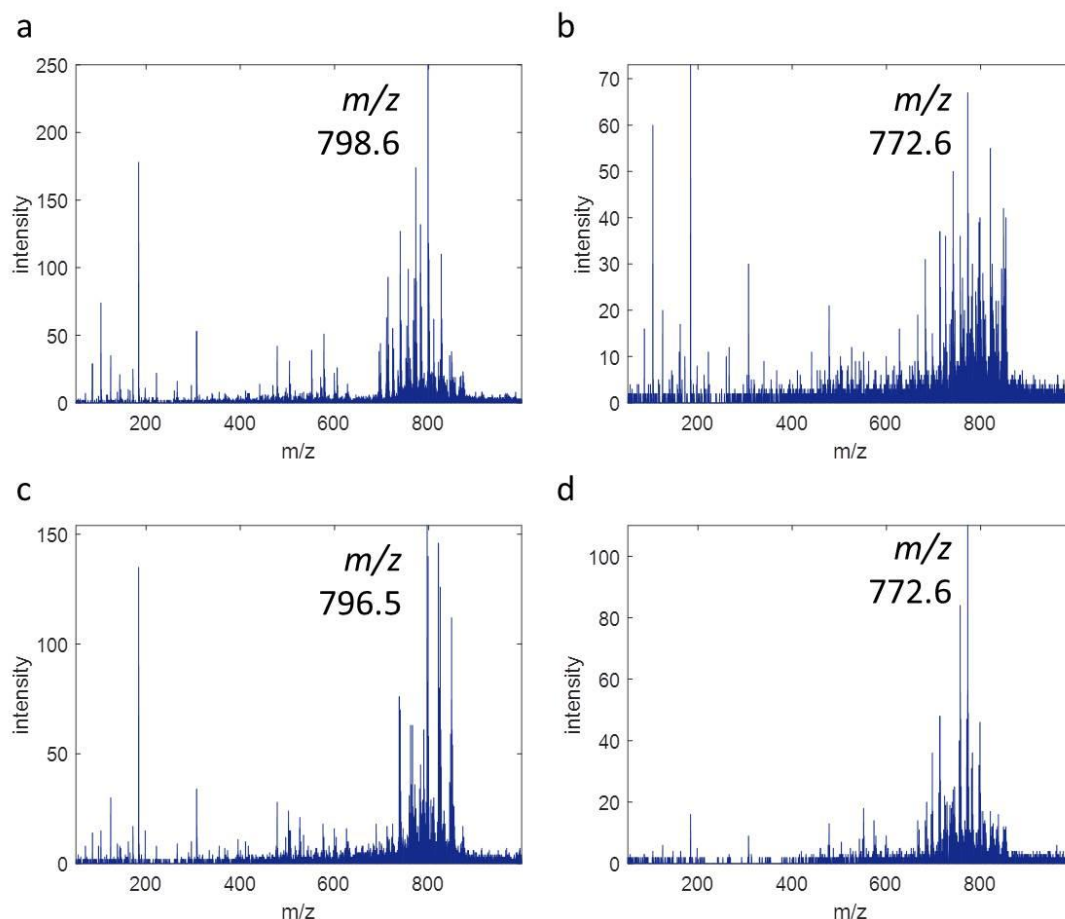
Figure 5.6 Example single pixel spectra acquired from various organs from cassette-dosed rat, the most abundant lipid species is labelled in each spectrum: a) spectrum acquired from brain tissue, most abundant lipid species was PC(34:1), b) spectrum acquired from kidney tissue, most abundant lipid species was PC(36:4), c) spectrum acquired from liver tissue, most abundant lipid species was PC(34:2), d) spectrum acquired from lung tissue, most abundant lipid species was PC(32:0).

Ion images from each tissue type are displayed in Figure 5.7. Partial section images were acquired from brain and liver tissue in order to save time. Lung and liver tissue

images do not reveal any particular anatomical features because they are relatively homogeneous tissue types. Ion images from brain and kidney tissue reveal features such as the hippocampus (brain) and the cortex/medulla (kidney). Such features present an additional facet to chemical imaging studies because the ability of a given technique to spatially resolve differences can be assessed. None of the dosed drug compounds could be detected as the $[M+H]^+$ or $[M+K]^+$ species or as any commonly reported metabolite.[153] This provides an early indication that the sensitivity of MALDI MS is lower than that of LESA (as used in combination with the particular instruments reported here).
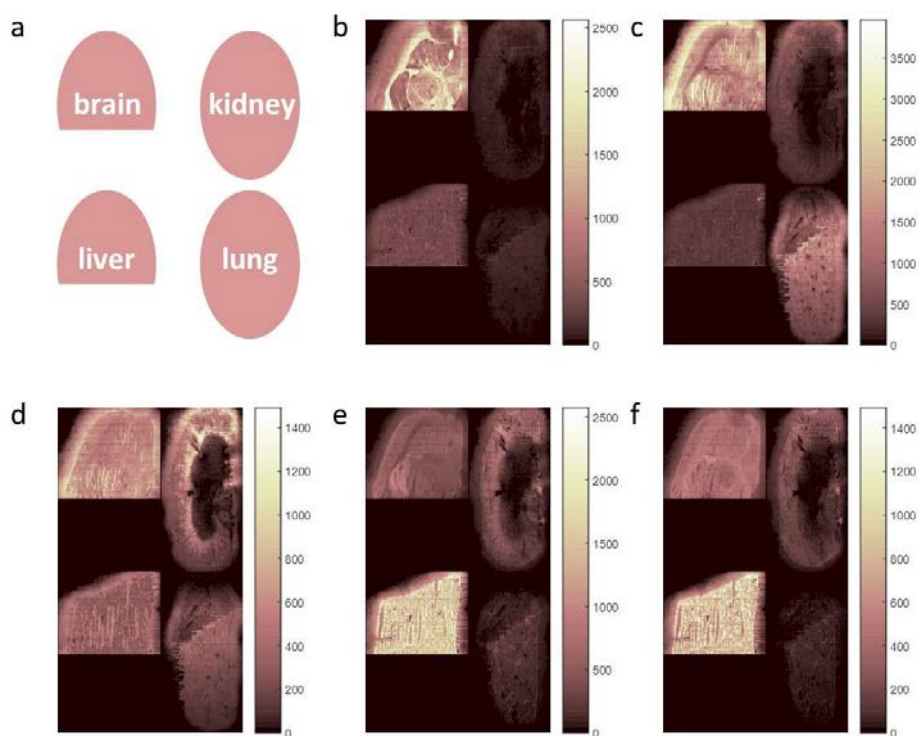
Figure 5.7 MALDI MS ion images of various organs from cassette-dosed rat, a) layout of sample, b-f) ions detected with *m/z* 826.6, 772.5, 741.6, 820.6, 848.6.

The abilities of each technique to detect a variety of analytes within these samples is summarised in

Table 5.1. SRS has been shown to be capable of detecting various pure drug compounds but the lack of specificity and the complex nature of Raman spectra acquired from biological tissue result in difficulties in imaging drug distribution in tissue. By careful selection of drug compounds which exhibit Raman scattering in the biologically 'silent' region, such as the nitrile group of erlotinib, it is theoretically possible to image a drug in tissue. However the sensitivity of the technique needs to be further assessed because if high dose levels (higher than the therapeutic level) are required to generate sufficient signal then this limits the usefulness of the technique. The sensitivity of MALDI MS was not sufficient to detect any of the dosed drug compounds but did detect a large number of lipid ions. Whist it is not possible to simultaneously detect proteins, the sample could be washed, re-coated with a different matrix compound and analysed again.[15] The relative sensitivity of LESA was demonstrated to be better than MALDI, and was sufficient to detect all four drug compounds, lipids and proteins simultaneously. A method in which all three techniques are applied sequentially to a single tissue section was subsequently implemented on a further section of kidney tissue which has been identified as a suitable target organ.

Table 5.1 Summary of the capabilities of each technique in terms of analytes detected.

Analytical technique	Analyte					
	Protein	Lipid	Erlotinib	Moxifloxacin	Terfenadine	olanzapine
SRS	✓	✓	✓	✗	✗	✗

MALDI	✗[1]	✓	✗	✗	✗	✗
LESA	✓	✓	✓	✓	✓	✓

5.3.3 High resolution imaging and quantification of erlotinib in tissue using SRS microscopy

Further tissue sections were taken from the cassette-dosed kidney tissue and used to investigate the potential usefulness of a multimodal SRS, LESA and MALDI imaging method. As a non-destructive technique which should not alter the sample, SRS was performed first. Kidney tissue was selected as a suitable tissue type in terms of expected analytes (all 4 drug compounds had been detected in kidney in a previous study[153] and in preliminary work) and size of anatomical features which could be visualized by the different resolution imaging modalities. Example SRS images of lipids and erlotinib in three different regions of the kidney section are featured in Figure 5.8. Different tissue structures and features can be observed in each of the images, in the medulla and inner cortex individual renal cell nuclei can be seen as darker spots in the lipid images. The renal cortex is responsible for ultrafiltration and the medulla is responsible for maintaining the salt and water content of the blood. It does not appear to be possible to distinguish individual cell boundaries or membranes within these images. The large branched structure appearing as a dark feature predominant in images of the outer cortex is possibly a proximal convoluted tubule – which forms part of a glomerulus. The

---

[1] Cannot be detected simultaneously with lipids; separate sample preparation methods required.

apparent signal from erlotinib is relatively high in these images – the difference in intensity between this and the previous dataset can be explained by the higher laser power used for image acquisition in this set. The difference in intensity between images of erlotinib and images acquired off-resonance is similar to that observed in the previous dataset. This could present a problem during quantification of the signal because good characterization of the background signal will be required in order for the true signal from erlotinib to be calculated.
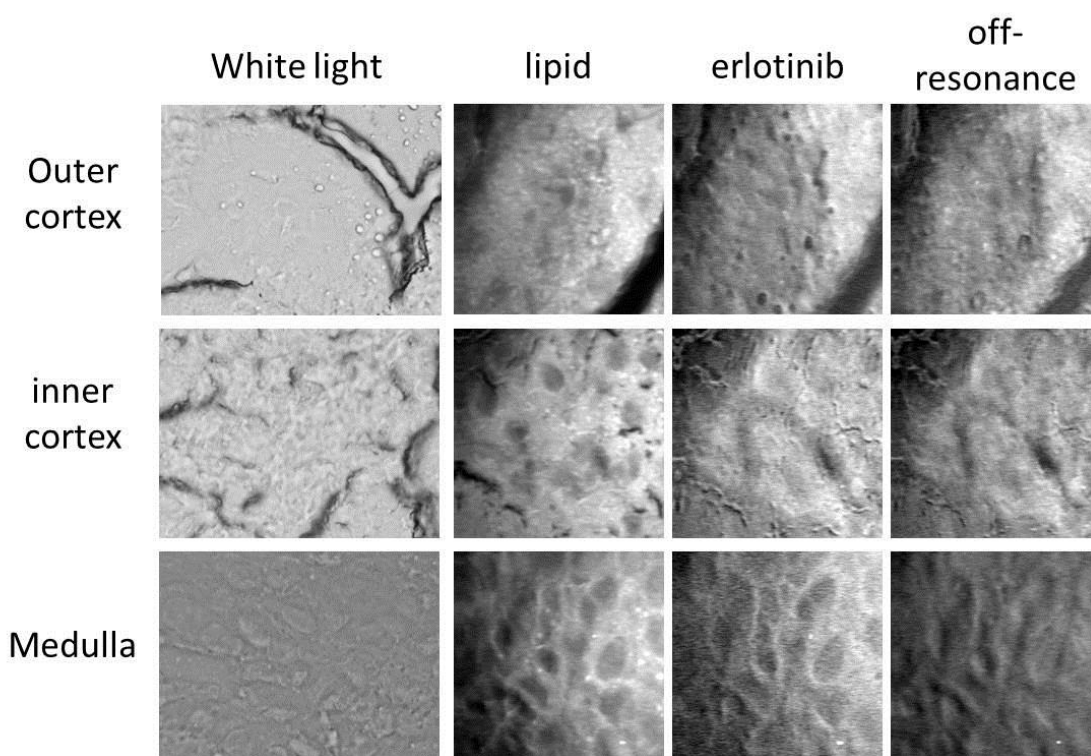
Figure 5.8 White light and SRS images acquired from three different regions of cassette-dosed kidney tissue. SRS images correspond to a 50 x 50 μm region.

An external calibration of pure erlotinib was prepared using a robotic spray device as outlined in the section 5.2.3. The SRS intensity of each known quantity of erlotinib could then be measured and plotted as a calibration curve. Three different regions of 50 x 50 μm were selected for each concentration of drug and the summed intensity of 10

images spanning 10 μm in the z-dimension was calculated for each region. The average intensity for the three different regions was then calculated. Example SRS images from the calibration sample are displayed in Figure 5.9. The calibration curve plotted from these data is also displayed in Figure 5.9. The SRS images suggest that the thin film deposited by the robotic sprayer is fairly inhomogeneous; this is therefore likely to be the largest source of error/variation within the calibration. Linear regression was performed to fit the data and an R^2 value of 0.96 was obtained. This demonstrates satisfactory linearity over the range of concentrations used in this work and suggests the method should be suitable for use in quantification studies. It is difficult to obtain a value for limit of detection from this graph because data points were not sufficiently closely spaced in order to find the lower limit of linearity.
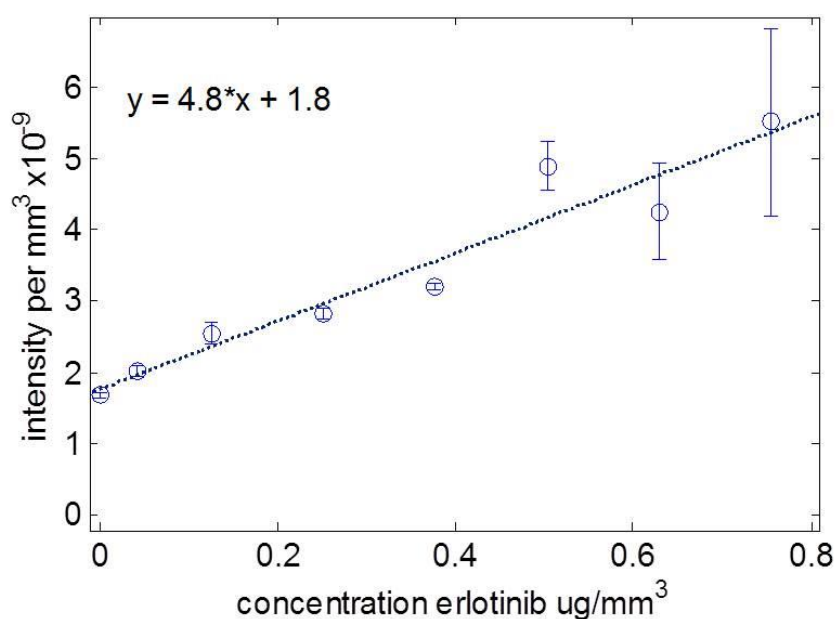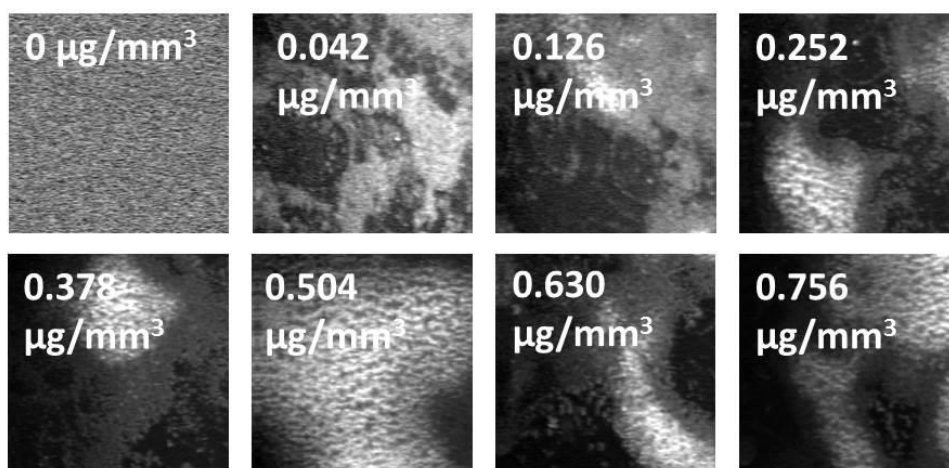
Figure 5.9 SRS images of erlotinib standard calibration sample and calibration curve. Average intensity was calculated over the summed intensity of three regions of each concentration. Error bars represent ±1 standard deviation, linear fit has an r^2 value of 0.96.

SRS data were acquired from the calibration sample and the tissue sample under the same conditions (controlled for image region size, laser power and integration time). The different regions of kidney selected for SRS imaging demonstrate different signal intensities for erlotinib from different tissue types. These will later be compared with relative concentration distributions observed by mass spectrometry imaging.

The concentration of erlotinib in kidney tissue can be calculated by converting measured intensity from tissue to concentration via equation 5.1 which was calculated by fitting to the calibration data.

$$I = 4.8 * C + 1.8$$

<div align="right">5.1</div>

For each set of SRS images the summed intensity of the erlotinib signal was calculated and the average signal which was detected off-resonance was subtracted. Once the concentration value had been obtained, this value was related back to the concentration of drug in tissue (in units of μg/g tissue) via the approximation of tissue density as 1 g/cm^3. The calculated concentration values for erlotinib in cortex kidney tissue are displayed in Table 5.2. These calculated values vary a lot from region to region and this is likely to be due to the poorly characterized background signal. This means that the calculated values must be treated with caution because they are likely to be inaccurate. The measured signal from erlotinib was very low and in some regions was lower than the measured signal off-resonance – this means that the concentration of erlotinib is very close to the limit of detection. In order to be confident that the SRS signal from tissue was real, an SRS spectrum should be acquired from the region around 2110 cm^{-1} to determine whether a real peak occurs here or whether background signal is measured in the erlotinib channel. A further experiment in which the animal was dosed with a larger amount of erlotinib would also establish whether this is a sensitivity problem. This should be a last resort in order to minimize animal studies. Having said this the amount of erlotinib detected in the cortex is higher than that detected in the medulla, which does suggest the method has worked to an extent because this was observed by

mass spectrometry imaging in the work by Swales *et al.* when they studied the same samples.

Table 5.2 Concentration of erlotinib in tissue as measured using SRS microscopy.

Kidney region		Total intensity erlotinib	μg erl per mm^3	Conc. in tissue (μg/g)
Outer cortex	1	9.08E+04	0.043319448	43.3
	2	8.69E+04	0.010612477	10.6
	3	1.11E+05	0.208616958	209.0
Inner cortex	1	9.03E+04	0.039368595	39.4
	2	9.28E+04	0.059640722	59.6
	3	5.94E+04	-0.219298487	0
medulla	1	8.78E+04	0.017962625	18.0
	2	6.41E+04	-0.179573862	0
	3	5.39E+04	-0.264964157	0

5.3.4 Sensitive analysis of multiple targets by LESA MS imaging

The tissue section which had been analysed by SRS was then imaged using LESA MS. It was established in Chapter 3 that in order to take full advantage of the sensitivity of LESA it must be performed prior to MALDI analysis. An example LESA mass spectrum and representative ion images are displayed in Figure 5.10. Using LESA MS it was possible to detect all four drug compounds, lipids and proteins simultaneously. Each of the four drug compounds (erlotinib, terfenadine, olanzapine and moxifloxacin)

was detected as the intact protonated species (ions detected with *m/z* 394.1808, 472.3264, 313.1517 and 402.1874 respectively). Erlotinib, terfenadine and olanzapine were detected with higher intensity in the cortex and lower intensity in the medulla. Moxifloxacin was detected with lower intensity in the cortex and higher intensity in the medulla. This is in agreement with the results from SRS analysis and with the findings of Swales *et al.*[153] Lipids were preferentially detected as the protonated species which is in agreement with results outlined in Chapter 3 in which LESA MS was used to analyse brain tissue. Intact, multiply charged protein ions were also detected. The species detected with ions centered at *m/z* 857.48 (charge state +10) is tentatively assigned as ubiquitin. The species detected at *m/z* 894.82 (+17) is tentatively assigned as α-hemoglobin. This simultaneous detection of multiple analyte classes under ambient conditions is a quality unique to LESA MS, typically with other techniques such as DESI or MALDI different sample preparation strategies or experimental parameters would be required to detect different classes of analyte and separate imaging procedures would need to be executed.
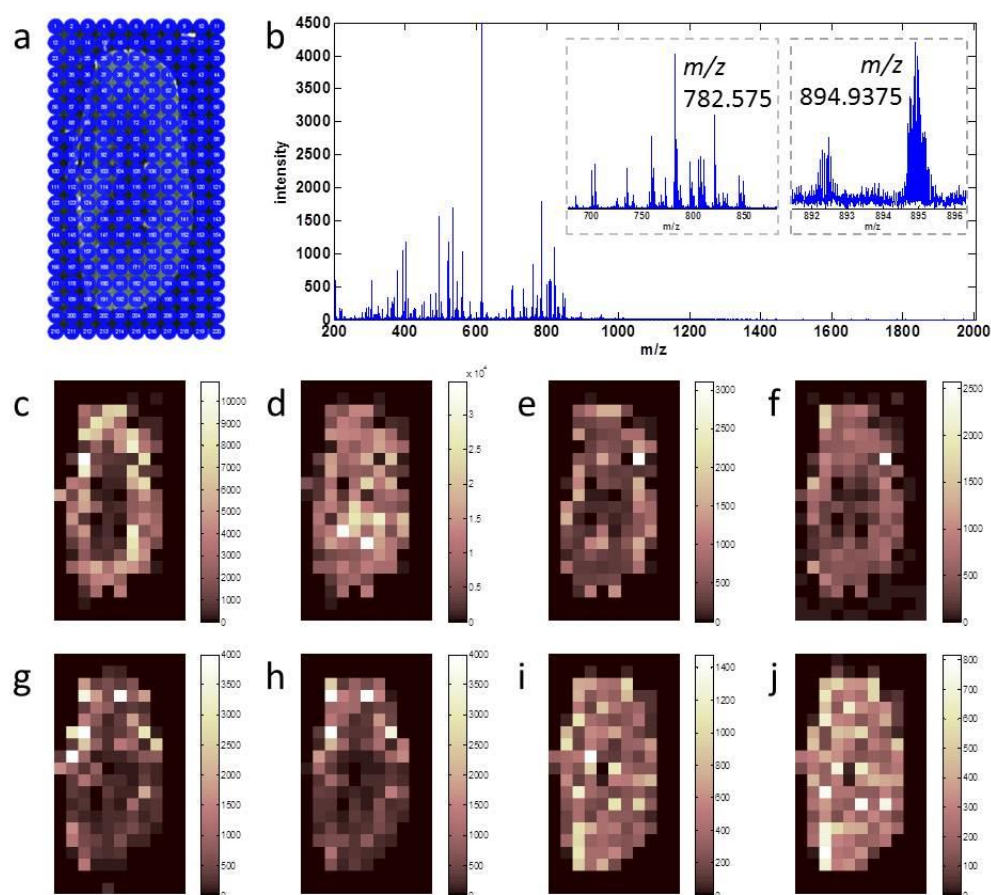
Figure 5.10 LESA MS imaging of drug dosed tissue: a) points selected for LESA sampling (220 pixels), b) example single pixel spectrum, (c-d) example LESA MS images corresponding to [M+H]+ ions of: c) erlotinib, d) moxifloxacin, e) olanzapine, f) terfenadine, g) PC 34:2, h) PC 39:6, i) unidentified protein ion (m/z 800.78 charge state +18), j) α-hemoglobin (m/z 894.93 charge state +17). In a single LESA extract singly charged lipid and drug species and multiply charged intact protein ions were detected – indicated inset (b).

The minimum pixel size possible using contact LESA MS is ~700 μm and is limited by the diameter of the pipette tip used for sampling; this could provide a route towards further reducing pixel size because smaller pipette tips could be used. A restriction in the software used to control the Triversa NanoMate puts a minimum restriction on the

spacing between points at 1 mm which means gaps between pixels resulting in unsampled tissue when contact LESA is used. The pixel size used in this experiment allowed sufficient spatial resolution to distinguish between gross anatomy within the organ (cortex vs medulla) but very little else. A higher resolution mass spectrometry imaging technique is required to provide this level of detail.

5.3.5 Specific analysis with high resolution imaging by MALDI MS

The kidney tissue section which had been sampled by LESA and SRS, along with a serial control section placed adjacent on the slide, was then imaged using MALDI MS. An example single pixel spectrum and ion images of various lipids from both tissue sections are displayed in Figure 5.11. The only class of analyte detected in this experiment was lipids, predominantly phosphatidylcholine lipids originating from the cell membrane. As indicated by the images in Figure 5.11, the spatial resolution possible with MALDI MS is far superior to LESA (pixel size used in this experiment was 100 μm). The total image region is approximately 1.5 x 2.5 cm which is large enough to image the entire tissue section. Total acquisition time for this MALDI MS image was approximately 2.5 hours. To image the equivalent region using SRS under the conditions used here would have taken 2730 hours or 113 days, which is fundamentally unfeasible. Faster SRS acquisition times are possible but would require higher laser power to produce the same signal for a shorter integration time. Differences in the structure of cortex vs medulla can clearly be seen in various MALDI lipid ion images, also structure within the kidney cortex which could be connective tissue can be seen as 'stripes'. The regions which were sampled by LESA are clearly visible in the MALDI MS images, characterized by a region of higher intensity in the middle of the spot and surrounded by a darker ring of lower intensity. This phenomenon was

described in Chapter 3, and it is suggested that this is caused by salt washing towards the outside of the LESA sampled spot, subsequent poor matrix crystal formation and desorption/ionization. It is interesting to note that similar effects are observed for a different tissue type in which higher concentrations of salt were expected. Ion images of some lipid species (PC 34:1, see Figure 5.11.d) show that in certain regions of the kidney, ions are enhanced by LESA more than they are in other regions i.e. the effect of LESA sampling is not uniform across the tissue section. These image features are useful for understanding the LESA sampling process (in terms of area sampled, sampling precision and repeatability) and could also help explain unexpected intensity distributions in LESA images. For example LESA pixels with low intensity might correspond with regions where a smaller region was sampled relative to the other pixels, although that was not observed in this experiment.
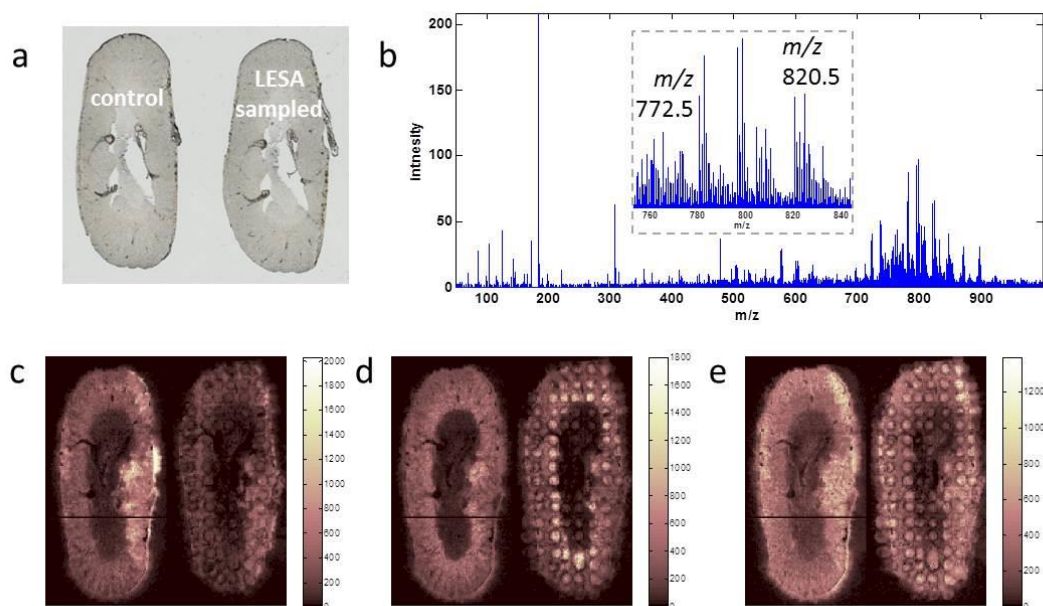
Figure 5.11 MALDI MSI performed after SRS and LESA: a) description of sample, b) example single pixel MALDI mass spectrum, (c-e) example ion images of abundant lipid ions tentatively assigned as $[M+K]^+$ molecules of: c) PC 36:4, d) DG 42:3, e) PC

32:0. Regions sampled by LESA can be identified in MALDI images by a localised increase in lipid ion intensity.

5.4 Conclusions

The work presented in this chapter has explored the possibility of a multimodal workflow to extract more information from a sample of relevance to pharmaceutical research. SRS was shown to provide high resolution images of biological tissue in which sub-cellular spatial resolution was possible. A possible route towards quantifying a drug in tissue using SRS was also investigated. It was found that further work to establish SRS off-resonant signals in kidney tissue would be required before this could be used for absolute quantification although this does show promise. LESA MS was capable of detecting all four dosed drug compounds along with lipids and proteins in a single extraction/analysis. MALDI MS imaging was capable of acquiring high resolution images of a single class of analyte over a wide 'field of view' in an acceptable time-frame. This workflow demonstrates the potential for combining separate techniques with individual benefits but requires further investigation to take full advantage of the capabilities of SRS. It would not have been possible to acquire this data via any single technique thus demonstrating the need for multimodal methods

Chapter 6

Liquid Surface Sampling Techniques: Quantitative Analysis by LESA

6.1 Introduction

The work presented in chapters 3, 4 and 5 showed how combining various chemical imaging methods could lead to improved understanding of fundamental processes whilst providing a more complete analysis of the sample. The remainder of the work focuses on the development of ambient mass spectrometry imaging methods for improved analysis in terms of quantification (Chapter 6), spatial resolution (Chapter 7) and sample types (Chapter 8).

The need for quantitative analysis was discussed in Chapters 4 and 5 and SRS microscopy was assessed for the quantification of pharmaceuticals in tissue. The potential benefits of using such a technique have been outlined; however, limitations in terms of sensitivity and range of analytical applications could hinder further development. Liquid chromatography coupled to mass spectrometry (LC-MS) is commonly employed in the routine quantification of proteins in biological samples. Usually this involves tagging the protein with a stable isotope, which can be introduced via metabolic, chemical or enzymatic means.[206,207] Relative quantification can be achieved by comparing the intensity of protein signals in different physiological states, absolute quantification requires comparison to the ion intensity detected from samples

of known composition. Commonly used methods include isotope-coded affinity tags (ICAT)[208], isobaric tags for relative and absolute quantification (iTRAQ)[209] and stable isotope labelling by amino acids in cell culture (SILAC).[206,207] Methods employing LC-MS do not typically retain spatial information; this means the specific origin of the protein cannot be accurately determined and potentially valuable biological information could be lost.

Various types of mass spectrometry imaging have been reported for quantitative analysis, for example MALDI, DESI and nano-DESI.[73-76,210-212] If one was to use MSI for quantitative analysis, an ambient method would seem to be the most appropriate choice due to the limited sample preparation (and hence alteration). Mass spectra acquired in the absence of a matrix compound would be simpler to interpret and lower ion suppression effects should be observed. Liquid sampling techniques in which desorption and ionisation stages are decoupled (such as LESA) are even more attractive because this affords the opportunity for off-line incorporation of an internal standard.

The work presented in this chapter explores the use of LESA MS for the quantification of intact proteins in biological tissue. Applications of such a method would include studies seeking to quantify differences in protein expression between control animals and disease models in which a certain protein was implicated; quantification of antibody or other protein-based therapeutic compounds; and quantification of multiple analytes simultaneously, for example a lipid or protein and a drug. This could enable the expression of an endogenous molecule to be monitored in relation to the concentration of a drug. Limitations in the current methods for absolute quantification of proteins such as the loss of spatial information, lengthy sample preparation and problems with bottom-up protein identification (inefficient digestion, failure to identify peptides and loss of post-translational modifications) could be overcome using a LESA

quantification method.[111] Furthermore, in some situations seeking to quantify two different variants of a protein it would be difficult to quantify by bottom-up methods.

6.2 Experimental

6.2.1 Tissue samples

Tissue samples were sectioned as described in section 2.2.1.1 at a thickness of 14 μm.

6.2.2 Preparation of mimetic tissue models for quantification

Mimetic tissue models were prepared using the method described in Figure 6.1. Ten whole rat brains (thawed) were homogenized using a handheld homogenizer. Approximately 2.5 mL of homogenate was apportioned into individual pre-weighed tubes and final weight homogenate per tube was calculated. Labelled ubiquitin solutions were prepared in methanol and water (30:70), to final concentrations such that 1% final volume of tissue was added to each sample, this prevented large volumes of solvent diluting the homogenate. 5mm magnetic stir bars were added to each tube and vortexed for 1 minute. Spiked homogenates were pipetted into plastic moulds before freezing for 1 hour at -80 °C. The final concentration of labelled ubiquitin in tissue was 0, 9.9, 19.9, 67.4, 68.6, 94.7, 122.6 and 163.0 nmol/g.
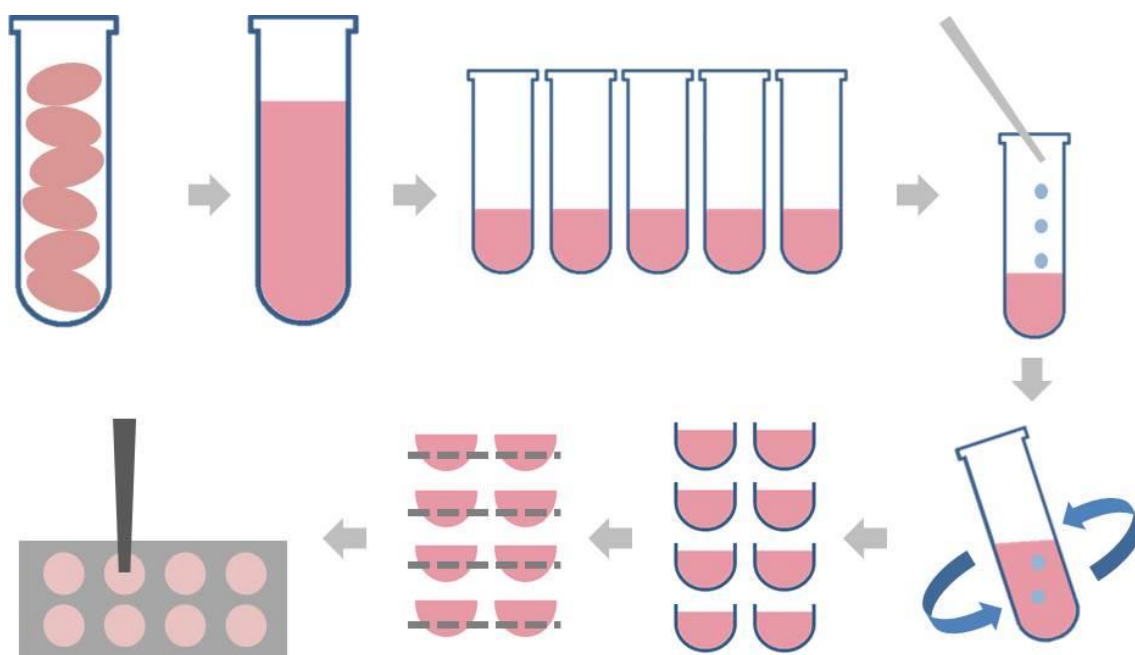
Figure 6.1 Method used to prepare mimetic tissue models: rat brains were homogenised, portions were separated into pre-weighed tubes, appropriate quantities of labelled protein were added, sampled were vortexed to mix, homogenate was portioned into moulds and frozen at -80°C, mimetics were sectioned at 14 µm and thaw-mounted on glass slides before LESA MS was carried out.

6.2.3 Direct infusion of labelled and unlabeled ubiquitin standard

Solutions of ubiquitin standard were prepared in methanol and water with 1% formic acid (69.3:29.7:1) to final concentrations of 117, 23.4, 4.67, 0.93, 0.18 and 0.037 µM. A solution of labelled ubiquitin was prepared at a concentration of 25 µM in methanol and water with 1% formic acid (69.3:29.7:1). 3 µL of each solution was introduced to the mass spectrometer via the Triversa NanoMate electrospray ionization chip with a gas pressure of 0.3 psi and a tip voltage of 1.75 kV. The AGC was turned off and the fill time was fixed at 0.6 ms. This fill time was optimized for the highest concentration solution; injection of lower concentration solutions with this fill time resulted in under-fill. Full scan mass spectra were recorded in the *m/z* range 200-2000 for 3 minutes; each scan comprised 5 coadded micro-scans.

6.2.4 LESA mass spectrometry

The surface sampling method was optimized for the analysis of rat brain and rat brain homogenate. Sampling coordinates were selected (a grid of 8 points per tissue mimetic and a grid of 7 x 11 points spanning one sagittal rat brain section) for LESA MS. The z coordinate was set to a height 1.2 mm above the sample surface; it was found that contact LESA was not suitable for this application due to high lipid signal observed using contact. The solvent system for extraction and electrospray was methanol, water and formic acid (69.3:29.7:1). A volume of 2.0 μL solvent was aspirated from the solvent well, 1.3 μL was dispensed on the surface and 1.5 μL was re-aspirated to ensure good recovery from the surface. The liquid microjunction was maintained for 10 seconds before re-aspiration. The sampling routine was repeated once before electrospray. Each sample was delivered for 3 minutes via the Triversa Nanomate with a gas pressure of 0.3 psi and a tip voltage of 1.75 kV. Positive ion mass spectra were acquired in full scan mode (m/z 600-2000) at a resolution of 120 000 at m/z 400. The Automatic Gain Control was turned off and the injection time fixed at 1 ms. Each scan was comprised of 5 coadded microscans.

6.3 Results and Discussion

6.3.1 Mass spectrometry analysis of stable-isotope labelled ubiquitin by direct infusion electrospray and LESA

Quantification by surface sampling methods such as LESA requires the incorporation of a structural analogue into the sample which acts as internal standard.[65] This compound is added to the sample in known quantities and acts as a reference to which endogenous signals can be compared. Chemical properties of the standard and the compound of interest can be assumed to be equivalent and therefore extraction, desorption and

ionisation efficiencies are likewise assumed to be the same. The internal standard can be spiked onto control tissue at a range of concentrations or added as a homogeneous layer to which endogenous signals can be normalised. These methods do not allow for differences in extraction from *within* the tissue, which may not be representative of the extraction of endogenous compounds. Alternatively the standard can be added in different concentrations to homogenised tissue to produce a series of tissue-like models with known composition from which a calibration curve can be produced.[73] Signal intensities observed from endogenous species may then be compared to this curve and unknown concentrations can be determined. Commonly a stable-isotope labelled version of the drug or compound to be quantified is used as the internal standard. This compensates for differences in extraction and ionisation efficiency between different tissue types.[65,74-76,210] It should be noted that previous work has only considered the quantification of small molecules. In this work carbon-13 and nitrogen-15 labelled ubiquitin was used to quantify ubiquitin in brain tissue. This is the first report of using such an approach to quantify intact proteins. Ubiquitin was selected as a suitable candidate because it is readily detected from brain and other tissue types using LESA-MS.

An example mass spectrum acquired by direct infusion electrospray ionisation of labelled ubiquitin is displayed in Figure 6.2. It was possible to detect the standard in a variety of charge states, the most abundant charge state was +7 (in the *m/z* window recorded in this work), which was detected with *m/z* centred around 1808.30. This corresponds with an intact monoisotopic mass of 9033.4779 which demonstrates that 98% of carbon and nitrogen atoms in ubiquitin have been isotopically labelled. Therefore signals from labelled and endogenous ubiquitin should be easily separable, which can be seen in Figure 6.2. Labelled ubiquitin was spotted onto a section of mouse

brain and LESA MS was performed; both endogenous and labelled ubiquitin were detected simultaneously.
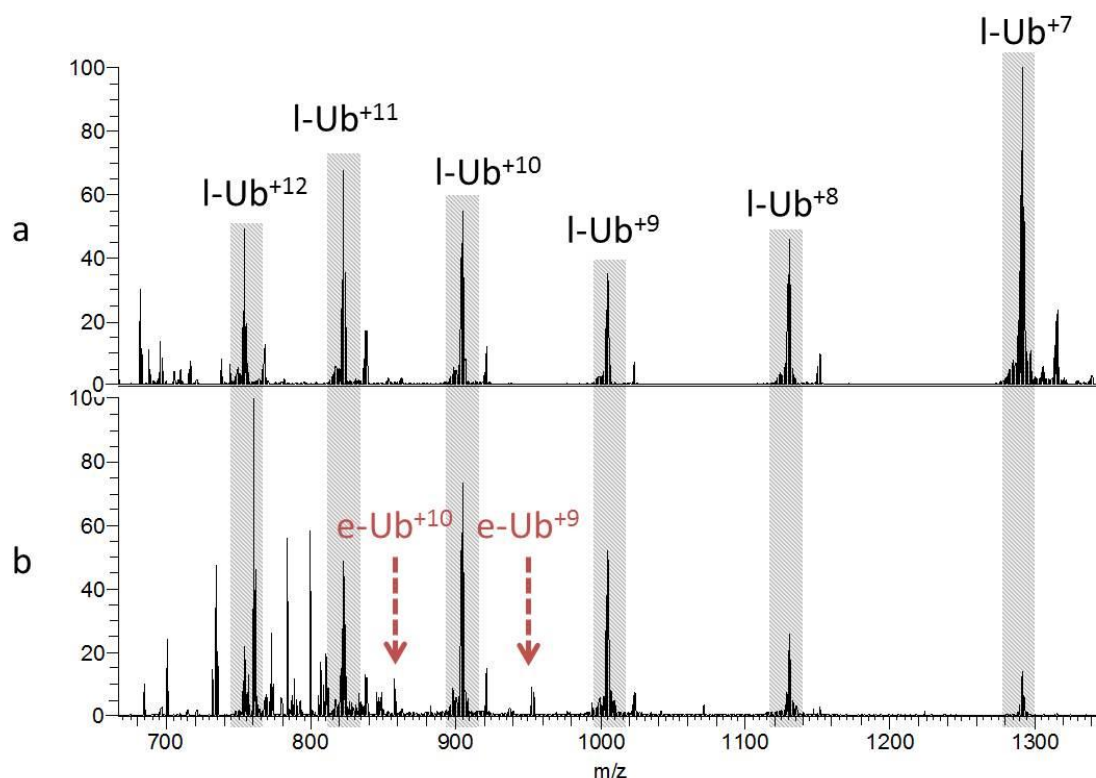
Figure 6.2 Mass spectrometry analysis of stable-isotope labelled ubiquitin, a) direct infusion electrospray ionisation mass spectrum, b) LESA mass spectrum acquired from brain tissue spotted with protein standard, both labelled (l-Ub) and endogenous (e-Ub) ubiquitin can be detected simultaneously.

6.3.2 LESA MS analysis of tissue mimetics

After establishing that labelled ubiquitin can be detected from a sample of brain tissue, a series of mimetic tissue models were prepared, see Figure 6.1. Example LESA mass spectra acquired from these samples can be seen in Figure 6.4. Ions with *m/z* attributed to labelled ubiquitin decrease in intensity with concentration, whereas the intensity of ions with *m/z* attributed to endogenous ubiquitin remain relatively constant. This suggests the method is capable of detecting differences in abundance.
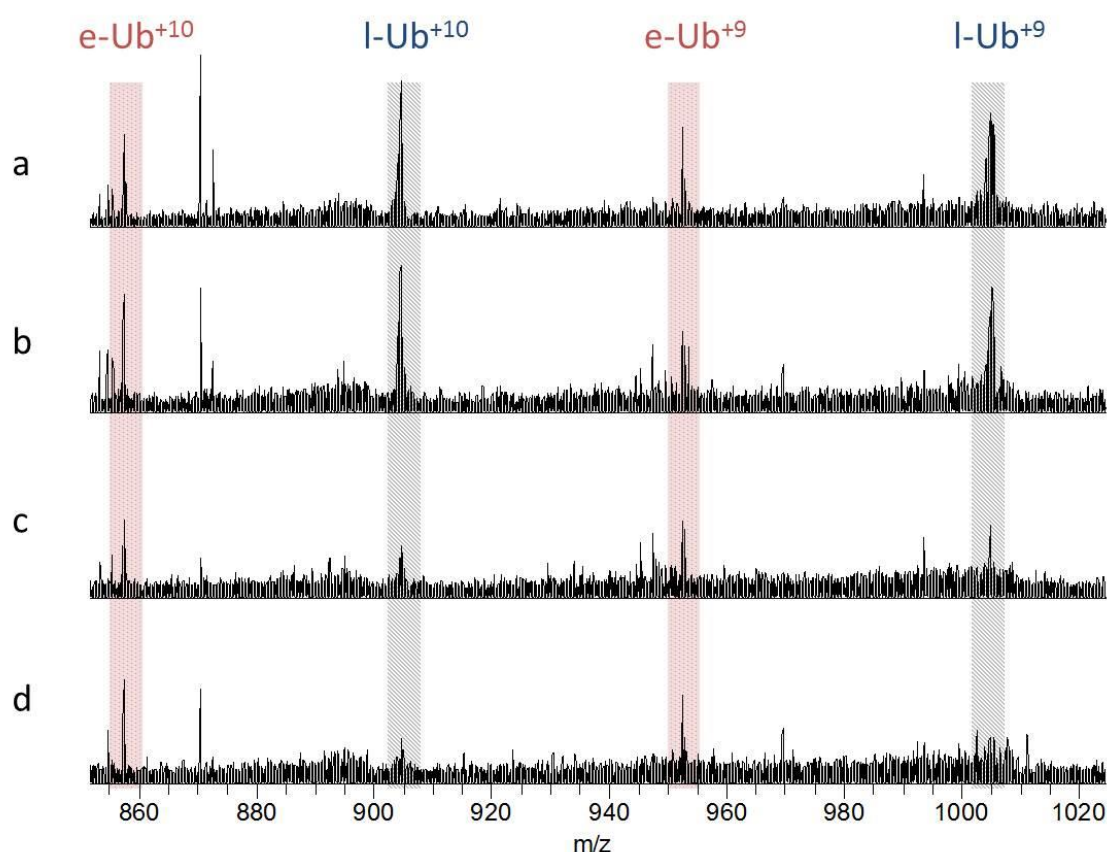
Figure 6.3. Example LESA mass spectra acquired from different concentration mimetic tissue models a) 163.0 nmol/g, b) 122.6nmol/g, c) 94.7 nmol/g, d) 68.6 nmol/g. Peaks corresponding to labelled ubiquitin (l-Ub) and endogenous ubiquitin (e-Ub) are labelled in each spectrum.

The intensity of labelled and endogenous ubiquitin (in +9 and +10 charge states) detected from mimetic tissue models are displayed in Figure 6.4. Eight separate locations were sampled per mimetic and each row of 8 pixels in the image corresponds to a different concentration mimetic. A gradient can clearly be observed for labelled ubiquitin whereas endogenous ubiquitin remains relatively constant. Variation observed within the intensity of endogenous ubiquitin represents either the error within the LESA method or variation in the concentration of labelled ubiquitin which could occur due to poor mixing during mimetic preparation. In order to probe which of these is responsible a further experiment was designed.
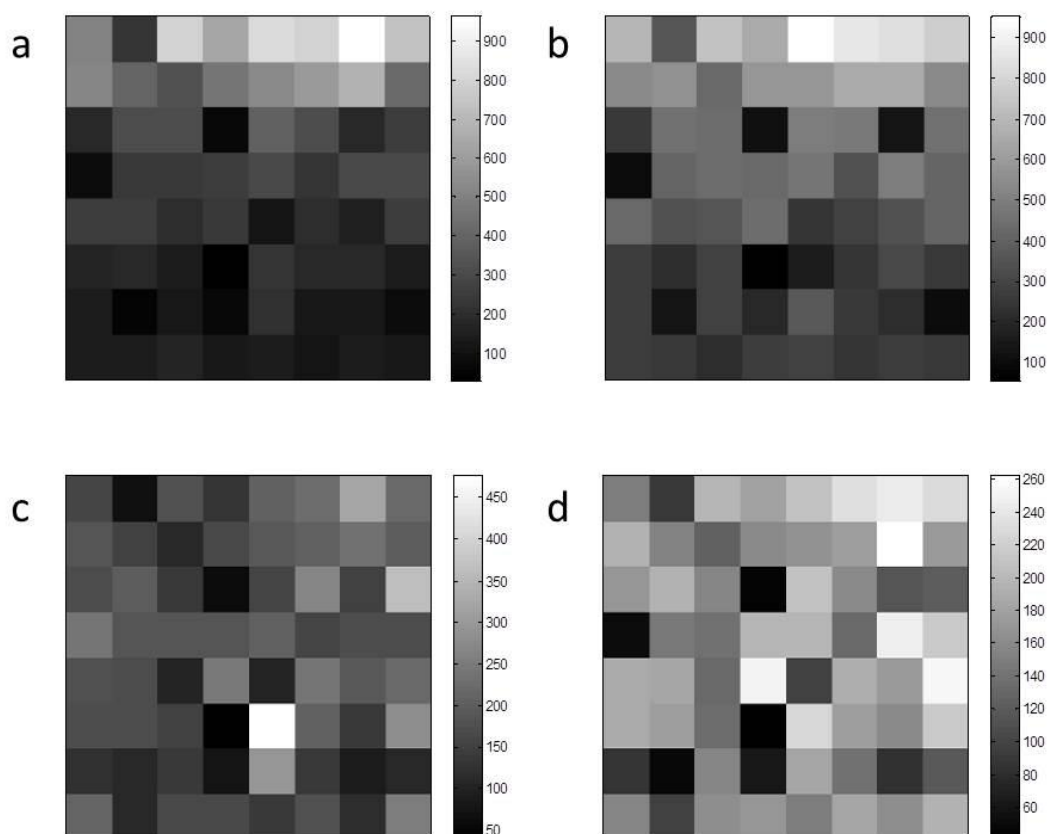
Figure 6.4. LESA MS data from mimetic tissue models, each horizontal line of pixels represents a different concentration mimetic, bottom-top: 0, 9.9, 19.9, 67.4, 68.6, 94.7, 122.6 and 163.0 nmol/g, a) ions with *m/z* 904.6543 (+10) labelled ubiquitin, b) ions with *m/z* 1004.9486 (+9) labelled ubiquitin, c) ions with *m/z* 857.3632 (+10) endogenous ubiquitin, d) ions with *m/z* 952.6230 (+9) endogenous ubiquitin.

6.3.3 Variation in LESA MS

Two sections were taken from the top and one from the bottom of the mimetic tissue model (see Figure 6.5) and all three were subject to LESA MS under the same sampling conditions. Ion images of endogenous and labelled ubiquitin were produced which reveal that a similar level of variation is seen for both species. This suggests that the labelled ubiquitin was distributed uniformly throughout the homogenate prior to

freezing. It also suggests that the variation in intensity is due to variation in LESA sampling and not due to inhomogeneity in the sample.
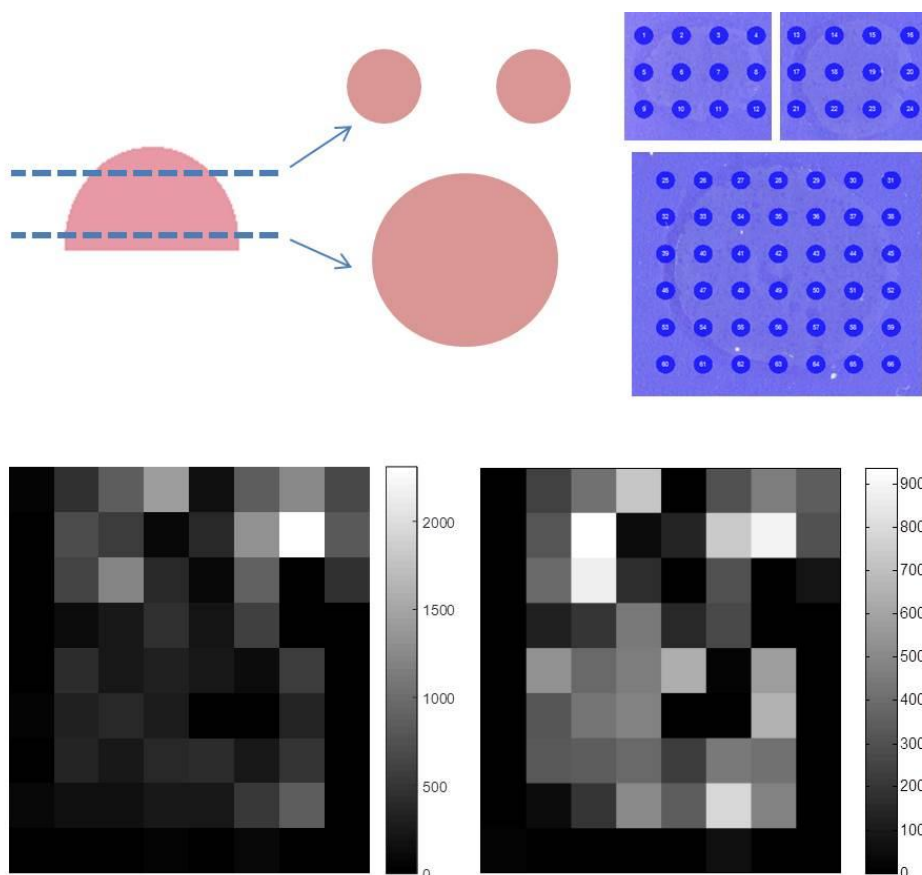
Figure 6.5 Clockwise from top left: schematic describing section locations within mimetic, locations selected for LESA sampling, LESA MS image of ions detected at *m/z* 904.6543 (l-Ub) and LESA MS image of ions detected at *m/z* 857.3632 (e-Ub).

6.3.4 Quantification of ubiquitin in rat brain

Using the LESA mimetic data the average intensity of the most abundant charge state (+10) of ubiquitin was calculated for each mimetic. Some electrospray injections failed due to liquid microjunction instability and loss of solvent on the sample surface, these data points were not included in the average. Average intensity was then plotted against concentration to produce a calibration curve, see Figure 6.6. Linear regression was

performed and the line fitted to the data with an R^2 of 0.986 demonstrating good linearity between ion intensity and concentration. The 3 lowest concentration data points were below the limit of linearity so were not included in the linear fit. The limit of detection is difficult to determine due to the small number of data points and the large variation observed in this work. The error bars plotted on the curve, which represent ±1 standard deviation, are large. The high degree of variation could be due to a number of reasons: sample inhomogeneity (which can be somewhat ruled out due to investigations presented above), variation in sampling and extraction efficiency and variation in electrospray stability. Observations made during data acquisition suggest that a combination of unstable liquid microjunctions and electrospray were responsible. In a number of samples the detected ion intensity was low and a corresponding failure in electrospray was noted. Variation could be reduced by improving the repeatability of the LESA method. It might be possible to improve the stability of the microjunction through further optimisation of sampling height relative to the surface and increasing the aqueous content of the solvent. The concentration range used in this work spans the limit of detection and only covers 2 orders of magnitude. A calibration curve was also plotted for the +9 charge state of labelled ubiquitin, see Figure 6.7. Linear regression from these data give an R^2 value of 0.958.
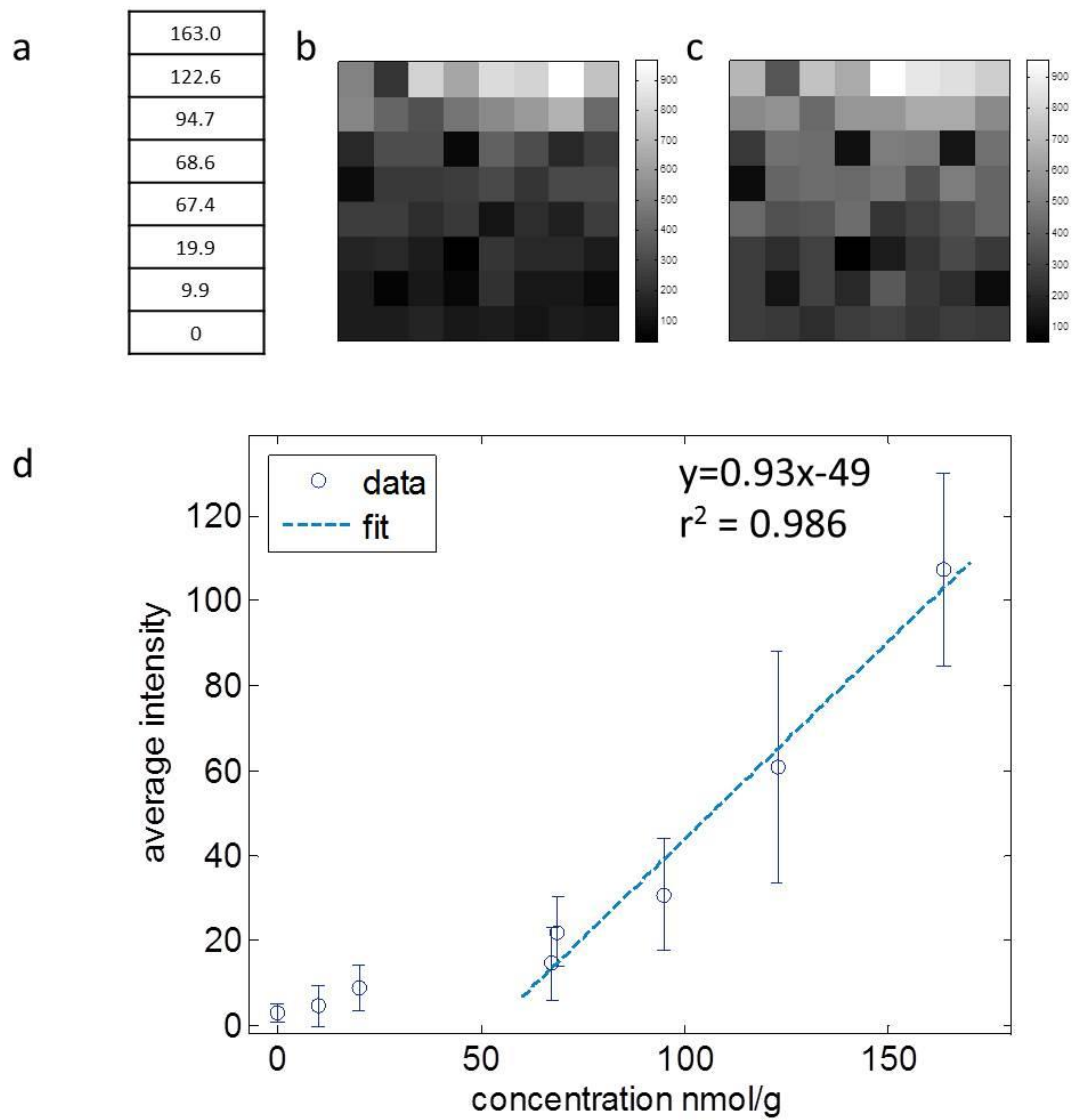
Figure 6.6 Calibration curve generated from LESA MS data from mimetic tissue models, a) location of different concentration mimetics (nmol/g), b-c) ion intensity diagram of labelled ubiquitin in +10 and +9 charge states, d) calibration curve plotted from average ion intensity detected the +10 charge state over 8 pixels against concentration; error bars represent ±1 standard deviation.
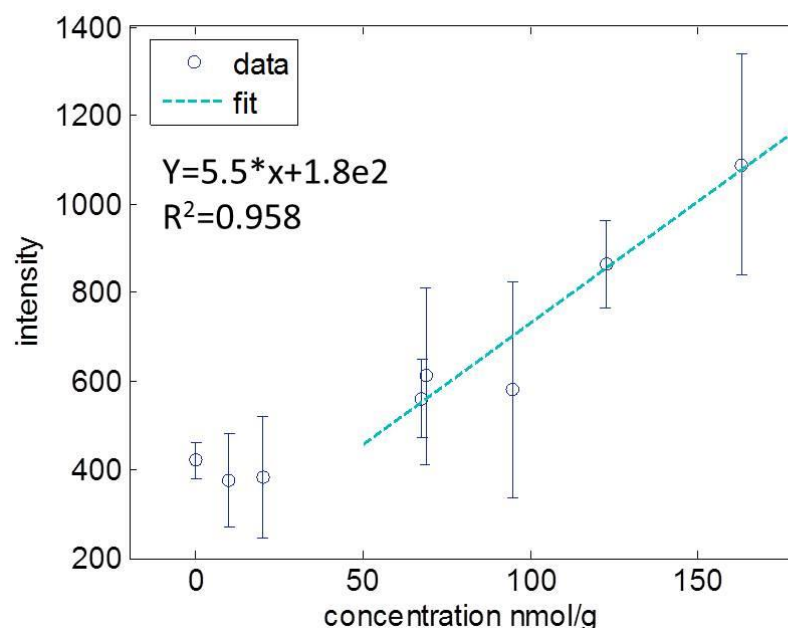
Figure 6.7 Calibration curve for labelled ubiquitin in the +9 charge state.

A single sagittal section of rat brain tissue was imaged using LESA MS under the same sampling parameters as the mimetic samples in order to quantify endogenous ubiquitin, see Figure 6.8. The average concentration of ubiquitin detected across the whole brain section was 113.45 nmol/g. Assuming an average rat brain mass of 2g, this equates to ~385 μg ubiquitin per brain. Kaiser *et al.* used a protein standard absolute quantification (PSAQ) method which uses LC-MS to quantify ubiquitin in mouse brain tissue and found that the total concentration of ubiquitin was ~121 pmol/mg tissue.[213] This equates to ~416 (±17) μg ubiquitin per brain. These numbers are in approximate agreement, the difference could be due to the biological differences between rat and mouse. The concentration of ubiquitin in rat brain was also calculated using the calibration curve for labelled ubiquitin in the +9 charge state. This gave a concentration of 94.54 nmol/g. The difference can be accounted for by the difference in linearity of the two curves which could be caused by the lower abundance of the +9 charge state. LESA images indicate that a higher concentration of ubiquitin is detected in the cerebellum compared with the

rest of the brain. Hsu *et al.* performed nano-DESI MSI on mouse brain tissue and found the distribution of ubiquitin to be near uniform, although the section they imaged was coronal and taken from a different region of the brain.[214] This work has demonstrated that LESA MS may be suitable for the quantification of proteins in biological tissue; however the limitations in spatial resolution mean accurate concentration values cannot be assigned to different anatomical regions of the tissue. To improve this, significantly smaller sampling pipettes or capillaries would be required so that inter-pixel distances could be reduced without over-sampling. Alternatively, a different surface sampling technique which allows for continuous surface sampling to be performed might present a more practical route towards higher resolution imaging.
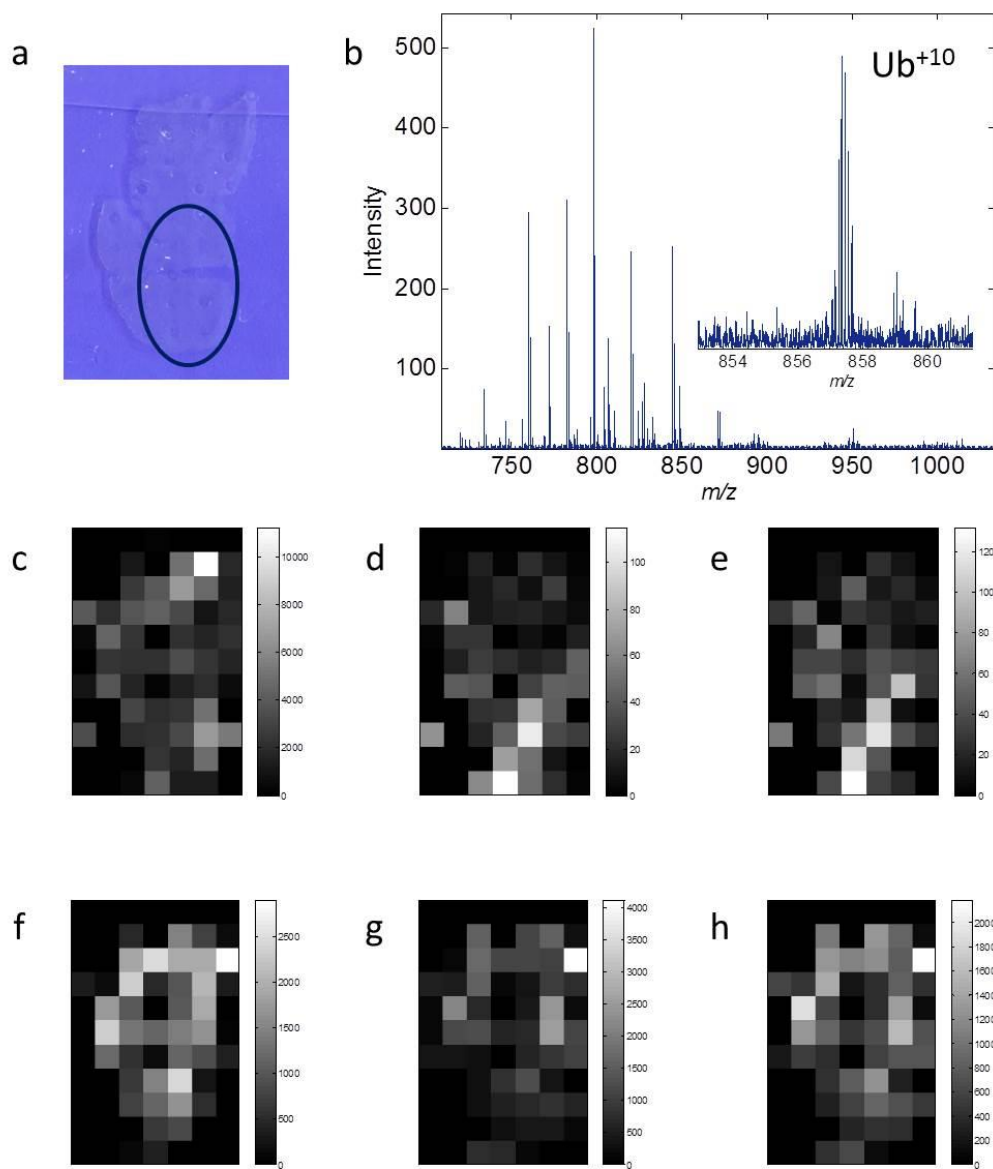
Figure 6.8. LESA MS imaging of rat brain tissue, a) optical image of tissue post-sampling, the ring indicates the location of the cerebellum, b) example LESA mass spectrum and enlarged section showing peaks at *m/z* 857.3632 owing to ubiquitin in the +10 charge state, c-e) ion images of ions with *m/z* 616.1717 (heme), *m/z* 857.3632 (Ub $^{+10}$) and *m/z* 952.6230 (Ub $^{+9}$).

6.4 Conclusions

A novel method for quantitation of intact proteins in biological tissue by LESA MS was developed. This method used stable-isotope labelled protein standard spiked into tissue

homogenate was developed and tested on a protein previously detected in LESA MS experiments. A calibration curve was produced from mimetic tissue models which had good linearity although variation in LESA sampling resulted in a large degree of variation. Further optimisation of the surface sampling method could help overcome this problem. The concentration of ubiquitin in rat brain was quantified and was found to be in approximate agreement with a value quoted in the literature for mouse brain. This observation suggests that the method is successful and has accurately measured the concentration of a protein in tissue under ambient conditions whilst maintaining spatial integrity.

Chapter 7

Liquid Surface Sampling Techniques: Flow-probe Mass Spectrometry Imaging

7.1 Introduction

LESA has now been demonstrated as an excellent tool for the analysis of intact proteins from tissue samples. Whilst LESA MS does provide spatial information, the pipette tips used for sampling limit the spatial resolution of images produced. Work towards liquid surface sampling with improved spatial resolution using the Flow-probe is presented in this chapter. Flow-probe mass spectrometry has been demonstrated in the analysis of lipids, drugs and metabolites.[49,114-117] Van Berkel and Kertesz demonstrated the detection of multiply charged ions by Flow-probe mass spectrometry, however the resolution of the mass spectrometer was insufficient to identify the ions.[113] This chapter presents the development of a Flow-probe MS method for imaging proteins in tissue and a comparison of the capabilities of Flow-probe and LESA mass spectrometry in terms of their relative sensitivity, spatial resolution and throughput.

7.2 Experimental

7.2.1 Tissue samples

Tissue samples were sectioned as described in section 2.2.1.1.

7.2.2 Flow-probe mass spectrometry

7.2.2.1 Tissue sampling

Flow-probe mass spectrometry was performed using the Prosolia™ (Indianapolis, US) system, as illustrated in Figure 7.1. Solvent was delivered to the sample surface via the outer of two coaxial capillaries. Solvent was aspirated from the surface via the inner capillary which is introduced to the mass spectrometer via an electrospray ionization source. The solvent system used in this work was 50:50 methanol:water with 1% formic acid and was optimized for the detection of proteins from tissue using the flow probe. Solvent was delivered at a flow rate of 2 µL/min, sheath gas pressure was manually altered based on visual inspection of the liquid microjunction stability. For static mode analysis of tissue, sampling locations were selected with an x,y spacing of 2 mm which allowed for spreading of the liquid microjunction without over-sampling, a total of 32 locations were sampled. The probe dwelled on the surface for 3 minutes before retracting and flushing with solvent for 162 seconds before moving to the next location. For raster mode analysis line locations were selected with y-spacing of 1mm – it was found that less spreading of the microjunction occurred when operating in raster mode. The raster stage speed used was 80 µm/second. The probe height above the surface was set to 4 µm. At the end of each acquisition the method was paused and the signal from heme was monitored to indicate when the system was flushed, the next line of data was then acquired.

7.2.2.2 Model system sampling

A model system of marker pen ink on glass was produced. This was sampled using the Flow-probe in raster mode. The solvent system was 50:50 methanol:water with 1% formic acid and the flow rate was 10 µL/min. The raster stage speed was 80 µm/second

and the spacing between lines in the y-dimension was 5 mm. The AGC was turned off and the fill time was fixed at 30 ms.

7.2.3 LESA mass spectrometry

Surface sampling was performed as described in section 2.2.2.1. Sampling locations (32 points) were selected for LESA MS across a single rat kidney section (serial to the one imaged by the Flow-probe). The z coordinate was set to a height 0.6 mm above the sample surface. The same solvent system was used for LESA and Flow-probe MS.

7.3 Results and Discussion

7.3.1 Flow-probe mass spectrometry: Static or 'spot mode' analysis of various tissue types

The Flow-probe allows surface sampling via a continuous flow of solvent which is delivered to the surface and aspirated away at a user-defined flow rate; the instrumental set-up is outlined in Figure 7.1. The probe tip has a diameter of approximately 600 μm and offers the possibility of improved throughput and spatial resolution by sampling the surface in a continuous raster mode.
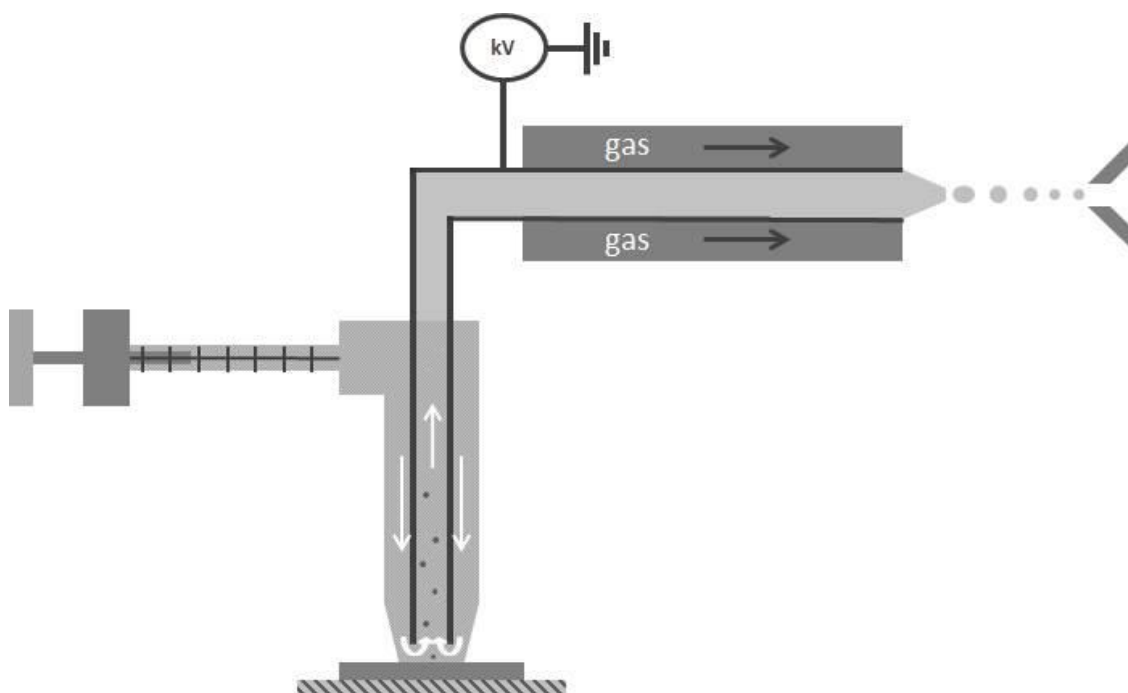
Figure 7.1 Schematic illustration of Flow-probe surface sampling experimental set-up: pump driven syringe delivers solvent to surface at user-defined flow rate through the outer of two co-axial capillaries, solvent with dissolved analytes is continuously aspirated from the surface via the inner capillary which is delivered to an electrospray ionisation source coupled to the inlet of the mass spectrometer.

Experiments were designed to assess the capabilities of the Flow-probe and to compare results with LESA mass spectrometry. Example mass spectra acquired from mouse brain using the Flow-probe are displayed in Figure 7.2. Peaks with *m/z* corresponding to ions of ubiquitin in a variety of charge states dominate the spectrum. Ions with *m/z* 857.56 were selected for CID and the mass spectrum of fragment ions is presented in Figure 7.2.b. Major fragment ions could be assigned to b and y fragment ions of ubiquitin. Sequence coverage of the assignment was 7.8% which is low; this is likely to be because the signal intensity of ions detected was low. A decrease in sensitivity relative to LESA is expected because the continuous flow of solvent acts to dilute the extracted sample at the tissue surface. In cases where the identity of the protein was not

known in advance it would be difficult to make an assignment from so few fragment ions.
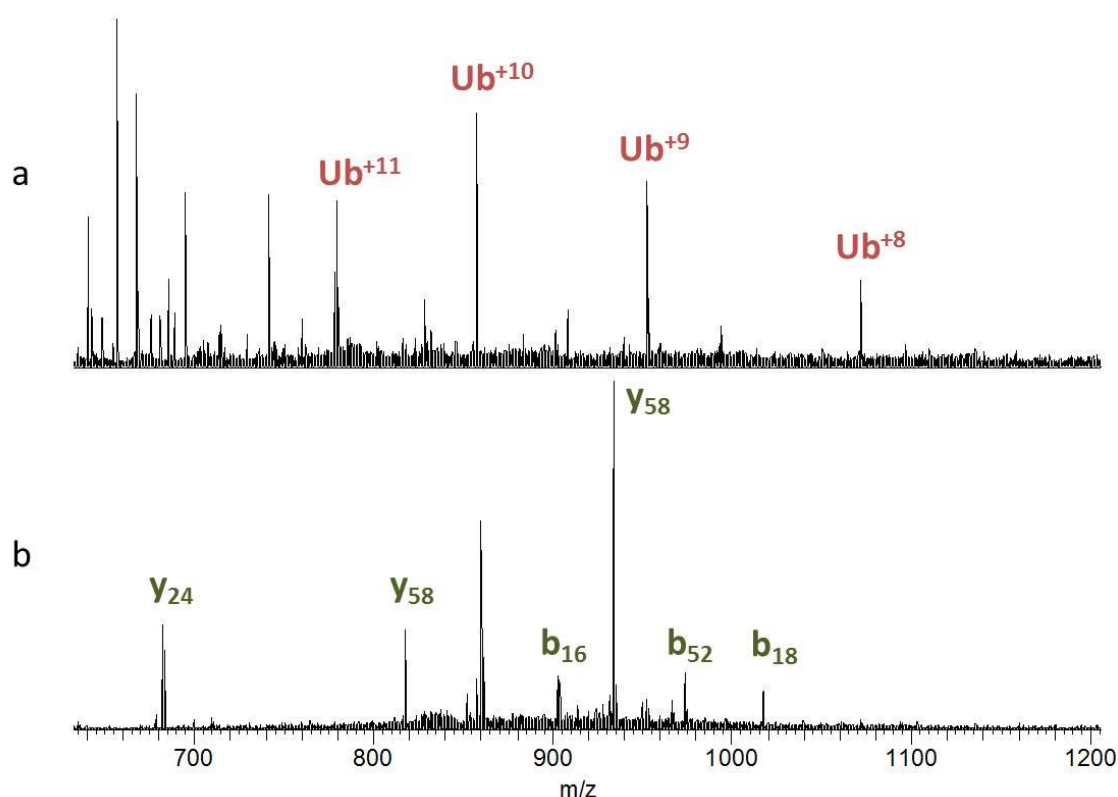
Figure 7.2. Example Flow-probe mass spectrum acquired from mouse brain tissue, a) full scan mass spectrum, the most abundant species detected was ubiquitin, b) CID mass spectrum acquired by fragmentation of ions with *m/z* 857.56, confirming the presence of ubiquitin which was identified with 7.8% coverage.

A further dataset was acquired using the Flow-probe to analyse mouse liver tissue. An example mass spectrum is presented in Figure 7.3. An abundance of proteins was detected in the *m/z* region 700 – 1300. Major protein peaks were identified as liver fatty-acid binding protein detected with monoisotopic mass of 14279.5935 (Δppm = 6.5) in charge states +13 to +16, haemoglobin subunit alpha detected with monoisotopic mass of 14972.7045 (Δppm = 2.3) in charge states +13 to +20 and haemoglobin subunit beta detected with monoisotopic mass of 15608.0580 (Δppm = 4.1) in charge states +13 to +19. This finding is in agreement with analysis of human liver tissue by LESA MS

reported by Sarsby, in which they detected liver fatty acid binding protein, haemoglobin subunit alpha and beta.[215]
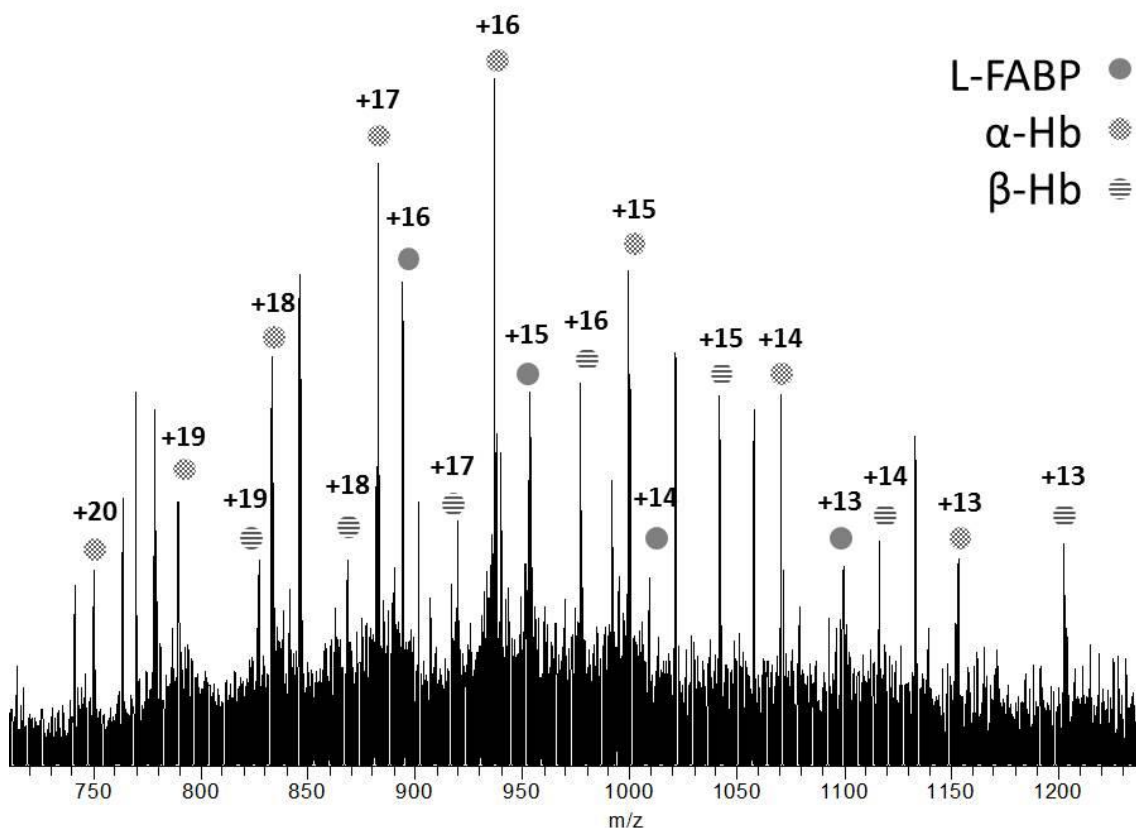
Figure 7.3 Example Flow-probe mass spectrum acquired from mouse liver tissue, the most abundant proteins detected were liver fatty-acid binding protein (L-FABP), hemoglobin subunit alpha (α-Hb) and hemoglobin subunit beta (β-Hb).

7.3.2 Static imaging of pharmaceutical dosed kidney tissue for direct comparison with LESA

After demonstrating that the Flow-probe is capable of producing data comparable with LESA, a further experiment to assess the imaging capabilities of the Flow-probe was carried out. Rat kidney tissue was selected due to the large anatomical features which could potentially be differentiated by pixel sizes of 1 or 2 mm. Example spectra acquired from the same location on serial sections of rat kidney are presented in Figure 7.4. Heme, α and β-hemoglobin dominate the spectra acquired using both techniques. It

should be noted that whilst lipids can be detected simultaneously with proteins by LESA, lipids are not detected in the Flow-probe mass spectrum. This is likely to be due to the relative solubility of lipids and proteins in the solvent system used which means the two classes of analyte are detected at different time points. Alternatively the reason could be due to signal suppression. Other than this, spectra look very similar.
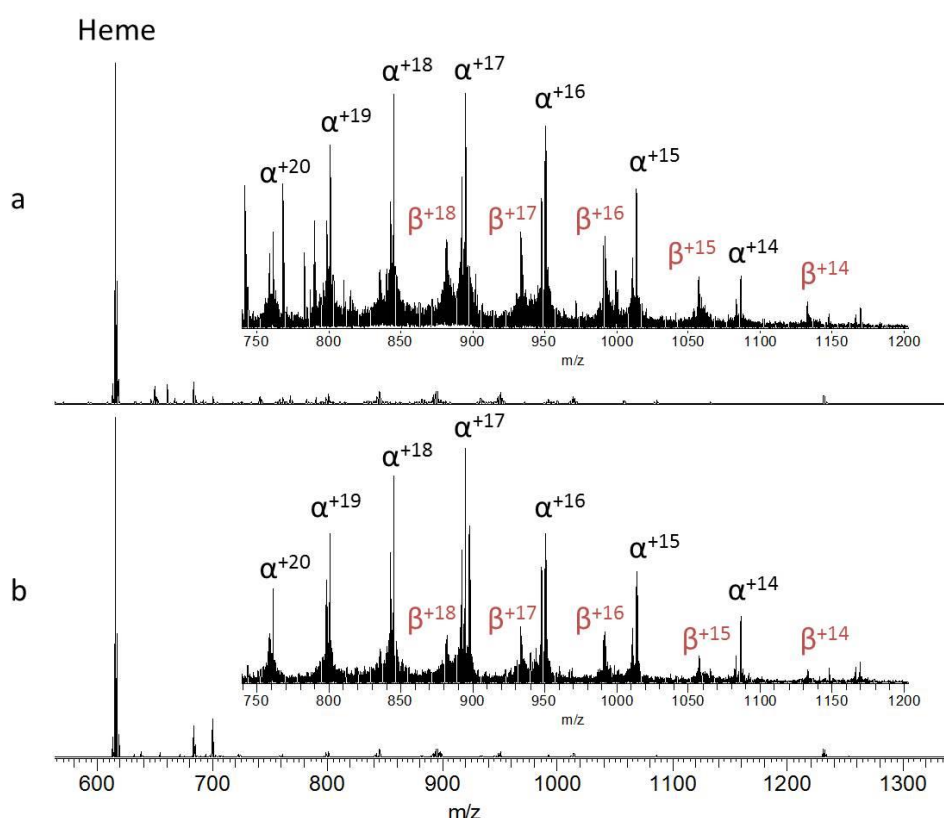
Figure 7.4. Comparison of spectra acquired by LESA and Flow-probe mass spectrometry, a) spectrum acquired by LESA mass spectrometry of rat kidney tissue, α- and β-Hb dominate the spectrum, b) spectrum acquired by Flow-probe mass spectrometry of same location on serial section of kidney tissue.

Imaging datasets were acquired from serial sections of rat kidney by both Flow-probe and LESA mass spectrometry. The Flow-probe was used to interrogate 32 discrete locations in a 'spot mode' analysis in which the probe descended onto the tissue and remained still before retracting, flushing for a set period of time and moving to the next coordinates. Spectra were acquired in a single datafile and a chromatogram of the

intensity of different ions over time was produced, see Figure 7.5. There is a delay between the probe coming into contact with the sample and the signal being detected which can be observed from this chromatogram. The total volume of the capillary is 5.3 µL, therefore at a flow rate of 2 µL/min, the time for analytes to travel from sample to inlet is ~2.6 minutes. The delay observed is actually ~5 minutes. This suggests there is a dead volume within the capillary or that flow phenomena occur at the surface. Such effects were observed by ElNaggar *et al.* where they found that the probe-to-surface distance and inter capillary distance was crucial to successful aspiration of analytes from the surface and solvent/analyte 'plugs' can form when these distances are too large. The co-localisation of chromatogram traces indicates that analytes do not separate within the capillary and are detected at the same time.
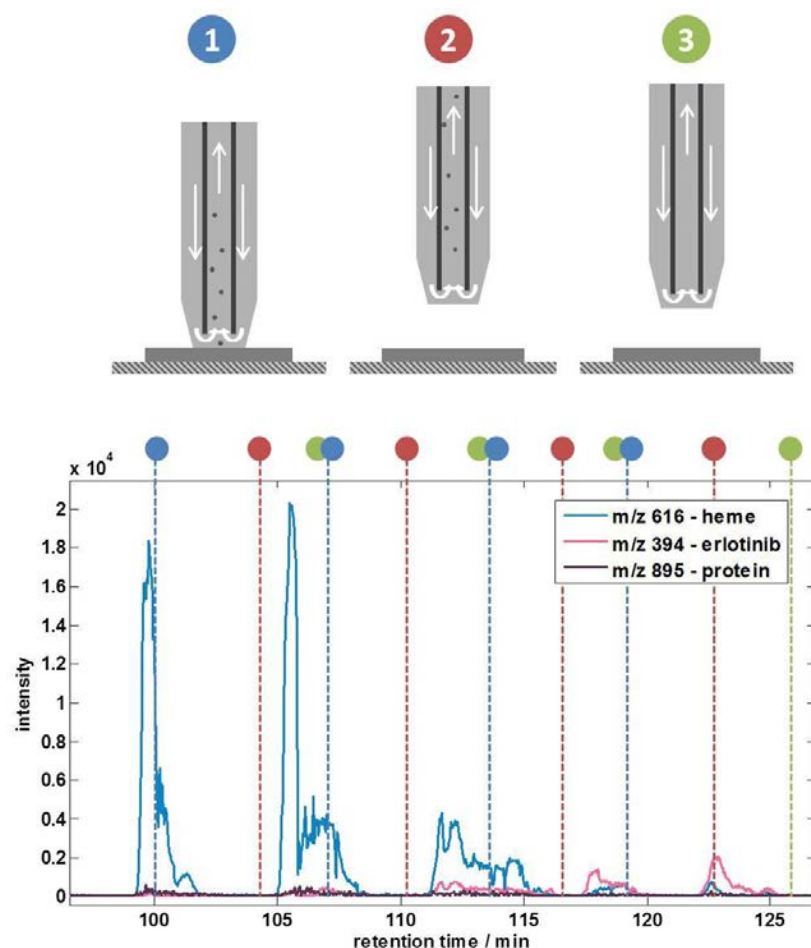
Figure 7.5 Illustration of data acquired by Flow-probe mass spectrometry, top – schematic illustration of surface sampling routine, bottom – example section of chromatogram acquired by sampling multiple locations on kidney tissue, time points marked demonstrate different stages in the sampling routine and indicate the delay between surface sampling and detection of analytes.

Example ion images acquired by each technique and the locations selected for sampling are presented in Figure 7.6. These images demonstrate that approximately the same distribution of ions is observed by each technique. The high concentration of heme and haemoglobin around the renal pelvis is expected due to the large blood vessels which are responsible for transporting blood into and out of the kidney at this location. Similar distributions were observed in separate LESA imaging experiments outlined in Chapter 5.
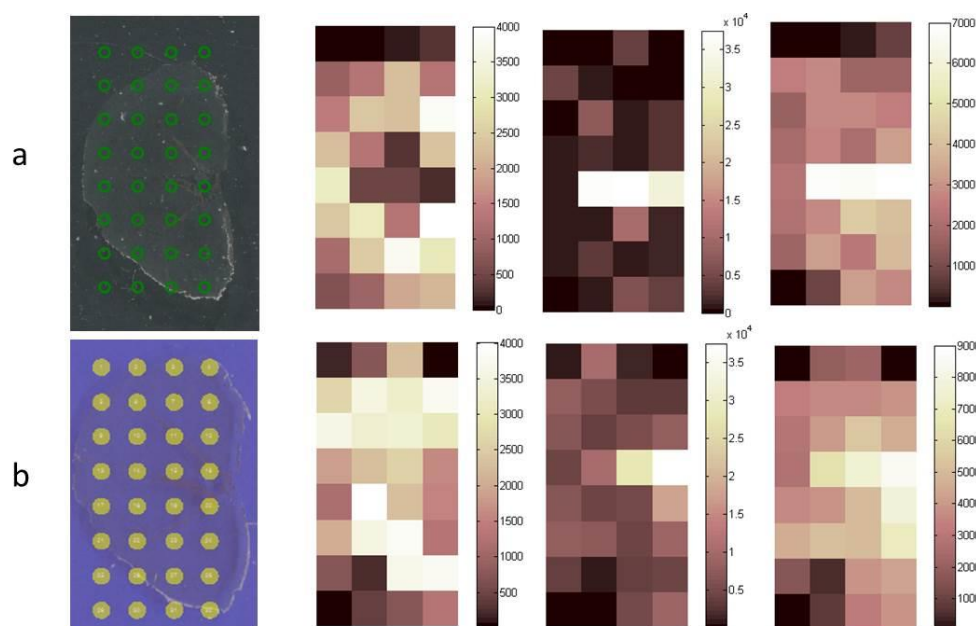
Figure 7.6. Comparison of LESA and Flow-probe mass spectrometry images acquired from serial sections of cassette-dosed rat kidney tissue with 2 mm pixel spacing, a) imaging using Flow-probe mass spectrometry, (left to right) ion intensity distributions of ions with *m/z* 394.18 (erlotinib), *m/z* 616.18 (heme) and *m/z* 894.86 (α-Hb), b) equivalent images of serial section and same ions using LESA mass spectrometry.

Visual inspection of the sample after Flow-probe analysis enabled identification and measurement of regions sampled, see Figure 7.7. The size of region sampled varied due to inconsistencies in stability of the liquid microjunction. This means that the region sampled per pixel varied and therefore images produced from this data cannot be assumed to be entirely representative of the sample and could account for differences observed between LESA and Flow-probe data. The method described in Chapter 3 could be used here. MALDI MS imaging of tissue which had been sampled by the Flow-probe could provide information about the regions surveyed, the repeatability of the technique and the differences observed between Flow-probe and LESA data.
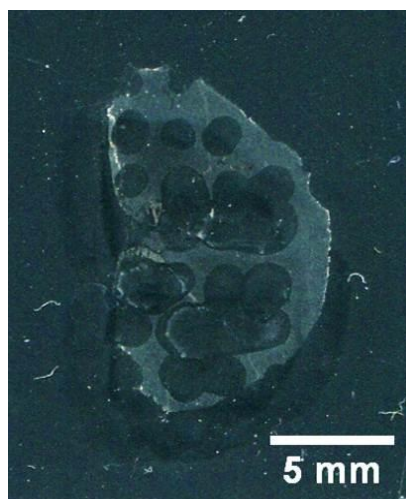
Figure 7.7. Optical image of rat kidney tissue after Flow-probe mass spectrometry, dark regions indicate contact with solvent. Inter-pixel distance in the x and y dimensions should be fixed at 2 mm however this can be seen to vary due to inconsistencies in solvent spreading.

7.3.3 Preliminary investigations into raster mode tissue imaging for higher spatial resolution MS imaging

The true benefits of Flow-probe mass spectrometry would be realised if sampling could be performed in raster mode in which the sample was continuously moved beneath the probe tip without retracting between pixels. This would allow for complete analysis of the tissue without gaps between pixels and higher-throughput analysis. Raster analysis is commonly used for DESI and nano-DESI MS imaging of tissue samples and is generally considered the preferred method of analysis.[85,211] To produce an image from data collected in raster mode, a single data file (containing a pre-defined number of scans) is acquired per line. Data for each pixel is produced by combining a certain number of scans. The time taken to acquire a single scan and the distance moved by the probe during that time determines the lateral resolution of the technique.

Before Flow-probe raster imaging can be performed, an understanding of the data produced is needed – this ensures confidence in the data and the location different signals originate from. It was demonstrated in the previous section that there is a delay between the probe contacting the surface and the detection of analytes from that surface. Measurement of this delay and analysis of model samples in which the location of analytes is known in advance will ensure confidence in data. An additional point of consideration for raster mode analysis is expected decrease in sensitivity over spot mode – the probe dwells on the surface for a shorter amount of time per unit area therefore has a shorter opportunity for desorption of analytes. Whether sensitivity is still sufficient to detect biological analytes will need to be assessed.

An experiment in which raster sampling of rat kidney tissue could be assessed was performed, see Figure 7.8. An example mass spectrum in which all scans across the tissue section were summed together is displayed in Figure 7.8.b. It was found that the liquid microjunction repeatedly failed when it encountered the edge of the tissue section. An example chromatogram of a single line raster is presented in Figure 7.9. A delay of approximately 5 minutes between the probe encountering the tissue and the detection of biological analytes was observed.
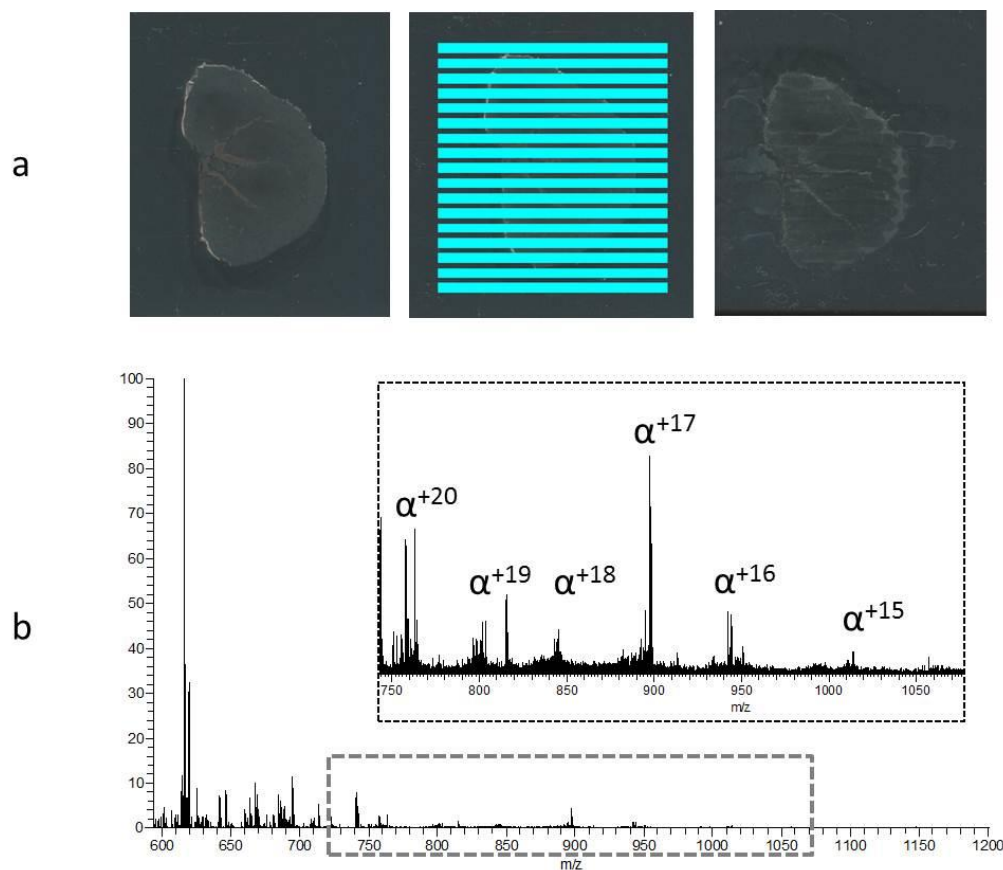
Figure 7.8 Flow-probe mass spectrometry imaging of rat kidney tissue using 'raster' mode sampling, a) optical image of section before sampling, the locations selected for sampling (lines separated by 1 mm in the y-dimension) and image taken after sampling, b) example mass spectrum acquired from tissue by flow-probe raster sampling, this spectrum is the sum of all scans acquired from tissue.
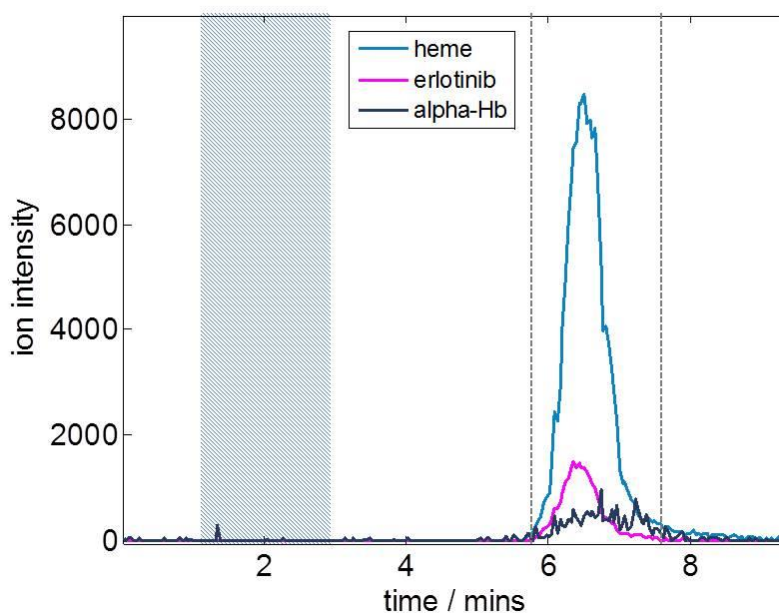
Figure 7.9 Example chromatogram of single line Flow-probe raster on kidney tissue, shaded region indicates the time point at which the probe was sampling tissue, grey lines indicate the approximate start and end time points of the detected signal.

In order to properly characterise the signal a simple model sample with known composition and dimensions was prepared; a red marker pen containing rhodamine B dye was used to draw a line on a glass slide which was then photographed prior to sampling. The time at which the signal should be observed relative to the start of the datafile was calculated as 128 seconds which accounts for the time taken for the probe to reach the ink (a distance of 8mm) and the time taken for the solvent to travel through the capillary which has a volume of 4.7 µL (NB a different capillary was used in section 7.3.2). This is in agreement with what was observed, with a major peak appearing in the chromatogram at ~2.1 minutes see Figure 7.10. It was calculated the width of the line was 400 µm and therefore with a stage speed of 80 µm/second the signal should last for approx. 5 seconds. It was found that the signal was detected for ~18 seconds which suggests that some diffusion of analytes could be occurring when the solvent travels through the capillary. Alternatively the analyte could be adhering to the capillary or the

probe which results in peak broadening. This would affect the size of features which could be successfully resolved in a raster imaging experiment. The chromatogram for the second raster line demonstrates that ink was detected before the probe reached the line on the glass. This suggests that either there was residual ink on the glass slide, in the capillary or on the probe. An alternative explanation would be that analytes were spread across the glass during the sampling and have been genuinely detected at different locations/time points. Optical images of the slide were acquired to investigate whether there was any evidence of this, see Figure 7.11. Whilst a small indentation appears where the probe travelled there is no indication of red ink smeared across the slide. This suggests that residual ink in the capillary is the cause of higher baseline intensity.
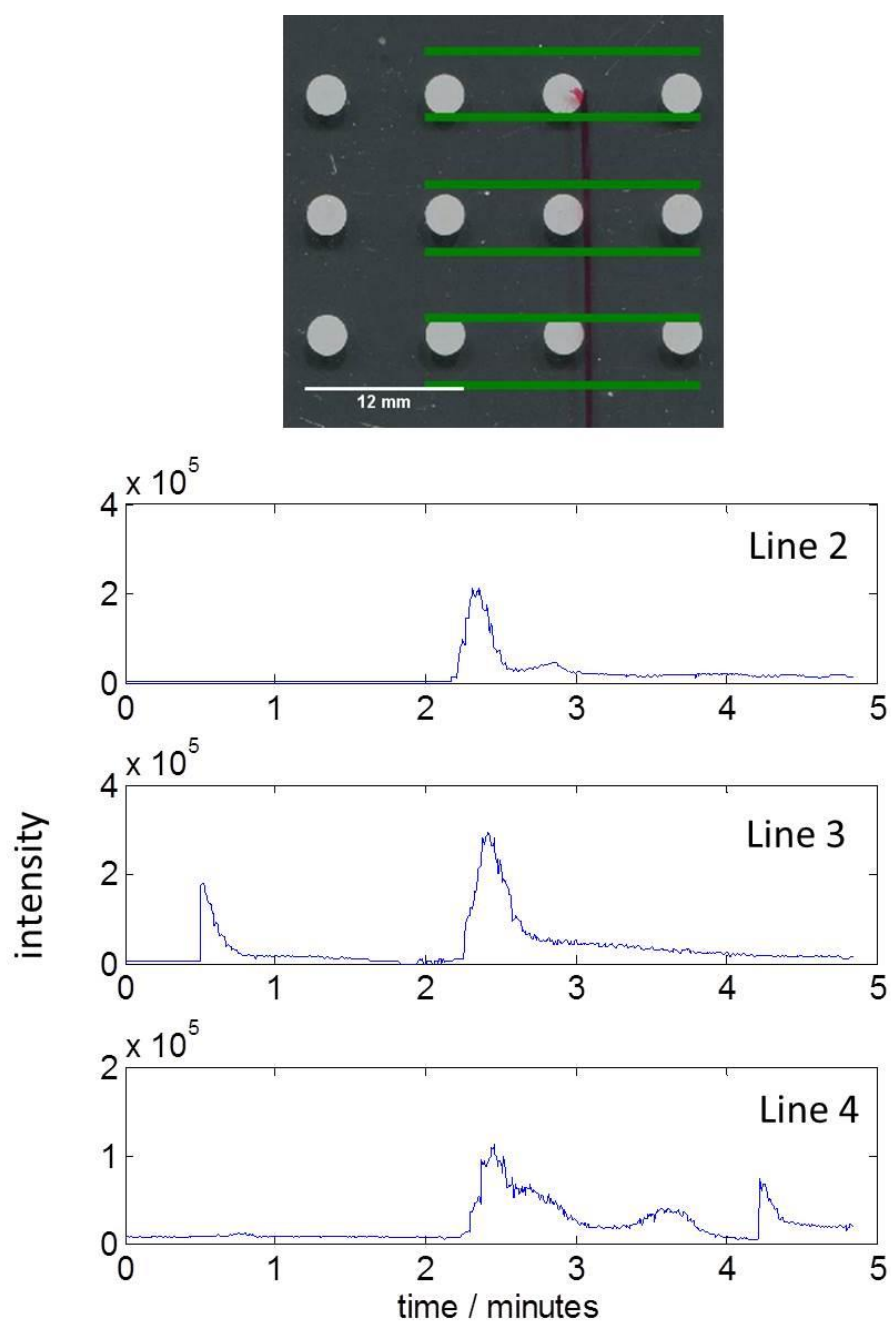
Figure 7.10 Investigations into Flow-probe raster sampling, top: red marker pen on glass slide and regions selected for raster sampling, bottom: example chromatograms (for ions with *m/z* 443.23) from the raster lines indicated.
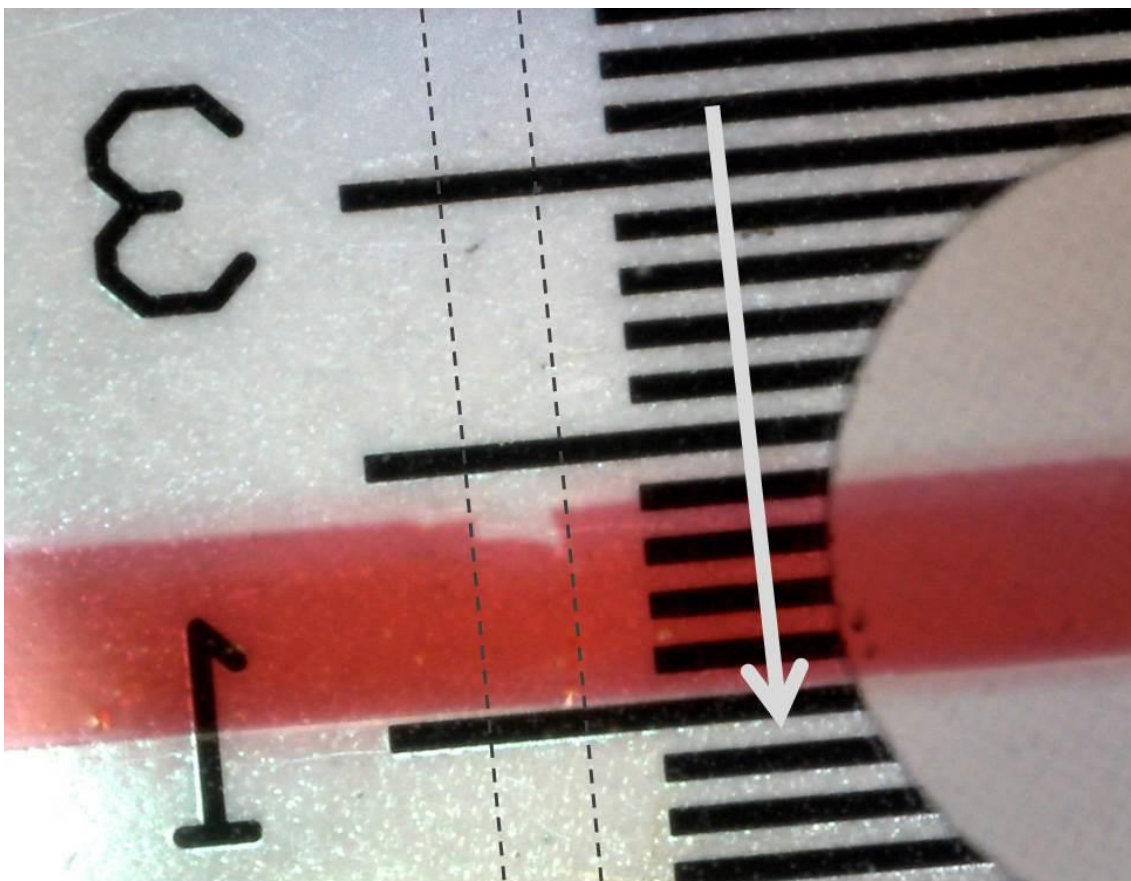
Figure 7.11 Optical image of sample after Flow-probe raster sampling, arrow indicates direction of travel of Flow-probe and dashed lines indicate approximate tracking of probe. There is little evidence here to suggest that the probe has caused delocalisation of ink across the sample indicating that carry over is caused by build-up within the capillary and not on the surface of the slide.

7.4 Conclusions

A method was developed which demonstrates for the first time that the imaging of proteins by Flow-probe MS is possible. It was found that Flow-probe MS can provide equivalent data to LESA mass spectrometry but with the potential for improved spatial resolution, through-put and financial costs (due to the lack of consumable items such as pipette tips and electrospray ionisations chips). The operation of the Flow-probe in raster mode was considered for the first time, and questions surrounding the diffusion of analytes within the capillary system were raised. Further work to ascertain and measure

dead volumes within the system must be performed before this mode of operation can be used with confidence. It is possible that spot mode analysis is the only suitable mode of operation for Flow-probe mass spectrometry, in which case the minimum pixel size possible would be 600 μm which is similar to that achieved with LESA MS imaging.

Chapter 8

Application of LESA Mass Spectrometry: Analysis of Proteins Directly from Bacterial Colonies

Work presented in this chapter was published in the following paper: Randall, E. C.; Bunch, J.; Cooper, H. J. *Analytical Chemistry* **2014**, *86*, 10504-10510. This is included in Appendix 2.

Introduction

This thesis has so far concentrated on the development of chemical imaging methods for the analysis of biological tissue. Methods for tissue samples are well established, but other sample types are highly relevant to both biomedical and pharmaceutical research. Bacterial samples have been the subject of mass spectrometry research since the 1970s.[216,217] Advances in software and instrumentation have helped create powerful tools for microbiological differentiation and identification.[42,218]

The analysis of intact protein species from bacterial colonies via LESA mass spectrometry will be the focus of this chapter. The limited spatial resolution of LESA MS imaging would not present a problem for this particular application because the size of spatial features is not expected to be smaller than the typical pixel sizes.[219] Here is presented the development of LESA mass spectrometry methods for the analysis, identification and imaging of intact proteins directly from living *Escherichia coli* colonies in petri dishes.

Experimental

8.1.1 Surface Sampling

Petri dishes containing *E. coli K-12* colonies were placed directly into the TriVersa Nanomate chip-based electrospray device (Advion, Ithaca, NY) adjacent to half a 96-well microtitre plate (ABgene PCR plate Thermo Fisher Scientific, Leicestershire, U.K.) into which the extraction solvent system is placed, see Figure 8.1. Surface sampling was performed using the advanced user interface (AUI) feature of the TriVersa NanoMate ChipSoft Manager software which allowed for more flexibility in selection of sampling locations. The volume of solvent for sampling was 3 µL solution and the solvent system was acetonitrile and water (39.6:59.4) with 1% formic acid. The exact sampling height of the pipette tip varied (from -9 mm to -11 mm from initial position of robotic arm), depending on the size of the colony and spread of agar in different samples; for increased extraction of proteins the pipette tip came into contact with the top surface of the colony but did not penetrate the agar below. Once in contact with the colony, the tip dispensed 2 µL solvent onto the colony which was held in contact for 3 seconds. The solution was then re-aspirated into the pipette and the tip engaged with the nanoelectrospray chip in order to start electrospray ionization and introduction of the sample into the mass spectrometer. The sample was electrosprayed with a gas pressure of 0.3 psi and a tip voltage of 1.75 kV. Mass spectra were collected in full scan mode (*m/z* 500-2000) at a resolution of 100 000 at *m/z* 400. AGC target was 1×10^6 charges. Each scan was comprised of 30 coadded microscans. Data were recorded for 5 minutes (~ 11 scans). (Note that a stable electrospray could be maintained for ~ 50 mins from a single LESA analysis).

8.1.2 Protein identification

CID was carried out in the linear ion trap and the fragment ions were detected in the orbitrap at a resolution of 100 000 at *m/z* 400. AGC target was 5 x 10^4 charges. CID experiments were performed with helium gas at normalized collision energy of 35% (optimized for sequence coverage – data not shown) and an isolation width of 10 Th. MS/MS spectra were collected in the range *m/z* 300-2000 and are comprised of 10 coadded microscans. Data were analyzed using Xcalibur 2.10 software (Thermo Fisher Scientific) where the Xtract program was used to calculate monoisotopic masses. For data analysis using ProSightPTM 2.0, CID MS/MS spectra were deconvoluted using the Xtract program (S/N threshold 3). Xtracted monoisotopic fragment masses were searched against the *E. coli K-12* database in ProSightPTM 2.0, with a fragment tolerance of 10 ppm, precursor tolerance 100 ppm, in order to assign putative protein identifications. Two search types were used in Prosight, 'absolute mass search' and 'sequence tag search'. Absolute mass search involves searching the mass of the precursor ion against intact masses of proteins within the chosen database. If a match is found then fragment masses can be matched to theoretical fragments of that protein. Sequence tag search involves compiling lists of amino acids which could correspond to observed fragment masses or differences in mass between two fragments. The amino acid sequences are then searched against the appropriate database to see if they correspond to sequences of known proteins. Protein identities were confirmed by manual analysis using Protein Prospector (http://prospector.ucsf.edu/prospector/mshome.htm).

8.1.3 LESA MS imaging

LESA MS imaging of bacterial colonies was performed using the advanced user interface of Chipsoft software (Advion). Coordinates were selected for 25 points in a

grid covering bacterial colony and surrounding media. Height relative to surface was ~ -0.2 mm and was manually adjusted according to sample topology. Surface sampling was performed as described above. Data were recorded for 8 minutes per pixel, an injection time of 1 ms was found to give sufficient signal, 30 microscans were coadded per scan. Data were processed using matlab and in-house software.

8.1.4 Post-sampling image analysis

Photographs of the colony surface were taken after LESA sampling. Areas which came into contact with solvent during sampling were measured using ImageJ software. Contact with solvent caused discolouration of the colony surface so the diameter of these regions could be visually identified in the photos. The image scale was set using features of known size in the image, either a ruler or coordinate spots of the universal adaptor plate.

Results and Discussion

8.1.5 Development of LESA MS for analysis of proteins from bacterial colonies

A sample of *E. coli* K-12 was inoculated on agar and incubated at 21°C for 3 days. The sampling set-up used in this work is illustrated in Figure 8.1. A set of coordinates was printed and attached to the bottom of the tray to allow more space for samples. The solvent system was placed into a 96-well plate adjacent to the petri-dish. The advanced-user interface function of Chipsoft was used to perform surface sampling; the sample plate required for LESA Points software was too deep to allow a petri dish to sit on top and still allow the robot to move freely. Coordinates for sampling were selected manually.
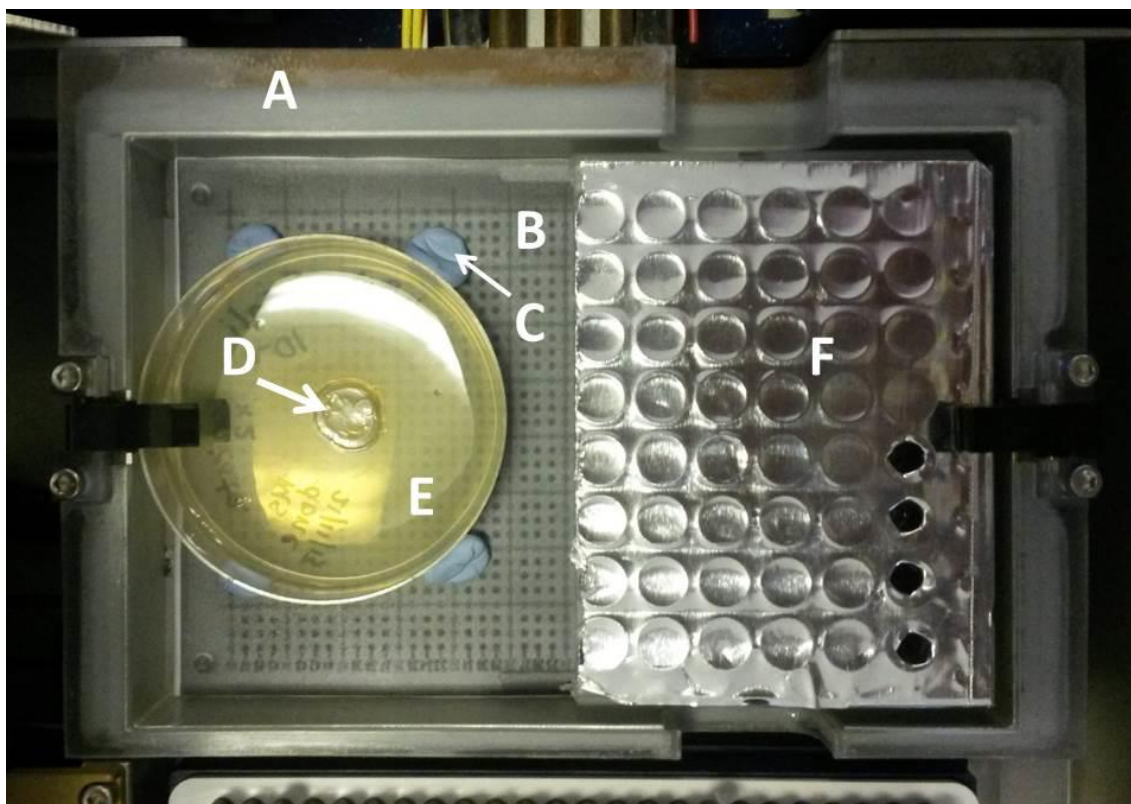
Figure 8.1 Experimental set up: (A) sample tray of Triversa Nanomate; (B) photocopy of the universal adaptor plate – for x,y coordinates; (C) adhesive putty (Blu-tack) to

secure petri dish in position: (D) *E. coli* colony: (E) petri dish containing agar; (F) half 96-well plate containing extraction/electrospray solvent system.

It has previously been demonstrated that acetonitrile and water is the best solvent system for the extraction of proteins from biological tissue.[215] Therefore acetonitrile and water was used as the solvent system for LESA in this work. It was found that numerous peaks corresponding to protein ions in various charge states were detected using this method, as demonstrated in Figure 8.2. It was found that the mass spectrum contained approximately 150 peaks corresponding to ~60 bacterial proteins in a range of charge states. The molecular weights of these proteins ranged from approx. 5 to 32 kDa. This mass range is in agreement with the findings of McFarland *et al* who report the detection of intact proteins in the range 4-37 kDa from *S.* Typhimurium by ESI orbitrap mass spectrometry.[220] The benefit of performing such analyses by LESA rather than ESI MS is the retention of spatial information. This could allow for the mapping of proteins, peptides and secondary metabolites produced in the presence of competing microbes.
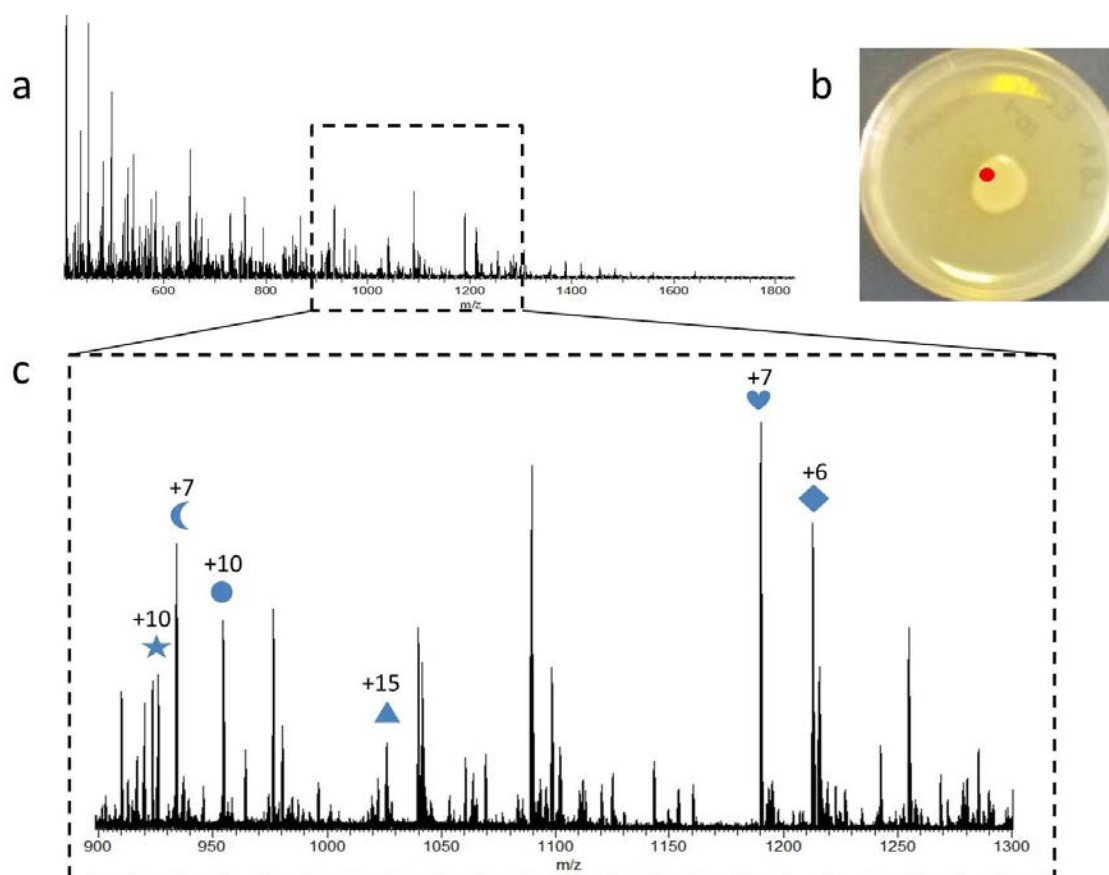
Figure 8.2 LESA mass spectrometry of *E. coli K-12* bacterial colony stored at 4 °C. a) Full scan mass spectrum; b) Photograph of bacterial colony growing on solid agar medium in petri dish. Red spot marks region sampled by LESA; c) Enlarged m/z region from full scan mass spectrum (*m/z* 900 – 1300) which contains the majority of peaks corresponding to protein ions. Symbols indicate peaks subsequently selected for CID.

The height to which the pipette tip descended during surface analysis was investigated to see how this affected mass spectra acquired. The surface was sequentially sampled at a single location, starting at approximately 0.2 mm above the surface, allowing the tip to descend 0.2 mm lower each time. Spectra were recorded at each respective sampling height, see Figure 8.3. It was found that proteins were only extracted when the pipette tip came into contact with the colony surface. Although a larger number of proteins were detected when the pipette tip sampled further below the colony surface (Figure 8.3.c), a compromise was made between good extraction of proteins and electrospray instability due to capillary blocking. The mass spectrum shown in Figure 8.3.d contains

175

peaks corresponding to singly-charged species as well as protein peaks indicating that the pipette tip may have punctured the agar below the colony.
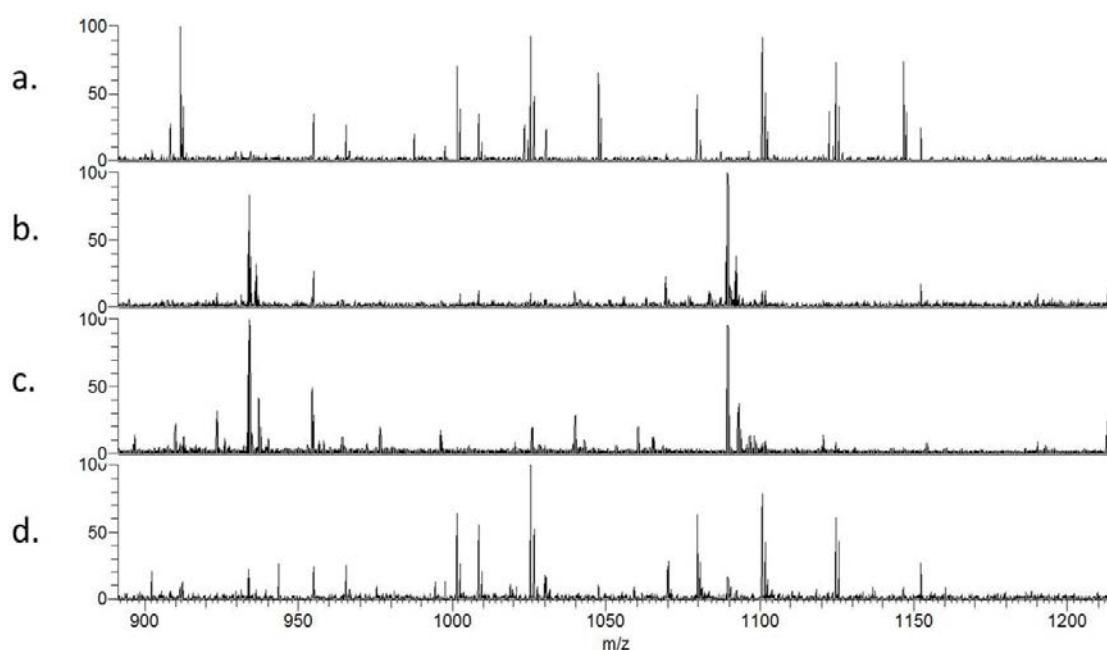
Figure 8.3 Mass spectra obtained by sampling the same location on the surface at different heights relative to the surface: a) 0.2 mm above surface; b) 0 mm above surface; c) -0.2 mm above surface; d) -0.4 mm above surface. Only when pipette tip comes into contact with the colony surface (b) and below are proteins extracted.

It is possible that the observation of increased numbers of proteins in mass spectra obtained following contact between the pipette tip and the surface is due to the insoluble nature of the extracellular matrix produced by colony bacteria. In placing the pipette tip in contact with the surface, this insoluble layer could have been physically disrupted allowing more efficient extraction of proteins contained within the colony. It should be noted that this 'contact' method of surface sampling is different from other LESA methods described in the literature, see Figure 8.4. Kai *et al* report the extraction of small molecule antibiotic compounds using LESA – a method in which only the solvent droplet came into contact with the bacteria.[43]
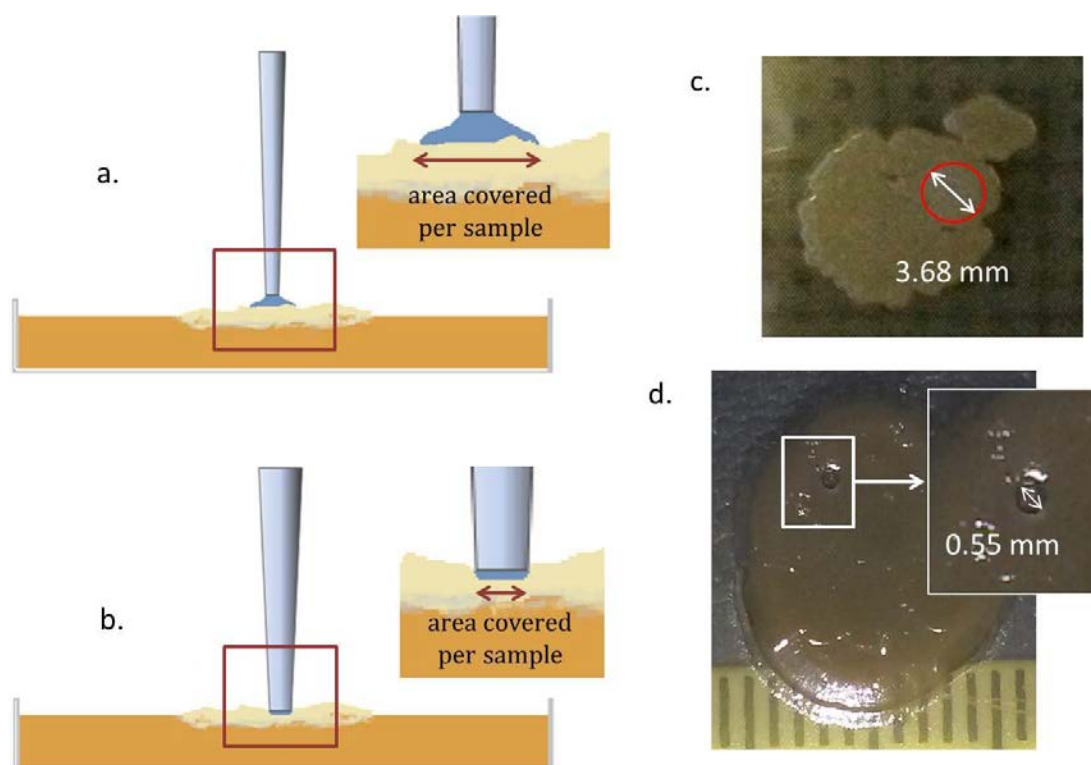
Figure 8.4 Improved sampling precision obtained from 'contact' LESA sampling: a) Schematic illustrating the surface area of sample covered by each solvent droplet when sampled by a liquid micro-junction (contact between surface and solvent only); b) schematic illustrating the smaller surface area covered by each sample droplet with the 'contact' method (contact between surface and pipette tip); c) sampled area following liquid microjunction sampling; d) sampled area following 'contact' LESA.

Measurement of the relative areas sampled using contact and non-contact LESA is presented in Figure 8.4. The process of placing the pipette tip in contact with the colony surface during sampling appears to limit the spread of solvent to the area of the pipette tip. It is possible that the low pressures used to dispense and aspirate the solvent droplet are insufficient to push the solvent beyond the end of the pipette tip and therefore the colony acts as a plug. This sampling mechanism appears to be slightly different from contact LESA described in previous chapters due to the soft nature of the sample. It is possible that the relatively large number of proteins detected is due to residual bacteria on the sampling pipette. This would effectively increase the sampling time so that

analytes could continue to dissolve into the solvent during electrospray. This would also happen to some extent during tissue analysis but only the very tip of the pipette would contact the tissue. Therefore one might expect this effect to be less pronounced. The total surface area sampled by the contact LESA method is ~0.24 mm^2, as measured using ImageJ on images of the puncture mark on colony surface after sampling. This observation represents a significant improvement when compared to the area covered by the usual LESA solvent droplet, which was measured to be ~10.64 mm^2 (solvent sampling discoloured the colony surface allowing for measurement of the area from photographic images). Note that the droplet volumes (3 μL) were the same for both methods.

The outer diameter of the pipette tips used for LESA sampling is 600 μm. The inner diameter of the pipette tips is 400 μm. As it is impossible to ascertain without further investigation whether solvent is contained fully within the inner portion of the pipette, it should be assumed that the minimum pixel size accessible by LESA is 600 μm. There are numerous reports of MALDI imaging of microbial colonies; these have a typical pixel size of 50-200 μm.[41,48,164,221] Whilst this is obviously better than LESA, there are various experimental problems encountered during MALDI analysis of wet agar samples. Deposition of a matrix onto a wet sample is not ideal due to the potential for lateral diffusion of analytes which could compromise spatial integrity of the sample.[221] Alternative approaches have included a dehydration[222] or transfer step in which microbial samples are imprinted onto a more suitable substrate.[223] Dehydration of the sample results in a flat, dry sample which is more amenable to certain sampling techniques, however the colony cannot be assumed to remain chemically unaltered during this step. Imprinting methods have provided a possible route for indirect imaging however selective transferal of analytes could occur leading to inaccurate results.

DESI and nano-DESI have both been reported for the ambient MS imaging of microbial samples. Typically pixel sizes in the range 150-200 μm have been used.[222,223] This has provided insight into the distribution and production of secondary metabolites and other small molecules under ambient conditions. As discussed in previous chapters, LESA MS has the capability to detect multiple classes of compound simultaneously. Whilst alternative solvent systems for LESA analysis of microbes have not been fully explored in this work, it is possible that by optimization of sampling conditions multiple analyte classes – such as lipids, proteins, drugs, and metabolites from more than one microbial species - could be simultaneously detected. This would be of interest for research focused on the behavior, interaction and response of microbes under varied conditions, for example assessment of drug efficacy.

8.1.6 Top-down identification of proteins from *E. coli* colonies

CID mass spectrometry experiments were carried out to identify a number of protein ions detected during LESA MS. Ions centered at *m/z* 923.51 (+10 charge state), 933.91 (+7), 954.43 (+10), 1028.14 (+15), 1190.31 (+7), and 1212.94 (+6) were fragmented. The product ions were searched against the *E. coli K-12* database in ProSightPTM 2.0, using either the 'absolute mass search' or the 'sequence tag search'. Tentative protein identifications were confirmed by manual analysis. The proteins identified and the protein sequence coverages are shown in Table 8.1. The sequence coverages ranged from 13 to 40%. A representative MS/MS spectrum from one of the identified proteins, DNA-binding protein HU-beta, is shown in Figure 8.5**.** MS/MS spectra from the other protein ions along with fragment assignments are included in Appendix 3.
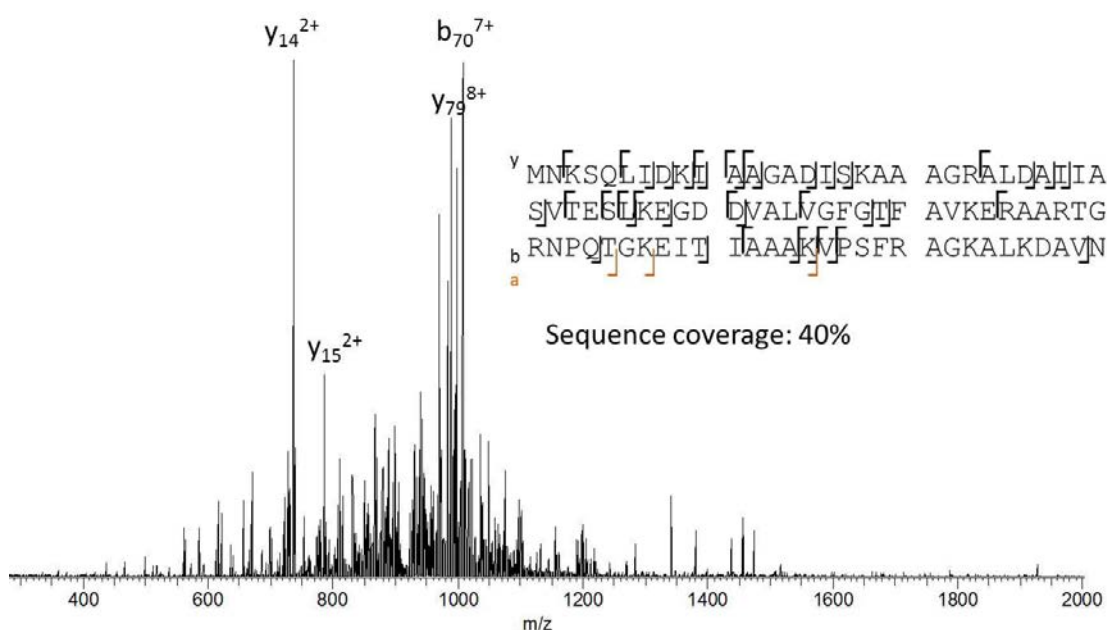
Figure 8.5 CID mass spectrum of ions centred at m/z 923.51 (+10 charge state), identified as DNA-binding protein HU-beta. Fragment ions observed are shown inset.

A total of 6 proteins were identified, see Table 8.1. DNA binding protein HU-alpha and HU-beta are both histone-like DNA binding proteins which are capable of wrapping DNA to stabilize and prevent its denaturation under extreme environmental conditions.[224] DNA binding protein H-NS increases thermal stability of DNA and inhibits transcription at low temperatures.[225] The function of protein YjbJ is poorly understood but is recognized as a highly abundant protein in *E. coli*.[226] CspA is a cold shock response protein, known to be induced at temperatures of 15°C or lower.[227] Multiple stress resistant protein BhsA is known to be induced under a range of stressful conditions including drastic pH changes, heat shock, presence of heavy metals and hydrogen peroxide. As a result this protein inhibits biofilm formation by repressing cell aggregation and increases cell viability under stressful conditions.[228] A number of these proteins (HU-alpha, HU-beta, YjbJ, H-NS) were also detected by ESI top-down MS/MS of *S.* Typhimurium reported by McFarland *et al.*[220]

Table 8.1 Details of proteins identified from LESA MS

m/z$_{meas}$	m/z$_{calc}$	Δppm	Charge state	% Sequence Coverage	Protein identity
954.5104	954.5133	-3.0	+10	28	DNA binding protein HU-alpha
1027.6038	1027.6069	-3.0	+15	18	DNA binding protein H-NS
1189.5921	1189.5919	0.2	+7	23	UPF0337 protein YjbJ
1212.2801	1212.2719	6.8	+6	13	CspA
923.0039	923.0067	-3.0	+10	40	DNA-binding protein HU-beta
933.4871	933.4822	5.2	+7	32	Multiple stress resistance protein BhsA

It should be noted that whilst a number of proteins have been identified in this study, it was not possible to identify all proteins from their MS/MS spectra. Ions of *m/z* 1254.99 (+7 charge state), were also fragmented and the product ions searched against the *E. coli K-12* database in ProSightPTM 2.0, using both the 'absolute mass search' and the 'sequence tag search'. Neither search returned hits corresponding to the correct intact mass. Top-down methods are used relatively infrequently compared to bottom-up identification techniques and as such the demand for software for top-down methods is lower. Whilst several platforms are available, e.g., Prosight PTM 2.0,[229] ROCCIT

(roccit.caltech.edu), neither reliably fully characterized the proteins in this work and a large amount of manual characterization was required. This aspect would need addressing if top-down methods were to become more established.

8.1.7 Investigation into storage effects

The selection of proteins detected and identified from colonies stored at 4°C are indicative of extreme environmental conditions, consistent with prolonged refrigerated storage conditions. After the initial incubation period to grow the colonies, samples were stored at 4°C for a number of days, which explains the induction of a cold shock response. For comparison, a further set of bacterial samples were grown. These colonies were stored at room temperature (~20°C) prior to mass spectrometric analysis and were never exposed to low temperatures.

LESA mass spectra obtained from bacteria grown and stored at room temperature are displayed in Figure 8.6. For comparison, a LESA mass spectrum acquired from a colony grown at room temperature for 3 days and then stored at 4 °C for two days is also presented. Peaks corresponding to all the proteins identified from the LESA mass spectrum shown in Figure 8.6 (in which bacteria had been grown for 3 days at room temperature before being stored at 4°C for 7 days) were observed, albeit with differing relative abundances. This could be due to differences in protein expression as a result of prolonged cold shock or may be due to differences in LESA extraction efficiency either as a result of prolonged cold shock or colony topology. Figure 8.6.b shows a mass spectrum obtained from a colony stored at room temperature for 3 days. The colony was sampled at three separate locations, as indicated on the photograph inset. At location 1, peaks corresponding to HU-alpha and HU-beta were observed but none of the other proteins identified above. At location 2 (Figure 8.6.b), peaks corresponding to HU-

alpha, HU-beta, and CspA were observed. At location 3, none of the proteins identified above were observed. The proteins BhsA and YjbJ were not observed in any location.
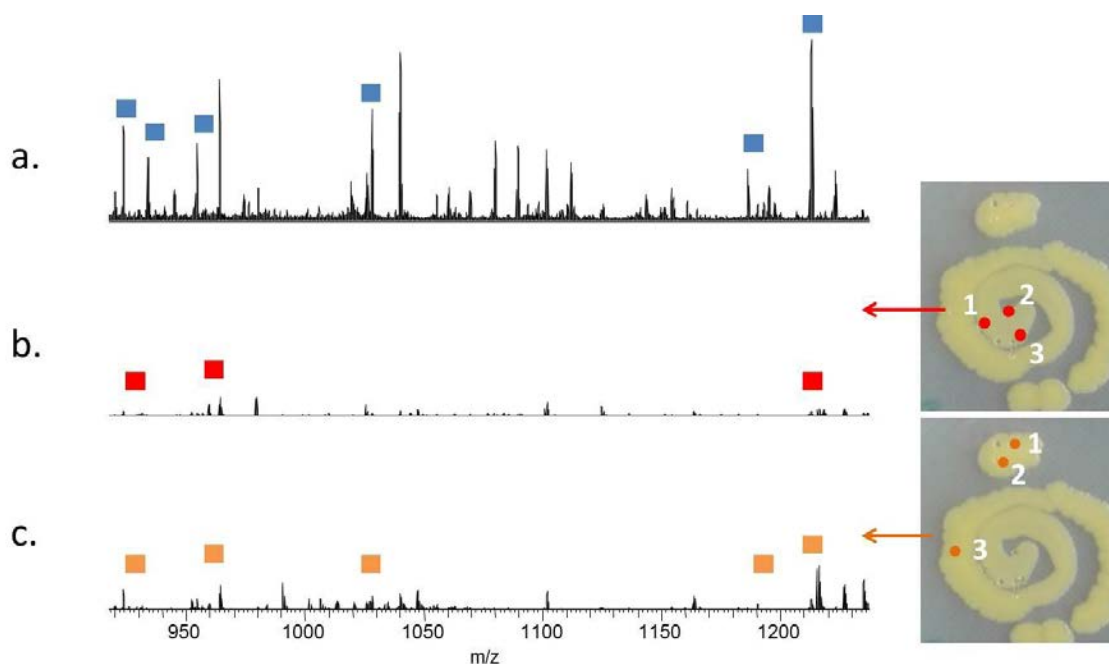
Figure 8.6 LESA mass spectra of bacteria stored at (a) 4 °C for 2 days (b) at room temperature (20 °C) for 3 days and (c) at room temperature (20 °C) for 10 days (y-axes are equivalent). Symbols denote identified stress response proteins. Inset: Photographs of colonies with sampling locations indicated.

A repeat analysis was carried out after the colonies had been stored at 20 °C for a further 7 days (Figure 8.6.c). Again, three separate locations were analysed, as indicated. In two of the locations, all but one (BhsA) of the stress response proteins previously detected in bacteria stored at 4°C were detected. At the other location, all but BhsA and YjbJ were detected. These results suggest that prolonged storage can induce various stress responses in bacteria. Multiple stress resistance protein BhsA, however, was not detected at any location from colonies stored at 20°C, either after 3 or 10 days, suggesting that either temperatures lower than 20°C, or storage for longer than 10 days is required for expression of this protein. As mentioned above BhsA has been shown to inhibit biofilm formation. It is possible that expression of BhsA under

refrigerated conditions resulted in reduced biofilm formation thus aiding the LESA process. These results suggest that bacterial response to external stimuli – in this case temperature – can be assessed by LESA mass spectrometry. It would be interesting to see whether proteomic responses to other factors, such as drug compounds could also be detected.

8.1.8 LESA MS imaging of bacterial colonies

After demonstrating the successful detection of proteins from bacterial samples an experiment was conducted to assess whether LESA was capable of detecting different distributions of species within a colony and the surrounding media. A grid of coordinates was selected for sampling, with an inter-pixel spacing of 2mm. Example ion images are displayed in Figure 8.7, these images indicate that it is possible to detect different distributions of ions and that different ions are more abundant in the centre of the colony and some at the edges. The distribution of HU-alpha (*m/z* 954.12) and H-NS (*m/z* 1027.36) have similar but not identical distributions. Protein species were only detected from samples extracted from the colony itself and not the surrounding media. Species detected from media were generally singly charged, two example ions are displayed in Figure 8.7. Without assessing the reproducibility of the method it is impossible to say whether differences in detected abundance are due to true differences in concentration or differences in extraction efficiency. Therefore differences in protein abundance between pixels taken from the colony could be due to real biological differences in expression or variation in extraction efficiency or electrospray stability.
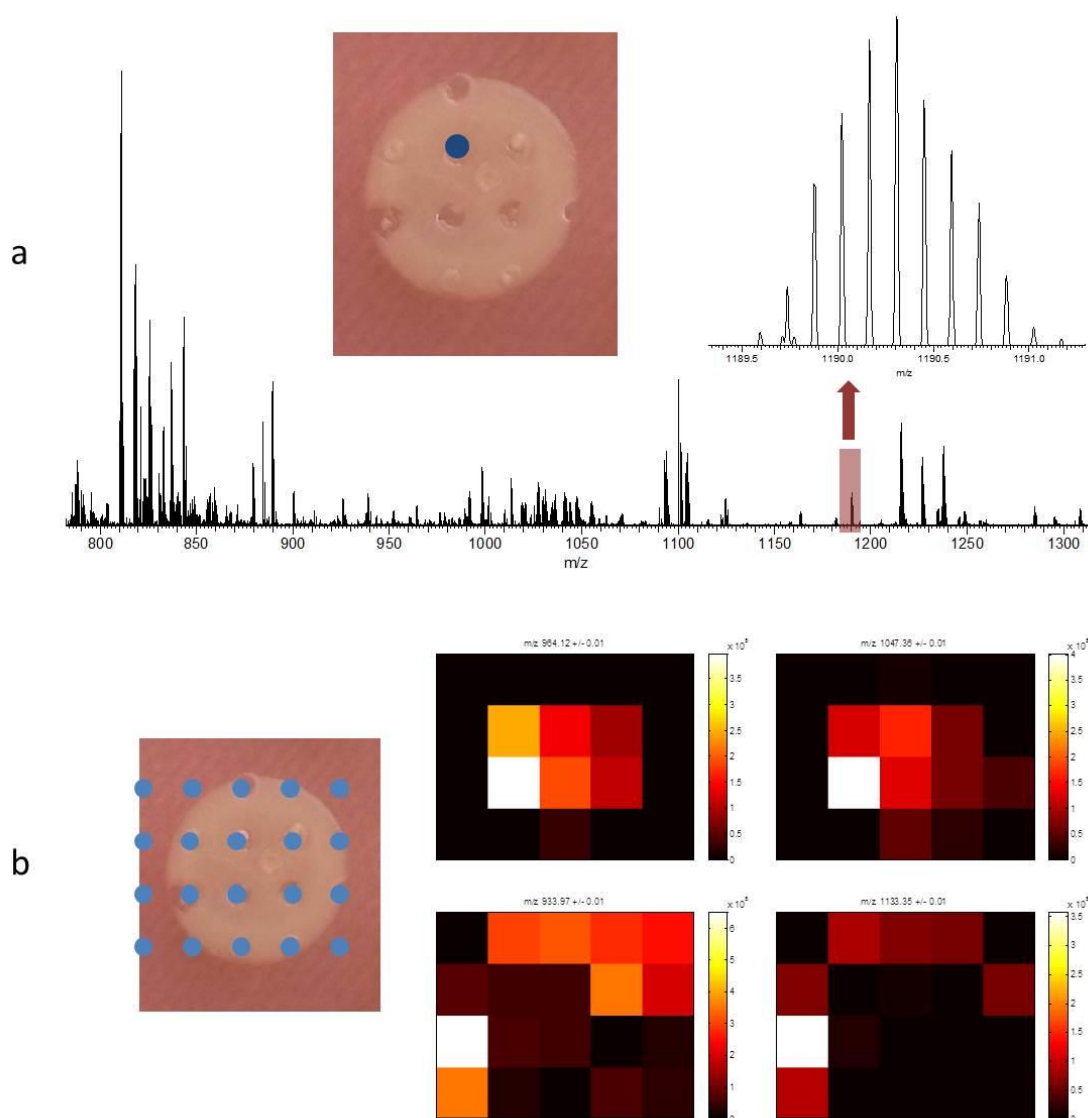
Figure 8.7 LESA MS imaging of E coli colony: a) example LESA mass spectrum acquired from location labelled in blue, b) locations for LESA sampling and example ion images of proteins and species located in the agar, (clockwise from top left) *m/z* 954.12 (HU-alpha), *m/z* 1027.36 (H-NS), *m/z* 933.97 (unidentified singly charged species), *m/z* 1133.35 (unidentified singly charged species).

By visual and photographic inspection of the sample after LESA it was clear that portions of the colony adhered to the pipette tip during sampling. The dimensions of an *E. coli* cell are approximately 1 x 2 μm and the diameter of the electrospray nozzle is 5.5 μm. It would therefore only require 2 or 3 bacteria to block the nozzle and prevent

186

stable electrospray ionisation. This is consistent with the instabilities and frequent nozzle blocking observed during experiments. It might be possible to overcome such problems by diluting the extracted sample in a separate solvent well after surface sampling. This could also act as a pipette wash and help remove residual bacteria from the tip. Alternatively, approaches reported in the literature such as imprinting, dehydrating or growing samples on a paper substrate could prevent nozzle blocking and make the method more reproducible.[221,223] Problems associated with these approaches have previously been discussed. In order to be confident that differences in abundance were true, a reproducible method would have to be established.

As discussed, a variety of other mass spectrometry methods have also been used for the imaging of microbiological samples. Each technique is associated with advantages and limitations. As previously stated the level of spatial detail provided by LESA is probably sufficient because the size of features within an image (such as excreted secondary metabolites) is unlikely to be smaller than 1 or 2 mm. A further advantage of LESA is that the sampling height can be varied between pixels which allows for variation in topology. Techniques which employ raster sampling such as DESI, nano-DESI and the Flow-probe encounter problems during the analysis of microbiological samples due to the probe to surface distance dependence of data and the varied topology of such samples.[49,87,223]

Conclusions

A method suitable for the top-down extraction, detection and identification of intact proteins from living bacterial colonies has been developed and investigated. The identities of these proteins appear to indicate the well-being of the colony. The method has implications for microbiological research as it may be suitable for the study of bacterial growth, communication and response to external factors such as

pharmaceuticals and pH. Moreover, the 'contact' LESA method offers improved sampling precision and could be useful for spatial profiling of bacterial colonies, or analysis of contaminated surfaces. Further investigation of complementary analysis and imaging methods could provide additional data regarding multiple analyte types

Chapter 9

Conclusions and Further Work

This thesis has discussed the development and integration of MSI and SRS microscopy for the analysis of various biological sample types. The optimisation of individual methods for specific applications was presented, alongside the development of combined methods which aimed to provide a more complete analysis of the sample in addition to probing aspects of the fundamentals of surface sampling. Quantitative analysis has been a theme throughout the thesis, and assessment of both MSI and SRS as quantitative techniques has been presented. Issues surrounding the variation involved in these measurements have been identified and suggestions for improvements have been made – these include adjustments to data acquisition methods as well as sample preparation. The following chapter will discuss these in more detail; ideas for further work which could further improve the methods described and applications in which they might provide insight will also be outlined.

The use of MALDI MSI in combination with LESA MSI was presented in Chapter 3. This approach enabled the analysis of drugs, lipids and proteins from a single sample, which has applications for pharmaceutical research in which the distribution of a drug and associated endogenous molecules need to be simultaneously mapped. It was found that MALDI imaging of LESA sampled tissue allowed for the visualisation of sampled regions and revealed changes in distribution of analytes within them. Accurate measurement of these regions allowed variation and spatial precision of LESA sampling

to be assessed. Changes to surface chemistry within these regions were assessed by a number of multivariate analysis methods and provided an indication of how analyte distribution changed after LESA sampling, for example the distribution of different lipid adducts was altered. This information would be important if one wanted to combine the methods in a multimodal workflow – because it is not possible to obtain the same data by LESA MS after a matrix has been applied for MALDI.

A combined LESA and MALDI MSI method could have applications in a variety of situations. Tissue washing steps are a common sample preparation strategy during MSI analysis, however a thorough understanding of how washes affect and change the tissue, and whether these changes occur uniformly across the tissue remain unclear. Results obtained in both Chapter 3 and 5 of this work indicate that the same solvent system applied to different regions of brain and kidney tissue affect the tissue to different extents. This could have a profound effect on MSI results because false contrast could be introduced to ion images. The method could therefore be used both as a screen to identify the most effective washing solutions or protocols and also to understand uniformity of washing. As the uptake in liquid-based surface sampling increases the demand for robust and repeatable methods will also increase. The method could therefore also be used to assess the variability in sampling methods – tissue homogenates or samples of known uniformity could be used to assess such things. So far the use of LESA MS in combination with SRS has not been attempted. However the use of SRS methods outlined for use with MALDI could provide valuable information regarding LESA sampling effects – for example SRS images acquired before and after LESA could indicate how the sample has changed and how much of a particular analyte has been removed. Certain practical issues such as how to ensure that the same region has been imaged before and after could be resolved through the use of fiducial markers.

The use of SRS to study MALDI surface sampling effects was discussed in Chapter 4. The design of model samples which were compatible with both techniques was a major factor within this work. Matrix compounds are typically selected due to their high UV-Vis absorption properties which results in a tendency to undergo two-photon absorption under irradiation of the lasers used for SRS microscopy. This interference results in non-linear absorption effects. Nonetheless a suitable model sample was produced and it was found that SRS was able to visualise and quantify MALDI surface sampling. The number of molecules of analyte and matrix removed during MALDI analysis under varied laser conditions (both fluence and repetition rate) were measured. SRS and spontaneous Raman microscopy were used to investigate ion yields produced using two different matrix compounds under varied repetition rate. It was found that these data supported theories postulated in the literature about photomodification of cinnamic acid derivatives preventing efficient desorption/ionisation at higher laser repetition rates. The SRS imaging of analyte distribution in matrix crystals was also performed. It was found that SRS was able to visualise the distribution of lipids extracted from tissue into DHB matrix crystals. This would provide insight into optimal sample preparation methods. In addition the level of co-crystallisation of an analyte and matrix compound was imaged by SRS; it was found that the two compounds investigated in this work did not completely co-localise and hot-spots of analyte were found within matrix crystals.

Further work should aim to improve variability inherent in these methods which is at least in part due to sample preparation methods which produce inhomogeneous layers of crystals on glass. Investigation into other substrates should also be conducted because different wettabilities could aid in the formation of smaller droplets on the surface and result in smaller crystal sizes. Optimisation of spraying parameters could also improve crystal size and surface coverage – for example higher nebulising gas temperature.

Alternative matrix/analyte deposition methods could also be of use, sublimation has been shown to produce more uniform layers of compounds however more complicated methods would be required to measure the thickness of the deposited layer. The eventual goal of this method would be to examine MALDI MS methods used on tissue. SRS could be used to image a tissue sample before analysis, after matrix deposition to assess extraction efficiency and after MALDI MS to quantify amounts removed. This would allow for monitoring of every stage of the MALDI process and would help optimise the process as well as quantify ion yields. However, the complex sample type incorporating tissue, matrix and possibly a drug compound would be impossible to image using the current SRS set-up. It would be difficult to isolate specific signals in the complex fingerprint region of the Raman spectrum and therefore individual analytes could not be imaged with confidence.

A multimodal SRS, LESA and MALDI imaging method was presented in Chapter 5. SRS microscopy produced images with a pixel size of ~200 nm. Individual cells and cell nuclei were visualised in these images – it is not possible to do this using the MS techniques described in this work. LESA MS was used on the same tissue sample and it was possible to detect multiple drug compounds, various lipid species and proteins simultaneously. The pixel size in these images was ~700 μm and this was sufficient to distinguish between different tissue anatomies in the rat kidney. MALDI MSI was performed after LESA imaging and enabled the exact regions sampled by LESA to be determined. This enabled more accurate determination of the locations where each analyte was detected by LESA. The quantitative abilities of SRS were also investigated in a method designed to quantify erlotinib in rat kidney from a dosed animal. A calibration curve was produced from a sample of known composition before measurements were taken from dosed tissue. It was concluded that the background

intensity detected from tissue was too high to allow for accurate determination of erlotinib concentration in this experiment.

In further work the background signal from tissue could be further characterised in order to better understand whether SRS can be used to provide quantitative measurements of erlotinib in tissue. In order to establish whether the signal from erlotinib is real, an SRS spectrum surrounding the probed resonance frequency could be produced. If a peak occurs in the right place then it can be concluded that erlotinib has been detected. This approach would also enable the level of background to be determined.

LESA MS was evaluated as a quantitative tool in Chapter 6. The sensitivity and breadth of analytical applications possible with LESA make it an attractive tool for ambient analysis. The incorporation of an internal standard into mimetic tissue models was used to provide a calibration which accounted for extraction efficiency. This was found to produce good linearity and a value for the concentration of ubiquitin in tissue was found to be in agreement with a literature value. The variation observed in measurements tallied with instable electrospray and poor liquid microjunction stability. These parameters can be improved via optimisation of sampling parameters and could be one focus of further work.

Expansion of this work could include the assessment of a more complete workflow for the quantification of proteins in tissue samples. Labelled ubiquitin used in this work was acquired from Sigma Aldrich however it is possible to express labelled proteins by culture of genetically modified bacteria in isotopically-labelled media. This would enable researchers to tailor their experiment and quantify (in theory) any protein of interest.

In Chapter 7 the use of Flow-probe mass spectrometry for the imaging of biological tissue was discussed. The Flow-probe operates a similar mode of surface sampling to LESA but presents the opportunity for higher resolution and throughput imaging. This technique has the potential to provide similar data but with better spatial resolution, higher throughput and more cheaply due to the redundancy of certain consumable items. Data acquired by the Flow-probe were compared with LESA data and were found to be of a similar quality judging by the number and type of proteins detected. A number of the same proteins were detected by both methods for a range of tissues including brain, liver and kidney. For the first time a method was presented in which the Flow-probe was operated in raster mode and was found to provide equivalent protein data to that obtained using spot mode analysis.. An investigation into the potential spatial resolution of the Flow-probe was designed, however further work is required to fully characterise this. Experimental problems with reproducibility prevented firm conclusions being drawn about the usefulness of the Flow-probe operated in raster mode for tissue imaging.

In further work better characterisation of raster sampling would be necessary. The use of tissue homogenate samples could help answer questions about whether variation in signal observed by raster analysis is due to real spatial differences within the sample or separation or flow effects within the capillary. Raster mode sampling has the potential to provide improved throughput but exactly how fast data of sufficient quality can be acquired requires further experimentation. The optimisation of stage speed, flow rate of solvent and scan rate of the instrument will all be integral to this analysis.

In Chapter 8 the use of LESA MS for analysis of a different sample type was assessed. A novel method for the analysis, identification and imaging of intact proteins from living bacterial colonies under ambient conditions was developed. It was found that a

large number of proteins could be detected without sample preparation or modification. A number of these proteins were identified via top-down methods. The distribution of proteins and singly charged species was mapped by LESA MSI although the variation observed within these images requires further characterisation. One of the most significant problems with this method is electrospray instability; most likely due to residual bacteria adhered to the pipette tip. Methods to improve electrospray instability should be the focus of initial further work.

There are a number of applications in which this method could prove useful. If it were possible to identify microbial species via MS analysis – now routinely achieved via MALDI-TOF MS analysis – the method could be used to analyse contaminated surfaces *in situ*. For example this would be useful in hospitals or workplaces; of course this would bring into question the sensitivity of the technique because a much larger number of cells would be present in a cultured sample.

Multimodal methods of chemical imaging have been demonstrated to enhance analysis during the study of tissue samples. Using a different and complementary technique to image a bacterial sample after LESA could provide both additional biological information – such as confirmation of distribution of analytes – and also information about the reproducibility of the method. For example, optical imaging methods (confocal microscopy or SRS) could be used to image samples before and after LESA analysis and provide a measure of how much material has been removed and how that which remains has been changed. This would provide some guidance over the issue of how far the solvent spreads during analysis – this information is crucial for accurate determination of pixel size. Multimodal imaging of microbial samples was demonstrated by Baig *et al.* who used confocal Raman microscopy to guide targeted SIMS imaging of quinolone metabolites from *Pseudomonas aeruginosa*.[230] A high

resolution imaging technique such as SRS could also be capable of imaging individual bacterial cells. It is possible that such images could indicate how bacteria have been affected by sampling methods such as LESA or MALDI and could help ascertain whether the samples are still viable.

Work in this thesis has explored how chemical imaging methods could be used for improved analysis of biological samples with relevance to both pharmaceutical and biomedical research. Widespread applicability of such methods will help the field expand and become more universally useful. The expanding field of mass spectrometry imaging will require further validation of methods over the coming years. The increasing attention from clinical fields in particular will require large-scale validation studies making use of varied patient populations. Standardised methods and instrumentation will aid the problems associated with user-dependency. Aspects of both the fundamentals and applications of MSI and SRS have been explored and discussed. To summarise, further work should focus on the validation of described methods by repeat analysis, improvements to sample preparation and application of methods on novel sample types.

References

(1) de Hoffmann, E.; Stroobant, V. *Mass Spectrometry: Principles and Applications*; Wiley, 2007.

(2) Griffiths, J. *Anal. Chem* **2008**, *80*, 5678-5683.

(3) Karas, M.; Bachmann, D.; Bahr, U. e.; Hillenkamp, F. *International Journal of Mass Spectrometry and Ion Processes* **1987**, *78*, 53-68.

(4) Whitehouse, C. M.; Dreyer, R.; Yamashita, M.; Fenn, J. *Science* **1989**, *246*, 64-71.

(5) Bahr, U.; Karas, M.; Hillenkamp, F. *Fresenius' journal of analytical chemistry* **1994**, *348*, 783-791.

(6) Hillenkamp, F.; Karas, M.; Beavis, R. C.; Chait, B. T. *Analytical Chemistry* **1991**, *63*, 1193A-1203A.

(7) Zenobi, R.; Knochenmuss, R. *Mass Spectrometry Reviews* **1998**, *17*, 337-366.

(8) Knochenmuss, R.; Zenobi, R. *Chemical reviews* **2003**, *103*, 441-452.

(9) Knochenmuss, R. *Analyst* **2006**, *131*, 966-986.

(10) Steven, R. T.; Bunch, J. *Analytical and bioanalytical chemistry* **2013**, *405*, 4719-4728.

(11) Beavis, R. C.; Chait, B. T.; Fales, H. *Rapid Communications in Mass Spectrometry* **1989**, *3*, 432-435.

(12) Dreisewerd, K. *Analytical and bioanalytical chemistry* **2014**, *406*, 2261-2278.

(13) Griffiths, R. L.; Sarsby, J.; Guggenheim, E. J.; Race, A. M.; Steven, R. T.; Fear, J.; Lalor, P. F.; Bunch, J. *Analytical Chemistry* **2013**, *85*, 7146-7153.

(14) Khatib-Shahidi, S.; Andersson, M.; Herman, J. L.; Gillespie, T. A.; Caprioli, R. M. *Analytical Chemistry* **2006**, *78*, 6448-6456.

(15) Steven, R. T.; Race, A. M.; Bunch, J. *Journal of The American Society for Mass Spectrometry* **2013**, *24*, 801-804.

(16) Kussman, M.; Nordhoff, E.; Rahbek-Nielsen, H.; Haebel, S.; Rossel-Larsen, M.; Jakobsen, L.; Gobom, J.; Mirgorod-Skaya, E.; Kroll-Kristensen, A.; Palm, L. *J. Mass spectrum*, *32*, 593-601.

(17) Fuchs, B.; Süß, R.; Schiller, J. *Progress in lipid research* **2010**, *49*, 450-475.

(18) Nielen, M. W. *Mass Spectrometry Reviews* **1999**, *18*, 309-344.

(19) Steven, R. T.; Dexter, A.; Bunch, J. *Methods* **2016**.

(20) Groseclose, M. R.; Andersson, M.; Hardesty, W. M.; Caprioli, R. M. *Journal of Mass Spectrometry* **2007**, *42*, 254-262.

(21) Caprioli, R. M.; Farmer, T. B.; Gile, J. *Analytical Chemistry* **1997**, *69*, 4751-4760.

(22) Hankin, J. A.; Barkley, R. M.; Murphy, R. C. *Journal of The American Society for Mass Spectrometry* **2007**, *18*, 1646-1652.

(23) Kebarle, P.; Tang, L. *Analytical Chemistry* **1993**, *65*, 972A-986A.

(24) Gaskell, S. J. *Journal of mass spectrometry* **1997**, *32*, 677-688.

(25) Gomez, A.; Tang, K. *Physics of Fluids* **1994**, *6*, 404-414.

(26) Dole, M.; Mack, L.; Hines, R.; Mobley, R.; Ferguson, L.; Alice, M. d. *The Journal of Chemical Physics* **1968**, *49*, 2240-2249.

(27) Iribarne, J. V.; Thomson, B. A. *The Journal of Chemical Physics* **1976**, *64*, 2287-2294.

(28) Fenn, J. B. *Journal of The American Society for Mass Spectrometry* **1993**, *4*, 524-535.

(29) Douglas, D. J.; Frank, A. J.; Mao, D. *Mass spectrometry reviews* **2005**, *24*, 1-29.

(30) Makarov, A. *Analytical Chemistry* **2000**, *72*, 1156-1162.

(31) Hu, Q.; Noll, R. J.; Li, H.; Makarov, A.; Hardman, M.; Graham Cooks, R. *Journal of mass spectrometry* **2005**, *40*, 430-443.

(32) Casadonte, R.; Caprioli, R. M. *Nature protocols* **2011**, *6*, 1695-1709.

(33) Castellino, S.; Groseclose, M. R.; Wagner, D. *Bioanalysis* **2011**, *3*, 2427-2441.

(34) Chaurand, P.; Cornett, D. S.; Angel, P. M.; Caprioli, R. M. *Molecular & Cellular Proteomics* **2011**, *10*, O110. 004259.

(35) Cornett, D. S.; Frappier, S. L.; Caprioli, R. M. *Analytical Chemistry* **2008**, *80*, 5648-5653.

(36) Djidja, M.-C.; Claude, E.; Snel, M. F.; Francese, S.; Scriven, P.; Carolan, V.; Clench, M. R. *Analytical and bioanalytical chemistry* **2010**, *397*, 587-601.

(37) Mirnezami, R.; Spagou, K.; Vorkas, P.; Lewis, M.; Kinross, J.; Want, E.; Shion, H.; Goldin, R.; Darzi, A.; Takats, Z. *Molecular oncology* **2013**.

(38) Oppenheimer, S. R.; Mi, D.; Sanders, M. E.; Caprioli, R. M. *Journal of proteome research* **2010**, *9*, 2182-2190.

(39) Reyzer, M. L.; Chaurand, P.; Angel, P. M.; Caprioli, R. M. In *Mass Spectrometry Imaging*; Springer, 2010, pp 285-301.

(40) Seeley, E. H.; Caprioli, R. M. *Trends in biotechnology* **2011**, *29*, 136-143.

(41) Watrous, J. D.; Dorrestein, P. C. *Nature Reviews Microbiology* **2011**, *9*, 683-694.

(42) Bizzini, A.; Durussel, C.; Bille, J.; Greub, G.; Prod'hom, G. *Journal of clinical microbiology* **2010**, *48*, 1549-1554.

(43) Kai, M.; González, I.; Genilloud, O.; Singh, S. B.; Svatoš, A. *Rapid Communications in Mass Spectrometry* **2012**, *26*, 2477-2482.

(44) Latimer, J.; Stokes, S. L.; Graham, A. I.; Bunch, J.; Jackson, R. J.; McLeod, C. W.; Poole, R. K. *Journal of microbiological methods* **2009**, *79*, 329-335.

(45) Watrous, J.; Hendricks, N.; Meehan, M.; Dorrestein, P. C. *Analytical Chemistry* **2010**, *82*, 1598-1600.

(46) Tyler, B. J.; Rangaranjan, S.; Möller, J.; Arlinghaus, H. F. *Applied surface science* **2006**, *252*, 6712-6715.

(47) Vaidyanathan, S.; Fletcher, J. S.; Goodacre, R.; Lockyer, N. P.; Micklefield, J.; Vickerman, J. C. *Analytical Chemistry* **2008**, *80*, 1942-1951.

(48) Liu, W.-T.; Yang, Y.-L.; Xu, Y.; Lamsa, A.; Haste, N. M.; Yang, J. Y.; Ng, J.; Gonzalez, D.; Ellermeier, C. D.; Straight, P. D.; Pevzner, P. A.; Pogliano, J.; Nizet, V.;

Pogliano, K.; Dorrestein, P. C. *Proceedings of the National Academy of Sciences* **2010**, *107*, 16286-16290.

(49) Hsu, C.-C.; ElNaggar, M. S.; Peng, Y.; Fang, J.; Sanchez, L. M.; Mascuch, S. J.; Møller, K. A.; Alazzeh, E. K.; Pikula, J.; Quinn, R. A. *Analytical Chemistry* **2013**, *85*, 7014-7018.

(50) Kaspar, S.; Peukert, M.; Svatos, A.; Matros, A.; Mock, H. P. *Proteomics* **2011**, *11*, 1840-1850.

(51) Tanaka, K.; Waki, H.; Ido, Y.; Akita, S.; Yoshida, Y.; Yoshida, T.; Matsuo, T. *Rapid communications in mass spectrometry* **1988**, *2*, 151-153.

(52) Hanton, S. D.; Hyder, I. Z.; Stets, J. R.; Owens, K. G.; Blair, W. R.; Guttman, C. M.; Giuseppetti, A. A. *Journal of The American Society for Mass Spectrometry* **2004**, *15*, 168-179.

(53) McEwen, C. N.; Jackson, C.; Larsen, B. S. *International journal of mass spectrometry and ion processes* **1997**, *160*, 387-394.

(54) Chaurand, P. *Journal of Proteomics* **2012**, *75*, 4883-4892.

(55) Reyzer, M. L.; Caprioli, R. M. *Mass Spectrometry for Drug Discovery and Drug Development* **2012**, 277-302.

(56) Zemski Berry, K. A.; Hankin, J. A.; Barkley, R. M.; Spraggins, J. M.; Caprioli, R. M.; Murphy, R. C. *Chemical reviews* **2011**, *111*, 6491-6512.

(57) Marvin, L. F.; Roberts, M. A.; Fay, L. B. *Clinica chimica acta* **2003**, *337*, 11-21.

(58) Gustafsson, J. O.; Oehler, M. K.; Ruszkiewicz, A.; McColl, S. R.; Hoffmann, P. *International journal of molecular sciences* **2011**, *12*, 773-794.

(59) Steurer, S.; Borkowski, C.; Odinga, S.; Buchholz, M.; Koop, C.; Huland, H.; Becker, M.; Witt, M.; Trede, D.; Omidi, M. *International Journal of Cancer* **2013**, *133*, 920-928.

(60) Pierson, J.; Norris, J. L.; Aerni, H.-R.; Svenningsson, P.; Caprioli, R. M.; Andrén, P. E. *Journal of proteome research* **2004**, *3*, 289-295.

(61) Kriegsmann, J.; Kriegsmann, M.; Casadonte, R. *International journal of oncology* **2015**, *46*, 893-906.

(62) Longuespée, R.; Casadonte, R.; Kriegsmann, M.; Pottier, C.; Muller, G. P.; Delvenne, P.; Kriegsmann, J.; Pauw, E. *PROTEOMICS-Clinical Applications* **2016**.

(63) Aichler, M.; Walch, A. *Laboratory Investigation* **2015**, *95*, 422-431.

(64) Trim, P. J.; Djidja, M.-C.; Atkinson, S. J.; Oakes, K.; Cole, L. M.; Anderson, D. M.; Hart, P. J.; Francese, S.; Clench, M. R. *Analytical and bioanalytical chemistry* **2010**, *397*, 3409-3419.

(65) Gessel, M. M.; Norris, J. L.; Caprioli, R. M. *Journal of proteomics* **2014**, *107*, 71-82.

(66) Jurchen, J. C.; Rubakhin, S. S.; Sweedler, J. V. *Journal of The American Society for Mass Spectrometry* **2005**, *16*, 1654-1659.

(67) Zavalin, A.; Todd, E. M.; Rawhouser, P. D.; Yang, J.; Norris, J. L.; Caprioli, R. M. *Journal of Mass Spectrometry* **2012**, *47*, 1473-1481.

(68) Guenther, S.; Römpp, A.; Kummer, W.; Spengler, B. *International Journal of Mass Spectrometry* **2011**, *305*, 228-237.

(69) Prideaux, B.; Stoeckli, M. *Journal of Proteomics* **2012**, *75*, 4999-5013.

(70) Reich, R. F.; Cudzilo, K.; Levisky, J. A.; Yost, R. A. *Journal of The American Society for Mass Spectrometry* **2010**, *21*, 564-571.

(71) Deininger, S.-O.; Cornett, D. S.; Paape, R.; Becker, M.; Pineau, C.; Rauser, S.; Walch, A.; Wolski, E. *Analytical and bioanalytical chemistry* **2011**, *401*, 167-181.

(72) Reyzer, M. L.; Hsieh, Y.; Ng, K.; Korfmacher, W. A.; Caprioli, R. M. *Journal of mass spectrometry* **2003**, *38*, 1081-1092.

(73) Groseclose, M. R.; Castellino, S. *Analytical Chemistry* **2013**, *85*, 10099-10106.

(74) Hsieh, Y.; Casale, R.; Fukuda, E.; Chen, J.; Knemeyer, I.; Wingate, J.; Morrison, R.; Korfmacher, W. *Rapid Communications in Mass Spectrometry* **2006**, *20*, 965-972.

(75) Hamm, G.; Bonnel, D.; Legouffe, R.; Pamelard, F.; Delbos, J.-M.; Bouzom, F.; Stauber, J. *Journal of proteomics* **2012**, *75*, 4952-4961.

(76) Pirman, D. A.; Yost, R. A. *Analytical Chemistry* **2011**, *83*, 8575-8581.

(77) Römpp, A.; Both, J.-P.; Brunelle, A.; Heeren, R. M.; Laprévote, O.; Prideaux, B.; Seyer, A.; Spengler, B.; Stoeckli, M.; Smith, D. F. *Analytical and bioanalytical chemistry* **2015**, *407*, 2329-2335.

(78) McDonnell, L. A.; Heeren, R. M.; Andrén, P. E.; Stoeckli, M.; Corthals, G. L. *Journal of proteomics* **2012**, *75*, 5113-5121.

(79) Schramm, T.; Hester, A.; Klinkert, I.; Both, J.-P.; Heeren, R. M.; Brunelle, A.; Laprévote, O.; Desbenoit, N.; Robbe, M.-F.; Stoeckli, M. *Journal of proteomics* **2012**, *75*, 5106-5110.

(80) Race, A. M.; Styles, I. B.; Bunch, J. *Journal of proteomics* **2012**, *75*, 5111-5112.

(81) Takáts, Z.; Wiseman, J. M.; Gologan, B.; Cooks, R. G. *Science* **2004**, *306*, 471-473.

(82) Wiseman, J. M.; Ifa, D. R.; Song, Q.; Cooks, R. G. *Angewandte Chemie International Edition* **2006**, *45*, 7188-7192.

(83) Wiseman, J. M.; Ifa, D. R.; Zhu, Y.; Kissinger, C. B.; Manicke, N. E.; Kissinger, P. T.; Cooks, R. G. *Proceedings of the National Academy of Sciences* **2008**, *105*, 18120-18125.

(84) Wiseman, J. M.; Puolitaival, S. M.; Takáts, Z.; Cooks, R. G.; Caprioli, R. M. *Angewandte Chemie* **2005**, *117*, 7256-7259.

(85) Cooks, R. G.; Manicke, N. E.; Dill, A. L.; Ifa, D. R.; Eberlin, L. S.; Costa, A. B.; Wang, H.; Huang, G.; Ouyang, Z. *Faraday discussions* **2011**, *149*, 247-267.

(86) Eberlin, L. S.; Liu, X.; Ferreira, C. R.; Santagata, S.; Agar, N. Y. R.; Cooks, R. G. *Analytical Chemistry* **2011**, *83*, 8366-8371.

(87) Watrous, J.; Roach, P.; Heath, B.; Alexandrov, T.; Laskin, J.; Dorrestein, P. C. *Analytical Chemistry* **2013**, *85*, 10385-10391.

(88) Ifa, D.; Gumaelius, L.; Eberlin, L.; Manicke, N.; Cooks, R. *Analyst* **2007**, *132*, 461-467.

(89) Jackson, A. T.; Williams, J. P.; Scrivens, J. H. *Rapid communications in mass spectrometry* **2006**, *20*, 2717-2727.

(90) Wu, C.; Ifa, D. R.; Manicke, N. E.; Cooks, R. G. *Analyst* **2010**, *135*, 28-32.

(91) Eberlin, L. S.; Dill, A. L.; Costa, A. B.; Ifa, D. R.; Cheng, L.; Masterson, T.; Koch, M.; Ratliff, T. L.; Cooks, R. G. *Analytical Chemistry* **2010**, *82*, 3430-3434.

(92) Eberlin, L. S.; Norton, I.; Dill, A. L.; Golby, A. J.; Ligon, K. L.; Santagata, S.; Cooks, R. G.; Agar, N. Y. R. *Cancer Research* **2012**, *72*, 645-654.

(93) Zhang, J. I.; Talaty, N.; Costa, A. B.; Xia, Y.; Tao, W. A.; Bell, R.; Callahan, J. H.; Cooks, R. G. *International Journal of Mass Spectrometry* **2011**, *301*, 37-44.

(94) Kertesz, V.; Van Berkel, G. J. *Analytical Chemistry* **2008**, *80*, 1027-1032.

(95) Green, F.; Stokes, P.; Hopley, C.; Seah, M.; Gilmore, I.; O'Connor, G. *Analytical Chemistry* **2009**, *81*, 2286-2293.

(96) Green, F.; Salter, T.; Gilmore, I.; Stokes, P.; O'Connor, G. *Analyst* **2010**, *135*, 731-737.

(97) Abbassi-Ghadi, N.; Jones, E. A.; Veselkov, K. A.; Huang, J.; Kumar, S.; Strittmatter, N.; Golf, O.; Kudo, H.; Goldin, R. D.; Hanna, G. B.; Takats, Z. *Analytical Methods* **2015**.

(98) Tillner, J.; McKenzie, J. S.; Jones, E. A.; Speller, A. V.; Walsh, J. L.; Veselkov, K. A.; Bunch, J.; Takats, Z.; Gilmore, I. S. *Analytical Chemistry* **2016**, *88*, 4808-4816.

(99) Van Berkel, G. J.; Sanchez, A. D.; Quirke, J. M. E. *Analytical Chemistry* **2002**, *74*, 6216-6223.

(100) Kertesz, V.; Van Berkel, G. J. *Journal of mass spectrometry* **2010**, *45*, 252-260.

(101) Van Berkel, G. J.; Kertesz, V.; Koeplinger, K. A.; Vavrek, M.; Kong, A. N. T. *Journal of mass spectrometry* **2008**, *43*, 500-508.

(102) Sarsby, J.; Griffiths, R. L.; Race, A. M.; Bunch, J.; Randall, E. C.; Creese, A. J.; Cooper, H. J. *Analytical Chemistry* **2015**, *87*, 6794-6800.

(103) Martin, N.; Bunch, J.; Cooper, H. *Journal of The American Society for Mass Spectrometry* **2013**, *24*, 1242-1249.

(104) Edwards, R.; Griffiths, P.; Bunch, J.; Cooper, H. *Journal of The American Society for Mass Spectrometry* **2012**, *23*, 1921-1930.

(105) Edwards, R. L.; Creese, A. J.; Baumert, M.; Griffiths, P.; Bunch, J.; Cooper, H. J. *Analytical Chemistry* **2011**, *83*, 2265-2270.

(106) Griffiths, R. L.; Cooper, H. J. *Analytical Chemistry* **2015**, *88*, 606-609.

(107) Martin, N. J.; Griffiths, R. L.; Edwards, R. L.; Cooper, H. J. *Journal of The American Society for Mass Spectrometry* **2015**, *26*, 1320-1327.

(108) Randall, E. C.; Bunch, J.; Cooper, H. J. *Analytical Chemistry* **2014**, *86*, 10504-10510.

(109) Sarsby, J.; Martin, N. J.; Lalor, P. F.; Bunch, J.; Cooper, H. J. *Journal of The American Society for Mass Spectrometry* **2014**, *25*, 1953-1961.

(110) Schey, K. L.; Anderson, D. M.; Rose, K. L. *Analytical Chemistry* **2013**, *85*, 6767-6774.

(111) Cui, W.; Rohrs, H. W.; Gross, M. L. *Analyst* **2011**, *136*, 3854-3864.

(112) Kertesz, V.; Van Berkel, G. J. *Analytical Chemistry* **2010**, *82*, 5917-5921.

(113) Van Berkel, G. J.; Kertesz, V. *Rapid Communications in Mass Spectrometry* **2013**, *27*, 1329-1334.

(114) Prideaux, B.; ElNaggar, M. S.; Zimmerman, M.; Wiseman, J. M.; Li, X.; Dartois, V. *International journal of mass spectrometry* **2015**, *377*, 699-708.

(115) S ElNaggar, M.; Prideaux, B.; Dartois, V.; M Wiseman, J. *Current Metabolomics* **2014**, *2*, 122-131.

(116) ElNaggar, M. S.; Van Berkel, G. J. *Journal of The American Society for Mass Spectrometry* **2011**, *22*, 1737-1743.

(117) Gaissmaier, T.; Siebenhaar, M.; Todorova, V.; Hüllen, V.; Hopf, C. *Analyst* **2016**, *141*, 892-901.

(118) Raman, C. V.; Krishnan, K. S. *Nature* **1928**, *121*, 711.

(119) Colthup, N. *Introduction to infrared and Raman spectroscopy*; Elsevier, 2012.

(120) Atkins, P. *Shriver and Atkins' inorganic chemistry*; Oxford University Press, USA, 2010.

(121) Evans, C. L.; Xie, X. S. *Annu. Rev. Anal. Chem.* **2008**, *1*, 883-909.

(122) Rae, A.; Stosch, R.; Klapetek, P.; Hight Walker, A. R.; Roy, D. *Methods* **2014**.

(123) Freudiger, C. W.; Min, W.; Saar, B. G.; Lu, S.; Holtom, G. R.; He, C.; Tsai, J. C.; Kang, J. X.; Xie, X. S. *Science* **2008**, *322*, 1857-1861.

(124) Cheng, J.-X.; Xie, X. S. *Science* **2015**, *350*, aaa8870.

(125) Evans, C. L.; Xie, X. S. *Annual Review of Analytical Chemistry* **2008**, *1*, 883-909.

(126) Saar, B. G.; Freudiger, C. W.; Reichman, J.; Stanley, C. M.; Holtom, G. R.; Xie, X. S. *Science* **2010**, *330*, 1368-1370.

(127) Fu, D.; Lu, F.-K.; Zhang, X.; Freudiger, C.; Pernik, D. R.; Holtom, G.; Xie, X. S. *Journal of the American Chemical Society* **2012**, *134*, 3623-3626.

(128) Fu, D.; Zhou, J.; Zhu, W. S.; Manley, P. W.; Wang, Y. K.; Hood, T.; Wylie, A.; Xie, X. S. *Nature chemistry* **2014**, *6*, 614-622.

(129) Zhang, X.; Roeffaers, M. B. J.; Basu, S.; Daniele, J. R.; Fu, D.; Freudiger, C. W.; Holtom, G. R.; Xie, X. S. *ChemPhysChem* **2012**, *13*, 1054-1059.

(130) Ji, M.; Lewis, S.; Camelo-Piragua, S.; Ramkissoon, S. H.; Snuderl, M.; Venneti, S.; Fisher-Hubbard, A.; Garrard, M.; Fu, D.; Wang, A. C. *Science translational medicine* **2015**, *7*, 309ra163-309ra163.

(131) Ji, M.; Orringer, D. A.; Freudiger, C. W.; Ramkissoon, S.; Liu, X.; Lau, D.; Golby, A. J.; Norton, I.; Hayashi, M.; Agar, N. Y. *Science translational medicine* **2013**, *5*, 201ra119-201ra119.

(132) Lu, F.-K.; Basu, S.; Igras, V.; Hoang, M. P.; Ji, M.; Fu, D.; Holtom, G. R.; Neel, V. A.; Freudiger, C. W.; Fisher, D. E. *Proceedings of the National Academy of Sciences* **2015**, *112*, 11624-11629.

(133) Ozeki, Y.; Umemura, W.; Otsuka, Y.; Satoh, S.; Hashimoto, H.; Sumimura, K.; Nishizawa, N.; Fukui, K.; Itoh, K. *Nature Photonics* **2012**, *6*, 845-851.

(134) Wei, L.; Yu, Y.; Shen, Y.; Wang, M. C.; Min, W. *Proceedings of the National Academy of Sciences* **2013**, *110*, 11226-11231.

(135) Clay, G. O.; Schaffer, C. B.; Kleinfeld, D. *Journal of Chemical Physics* **2007**, *126*, 25102-26100.

(136) Mansfield, J. C.; Littlejohn, G. R.; Seymour, M. P.; Lind, R. J.; Perfect, S.; Moger, J. *Analytical Chemistry* **2013**, *85*, 5055-5063.

(137) Petit, V. W.; Réfrégiers, M.; Guettier, C.; Jamme, F. d. r.; Sebanayakam, K.; Brunelle, A.; Laprévote, O.; Dumas, P.; Le Naour, F. o. *Analytical Chemistry* **2010**, *82*, 3963-3968.

(138) Jungmann, J. H.; Heeren, R. M. *Journal of proteomics* **2012**, *75*, 5077-5092.

(139) Chughtai, S.; Chughtai, K.; Cillero-Pastor, B.; Kiss, A.; Agrawal, P.; MacAleese, L.; Heeren, R. M. *International Journal of Mass Spectrometry* **2012**, *325*, 150-160.

(140) van Hove, E. R. A.; Blackwell, T. R.; Klinkert, I.; Eijkel, G. B.; Heeren, R. M.; Glunde, K. *Cancer research* **2010**, *70*, 9012-9021.

(141) Fournier, I.; Tabet, J.; Bolbach, G. *International Journal of Mass Spectrometry* **2002**, *219*, 515-523.

(142) Tarzi, O. I.; Nonami, H.; Erra-Balsells, R. *Journal of mass spectrometry* **2009**, *44*, 260-277.

(143) Leisner, A.; Rohlfing, A.; Röhling, U.; Dreisewerd, K.; Hillenkamp, F. *The Journal of Physical Chemistry B* **2005**, *109*, 11661-11666.

(144) Soltwisch, J.; Jaskolla, T. W.; Dreisewerd, K. *Journal of The American Society for Mass Spectrometry* **2013**, *24*, 1477-1488.

(145) Dai, Y.; Whittal, R. M.; Li, L. *Analytical Chemistry* **1996**, *68*, 2494-2500.

(146) Horneffer, V.; Forsmann, A.; Strupat, K.; Hillenkamp, F.; Kubitscheck, U. *Analytical Chemistry* **2001**, *73*, 1016-1022.

(147) Horneffer, V.; Reichelt, R.; Strupat, K. *International Journal of Mass Spectrometry* **2003**, *226*, 117-131.

(148) Passarelli, M. K.; Wang, J.; Mohammadi, A. S.; Trouillon, R. l.; Gilmore, I.; Ewing, A. G. *Analytical Chemistry* **2014**, *86*, 9473-9480.

(149) Körsgen, M.; Pelster, A.; Dreisewerd, K.; Arlinghaus, H. F. *Journal of The American Society for Mass Spectrometry* **2016**, *27*, 277-284.

(150) Marshall, P.; Toteu-Djomte, V.; Bareille, P.; Perry, H.; Brown, G.; Baumert, M.; Biggadike, K. *Analytical Chemistry* **2010**, *82*, 7787-7794.

(151) Quanico, J.; Franck, J.; Dauly, C.; Strupat, K.; Dupuy, J.; Day, R.; Salzet, M.; Fournier, I.; Wisztorski, M. *Journal of proteomics* **2013**, *79*, 200-218.

(152) Tomlinson, L.; Fuchser, J.; Fütterer, A.; Baumert, M.; Hassall, D. G.; West, A.; Marshall, P. S. *Rapid communications in mass spectrometry* **2014**, *28*, 995-1003.

(153) Swales, J. G.; Tucker, J. W.; Strittmatter, N.; Nilsson, A.; Cobice, D.; Clench, M. R.; Mackay, C. L.; Andren, P. E.; Takáts, Z.; Webborn, P. J. *Analytical Chemistry* **2014**, *86*, 8473-8480.

(154) Garrett, T. J.; Prieto-Conaway, M. C.; Kovtoun, V.; Bui, H.; Izgarian, N.; Stafford, G.; Yost, R. A. *International Journal of Mass Spectrometry* **2007**, *260*, 166-176.

(155) Eijkel, G. B.; Kükrer Kaletaş, B.; van der Wiel, I. M.; Kros, J. M.; Luider, T. M.; Heeren, R. M. A. *Surface and Interface Analysis* **2009**, *41*, 675-685.

(156) Cross, S. A.; Groves, A.; Hesselbo, T. *The International journal of applied radiation and isotopes* **1974**, *25*, 381-382.

(157) Eikel, D.; Vavrek, M.; Smith, S.; Bason, C.; Yeh, S.; Korfmacher, W. A.; Henion, J. D. *Rapid Communications in Mass Spectrometry* **2011**, *25*, 3587-3596.

(158) Sunkin, S. M.; Ng, L.; Lau, C.; Dolbeare, T.; Gilbert, T. L.; Thompson, C. L.; Hawrylycz, M.; Dang, C. *Nucleic acids research* **2013**, *41*, D996-D1008.

(159) Blair, J. M. A.; Webber, M. A.; Baylay, A. J.; Ogbolu, D. O.; Piddock, L. J. V. *Nat Rev Micro* **2015**, *13*, 42-51.

(160) Forum, W. E., Ed., 2015.

(161) Forum, W. E., Ed., 2013.

(162) Forum, W. E., Ed., 2014.

(163) Lanekoff, I.; Geydebrekht, O.; Pinchuk, G. E.; Konopka, A. E.; Laskin, J. *Analyst* **2013**, *138*, 1971-1978.

(164) Moree, W. J.; Phelan, V. V.; Wu, C.-H.; Bandeira, N.; Cornett, D. S.; Duggan, B. M.; Dorrestein, P. C. *Proceedings of the National Academy of Sciences* **2012**, *109*, 13811-13816.

(165) Egertson, J. D.; Kuehn, A.; Merrihew, G. E.; Bateman, N. W.; MacLean, B. X.; Ting, Y. S.; Canterbury, J. D.; Marsh, D. M.; Kellmann, M.; Zabrouskov, V. *Nature Methods* **2013**, *10*, 744-746.

(166) Race, A. M.; Steven, R. T.; Palmer, A. D.; Styles, I. B.; Bunch, J. *Analytical Chemistry* **2013**, *85*, 3071-3078.

(167) Van Der Maaten, L. *The Journal of Machine Learning Research* **2014**, *15*, 3221-3245.

(168) El-Mashtoly, S. F.; Petersen, D.; Yosef, H. K.; Mosig, A.; Reinacher-Schick, A.; Kötting, C.; Gerwert, K. *Analyst* **2014**, *139*, 1155-1161.

(169) Marko-Varga, G.; Fehniger, T. E.; Rezeli, M.; Döme, B.; Laurell, T.; Végvári, Á. *Journal of proteomics* **2011**, *74*, 982-992.

(170) Signor, L.; Varesio, E.; Staack, R. F.; Starke, V.; Richter, W. F.; Hopfgartner, G. *Journal of mass spectrometry* **2007**, *42*, 900-909.

(171) Orkoula, M.; Kontoyannis, C.; Markopoulou, C.; Koundourellis, J. *Talanta* **2007**, *73*, 258-261.

(172) Passarelli, M. K.; Newman, C. F.; Marshall, P. S.; West, A.; Gilmore, I. S.; Bunch, J.; Alexander, M. R.; Dollery, C. T. *Analytical Chemistry* **2015**, *87*, 6696-6702.

(173) Prideaux, B.; Dartois, V.; Staab, D.; Weiner, D. M.; Goh, A.; Via, L. E.; Barry III, C. E.; Stoeckli, M. *Analytical Chemistry* **2011**, *83*, 2112-2118.

(174) Duan, J.; Vogt, F. G.; Li, X.; Hayes Jr, D.; Mansour, H. M. *International journal of nanomedicine* **2013**, *8*, 3489.

(175) Schriemer, D. C.; Li, L. *Analytical Chemistry* **1996**, *68*, 2721-2725.

(176) Källback, P.; Shariatgorji, M.; Nilsson, A.; Andrén, P. E. *Journal of proteomics* **2012**, *75*, 4941-4951.

(177) Nilsson, A.; Fehniger, T. E.; Gustavsson, L.; Andersson, M.; Kenne, K.; Marko-Varga, G.; Andrén, P. E. *PloS one* **2010**, *5*, e11411.

(178) Goodwin, R. J.; Nilsson, A.; Borg, D.; Langridge-Smith, P. R.; Harrison, D. J.; Mackay, C. L.; Iverson, S. L.; Andrén, P. E. *Journal of proteomics* **2012**, *75*, 4912-4920.

(179) Römpp, A.; Guenther, S.; Takats, Z.; Spengler, B. *Analytical and bioanalytical chemistry* **2011**, *401*, 65-73.

(180) Kertesz, V.; Van Berkel, G. J.; Vavrek, M.; Koeplinger, K. A.; Schneider, B. B.; Covey, T. R. *Analytical Chemistry* **2008**, *80*, 5168-5177.

(181) Nemes, P.; Vertes, A. *Analytical Chemistry* **2007**, *79*, 8098-8106.

(182) Crecelius, A. C.; Cornett, D. S.; Caprioli, R. M.; Williams, B.; Dawant, B. M.; Bodenheimer, B. *Journal of The American Society for Mass Spectrometry* **2005**, *16*, 1093-1099.

(183) Chinthaka, S.; Rodgers, M. *Journal of The American Society for Mass Spectrometry* **2012**, *23*, 676-689.

(184) Batoy, S.; Akhmetova, E.; Miladinovic, S.; Smeal, J.; Wilkins, C. *Applied Spectroscopy Reviews* **2008**, *43*, 485-550.

(185) Demeure, K.; Quinton, L.; Gabelica, V.; De Pauw, E. *Analytical Chemistry* **2007**, *79*, 8678-8685.

(186) Thomas, A. l.; Charbonneau, J. L.; Fournaise, E.; Chaurand, P. *Analytical Chemistry* **2012**, *84*, 2048-2054.

(187) Carter, C. L.; McLeod, C. W.; Bunch, J. *Journal of The American Society for Mass Spectrometry* **2011**, *22*, 1991-1998.

(188) Fonville, J. M.; Carter, C. L.; Pizarro, L.; Steven, R. T.; Palmer, A. D.; Griffiths, R. L.; Lalor, P. F.; Lindon, J. C.; Nicholson, J. K.; Holmes, E. *Analytical Chemistry* **2013**, *85*, 1415-1423.

(189) Ehring, H.; Costa, C.; Demirev, P. A.; Sundqvist, B. U. *Rapid communications in mass spectrometry* **1996**, *10*, 821-824.

(190) Porta, T.; Grivet, C.; Knochenmuss, R.; Varesio, E.; Hopfgartner, G. *Journal of Mass Spectrometry* **2011**, *46*, 144-152.

(191) Steven, R. T.; Race, A. M.; Bunch, J. *Journal of The American Society for Mass Spectrometry* **2016**, 1-10.

(192) Qiao, H.; Spicer, V.; Ens, W. *Rapid Communications in Mass Spectrometry* **2008**, *22*, 2779-2790.

(193) Dreisewerd, K.; Schürenberg, M.; Karas, M.; Hillenkamp, F. *International Journal of Mass Spectrometry and Ion Processes* **1995**, *141*, 127-148.

(194) Guenther, S.; Koestler, M.; Schulz, O.; Spengler, B. *International Journal of Mass Spectrometry* **2010**, *294*, 7-15.

(195) Dreisewerd, K. *Chemical reviews* **2003**, *103*, 395-426.

(196) Knochenmuss, R.; Zhigilei, L. V. *Journal of mass spectrometry* **2010**, *45*, 333-346.

(197) Steven, R. T.; Palmer, A. D.; Bunch, J. *Journal of The American Society for Mass Spectrometry* **2013**, *24*, 1146-1152.

(198) Holle, A.; Haase, A.; Kayser, M.; Hoehndorf, J. *Journal of Mass Spectrometry* **2006**, *41*, 705-716.

(199) Rohlfing, A.; Menzel, C.; Kukreja, L. M.; Hillenkamp, F.; Dreisewerd, K. *The Journal of Physical Chemistry B* **2003**, *107*, 12275-12286.

(200) Fournier, I.; Beavis, R.; Blais, J.; Tabet, J.; Bolbach, G. *International journal of mass spectrometry and ion processes* **1997**, *169*, 19-29.

(201) Hoyer, T.; Tuszynski, W.; Lienau, C. *Chemical physics letters* **2007**, *443*, 107-112.

(202) Ghosh, M.; Chakrabarti, S.; Misra, T. *Journal of Raman spectroscopy* **1998**, *29*, 263-267.

(203) *Nat Immunol* **2010**, *11*, 971-971.

(204) Bass, A. S.; Cartwright, M. E.; Mahon, C.; Morrison, R.; Snyder, R.; McNamara, P.; Bradley, P.; Zhou, Y.-Y.; Hunter, J. *Journal of pharmacological and toxicological methods* **2009**, *60*, 69-78.

(205) Berman, J.; Halm, K.; Adkison, K.; Shaffer, J. *Journal of medicinal chemistry* **1997**, *40*, 827-829.

(206) Yates, J. R.; Ruse, C. I.; Nakorchevsky, A. *Annual review of biomedical engineering* **2009**, *11*, 49-79.

(207) Bantscheff, M.; Schirle, M.; Sweetman, G.; Rick, J.; Kuster, B. *Analytical and bioanalytical chemistry* **2007**, *389*, 1017-1031.

(208) Han, D. K.; Eng, J.; Zhou, H.; Aebersold, R. *Nature biotechnology* **2001**, *19*, 946-951.

(209) Wiese, S.; Reidegeld, K. A.; Meyer, H. E.; Warscheid, B. *Proteomics* **2007**, *7*, 340-350.

(210) Reyzer, M. L.; Hsieh, Y.; Ng, K.; Korfmacher, W. A.; Caprioli, R. M. *Journal of Mass Spectrometry* **2003**, *38*, 1081-1092.

(211) Bergman, H.-M.; Lundin, E.; Andersson, M.; Lanekoff, I. *Analyst* **2016**, *141*, 3686-3695.

(212) Vismeh, R.; Waldon, D. J.; Teffera, Y.; Zhao, Z. *Analytical Chemistry* **2012**, *84*, 5439-5445.

(213) Kaiser, S. E.; Riley, B. E.; Shaler, T. A.; Trevino, R. S.; Becker, C. H.; Schulman, H.; Kopito, R. R. *Nature methods* **2011**, *8*, 691-696.

(214) Hsu, C.-C.; Chou, P.-T.; Zare, R. N. *Analytical Chemistry* **2015**, *87*, 11171-11175.

(215) Sarsby, J. *Liquid micro-junction surface sampling and MALDI imaging of small and large molecules in human liver disease*. University of Birmingham2016.

(216) Anhalt, J. P.; Fenselau, C. *Analytical Chemistry* **1975**, *47*, 219-225.

(217) Seng, P.; Drancourt, M.; Gouriet, F.; La Scola, B.; Fournier, P.-E.; Rolain, J. M.; Raoult, D. *Clinical Infectious Diseases* **2009**, *49*, 543-551.

(218) Saffert, R. T.; Cunningham, S. A.; Ihde, S. M.; Jobe, K. E. M.; Mandrekar, J.; Patel, R. *Journal of clinical microbiology* **2011**, *49*, 887-892.

(219) Holzlechner, M.; Reitschmidt, S.; Gruber, S.; Zeilinger, S.; Marchetti-Deschmann, M. *Proteomics* **2016**.

(220) McFarland, M. A.; Andrzejewski, D.; Musser, S. M.; Callahan, J. H. *Analytical Chemistry* **2014**.

(221) Li, B.; Comi, T. J.; Si, T.; Dunham, S. J.; Sweedler, J. V. *Journal of Mass Spectrometry* **2016**.

(222) Angolini, C. l. F. F.; Vendramini, P. H.; Araújo, F. D.; Araújo, W. L.; Augusti, R.; Eberlin, M. N.; de Oliveira, L. G. *Analytical Chemistry* **2015**, *87*, 6925-6930.

(223) Tata, A.; Perez, C.; Campos, M. L.; Bayfield, M. A.; Eberlin, M. N.; Ifa, D. R. *Analytical Chemistry* **2015**, *87*, 12298-12305.

(224) Kano, Y.; Osato, K.; Wada, M.; Imamoto, F. *Molecular and General Genetics MGG* **1987**, *209*, 408-410.

(225) Göransson, M.; Sondén, B.; Nilsson, P.; Dagberg, B.; Foreman, K.; Emanuelsson, K.; Uhlin, B. E. **1990**.

(226) Link, A. J.; Phillips, D.; Church, G. M. *Journal of Bacteriology* **1997**, *179*, 6228-6237.

(227) Phadtare, S.; Alsina, J.; Inouye, M. *Current opinion in microbiology* **1999**, *2*, 175-180.

(228) Zhang, X.-S.; García-Contreras, R.; Wood, T. K. *Journal of Bacteriology* **2007**, *189*, 3051-3062.

(229) Zamdborg, L.; LeDuc, R. D.; Glowacz, K. J.; Kim, Y.-B.; Viswanathan, V.; Spaulding, I. T.; Early, B. P.; Bluhm, E. J.; Babai, S.; Kelleher, N. L. *Nucleic acids research* **2007**, *35*, W701-W706.

(230) Baig, N. F.; Dunham, S. J.; Morales-Soto, N.; Shrout, J. D.; Sweedler, J. V.; Bohn, P. W. *Analyst* **2015**, *140*, 6544-6552.

Appendices

Appendix 1: Randall, E. C.; Race, A. M.; Cooper, H. J.; Bunch, J. *Analytical Chemistry* **2016**, 88, 8433-8440.

analytical chemistry

MALDI Imaging of Liquid Extraction Surface Analysis Sampled Tissue

Elizabeth C. Randall,[†,§] Alan M. Race,[§] Helen J. Cooper,[‡] and Josephine Bunch*[,§,||]

[†]Physical Sciences of Imaging in Biomedical Sciences Doctoral Training Centre, School of Chemistry, and [‡]School of Biosciences, University of Birmingham, Edgbaston, Birmingham, B15 2TT, United Kingdom
[§]National Physical Laboratory, Hampton Road, Teddington, Middlesex, TW11 0LW, United Kingdom
[||]School of Pharmacy, University of Nottingham, University Park, Nottingham, NG7 2RD, United Kingdom

S *Supporting Information*

ABSTRACT: Combined mass spectrometry imaging methods in which two different techniques are executed on the same sample have recently been reported for a number of sample types. Such an approach can be used to examine the sampling effects of the first technique with a second, higher resolution method and also combines the advantages of each technique for a more complete analysis. In this work matrix-assisted laser desorption ionization mass spectrometry imaging (MALDI MSI) was used to study the effects of liquid extraction surface analysis (LESA) sampling on mouse brain tissue. Complementary multivariate analysis techniques including principal component analysis, non-negative matrix factorization, and *t*-distributed stochastic neighbor embedding were applied to MALDI MS images acquired from tissue which had been sampled by LESA to gain a better understanding of localized tissue washing in LESA sampling. It was found that MALDI MS images could be used to visualize regions sampled by LESA. The variability in sampling area, spatial precision, and delocalization of analytes in tissue induced by LESA were assessed using both single-ion images and images provided by multivariate analysis.
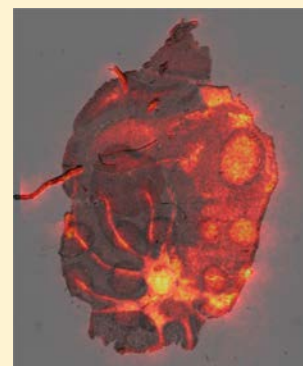
L iquid extraction surface analysis (LESA) mass spectrometry offers improved sensitivity through a combination of efficient analyte extraction and increase in the relative area sampled. LESA involves use of a small droplet of solvent to extract soluble analytes at the solid−liquid interface called the liquid microjunction.[1] In a traditional LESA experiment the minimum pixel size is limited by the diameter of the solvent droplet, ∼1 mm.[1] Smaller pixel sizes may be achieved through a modification to the surface sampling routine whereby the pipet tip makes contact with the sample surface and the pixel size is limited by the diameter of the pipet tip.[2,3] Brenton and Godfrey have suggested alternative methods for the improvement of spatial resolution possible by LESA mass spectrometry imaging (MSI).[4]

LESA MS has been reported for detection of lipids, peptides, proteins, drugs, and metabolites directly from thin tissue sections under ambient conditions with no sample preparation.[5−9] A further benefit of LESA MS is the decoupling of desorption and ionization events. This provides opportunities for postextraction separation (for example, via HPLC),[10] derivatization, or inclusion of internal standards for quantification.[9] Electrospray ionization (ESI) can produce multiply charged ions; therefore, mass analyzers with a limited mass-to-charge ratio (*m*/*z*) range can be used and a wider range of fragmentation techniques can be employed.

Through combining techniques such as matrix-assisted laser desorption ionization (MALDI) and LESA, one can maximize the advantages of each and use them in complement. Several examples of such an approach exist in the literature: MALDI MSI and LESA MS have been used on adjacent tissue sections

to study drug absorption into skin; LESA MS was used as a verification step to complement the MALDI MSI data.[11] Quanico et al. used a MALDI MSI-guided approach to identify regions of anatomical interest. These regions of an adjacent section were then analyzed by LESA coupled to liquid chromatography−mass spectrometry (LC−MS) for improved sensitivity, resulting in more complete identification of proteins.[9] Griffiths et al. used MALDI MSI and LESA MS to demonstrate that a sample preparation technique for improved lipid analysis yielded similar results when two different ionization methods were employed.[6] The potential for inclusion of internal standards in LESA extraction solvents was exploited by Tomlinson et al. who used LESA coupled to nanoelectrospray ionization and LC−MS to investigate ion suppression effects in MALDI.[12] Swales et al. demonstrated the complementary capabilities of various MSI techniques including MALDI MSI and LESA MS. They employed each on adjacent sections of organs from cassette- and discrete-dosed animals and compared their ability to detect four different target compounds.[13] It is important to note that each of these methods have employed MALDI MSI and LESA MS on adjacent sections which are therefore nonidentical. This increases the challenge when attempting to correlate, compare, or combine the data acquired with each technique. Additionally,

this would be impossible in situations where no adjacent section is available.

Repeat analysis by MALDI MSI of a single tissue section was reported by Steven and Bunch[14] and Garrett et al.,[15] who demonstrated that multiple MSI data sets could be acquired from a single sample, either by taking advantage of remaining matrix after initial analysis or by addition of a tissue wash and reapplication of matrix. These results show that reanalysis of tissue samples is an avenue towards obtaining complementary data. The importance of executing multimodal MSI workflows on the same tissue section has been recognized in studies seeking to combine other mass spectrometry techniques. Eberlin et al. reported a method for combining desorption electrospray ionization (DESI) MSI for lipid imaging, MALDI MSI for protein imaging, and hematoxylin and eosin (H&E) staining for morphological information on the same tissue section.[16] Eijkel et al. performed MALDI MSI and secondary ion mass spectrometry (SIMS) imaging on the same tissue section and outlined a workflow for correlating these data sets.[17]

In addition to extracting more information about the content of a sample, a number of "multimodal" studies have been conducted with the aim of using one method to understand another. Passarelli et al. reported time-of-flight SIMS (TOF-SIMS) imaging of matrix crystals prepared for use in MALDI MS imaging experiments and determined crystal size, analyte distribution, and delocalization of analytes upon matrix addition. Korsgen et al. also report TOF-SIMS imaging of analyte incorporation in matrix crystals prepared under different conditions, shedding light on the effects of sample preparation and leading to more optimal analysis.

As a relatively new technique LESA requires further study to fully understand the sampling process. Recent work by Kertesz and Van Berkel evaluated the reliability of liquid junction formation, sampling precision, spatial resolution, and extraction efficiency of a droplet-based extraction system with a simple model sample (ink on glass).[18] They found that, through control of probe-to-surface distance, dispensation volume, and aqueous solvent content, a stable liquid junction may be formed with good spatial precision. The stability of a liquid junction depends on sample surface properties such as wettability; this is sample-dependent, and therefore, these conclusions may not hold true when sampling tissue instead of glass.

Here we present the combination of MALDI and LESA for analysis of lipids, drugs, and proteins in a single tissue section. In this work MALDI MSI was used to image analyte distributions in tissue, post-LESA and therefore indicated how LESA sampling had altered the sample composition. This experiment provided insight into aspects of LESA sampling such as the area of tissue surveyed and variation and spatial precision of sampling. Previously this has only been assessed using optical images. Complementary multivariate analysis techniques were applied to the MALDI MSI data to determine spectral and spatial changes to the sample which occurred as a result of LESA sampling. This analysis indicated how MALDI spectra change as a result of LESA sampling.

■ EXPERIMENTAL SECTION

Materials. Ethanol, methanol, and formic acid were purchased from Fisher Scientific (Leicestershire, U.K.). Trifluoroacetic acid was purchased from Acros Organics. α-Cyano-4-hydroxycinnamic acid (CHCA) matrix was purchased from Sigma-Aldrich (Gillingham, U.K.), and glass slides were

from Thermo Scientific. Fresh frozen mouse brain tissue was provided by Professor Steve Watson at the University of Birmingham. Erlotinib was provided by Dr. Richard Goodwin at AstraZeneca.

Tissue Sample Preparation. Mouse brain tissue was sectioned (Leica CM 1850 cryostat, Milton Keynes, U.K.) at 10 μm thickness and thaw-mounted onto glass slides. The section which was destined for imaging by LESA MS had 0.3 μL of 200 nM erlotinib solution (80/20 methanol/water) deposited at a specific location (see text below).

Liquid Extraction Surface Analysis Mass Spectrometry. Surface sampling was performed using a TriVersa Nanomate chip-based electrospray device (Advion, Ithaca, NY). The electrospray device was coupled to a Thermo Fisher Orbitrap Velos (Thermo Fisher Scientific, Bremen, Germany) instrument. The robotic system was controlled through LESA Points and ChipSoft 8.3.3 software. A glass slide with tissue sections affixed was mounted in the LESA universal adaptor plate and scanned using an Epson flatbed scanner. The scanned image was imported into LESA Points, and the sampling locations were defined. A grid of 108 sampling locations was selected with an x, y spacing of 1 mm, covering the whole tissue section. The z coordinate was set to a height 0 mm relative to the sample surface to allow the pipette tip to come into contact with the sample ("contact" LESA). For "noncontact" LESA experiments, the pipette tip descended to a height ~0.2 mm above the surface of the sample. The solvent system for extraction and electrospray was methanol, water, and formic acid (69.3:29.7:1). The robotic arm collected a conductive pipet tip and aspirated 0.7 μL of solvent from the reservoir. The arm relocated to the x, y coordinates specified by LESA Points software. The pipette tip descended to the predetermined height (see above) and dispensed 0.5 μL of solvent. The liquid microjunction was maintained for 4 s before reaspiration. Each sample was delivered for 1 min via the Triversa Nanomate with a gas pressure of 0.3 psi and a tip voltage of 1.4 kV. Positive ion mass spectra were acquired in full scan mode (m/z 150−2000) at a resolution of 100 000 at m/z 400. The automatic gain control was turned off, and the injection time fixed at 100 ms. Each scan was composed of five coadded microscans.

MALDI Mass Spectrometry Imaging. Mouse brain sections were coated with CHCA matrix (5 mg/mL in 80% MeOH, 0.1% TFA) using a TM-Sprayer (HTX Technologies, LLC). Matrix was sprayed with a flow rate 0.115 mL/min and track speed of 1333 mm/min. The capillary temperature was 90 °C, and the spacing between tracks was 3 mm. Inspection of microscope images revealed that eight cycles of this method, with alternating rotation by 90° and 1.3 mm track offset, was found to produce relatively homogeneous sample coverage. MALDI MS imaging was carried out on a QSTAR XL QqTOF mass spectrometer (AB Sciex). An Elforlight (Daventry, U.K.) Nd:YAG laser with $λ$ = 355 nm was coupled to the MALDI source via a 100 μm diameter fiber (OZ Optics Ltd.) and was operated at a frequency of 1 kHz. The fluence at the sample surface was ~120 J m^{-2}. The sampling raster speed was 0.2 mm/s. Data were acquired in positive ion mode with a pixel size of 100 μm × 100 μm or 50 μm × 50 μm.

Hematoxylin and Eosin Staining. H&E staining was performed by Epistem according to standard protocols.

Optical Microscopy. Optical microscopy was performed on a Pathscan Enabler IV slide scanner and an Olympus CX40 microscope fitted with a 5× magnification objective lens.
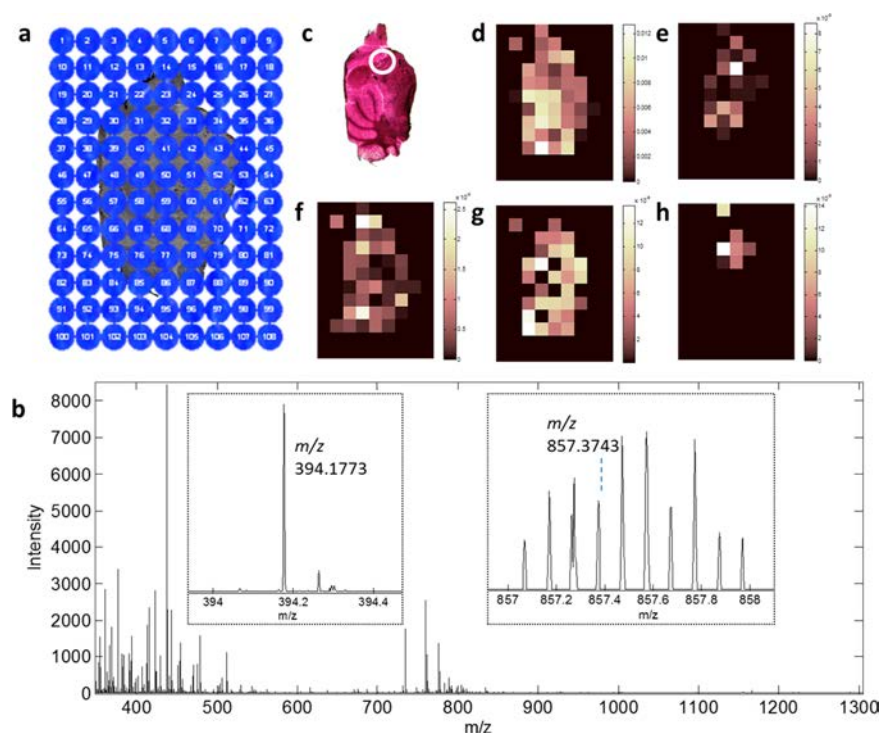
Figure 1. LESA MS of mouse brain tissue: (a) Locations selected for LESA sampling. (b) Example full scan LESA mass spectrum; peaks with m/z in the range of 700−900 correspond to lipid ions; enlargements of peaks corresponding to erlotinib (m/z 394.1773) and ubiquitin (m/z 857.3743) are shown the inset. (c) Circle indicates location selected for erlotinib deposition, covering both grey and white matter as indicated using H&E stained reference. (d) LESA MS image of ions with m/z 184.0739 corresponding to the phosphatidylcholine lipid headgroup. (e) LESA MS image of ions with m/z 760.5870 corresponding to $[M + H]^+$ ions of PC 34:1. (f) LESA MS image of ions with m/z 616.1782 corresponding to heme. (g) LESA MS image of ions with m/z 857.3743 corresponding to ubiquitin (+10 charge state). (h) LESA MS image of ions with m/z 394.1773 corresponding to $[M + H]^+$ ions of erlotinib.

Image Generation. A separate RAW file was generated for each LESA experiment (corresponding to a single pixel), consisting of multiple scans. Data were converted from RAW to mzML using msconvert as part of ProteoWizard.[19] The mean spectrum within a single mzML file (for each pixel) was calculated and output to a new mzML file, resulting in a spectrum per pixel. These were combined, along with the spectra locations, into an imzML file using imzMLConverter to produce an MS image.[20]

WIFF files generated by the QSTAR XL QqTOF mass spectrometer were converted to mzML files using MS Data Converter (AB Sciex). One mzML file was produced per raster line of the image. These were converted to a single imzML file using imzMLConverter.[20]

Data Analysis. Image files (imzML) were viewed and processed using in-house software, running in MATLAB (R2014b). Memory efficient principal component analysis (PCA) and k-means ($k = 7$) were applied as described by Race et al.[21] with the smoothing step in the preprocessing workflow modified to dual-pass Savitzky−Golay (window size of 11).

Principal component 1 and principal component 2 score images were used in combination to generate a binary mask for isolating the on-tissue spectra. MALDI MSI on tissue spectra were further reduced by selecting peaks from the total spectrum using a gradient-based method,[21] using the modified preprocessing workflow described above. NMF ($k = 25$. MATLAB) and t-SNE[22] were applied to the reduced data.

■ RESULTS AND DISCUSSION

LESA MS Imaging. An automated surface sampling routine was defined and implemented using the TriVersa Nanomate. The locations selected for contact LESA sampling are demonstrated in Figure 1a. Full scan mass spectra were obtained from each sample location (for example, see Figure 1b). Here we demonstrate for the first time that LESA MS is able to detect multiple classes of analyte in a single extraction/ electrospray event. Peaks in the m/z range of 700−850 correspond to various phosphatidylcholine (PC) lipid ions, preferentially detected as the protonated species. Ions detected with m/z 734.5708, 760.5870, and 782.5703 are tentatively assigned as protonated molecules of (PC) 32:0 (Δppm = 1.9), (PC) 34:1 (Δppm = 2.5), and (PC) 36:4 (Δppm = 1.2), respectively. Multiply charged protein ions predominantly appear in the m/z range of 600−1200. Ions at m/z 857.3743 (charge state +10) are tentatively assigned as ubiquitin (Δppm = 2.1), which has previously been detected from mouse brain tissue using LESA MS.[5] Other protein ions (unidentified) were detected with charge states ranging between +7 and +22. The tissue was spiked with 0.3 μL of 200 nM erlotinib solution, for location of drug spike see Figure 1c. Taking into account the area over which the droplet spread, we estimate that approximately 4.8 fmol of erlotinib was present per 0.4 mm^2 (the approximate area covered by a single contact LESA extraction, more discussion to follow). The drug was detected in every LESA spectrum sampled from this region. Example LESA MS images are displayed in Figure 1d−h, indicating the different distributions of PC 34:1, ubiquitin, heme, and erlotinib, across the tissue section. In this work we have
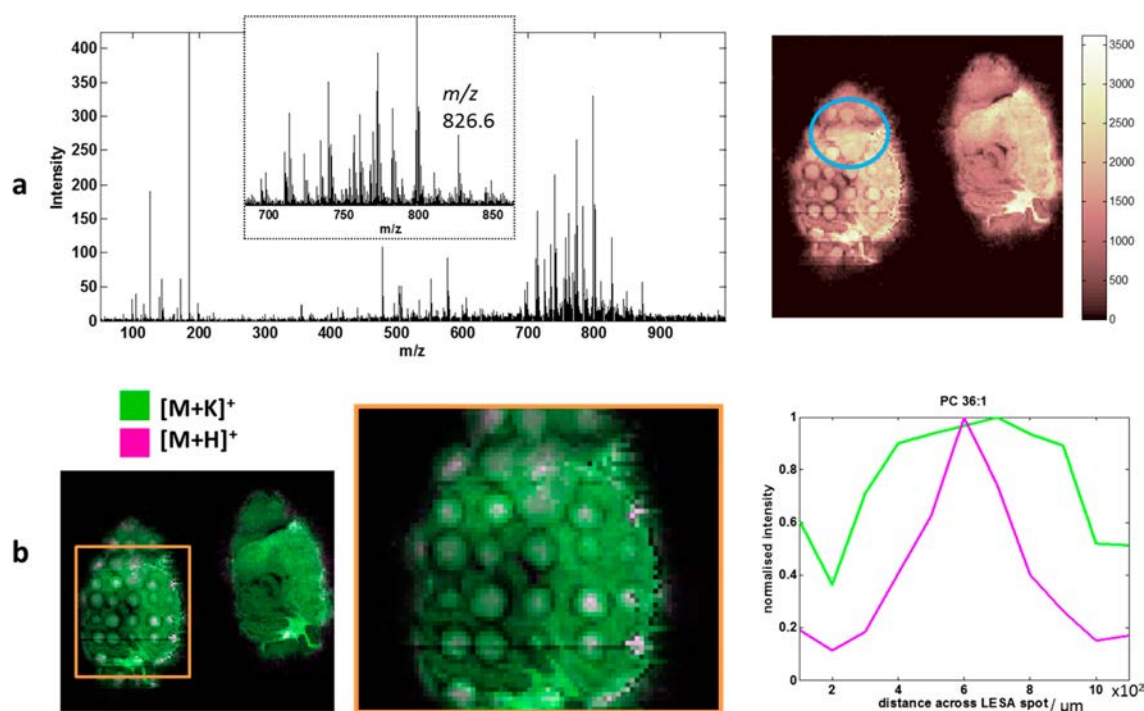
Figure 2. MALDI MS imaging of tissue after LESA sampling: (a) Left, example single-pixel spectrum, peaks in the m/z range of 700−900 correspond to lipid ions; right, MALDI MS image of ions with m/z 826.6, tentatively assigned as $[M + K]^+$ ions of PC 36:1; blue circle indicates the region spiked with erlotinib solution. (b) Left, overlaid MALDI MS ion images of protonated and potassium adduct of PC 36:1; right, overlaid intensity line profiles across the center of one LESA-sampled region; plot in pink corresponds to $[M + H]^+$ ion intensity which peaks sharply towards the center of the spot; plot in green corresponds to $[M + K]^+$ ions which are more homogeneously distributed across the spot.

found that a LESA solvent system comprising 70% MeOH, 1% formic acid is suitable for the simultaneous analysis of singly charged small molecules, multiply charged protein species, and the drug compound erlotinib, which was detected with m/z 394.1773 corresponding to $[M + H]^+$ ions.

The spacing between LESA sampling locations was defined as 1 mm, the minimum distance permitted by LESA Points software. The sampling routine used to acquire this data set was modified to minimize solvent spreading and allow for greater sampling precision; the method has previously been termed "contact" LESA.[2] The method involves bringing the sampling pipette into contact with the sample surface prior to solvent dispensation and an assumption that the solvent is entirely contained within the pipette tip during sampling—"plugged" by the sample itself. Optical images of the tissue section after "noncontact" (in which only the solvent was allowed to come into contact with the surface, all other sampling parameters remained the same) and "contact" LESA sampling demonstrate a decrease in relative size of area sampled (spot diameter decreased from ~1158 to ~690 μm), see Supporting Information Figure 1. These images also highlight unsampled regions of tissue which result from sample spacing of 1 mm and sampling diameter of less than 1 mm. Reliability of sampling was found to be improved using contact LESA because there was no requirement for formation of a stable liquid microjunction. Sampling precision was also found to be improved using contact LESA; the pipette tip walls prevent solvent droplet spreading to the same extent observed during normal LESA sampling, although some spreading beyond the expected contact area of the pipette tip is still observed. Aspects of sampling reliability and precision will be further discussed below.

Post-LESA MALDI MS Imaging. After the sample had been imaged by LESA MS, both this section and a serial section placed adjacent on the slide were coated with matrix and imaged using MALDI MS. There were several reasons for doing this: to provide higher resolution tissue images which complement the LESA MS data, to establish whether performing LESA prior to MALDI in a multimodal workflow is feasible (i.e., to determine whether MALDI image integrity is maintained), and to ascertain whether higher resolution MALDI MS images can be used to better understand LESA sampling. The adjacent tissue section served as a control and allowed changes induced by LESA sampling to be assessed.

The MALDI MSI method was optimized for lipid analysis; an example single-pixel spectrum from the tissue section which had not been sampled by LESA is displayed in Figure 2a. A number of lipid species were detected in the m/z range of 600−900; an example ion image (tentatively assigned as PC 36:1) can also be seen in Figure 2a. The lipids were preferentially detected as the potassium adduct. Ions detected at m/z's corresponding to the sodium adduct and protonated molecule were also observed but with a lower intensity. In these images it is possible to see the regions which were sampled by LESA. These features are generally classified by a region of higher ion intensity surrounded by a dark ring in which very few ions were detected. These features were not observed in the control image. It would appear that LESA sampling acts as a localized tissue wash, enhancing lipid detection via the extraction of analyte to the tissue surface and extraction and washing of salts resulting in a concentration gradient, highest at the edge of the spot. The region of tissue which was spiked with erlotinib solution appears as a similar although larger feature in the image. This supports the theory that analyte extraction, rather
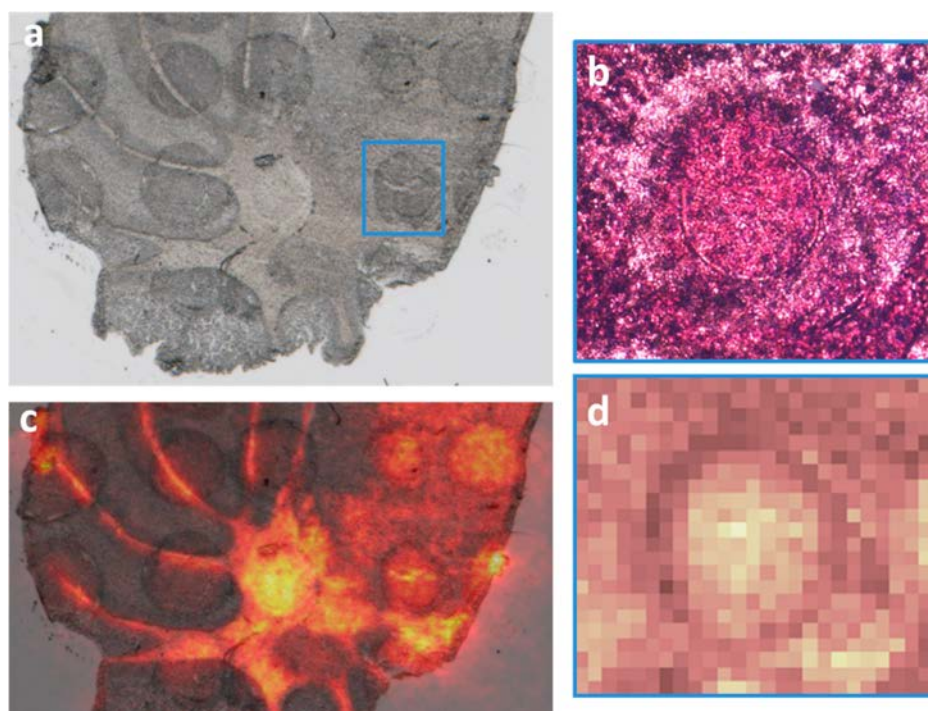
Figure 3. (a) Optical image of tissue section after LESA MS; darker regions indicate solvent contact with tissue; the smaller circle in the middle of the dark region is caused by imprint of the pipette tip. (b) Optical image of LESA-sampled region after coating with CHCA matrix; the lighter region at the perimeter of the LESA spot indicates thinner crystal layer. (c) Overlaid MALDI MS image of ions with m/z 826.6 and optical image. (d) Enlargement of MALDI MS image of ions with m/z 826.6 to show the same LESA-sampled region as displayed in panel b; the dark region in the ion image corresponds with the thinner region of matrix crystals in the optical image.

than mitigation of suppression effects, is responsible for the observed intensity increase because the spiked solution was allowed to remain on the tissue and therefore did not remove any dissolved species. To further probe the distribution of lipid species across the LESA-sampled area, a composite ion image of the protonated and potassiated molecules of PC 36:1 was generated, and intensity line profiles across a single LESA spot were plotted, see Figure 2b. It was found that $[M + H]^+$ ions were preferentially detected towards the center of the LESA-sampled area, whereas $[M + K]^+$ ions were more abundant towards the outside or homogeneously distributed across the spot. This behavior was also observed for a number of other lipid species. This is presumably caused by solvent washing salts towards the edge of the sampled area and depositing larger amounts at the outer perimeter as the residual solvent on the surface dries postsampling. Accumulation of salt at this outer perimeter could also be responsible for the "dark ring" observed in MALDI MS lipid images; matrix crystals exhibit different morphology when formed from solution containing different proportions of salts.[6] Optical images of a LESA-sampled tissue section before and after coating with matrix are displayed in Figure 3, parts a and b. The regions sampled by LESA appear as darker regions compared to unsampled tissue; a circular imprint can be observed in the middle of this region which results from the pipette tip coming into contact with the tissue. A larger, more irregular dark region surrounds this mark, which suggests the solvent spread further than the confines of the pipette tip. An experiment in which contact LESA was performed without any solvent confirmed that solvent washing effects and not compression or damage of the tissue during contact were responsible for the observed intensity changes in MALDI images, see Supporting Information Figure 2. The image

displayed in Figure 3b demonstrates the size and distribution of CHCA crystals on the tissue surface after matrix coating. A region of sparse, thin crystals can be seen around the outer edges which correspond with the dark region of the ion image displayed in Figure 3d, suggesting that changes to matrix morphology resulting in poor analyte inclusion and subsequent ablation/ionization are responsible for low ion counts from this region. An example MALDI MS image (m/z 826.6) overlaid with the optical image demonstrates that regions of higher intensity in the ion image correspond with darker regions observed in the optical image, see Figure 3c.

MALDI MS ion images reveal details about locations, size, and variation of LESA-sampled areas. Previous work has relied on optical images alone to provide this information, whereas we now present mass spectral data which verifies that visual changes to the tissue correspond with spectral changes indicative of solvent contact. Additionally, dislocation, leaching, and other changes in analyte distribution within the sampled area (which appears as a homogeneous area in the optical image) can be visualized using MALDI MSI. Two MALDI MSI data sets were obtained from tissue sampled by LESA, with pixel sizes of 100 and 50 μm, respectively. While no further features could be observed with the increased image detail afforded by 50 μm pixels, the outer limits of the sampled region could be more accurately defined. As such, MALDI MS images with 50 μm pixels were used to take measurements. The average area sampled per contact LESA spot is 0.41 mm^2. Differences in size of these areas is caused either by differing degrees of solvent spreading during sampling or differing volumes of residual solvent left on the tissue after LESA sampling, or some combination of both. The distance between these areas in x and y dimensions varies considerably, as
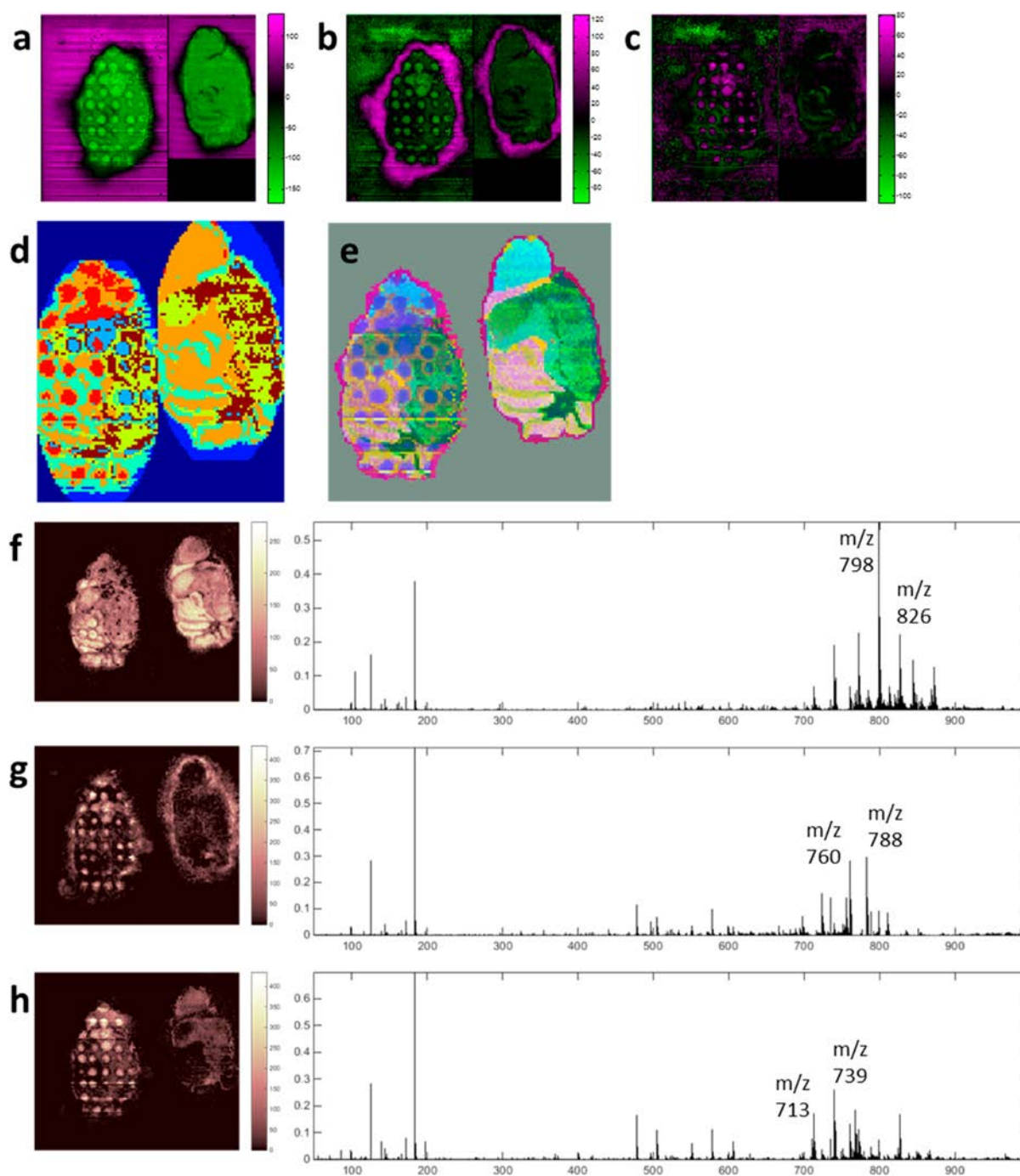
Figure 4. Results from multivariate analysis: (a–c) Score images of principal components 1, 5, and 6, respectively; principal component 1 indicates that the greatest variance is between tissue and background, principal component 5 indicates variance between LESA-sampled areas and the rest of the tissue, and principal component 6 indicates that LESA-sampled regions on white matter are more different from the original tissue type than those from grey matter. (d) k-Means clustering (k = 7) on masked image to remove background; the same clusters corresponding to anatomical features within the tissue are found in both LESA-sampled tissue and the control section indicating that LESA only induced localized changes; these are identified as different clusters in grey and white matter; further clusters identify the outer perimeter of LESA-sampled regions. (e) t-SNE reveals the same clusters identifying different tissue anatomies in LESA-sampled tissue and control tissue; LESA-sampled regions are assigned different clusters depending on the original type of tissue; however, these are more similar to each other than the original type of tissue; the region where the drug was spiked is also similar to the LESA-sampled regions but more similar to the original tissue type presumably because the solvent was not removed from the tissue and therefore did not deplete the tissue in the same way. (f–h) Examples of three factors identified by NMF, their spatial distributions, and contributing spectral components.

indicated by images in Figure 3. In order to maximize the total surface sampled by LESA in an imaging experiment, individual samples should be taken next to each other with as small a gap between them as possible but without overlapping (this would result in oversampling which, although common practice in MALDI MSI, is inappropriate for LESA MS because signal can be acquired multiple times from the same location). The spacing required between points for maximum coverage using

contact LESA would be ~700 μm, providing sampling spatial precision was accurate. However, MALDI MSI images reveal that intersample distances (measured from center to center) vary between 0.8 and 1.3 mm. Accurate determination of these variations is important in furthering LESA MS as an imaging technique.

In order to fully assess changes between the LESA-sampled section and serial control it is necessary to consider variation within the whole spectrum, as well as individual m/z channels. This also aids in interpretation of MALDI data obtained after LESA sampling. Complementary multivariate analysis techniques were applied to the data in order to study the effects of LESA sampling. PCA score images are displayed in Figure 4a–c and can be used to identify sources of variance within the data. The largest source of variance in the data set is the difference between tissue and background, shown by principal component 1. Principal component 5 shows the "halo" region, a common feature of MALDI MSI experiments. Principal component 6 identifies LESA sampling regions, where the regions sampled on areas of white matter are more intense than those on grey matter. This is interesting because it suggests that changes associated with LESA sampling do not appear uniformly across the tissue. This has implications for any sample preparation procedures which undergo a wash step because it implies that inhomogeneous washing occurs across the tissue and therefore false contrast could be introduced in ion images. Thresholded PCA score images, principal component 1 (matrix region), and principal component 5 ("halo" region) shown in Figure 4, parts a and b, respectively, were used to generate a mask to segment the background from the tissue for further multivariate analysis. k-Means clustering was applied to the PCA-reduced data set to identify pixels with similar spectral profiles and label them with a randomly assigned color, see Figure 4d. k-Means clustering successfully separated the different brain anatomies and LESA-sampled regions on white and grey brain tissue. The results from this analysis are easy to interpret and demonstrate agreement with individual lipid ion images. Two clusters are identified which are unique to the LESA-sampled tissue section and are labeled red and pale blue in Figure 4d. Clustering, with the parameters used, does separate the outer perimeter of these regions into a unique cluster. In general, k-means clustering provides no visual indication of how spectrally similar the identified clusters are. t-Distributed stochastic neighbor embedding (t-SNE) is a dimensionality reduction technique which has been used in MSI for visualization of complex data sets.[23] The color of each pixel is related to its location in the reduced space, thus providing a visual indication of how similar two pixels are spectrally. When applied to this data set, t-SNE reveals very similar results for control tissue and unsampled regions of section sampled by LESA. The regions sampled by LESA appear significantly different to the unsampled regions, with slight differences observable depending on whether the sampled region was grey or white matter, see Figure 4e. Although this data visualization approach is useful in identifying regions of spectral similarity and gradients of change affected by LESA sampling, no spectral information about the different regions is provided, and therefore, it is hard to identify which spectral features have contributed. Non-negative matrix factorization (NMF) decomposes the data into a set of unique spatial distributions and associated spectral profiles. NMF applied to this data set identifies a number of spatial distributions arising from LESA sampling, see Figure 4f–h. The image in Figure 4f identifies a distribution corresponding

to white matter in the tissue sections. Major m/z values contributing to this distribution are 798 and 826, which are tentatively assigned as the potassium adducts of PC 34:1 and PC 36:1, respectively, i.e., the most abundant lipid species detected from mouse brain tissue. The image in Figure 4g identifies regions at the center of the LESA-sampled regions; examination of individual ion images revealed that protonated molecules of lipids were detected with higher intensity here. Peaks with m/z 760 and 788 (tentatively assigned as protonated molecules of PC 34:1 and PC 36:1, respectively) are identified by NMF as major contributors to this distribution, supporting conclusions drawn from manual analysis.

It was found that features introduced into some MALDI MS ion images can be largely removed via total intensity normalization, see Supporting Information Figure 3. For other ion images this normalization strategy is less successful, see Supporting Information Figure 3. This is to be expected based on asserted changes to distribution of lipid adducts. An understanding of MALDI mass spectral changes associated with LESA sampling could help inform more sophisticated and appropriate normalization methods; for example, factors identified by NMF could be used to correct for changes in intensity and distribution.

CONCLUSION

We have presented a combined workflow which exploits the combined advantages of LESA and MALDI MSI and additionally provides insight into aspects of ambient surface sampling. LESA provided sensitive analysis of multiple classes of analyte simultaneously with spatial information. MALDI provided high spatial resolution images which detailed the anatomical features within tissue which were too small for LESA to successfully resolve. MALDI images were also used to accurately define the exact locations sampled by LESA, their size, and variation. Importantly, LESA does not appear to blur or distort anatomical features. Several multivariate techniques were employed to assess changes to distribution induced by LESA. Future implementations of MALDI MSI after LESA analysis could assess different washing protocols, or how the same wash affects different regions of tissue. This could also be used to assess improvements or changes made to the automated LESA sampling routines described here, for example, to determine the spacing of sampled areas and ensure that no oversampling had occurred. LESA MS is somewhat limited as an imaging technique by the poor spatial resolution it affords; however, there are opportunities for further decreasing pixel size via contact LESA and smaller sampling pipette tips. As the technique improves in terms of sampling precision and repeatability, combining it with MALDI will become an even more attractive option. The potential for inclusion of standards by LESA is also attractive, and provides possible routes towards quantitative analysis. The combined LESA–MALDI MSI workflow could then be applied to drug in tissue studies which could provide quantitative analysis of drug/lipid/protein via LESA and a higher spatial resolution reference in MALDI MS images.

ASSOCIATED CONTENT

Ⓢ Supporting Information

The Supporting Information is available free of charge on the ACS Publications website at DOI: 10.1021/acs.analchem.5b04281.

Optical images of tissue after contact and noncontact LESA sampling, MALDI ion images after LESA sampling with and without solvent, example MALDI ion images which have undergone various normalization strategies, further examples of different MALDI lipid ion images, and example LESA mass spectrum acquired from tissue after MALDI analysis (PDF)

■ AUTHOR INFORMATION

Corresponding Author
*E-mail: josephine.bunch@npl.co.uk.

Notes
The authors declare no competing financial interest.

■ ACKNOWLEDGMENTS

■ REFERENCES

(1) Kertesz, V.; Van Berkel, G. J. *J. Mass Spectrom.* **2010**, *45*, 252−260.

(2) Randall, E. C.; Bunch, J.; Cooper, H. J. *Anal. Chem.* **2014**, *86*, 10504−10510.

(3) Almeida, R.; Berzina, Z.; Arnspang, E. C.; Baumgart, J.; Vogt, J.; Nitsch, R.; Ejsing, C. S. *Anal. Chem.* **2015**, *87*, 1749−1756.

(4) Brenton, A. G.; Godfrey, A. R. *Anal. Chem.* **2014**, *86*, 3323−3329.

(5) Schey, K. L.; Anderson, D. M.; Rose, K. L. *Anal. Chem.* **2013**, *85*, 6767−6774.

(6) Griffiths, R. L.; Sarsby, J.; Guggenheim, E. J.; Race, A. M.; Steven, R. T.; Fear, J.; Lalor, P. F.; Bunch, J. *Anal. Chem.* **2013**, *85*, 7146−7153.

(7) Sarsby, J.; Martin, N. J.; Lalor, P. F.; Bunch, J.; Cooper, H. J. *J. Am. Soc. Mass Spectrom.* **2014**, *25*, 1953−1961.

(8) Eikel, D.; Vavrek, M.; Smith, S.; Bason, C.; Yeh, S.; Korfmacher, W. A.; Henion, J. D. *Rapid Commun. Mass Spectrom.* **2011**, *25*, 3587−3596.

(9) Quanico, J.; Franck, J.; Dauly, C.; Strupat, K.; Dupuy, J.; Day, R.; Salzet, M.; Fournier, I.; Wisztorski, M. *J. Proteomics* **2013**, *79*, 200−218.

(10) Martin, N.; Bunch, J.; Cooper, H. *J. Am. Soc. Mass Spectrom.* **2013**, *24*, 1242−1249.

(11) Marshall, P.; Toteu-Djomte, V.; Bareille, P.; Perry, H.; Brown, G.; Baumert, M.; Biggadike, K. *Anal. Chem.* **2010**, *82*, 7787−7794.

(12) Tomlinson, L.; Fuchser, J.; Fütterer, A.; Baumert, M.; Hassall, D. G.; West, A.; Marshall, P. S. *Rapid Commun. Mass Spectrom.* **2014**, *28*, 995−1003.

(13) Swales, J. G.; Tucker, J. W.; Strittmatter, N.; Nilsson, A.; Cobice, D.; Clench, M. R.; Mackay, C. L.; Andren, P. E.; Takáts, Z.; Webborn, P. J.; Goodwin, R. J. A. *Anal. Chem.* **2014**, *86*, 8473−8480.

(14) Steven, R. T.; Bunch, J. *Anal. Bioanal. Chem.* **2013**, *405*, 4719−4728.

(15) Garrett, T. J.; Prieto-Conaway, M. C.; Kovtoun, V.; Bui, H.; Izgarian, N.; Stafford, G.; Yost, R. A. *Int. J. Mass Spectrom.* **2007**, *260*, 166−176.

(16) Eberlin, L. S.; Liu, X.; Ferreira, C. R.; Santagata, S.; Agar, N. Y. R.; Cooks, R. G. *Anal. Chem.* **2011**, *83*, 8366−8371.

(17) Eijkel, G. B.; Kükrer Kaletaş, B.; van der Wiel, I. M.; Kros, J. M.; Luider, T. M.; Heeren, R. M. A. *Surf. Interface Anal.* **2009**, *41*, 675−685.

(18) Kertesz, V.; Van Berkel, G. J. *Rapid Commun. Mass Spectrom.* **2014**, *28*, 1553−1560.

(19) Egertson, J. D.; Kuehn, A.; Merrihew, G. E.; Bateman, N. W.; MacLean, B. X.; Ting, Y. S.; Canterbury, J.D.; Marsh, D. M.; Kellmann, M.; Zabrouskov, V.; Wu, C. C.; MacCoss, M. J. *Nat. Methods* **2013**, *10*, 744−746.

(20) Race, A. M.; Styles, I. B.; Bunch, J. *J. Proteomics* **2012**, *75*, 5111−5112.

(21) Race, A. M.; Steven, R. T.; Palmer, A. D.; Styles, I. B.; Bunch, J. *Anal. Chem.* **2013**, *85*, 3071−3078.

(22) Van Der Maaten, L. *Journal of Machine Learning Research* **2014**, *15*, 3221−3245.

(23) Fonville, J. M.; Carter, C. L.; Pizarro, L.; Steven, R. T.; Palmer, A. D.; Griffiths, R. L.; Lalor, P. F.; Lindon, J. C.; Nicholson, J. K.; Holmes, E.; Bunch, J. *Anal. Chem.* **2013**, *85*, 1415−1423.

Appendix 2: Randall, E. C.; Bunch, J.; Cooper, H. J. *Analytical Chemistry* **2014**, *86*, 10504-10510.

Editors' Highlight

Direct Analysis of Intact Proteins from *Escherichia coli* Colonies by Liquid Extraction Surface Analysis Mass Spectrometry

Elizabeth C. Randall,[†] Josephine Bunch,*[,‡,§] and Helen J. Cooper*[,†]

[†]School of Biosciences, University of Birmingham, Edgbaston, Birmingham, B15 2TT, United Kingdom
[‡]National Physical Laboratory, Hampton Road, Teddington, Middlesex TW11 0LW, United Kingdom
[§]School of Pharmacy, University of Nottingham, University Park, Nottingham, NG7 2RD, United Kingdom

Ⓢ *Supporting Information*

ABSTRACT: Top-down identification of proteins by liquid extraction surface analysis (LESA) mass spectrometry has previously been reported for tissue sections and dried blood spot samples. Here, we present a modified "contact" LESA method for top-down analysis of proteins directly from living bacterial colonies grown in Petri dishes, without any sample pretreatment. It was possible to identify a number of proteins by use of collision-induced dissociation tandem mass spectrometry followed by searches of the data against an *E. coli* protein database. The proteins identified suggest that the method may provide insight into the bacterial response to environmental conditions. Moreover, the results show that the "contact" LESA approach results in a smaller sampling area than typical LESA, which may have implications for spatial profiling.
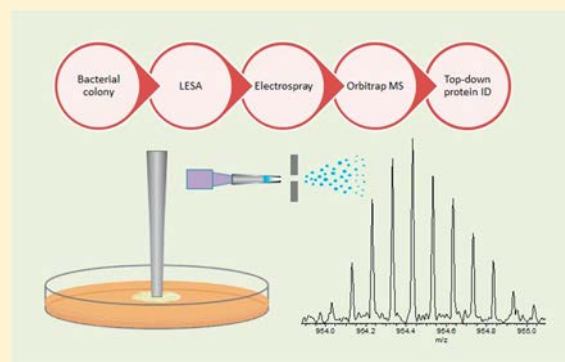
It was first demonstrated that mass spectrometry could be applied to the identification and differentiation of species of bacteria over 30 years ago;[1,2] subsequent advances in software and instrumentation now make it a powerful tool for microbiological research.[3,4] MALDI-TOF mass spectrometry has been reported for the identification of bacterial species from isolates of over 1000 species. Identification involves searching mass spectra against spectral libraries of abundant intact proteins which are characteristic of that species.[2,3] It has been suggested that this method will replace traditional identification methods such as Gram stain, colony morphology, and biochemical tests.[3] MALDI MS has also been used to image bacterial colonies with a spatial resolution capable of capturing metabolic output of bacteria, which can be compared between mutant and wildtype strains.[5−7] The identification of metabolites from mass spectral images of bacteria can help in the elucidation of biochemical pathways underlying microbial processes, which are often poorly characterized. Techniques capable of detecting chemical signals in a spatially resolved manner could also aid our understanding of bacterial inter- and intraspecies interactions.[8]

The majority of proteins detected by MALDI methods are small ribosomal proteins (typically <15 kDa) which are ideally suited to and relied upon for the robust identification of bacterial species and subspecies. However, the routine detection of larger bacterial proteins remains elusive. Electrospray ionization (ESI) top-down mass spectrometry methods provide an increased mass range and total number of proteins detected. Top-down analysis[9] involves fragmentation of intact protein ions and overcomes the limitation of information loss

suffered by bottom-up analysis[10] of proteolytic peptides. For example, Fenselau and co-workers[11] applied top-down LC MS/MS to the analysis of bacterial lysates from *Erwinia herbicola* and *Enterobacter cloacae*. Fourteen proteins were identified in *E. herbicola*, ten of which were ribosomal. Fifteen proteins were identified in *E. cloacae*, five of which were ribosomal and three were cold shock proteins. More recently, McFarland et al.[12] applied top-down LC MS/MS to the analysis of lysates from *Salmonella enterica* serovars. They identified 73 proteins in the mass range of 4−36 kDa.

The development of ambient mass spectrometry techniques such as desorption electrospray ionization (DESI)[13] and liquid extraction surface analysis (LESA)[14] have enabled direct sampling of bacterial colonies with little or no sample preparation. DESI involves desorbing analytes from a surface by directing a stream of charged electrospray droplets at the surface of interest. The sample inlet of the mass spectrometer is positioned above the surface at the optimum angle to capture analyte ions which have been desorbed. LESA involves using a droplet of solvent into which soluble analytes are extracted. The droplet is dispensed from a pipet tip and held in contact with the sample surface for a specified length of time to form a liquid microjunction. The droplet is then reaspirated and injected through an electrospray capillary into the mass spectrometer. These techniques benefit from the advantages provided by ESI-MS, with the added bonus of direct surface sampling. One
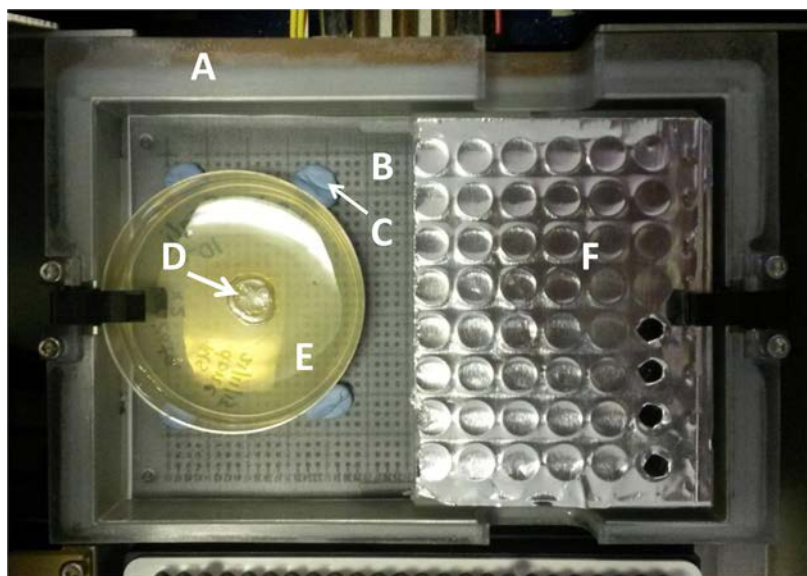
Figure 1. Experimental setup: (A) sample tray of Triversa Nanomate; (B) photocopy of the universal adaptor plate, for *x,y* coordinates; (C) adhesive putty (Blu-tack) to secure Petri dish in position; (D) *E. coli* colony; (E) Petri dish containing agar; (F) half 96-well plate containing extraction/electrospray solvent system.

possible application of these methods is the direct sampling of surfaces contaminated with unknown strains of bacteria, which could have implications for clinical diagnostics, quality control, and environmental monitoring.

Ambient mass spectrometry techniques are ideal for the analysis of bacterial colonies because they can directly sample living colonies growing in Petri dishes.[15] A recent report outlines the spatially resolved detection of glycolipids and metabolites from living bacterial colonies using nano-DESI.[16] This technique was capable of detecting metabolites secreted by bacteria into the surrounding agar without any sample preparation or pretreatment. A further paper detailed the use of nano-DESI to study interactions between neighboring colonies and in mixed-species biofilms,[17] with detection of a wide range of lipids, peptides, and other small molecules reported. A further motivator for the chemical analysis of bacteria is the search for novel therapeutic agents: more than 60% of current pharmaceuticals have been developed from natural products.[8] It has been demonstrated that a thiazolyl peptide antibiotic could be extracted from *Actinobacteria* colonies by LESA and analyzed by nanoelectrospray mass spectrometry.[18] In 2013, the use of an ambient electrospray ionization flow-probe was demonstrated for the metabolic profiling of a range of micro-organisms. Diverse classes of natural products have been detected using the flow-probe including small redox compounds, lipids, and peptides.[19] Although a wide variety of small molecules has been detected from bacterial colonies by techniques such as DESI, nano-DESI, LESA, and the continuous flow-probe coupled to mass spectrometry, analysis of intact proteins from bacteria by ambient mass spectrometry has not previously been reported.

LESA-MS has been demonstrated to be capable of extracting intact proteins directly from surfaces without any pretreatment. In 2011, Edwards et al. reported a LESA-MS method for detecting hemoglobin variants from neonatal dried blood spot samples. The mass spectra obtained contained peaks corresponding to the different subunits of hemoglobin, and it was possible to confirm the presence of known variants, including those differing in mass by <1 Da, by MS/MS.[20] It was

later shown that LESA MS/MS could be applied for the analysis of unknown hemoglobin variants.[21] Schey et al. reported the liquid extraction of intact proteins from tissue sections. An acetonitrile/water solvent system was used to manually extract proteins from thin tissue sections of mouse brain, mouse kidney, and bovine ocular lens. Peaks in the mass spectra of extracts were fragmented by ETD and subsequently identified.[22] Sarsby et al. applied automated LESA MS/MS for the analysis of intact protein biomarkers of nonalcoholic liver disease.[23]

Here, we present LESA mass spectrometry of intact proteins directly from *Escherichia coli* colonies growing on solid agar in Petri dishes. The LESA sampling system was coupled to a high mass resolution orbitrap mass spectrometer. Optimization of the surface sampling process revealed that a modified surface sampling routine, in which the pipet tip came into contact with the colony surface, resulted in detection of greater numbers of protein signals. This sampling process may offer the additional advantage of limiting the spread of solvent to an area the size of the pipet tip, which has implications for the spatial resolution of any images produced. In order to identify proteins, ions corresponding to intact proteins were selected and subjected to CID. The resulting MS/MS data were searched against an *E. coli K-12* protein database using Prosight PTM 2.0 software. Six proteins were identified including DNA binding proteins and shock response proteins.

■ EXPERIMENTAL SECTION

Materials. A strain of *Escherichia coli K-12* was inoculated onto solid LBA medium (LB 20 g L^{-1}, agar 20 g L^{-1}) in 6 cm diameter Petri dishes. The smaller size of Petri dish allows it to fit inside the sample tray of the Advion TriVersa NanoMate system. Bacteria were incubated at 21 °C for 3 days before storing in the dark at 4 °C or were allowed to grow at room temperature on the bench and were stored at room temperature (∼20 °C). The solvent system for surface sampling/electrospray ionization consisted of acetonitrile (J.T. Baker, The Netherlands) and water (J.T. Baker, The Nether-

lands) (39.6:59.4) with 1% formic acid (Sigma-Aldrich Company Ltd., Dorset, U.K.).

Surface Sampling. Petri dishes containing *E. coli K-12* colonies were placed directly into the TriVersa Nanomate chip-based electrospray device (Advion, Ithaca, NY) adjacent to half a 96-well microtiter plate (ABgene PCR plate Thermo Fisher Scientific, Leicestershire, U.K.) into which the extraction solvent system is placed; see Figure 1. The electrospray device was coupled to a Thermo Fisher Orbitrap Velos ETD (Thermo Fisher Scientific, Bremen, Germany) instrument. Surface sampling was performed using the advanced user interface (AUI) feature of the TriVersa NanoMate ChipSoft Manager software which controls the TriVersa NanoMate robotic system. A coordinate (*x*,*y*,*z*) system was used to direct the robotic arm in a surface sampling routine. The arm picked up a conductive pipet tip from the tip rack and relocated to a position above the well containing extraction solvent. The tip descended into the well and aspirated 3 μL of solvent. The arm relocated to a defined position above the bacterial colony; the tip descended to a depth just below the surface of the colony. The exact sampling height varied (from −9 to −11 mm from the initial position of the robotic arm), depending on the size of the colony and spread of agar in different samples; for increased extraction of proteins, the pipet tip came into contact with the top surface of the colony but did not penetrate the agar below. Once in contact with the colony, the tip dispensed 2 μL of solvent onto the colony which was held in contact for 3 s to allow soluble analytes to desorb into the droplet. The solution was then reaspirated into the pipet, and the tip engaged with the nanoelectrospray chip in order to start electrospray ionization and introduction of the sample into the mass spectrometer.

Mass Spectrometry. All mass spectrometry experiments were performed on a Thermo Fisher Orbitrap Velos ETD (Thermo Fisher Scientific, Bremen, Germany) instrument. The sample was introduced via the Triversa Nanomate with a gas pressure of 0.3 psi and a tip voltage of 1.75 kV. Mass spectra were collected in full scan mode (*m/z* 500−2000) at a resolution of 100 000 at *m/z* 400. The AGC target was 1×10^6 charges. Each scan was composed of 30 coadded microscans. Data were recorded for 5 min (∼11 scans). (Note that a stable electrospray could be maintained for ∼50 min from a single LESA analysis.) CID was carried out in the linear ion trap, and the fragment ions were detected in the orbitrap at a resolution of 100 000 at *m/z* 400. AGC target was 5×10^4 charges. CID experiments were performed with helium gas at normalized collision energy of 35% (optimized for sequence coverage, data not shown) and an isolation width of 10 Th. MS/MS spectra were collected in the range of *m/z* 300−2000 and are composed of 10 coadded microscans. Data were analyzed using Xcalibur 2.10 software (Thermo Fisher Scientific) where the Xtract program was used to calculate monoisotopic masses. For data analysis using ProSightPTM 2.0, CID MS/MS spectra were deconvoluted using the Xtract program (S/N threshold 3). Xtracted monoisotopic fragment masses were searched against the *E. coli K-12* database in ProSightPTM 2.0, with a fragment tolerance of 10 ppm and precursor tolerance of 100 ppm, in order to assign putative protein identifications. Two search types were used in Prosight, "absolute mass search" and "sequence tag search". Absolute mass search involves searching the mass of the precursor ion against intact masses of proteins within the chosen database. If a match is found, then fragment masses can be matched to theoretical fragments of that protein.

A sequence tag search involves compiling lists of amino acids which could correspond to observed fragment masses or differences in mass between two fragments. The amino acid sequences are then searched against the appropriate database to see if they correspond to sequences of known proteins. Protein identities were confirmed by manual analysis using Protein Prospector (http://prospector.ucsf.edu/prospector/mshome. htm).

Postsampling Image Analysis. Photographs of the colony surface were taken after LESA sampling. Areas which came into contact with solvent during sampling were measured using ImageJ software. Contact with solvent caused discoloration of the colony surface so the diameter of these regions could be visually identified in the photos. The image scale was set using features of known size in the image, either a ruler or coordinate spots of the universal adaptor plate.

■ RESULTS AND DISCUSSION

Optimization of LESA Method. When setting up a LESA method, there are several parameters which are user-defined and can affect the extraction efficiency including the solvent system used for extraction and the height to which the pipet descends above the sample surface. These parameters were optimized for extraction of intact proteins from bacteria. A survey of common LESA solvent systems was conducted (data not shown) and indicated that an acetonitrile/water mixture was the only solvent capable of extracting proteins. The optimum pipet tip height above the surface was investigated by sequentially sampling the surface, starting at approximately 0.2 mm above the surface, allowing the tip to descend 0.2 mm lower each time and recording spectra at each respective sampling height; see Supplementary Figure 1, Supporting Information. (Mass spectra shown in Supplementary Figure 1, Supporting Information, were recorded from the same location.) It was found that proteins were extracted when the pipet tip came into contact with the colony surface. (Peaks observed in the mass spectrum shown in Supplementary Figure 1a, Supporting Information, correspond to singly charged species.) Although a larger number of proteins were detected when the pipet tip sampled further below the colony surface (see Supplementary Figure 1c, Supporting Information), a compromise must be made between good extraction of proteins and electrospray instability due to capillary blocking. The mass spectrum shown in Supplementary Figure 1d, Supporting Information, contains peaks corresponding to singly, doubly, and triply charged species indicating that the pipet tip may have punctured the agar below the colony. For comparison, a mass spectrum obtained following LESA sampling of agar is shown in Supplementary Figure 2, Supporting Information. We hypothesize that the observation of increased numbers of proteins in mass spectra obtained following contact between the pipet tip and the surface is due to the insoluble nature of the extracellular matrix produced by colony bacteria; in placing the pipet tip in contact with the surface, this insoluble layer is physically disrupted allowing more efficient extraction of proteins contained within the colony. It should be noted that this "contact" method of surface sampling is different from other LESA methods described in the literature; see Figure 2a,b. Kai et al. report the extraction of small molecule antibiotic compounds using LESA, a method in which only the solvent droplet came into contact with the bacteria.[18]

An interesting consequence of the "contact" surface sampling routine is illustrated in Figure 2. The process of placing the
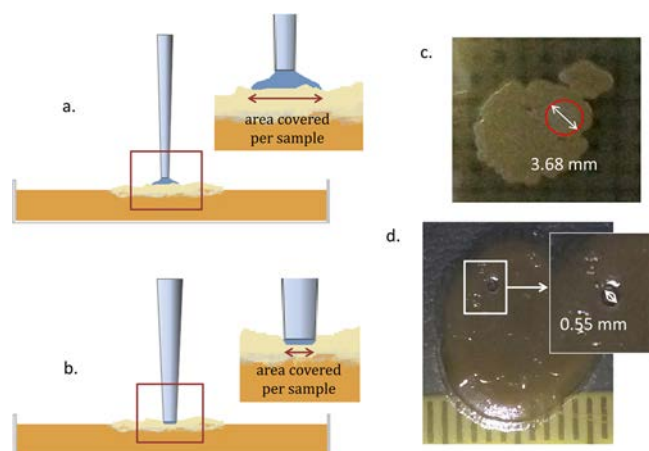
Figure 2. Improved sampling precision obtained from "contact" LESA sampling: (a) Schematic illustrating the surface area of sample covered by each solvent droplet when sampled by a liquid microjunction (contact between surface and solvent only); (b) schematic illustrating the smaller surface area covered by each sample droplet with the "contact" method (contact between surface and pipet tip); (c) sampled area following liquid microjunction sampling; (d) sampled area following "contact" LESA.

pipet tip in contact with the colony surface during sampling appears to limit the spread of the solvent droplet to the area of the pipet tip end. We postulate that the low pressures used to dispense and aspirate the solvent droplet are insufficient to push the solvent beyond the end of the pipet tip and therefore the colony acts as a plug. The spread of solvent during LESA sampling determines the area of the sampling region. In the case of hydrophilic surfaces, the area over which the

microjunction spreads is large; see Figure 2a,c. The method described here prevents any solvent spread beyond the edges of the pipet tip because the solvent is completely encased within the end of the tip; see Figure 2b,d. The total surface area sampled by this method is $\sim$0.24 mm^2, as measured using ImageJ on images of the puncture mark on the colony surface after sampling. This observation represents a significant improvement when compared to the area covered by the usual LESA solvent droplet, which was measured to be $\sim$10.64 mm^2 (solvent sampling discolored the colony surface allowing for measurement of the area from photographic images). Note that the droplet volumes were the same for both methods.

Top-Down LESA Mass Spectrometry of *E. coli* Colonies. Figure 3a shows a representative full scan mass spectrum obtained following LESA sampling of an *E. coli* colony (previously stored at 4 °C) growing on agar; see Figure 3b for the location of the spot sampled. The mass spectrum contains approximately 150 peaks corresponding to $\sim$60 bacterial proteins in a range of charge states. The molecular weights of these proteins ranged from approximately 5 to 32 kDa. This mass range is in agreement with the findings of McFarland et al., who report the detection of intact proteins in the range of 4−37 kDa from *S. typhimurium* by ESI orbitrap mass spectrometry.[12]

Figure 3c shows an enlarged section of the mass spectrum with peaks selected for CID indicated. Supplementary Figure 3, Supporting Information, shows the same region of the mass spectra obtained following LESA sampling at various locations as indicated (Figure 3c is also Supplementary Figure 3c, Supporting Information). The relative abundance of the protein peaks is greater in the mass spectra obtained from locations close to the edge of the colony. That observation may be the
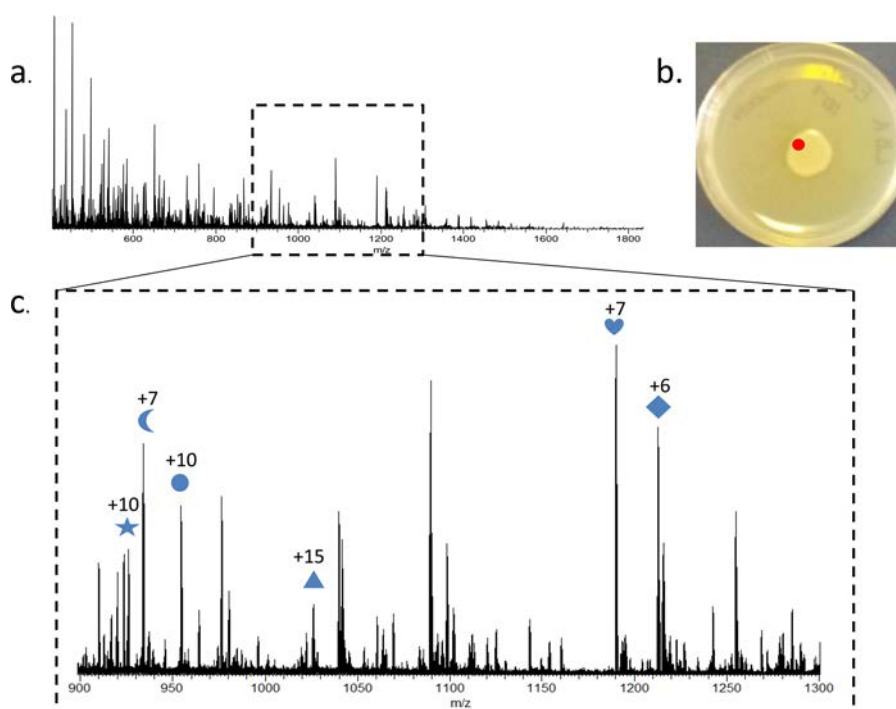
Figure 3. LESA mass spectrometry of an *E. coli* K-12 bacterial colony previously stored at 4 °C. (a) Full scan mass spectrum; (b) photograph of bacterial colony growing on solid agar medium in a Petri dish. Red spot marks the region sampled by LESA; (c) enlarged *m/z* region from a full scan mass spectrum (*m/z* 900−1300) which contains the majority of peaks corresponding to protein ions. Symbols indicate peaks subsequently selected for CID.

Table 1. Summary of Proteins Identified from *E. coli K-12* Colonies Following "Contact" LESA Top-Down Mass Spectrometry

m/z_{meas}	m/z_{calc}	Δppm	charge state	MW_{calc}	% sequence coverage	protein identity	protein function
954.5104	954.5133	−3.0	+10	9530.24	28	DNA binding protein HU-alpha	stabilizes DNA under extreme environmental conditions
1027.6038	1027.6069	−3.0	+15	15399.95	18	DNA binding protein H-NS	increases thermal stability of DNA
1189.5921	1189.5919	0.2	+7	8321.10	23	UPF0337 protein YjbJ	predicted shock response protein
1212.2801	1212.2719	6.8	+6	7268.60	13	CspA	cold shock response protein
923.0039	923.0067	−3.0	+10	9221.00	40	DNA-binding protein HU-beta	stabilizes DNA under extreme environmental conditions
933.4871	933.4822	5.2	+7	6528.35	32	multiple stress resistance protein BhsA	inhibits biofilm formation by repressing cell aggregation
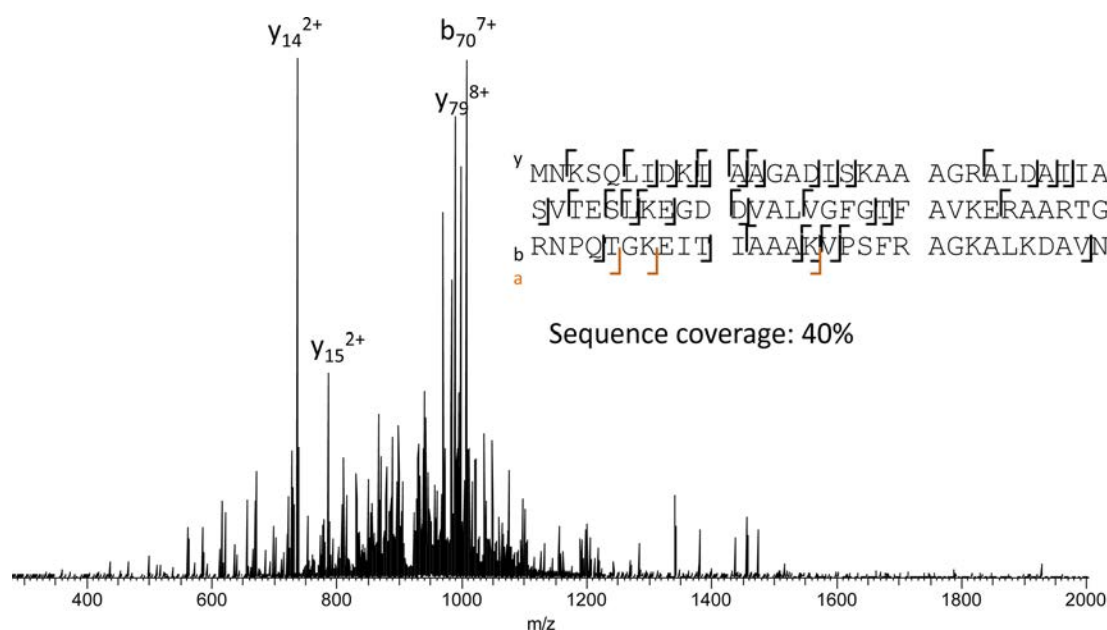
Figure 4. CID mass spectrum of ions centered at m/z 923.51 (+10 charge state), identified as DNA-binding protein HU-beta. Fragment ions observed are shown the inset.

result of easier disruption of the extracellular matrix and improved extraction efficiency at the colony edge.

Ions centered at m/z 923.51 (+10 charge state), 933.91 (+7), 954.43 (+10), 1028.14 (+15), 1190.31 (+7), and 1212.94 (+6) were fragmented. The product ions were searched against the *E. coli K-12* database in ProSightPTM 2.0, using either the "absolute mass search" or the "sequence tag search". Putative protein identifications were confirmed by manual analysis. The proteins identified and the protein sequence coverages are shown in Table 1. The sequence coverages ranged from 13% to 40%. A representative MS/MS spectrum from one of the identified proteins, DNA-binding protein HU-beta, is shown in Figure 4. The remaining MS/MS spectra are shown in Supplementary Figures 4−8, Supporting Information. Product ion assignments are shown in Supplementary Tables 1−6, Supporting Information.

A total of 6 proteins were identified. DNA binding protein HU-alpha and HU-beta are both histone-like DNA binding proteins which are capable of wrapping DNA to stabilize and prevent its denaturation under extreme environmental conditions.[24] DNA binding protein H-NS increases thermal stability of DNA and inhibits transcription at low temperatures.[25] The function of protein YjbJ is poorly understood but is recognized as a highly abundant protein in *E. coli*.[26] CspA is a cold shock response protein, known to be induced at temperatures of 15 °C or lower.[27] Multiple stress resistant

protein BhsA is known to be induced under a range of stressful conditions including drastic pH changes, heat shock, the presence of heavy metals, and hydrogen peroxide. As a result, this protein inhibits biofilm formation by repressing cell aggregation and increases cell viability under stressful conditions.[28] A number of these proteins (HU-alpha, HU-beta, YjbJ, H-NS) were also detected by ESI top-down MS/MS of *S. typhimurium* reported by McFarland et al.

It should be noted that, while a number of proteins have been identified in this study, it was not possible to identify all proteins from their MS/MS spectra. Ions of m/z 1254.99 (+7 charge state) were also fragmented, and the product ions were searched against the *E. coli K-12* database in ProSightPTM 2.0, using both the "absolute mass search" and the "sequence tag search". Neither search returned hits corresponding to the correct intact mass. Top-down methods are used infrequently relative to bottom-up identification techniques, and as such, the demand for software for identification of proteins by top-down methods is lower. While several platforms are available, e.g., Prosight PTM 2.0,[29] ROCCIT (roccit.caltech.edu), the proteins in this work were not reliably fully characterized and a large amount of manual characterization was required. This aspect would need to be addressed if top-down methods were to become more established.

The selection of proteins detected and identified from colonies stored at 4 °C is indicative of extreme environmental
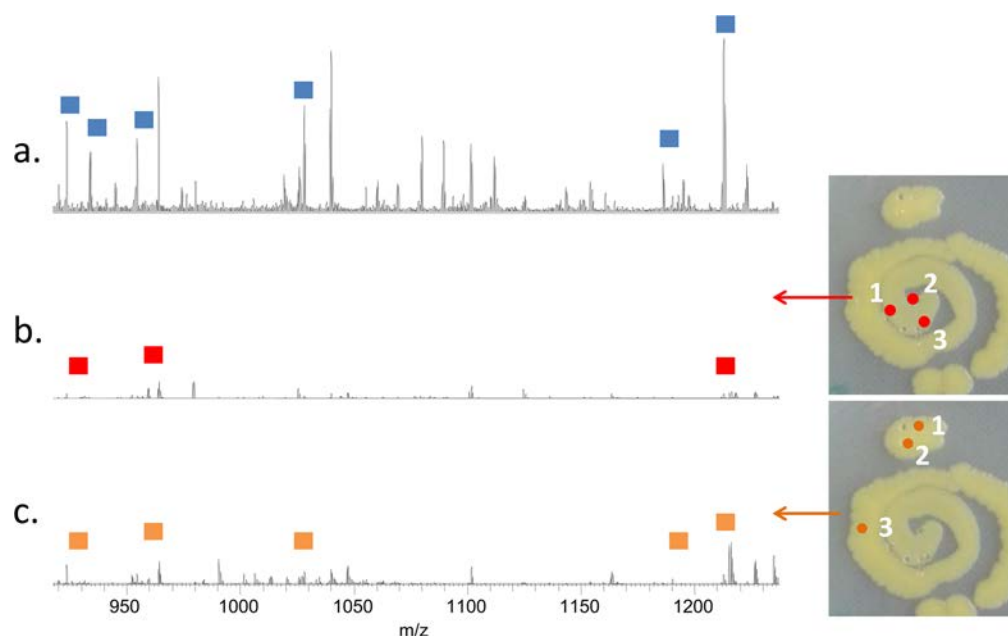
Figure 5. LESA mass spectra of bacteria stored at (a) 4 °C for 2 days, (b) at room temperature (20 °C) for 3 days, and (c) at room temperature (20 °C) for 10 days. (y-axes are equivalent.) Symbols denote identified stress response proteins. Inset: Photographs of colonies with sampling locations indicated.

conditions, consistent with prolonged refrigerated storage conditions. After the initial incubation period to grow the colonies, samples were stored at 4 °C for a number of days, which explains the induction of a cold shock response. For comparison, a further set of bacterial samples were grown. These colonies were stored at room temperature (∼20 °C) prior to mass spectrometric analysis and were never exposed to low (refrigerated) temperatures.

Figure 5 shows LESA mass spectra obtained from bacteria grown and stored at room temperature. For comparison, a LESA mass spectrum from a colony grown at room temperature for 3 days and then stored at 4 °C for 2 days is shown in Figure 5a. Peaks corresponding to all the proteins identified from the LESA mass spectrum shown in Figure 3 (in which bacteria had been grown for 3 days at room temperature before being stored at 4 °C for 7 days) were observed, albeit with differing relative abundances. That may be due to differences in protein expression as a result of prolonged cold shock or may be due to differences in LESA extraction efficiency either as a result of prolonged cold shock or colony topology. Figure 5b shows a mass spectrum obtained from a colony stored at room temperature for 3 days. The colony was sampled at three separate locations, as indicated on the photograph inset. (Individual mass spectra from each location are shown in Supplementary Figure 9, Supporting Information.) At location 1, peaks corresponding to HU-alpha and HU-beta were observed, but none of the other proteins identified above were seen. At location 2 (Figure 5b), peaks corresponding to HU-alpha, HU-beta, and CspA were observed. At location 3, none of the proteins identified above were observed. The proteins BhsA and YjbJ were not observed in any location.

A repeat analysis was carried out after the colonies had been stored at 20 °C for a further 7 days (Figure 5c). Again, three separate locations were analyzed, as indicated. (Individual mass spectra obtained from each location are shown in Supplementary Figure 10, Supporting Information.) In two of the

locations (2 and 3), all but one (BhsA) of the stress response proteins previously detected in bacteria stored at 4 °C were detected. At location 1, all but BhsA and YjbJ were detected. These results suggest that prolonged storage can induce various stress responses in bacteria. Multiple stress resistance protein BhsA, however, was not detected at any location from colonies stored at 20 °C, either after 3 or 10 days, suggesting that either temperatures lower than 20 °C or storage for longer than 10 days is required for the induction of this protein. As mentioned above, BhsA has been shown to inhibit biofilm formation. It is possible that expression of BhsA under refrigerated conditions resulted in reduced biofilm formation thus aiding the LESA process.

CONCLUSIONS

We have demonstrated a method suitable for the top-down extraction, detection, and identification of intact proteins from living bacterial colonies. The identities of these proteins appear to indicate the well-being of the colony. The method has implications for microbiological research as it may be suitable for the study of bacterial growth, communication, and response to external factors such as pharmaceuticals and pH. Moreover, the "contact" LESA method offers improved sampling precision and could be useful for spatial profiling of bacterial colonies or analysis of contaminated surfaces.

ASSOCIATED CONTENT

Ⓢ Supporting Information

LESA mass spectra, LESA CID MS/MS spectra, and CID fragment assignments. This material is available free of charge via the Internet at http://pubs.acs.org/.

AUTHOR INFORMATION

Corresponding Authors
*E-mail: josephine.bunch@npl.co.uk.
*E-mail: h.j.cooper@bham.ac.uk.

Notes

The authors declare no competing financial interest.

REFERENCES

(1) Anhalt, J. P.; Fenselau, C. *Anal. Chem.* **1975**, *47*, 219−225.
(2) Seng, P.; Drancourt, M.; Gouriet, F.; La Scola, B.; Fournier, P.-E.; Rolain, J. M.; Raoult, D. *Clin. Infect. Dis.* **2009**, *49*, 543−551.
(3) Bizzini, A.; Durussel, C.; Bille, J.; Greub, G.; Prod'hom, G. *J. Clin. Microbiol.* **2010**, *48*, 1549−1554.
(4) Saffert, R. T.; Cunningham, S. A.; Ihde, S. M.; Jobe, K. E. M.; Mandrekar, J.; Patel, R. *J. Clin. Microbiol.* **2011**, *49*, 887−892.
(5) Liu, W.-T.; Yang, Y.-L.; Xu, Y.; Lamsa, A.; Haste, N. M.; Yang, J. Y.; Ng, J.; Gonzalez, D.; Ellermeier, C. D.; Straight, P. D.; Pevzner, P. A.; Pogliano, J.; Nizet, V.; Pogliano, K.; Dorrestein, P. C. *Proc. Natl. Acad. Sci. U. S. A.* **2010**, *107*, 16286−16290.
(6) Watrous, J. D.; Dorrestein, P. C. *Nat. Rev. Microbiol.* **2011**, *9*, 683−694.
(7) Moree, W. J.; Phelan, V. V.; Wu, C.-H.; Bandeira, N.; Cornett, D. S.; Duggan, B. M.; Dorrestein, P. C. *Proc. Natl. Acad. Sci. U. S. A.* **2012**, *109*, 13811−13816.
(8) Watrous, J.; Hendricks, N.; Meehan, M.; Dorrestein, P. C. *Anal. Chem.* **2010**, *82*, 1598−1600.
(9) Cui, W.; Rohrs, H. W.; Gross, M. L. *Analyst* **2011**, *136*, 3854−3864.
(10) Lin, D.; Tabb, D. L.; Yates, J. R., III *Biochim. Biophys. Acta, Proteins Proteomics* **2003**, *1646*, 1−10.
(11) Wynne, C.; Edwards, N. J.; Fenselau, C. *Proteomics* **2010**, *10*, 3631−3643.
(12) McFarland, M. A.; Andrzejewski, D.; Musser, S. M.; Callahan, J. H. *Anal. Chem.* **2014**, *86*, 6879−6886.
(13) Takats, Z.; Wiseman, J. M.; Gologan, B.; Cooks, R. G. *Science* **2004**, *306*, 471−473.
(14) Kertesz, V.; Van Berkel, G. J. *J. Mass Spectrom.* **2010**, *45*, 252−260.
(15) Latimer, J.; Stokes, S. L.; Graham, A. I.; Bunch, J.; Jackson, R. J.; McLeod, C. W.; Poole, R. K. *J. Microbiol. Methods* **2009**, *79*, 329−335.
(16) Lanekoff, I.; Geydebrekht, O.; Pinchuk, G. E.; Konopka, A. E.; Laskin, J. *Analyst* **2013**, *138*, 1971−1978.
(17) Watrous, J.; Roach, P.; Heath, B.; Alexandrov, T.; Laskin, J.; Dorrestein, P. C. *Anal. Chem.* **2013**, *85*, 10385−10391.
(18) Kai, M.; González, I.; Genilloud, O.; Singh, S. B.; Svatoš, A. *Rapid Commun. Mass Spectrom.* **2012**, *26*, 2477−2482.
(19) Hsu, C.-C.; ElNaggar, M. S.; Peng, Y.; Fang, J.; Sanchez, L. M.; Mascuch, S. J.; Møller, K. A.; Alazzeh, E. K.; Pikula, J.; Quinn, R. A. *Anal. Chem.* **2013**, *85*, 7014−7018.
(20) Edwards, R. L.; Creese, A. J.; Baumert, M.; Griffiths, P.; Bunch, J.; Cooper, H. J. *Anal. Chem.* **2011**, *83*, 2265−2270.
(21) Edwards, R.; Griffiths, P.; Bunch, J.; Cooper, H. *J. Am. Soc. Mass Spectrom.* **2012**, *23*, 1921−1930.
(22) Schey, K. L.; Anderson, D. M.; Rose, K. L. *Anal. Chem.* **2013**, *85*, 6767−6774.
(23) Sarsby, J.; Martin, N. J.; Lalor, P. F.; Bunch, J.; Cooper, H. J. *J. Am. Soc. Mass Spectrom.* **2014**, *25*, 1953−1961.
(24) Kano, Y.; Osato, K.; Wada, M.; Imamoto, F. *Mol. Gen. Genet. MGG* **1987**, *209*, 408−410.
(25) Göransson, M.; Sondén, B.; Nilsson, P.; Dagberg, B.; Forsman, K.; Emanuelsson, K.; Uhlin, B. E. *Nature* **1990**, *344*, 682−685.
(26) Link, A. J.; Phillips, D.; Church, G. M. *J. Bacteriol.* **1997**, *179*, 6228−6237.
(27) Phadtare, S.; Alsina, J.; Inouye, M. *Curr. Opin. Microbiol.* **1999**, *2*, 175−180.
(28) Zhang, X.-S.; García-Contreras, R.; Wood, T. K. *J. Bacteriol.* **2007**, *189*, 3051−3062.
(29) Zamdborg, L.; LeDuc, R. D.; Glowacz, K. J.; Kim, Y.-B.; Viswanathan, V.; Spaulding, I. T.; Early, B. P.; Bluhm, E. J.; Babai, S.; Kelleher, N. L. *Nucleic Acids Res.* **2007**, *35*, W701−W706.

Appendix 3: CID mass spectra from various protein ions detected from bacterial colonies and fragmentation assignments.

Table 1: Fragments observed following CID of +7 ions centred at m/z 923.51 (identified as HU-beta).

m/z measured	*m/z* theoretical	Fragment assignment	Δppm
815.4447	815.4444	b_7^+	0.4
878.9677	878.9667	b_{17}^{+2}	1.1
894.4856	894.4850	b_{27}^{+3}	0.7
930.4719	930.4713	b_8^+	0.6
949.0361	949.0363	$y_{19}\text{-}NH_3^{+2}$	-0.2
953.5203	953.5224	a_{75}^{+8}	-2.2
957.3126	957.3127	b_{48}^{+5}	-0.1
957.5332	957.5296	y_{55}^{+6}	3.8
959.5201	959.5213	$b_{38}\text{-}NH_3^{+4}$	-1.3
985.5389	985.5410	$y_{67}\text{-}H_2O^{+7}$	-2.1
1016.5607	1016.5605	$b_{31}\text{-}H_2O^{+3}$	0.2
1026.1294	1026.1238	$b_{70}\text{-}H_2O^{+7}$	5.5

1058.5663	1058.5663	b_9^+	0.0
1171.6500	1171.6504	b_{10}^+	-0.3
1242.6869	1242.6875	b_{11}^+	-0.5
1313.7247	1313.7246	b_{12}^+	0.1
1456.7910	1456.7907	$y_{14}\text{-}NH_3^+$	0.2
1473.8176	1473.8172	y_{14}^+	0.3
1555.8600	1555.8591	$y_{15}\text{-}NH_3^+$	0.6
1556.8106	1556.8101	b_{15}^+	0.3
1572.8861	1572.8857	y_{15}^+	0.3
1669.8941	1669.8942	b_{16}^+	-0.1
1700.9815	1700.9806	y_{16}^+	0.5
2610.4044	2610.4032	b_{26}^+	0.5
2794.5261	2794.5244	b_{28}^+	0.6
3594.9530	3594.9524	b_{36}^+	0.2
3764.1165	3764.1154	y_{36}^+	0.3
4139.1693	4139.1653	b_{41}^+	1.0

4700.5854	4700.5860	y_{45}^{+}	-0.1
4799.6483	4799.6544	y_{46}^{+}	-1.3
5197.8741	5197.8709	y_{50}^{+}	0.6
5627.0513	5627.0569	y_{54}^{+}	-1.0
5827.1691	5827.1730	y_{56}^{+}	-0.7
6057.2643	6057.2632	y_{58}^{+}	0.2
6823.5966	6823.6639	a_{67}^{+}	-9.9
7521.0290	7521.0286	b_{74}^{+}	0.1
7552.1256	7552.1151	y_{74}^{+}	1.4
7730.1764	7730.1814	$b_{76}\text{-}H_2O^{+}$	-0.6
7748.1860	7748.1920	b_{76}^{+}	-0.8
7979.3226	7979.3218	y_{79}^{+}	0.1
8033.3419	8033.3323	$y_{80}\text{-}NH_3^{+}$	1.2
8050.3528	8050.3589	y_{80}^{+}	-0.8
8163.4420	8163.4429	y_{81}^{+}	-0.1
8975.9183	8975.9185	y_{88}^{+}	0.0

			2.9
9088.9750	9088.9485	b_{89}^{+}	

Figure 1: CID mass spectrum of ions centred at *m/z* 933.91 (+7 charge state), identified as multiple stress resistance protein BhsA. Fragment ions observed are shown inset.

Table 2: Fragments observed following CID of +7 ions centred at m/z 933.91 (identified as BhsA).

m/z measured	*m/z* theoretical	Fragment assignment	Δppm
715.3632	715.3621	b_7^{+}	1.5
911.4726	911.4707	$b_{18}\text{-}H_2O^{+2}$	2.1
984.5356	984.5513	$y_9\text{-}NH_3^{+}$	-15.9

1481.7619	1481.7594	b_{14}^{+}	1.7
1639.8315	1639.8286	b_{16}^{+}	1.8
1734.9046	1734.9021	$b_{17}-H_2O^{+}$	1.4
1752.9160	1752.9127	$y_{51}-H_2O^{+3}$	1.9
4048.0870	4048.0808	y_{38}^{+}	1.5
4275.2138	4275.2078	y_{40}^{+}	1.4
4433.2850	4433.2769	y_{42}^{+}	1.8
4504.3217	4504.3141	y_{43}^{+}	1.7
4618.3652	4618.3570	y_{44}^{+}	1.8
4776.4358	4776.4261	y_{46}^{+}	2.0
4889.5194	4889.5102	y_{47}^{+}	1.9
5029.5805	5029.5688	$y_{49}-H_2O^{+}$	2.3
5047.5869	5047.5793	y_{49}^{+}	1.5
5146.6648	5146.6477	y_{50}^{+}	3.3
5795.9756	5795.9661	$y_{56}-H_2O^{+}$	1.6
5813.9871	5813.9767	y_{56}^{+}	1.8

5915.0323	5915.0244	y_{57}^{+}	1.3
5984.0550	5984.0458	$y_{58}\text{-}H_2O^{+}$	1.5
6002.0658	6002.0564	y_{58}^{+}	1.6
6112.1149	6112.1044	$y_{59}\text{-}H_2O^{+}$	1.7
6130.1262	6130.1150	y_{59}^{+}	1.8
6229.1980	6229.1834	y_{60}^{+}	2.3
6358.2065	6358.2260	y_{61}^{+}	-3.1

Figure 2: CID mass spectrum of ions centred at *m/z* 954.43 (+10 charge state), identified as DNA-binding protein HU-alpha. Fragment ions observed are shown inset.
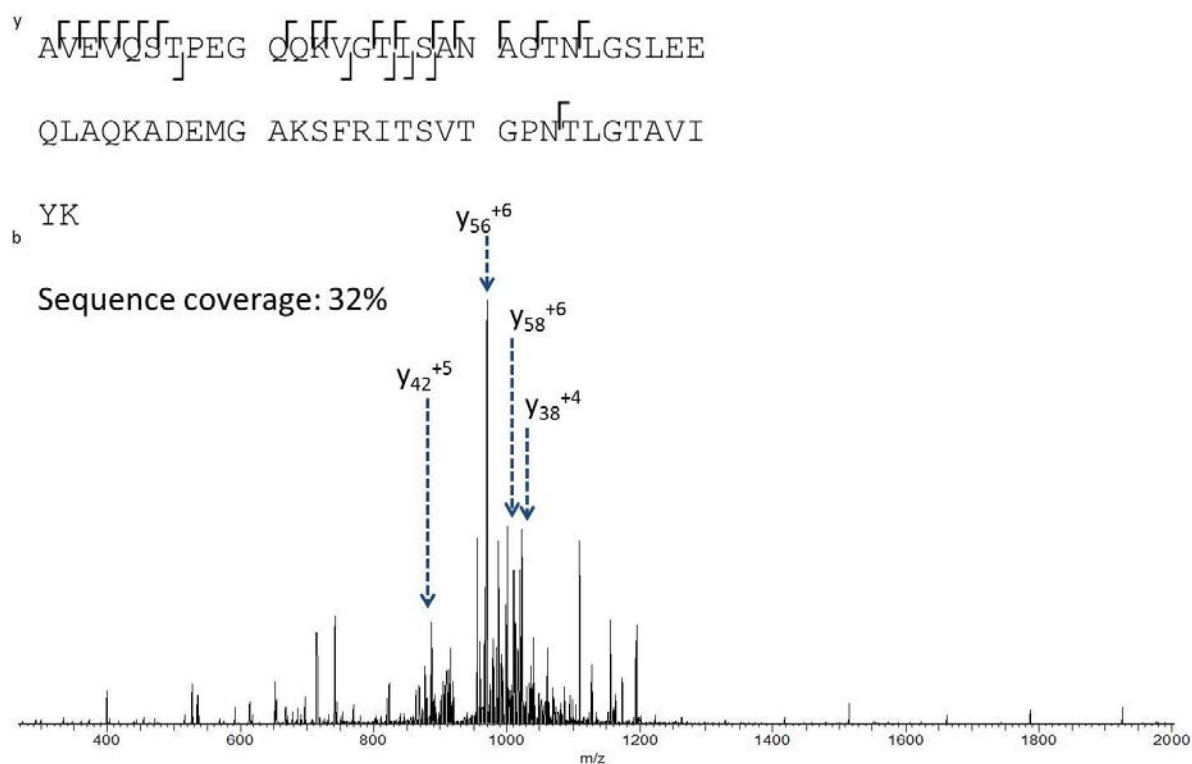
Table 3: Fragments observed following CID of +10 ions centred at m/z 954.43 (identified as HU-alpha).

m/z measured	*m/z* theoretical	Fragment assignment	Δppm
1430.8382	1430.8366	y_{14}^{+}	1.1
1643.9498	1643.9479	y_{16}^{+}	1.2
1714.9870	1714.9850	y_{17}^{+}	1.2
1786.0244	1786.0221	y_{18}^{+}	1.3
1857.0615	1857.0593	y_{19}^{+}	1.2

1970.1458	1970.1433	y_{20}^{+}	1.3
2211.3248	2211.3223	y_{22}^{+}	1.1
2441.3456	2441.3432	b_{22}^{+}	1.0
2696.5048	2696.5015	b_{25}^{+}	1.2
3197.7492	3197.7450	b_{30}^{+}	1.3
3268.7848	3268.7821	b_{31}^{+}	0.8
3381.8691	3381.8662	b_{32}^{+}	0.9
4241.2656	4241.2585	b_{40}^{+}	1.7
4312.3008	4312.2956	b_{41}^{+}	1.2
4878.6936	4878.6966	y_{46}^{+}	-0.6
5591.0415	5591.0357	y_{53}^{+}	1.0
6149.4036	6149.3371	y_{58}^{+}	10.8
7319.8853	7319.8809	b_{68}^{+}	0.6
7561.0638	7561.0599	b_{70}^{+}	0.5
7745.2929	7745.1811	b_{72}^{+}	14.4
7816.2066	7816.2182	b_{73}^{+}	-1.5

7887.2699	7887.2553	b_{74}^+	1.9
8046.3405	8046.3891	y_{77}^+	-6.0
8083.3512	8083.3401	$b_{76}\text{-}NH_3^+$	1.4
8100.3646	8100.3667	b_{76}^+	-0.3
9055.9353	9055.9699	y_{86}^+	-3.8
9139.0079	9139.0070	$y_{87}\text{-}H_2O^+$	0.1
9157.0190	9157.0176	y_{87}^+	0.2
9185.9276	9185.9900	a_{87}^+	-6.8
9285.1182	9285.1125	y_{88}^+	0.6
9384.13423	9384.0904	b_{89}^+	4.7

Supplementary Figure 3: CID mass spectrum of ions centred at *m/z* 1028.14 (+15 charge state), identified as H-NS. Fragment ions observed are shown inset.
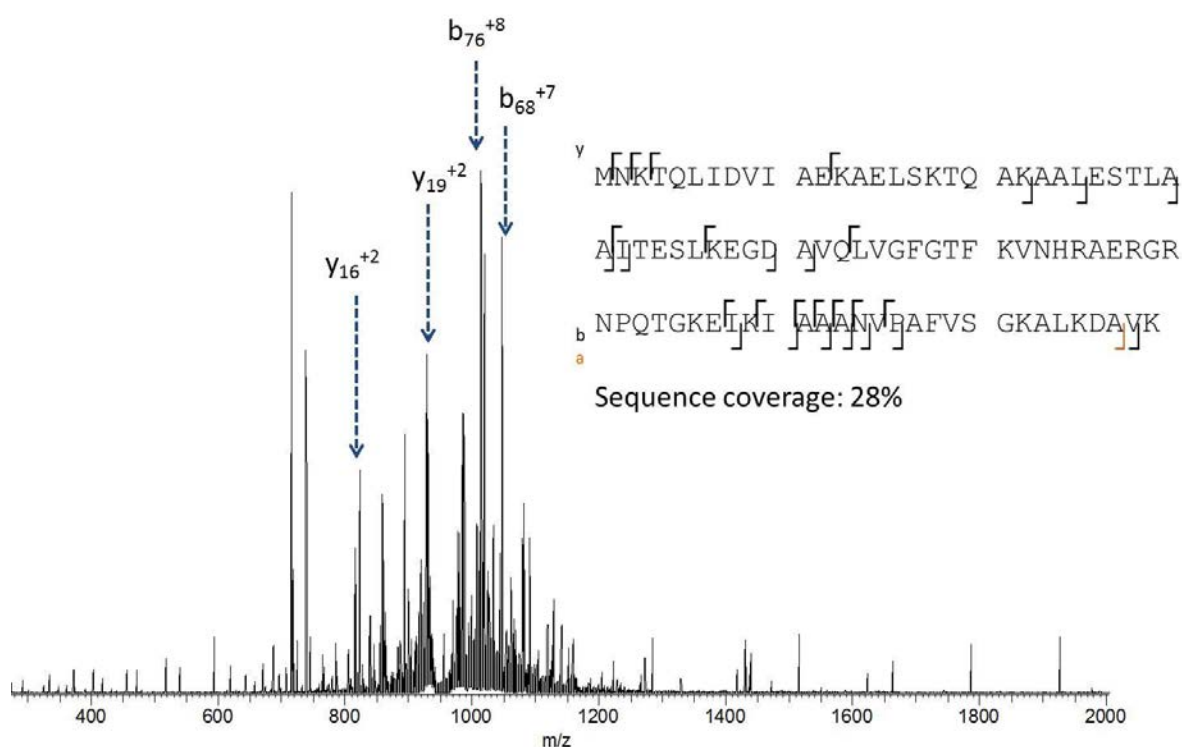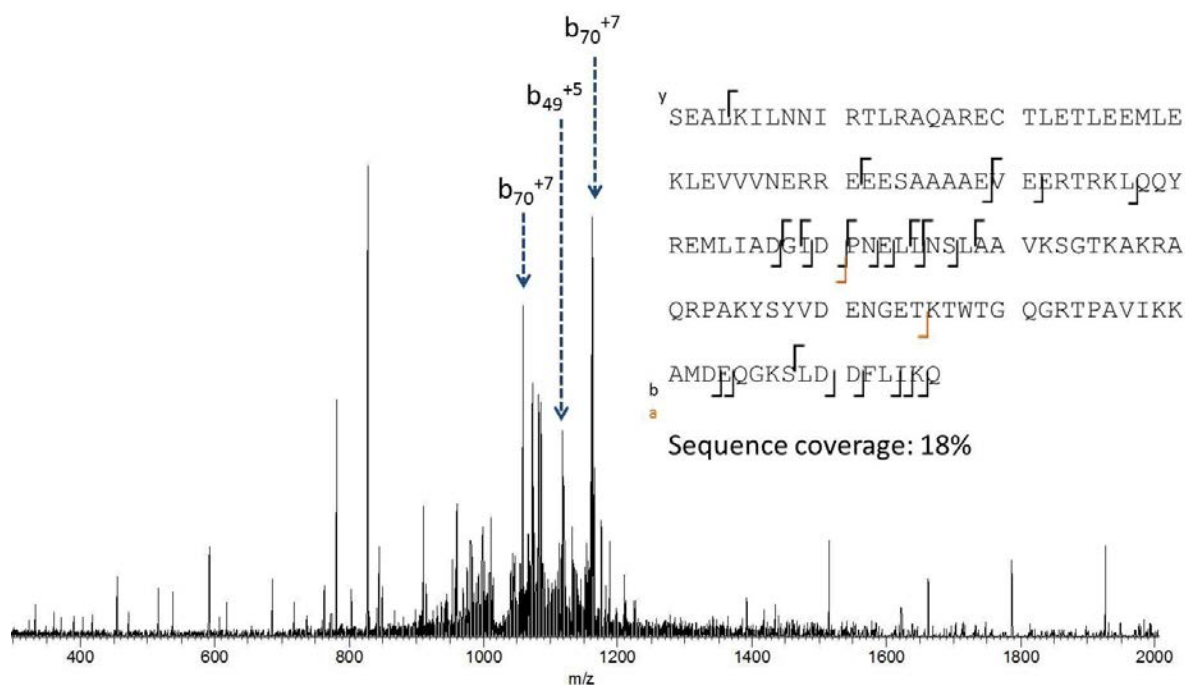
Table 4: Fragments observed following CID of +15 ions centred at m/z 1028.14 (identified as H-NS).

m/z measured	*m/z* theoretical	Fragment assignment	Δppm
1010.7751	1010.7776	$a_{70}\text{-NH}_3^{+8}$	-2.5
1057.1649	1057.1477	$y_{95}\text{-NH}_3^{+10}$	16.3
1061.5431	1061.5514	$y_8\text{-NH}_3^+$	-7.8
1070.4087	1070.4231	$y_{68}\text{-H}_2\text{O}^{+7}$	-13.5
1078.5599	1078.5649	b_{124}^{+13}	-4.6

			-6.1
1078.7030	1078.7096	$y_{69}-NH_3^{+7}$	
			7.6
1082.4905	1082.4823	$a_{115}-NH_3^{+12}$	
			2.9
1096.5819	1096.5787	$b_{57}-NH_3^{+6}$	
			-9.7
2141.0992	2141.1199	$y_{132}-H_2O^{+7}$	
			-4.5
5579.8547	5579.8796	b_{49}^{+}	
			-5.0
5807.9615	5807.9906	b_{51}^{+}	
			-4.9
6396.3210	6396.3521	y_{58}^{+}	
			-5.1
6710.4766	6710.5111	y_{61}^{+}	
			-4.9
6823.5621	6823.5952	y_{62}^{+}	
			-5.2
7276.7796	7276.8175	y_{66}^{+}	
			-5.0
7839.0195	7839.0590	b_{67}^{+}	
			-5.3
8009.1223	8009.1645	b_{69}^{+}	
			-5.8
8106.1335	8106.1809	$b_{70}-H_2O^{+}$	
			-5.8
8124.1447	8124.1915	b_{70}^{+}	
			-4.8
8335.2471	8335.2872	b_{72}^{+}	
			-5.8
8464.2807	8464.3297	b_{73}^{+}	

8690.4577	8690.4979	b_{75}^{+}	-4.6
8873.5192	8873.5623	$b_{77}-H_2O^{+}$	-4.9
9821.0766	9821.1294	y_{87}^{+}	-5.4
13880.1476	13880.2135	b_{123}^{+}	-4.7
14637.5013	14637.5741	b_{130}^{+}	-5.0
14752.5413	14752.6011	b_{131}^{+}	-4.1
14994.6602	14994.7430	$b_{133}-H_2O^{+}$	-5.5
15108.7440	15108.8111	$b_{134}-NH_3^{+}$	-4.4
15253.8508	15253.9326	b_{135}^{+}	-5.4

Figure 4: CID mass spectrum of ions centred at *m/z* 1190.31 (+7 charge state), identified as YjbJ. Fragment ions observed are shown inset.

MNKDEAGGNW KQFKGKVKEQ WGKLTDDDMT

IIEGKRDQLV GKIQERYGYQ KDQAEKEVVD

WETRNEYRW

Coverage: 23%

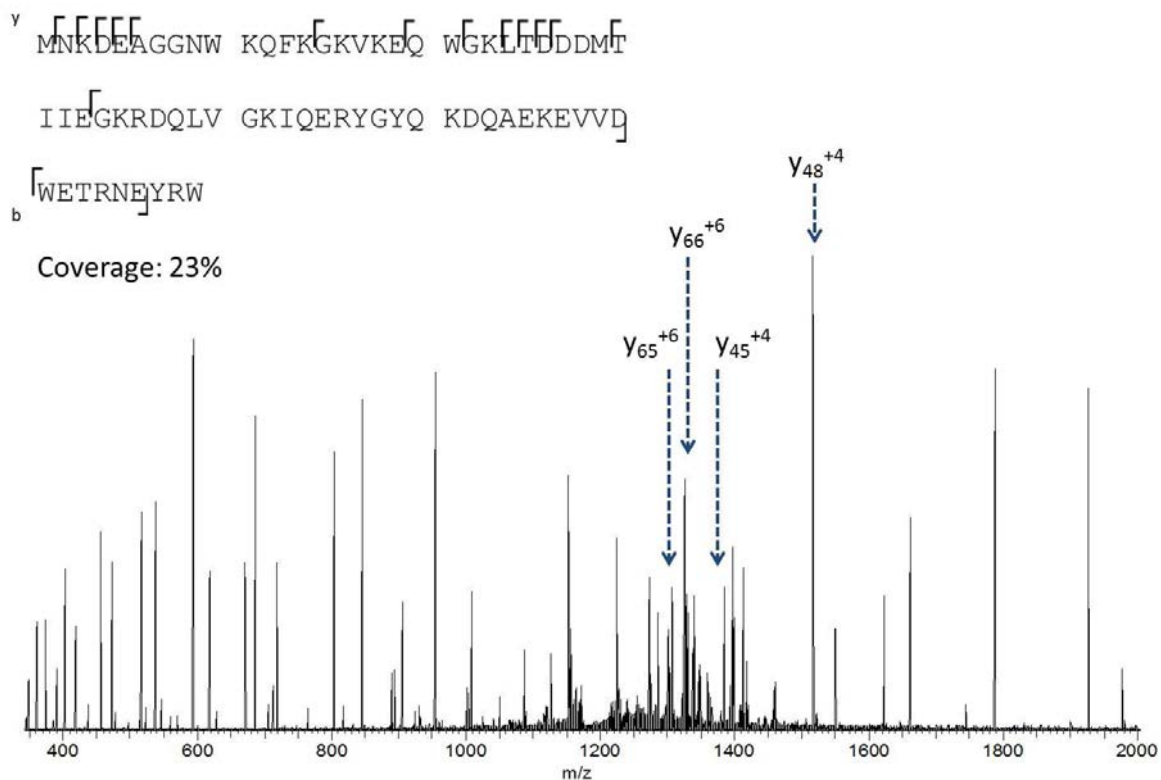**Table 5:** Fragments observed following CID of +7 ions centred at m/z 1190.31 (identified as YjbJ).

m/z measured	*m/z* theoretical	Fragment assignment	Δppm
1339.6154	1339.6178	y_9^+	-1.8
4500.2426	4500.2443	y_{36}^+	-0.4
4956.5011	4956.5027	y_{40}^+	-0.3
5317.5992	5317.5971	y_{43}^+	0.4
5432.6217	5432.6240	y_{44}^+	-0.4

5533.6703	5533.6717	y_{45}^+	-0.3
5646.7570	5646.7558	y_{46}^+	0.2
5831.8724	5831.8722	y_{48}^+	0.0
6128.9856	6128.9836	$y_{50}\text{-}NH_3^+$	0.3
6687.3295	6687.3325	y_{55}^+	-0.4
6982.4865	6982.4891	b_{60}^+	-0.4
7703.8486	7703.8517	y_{64}^+	-0.4
7797.8416	7797.8453	b_{66}^+	-0.5
7814.8725	7814.8837	$y_{65}\text{-}H_2O^+$	-1.4
7832.8903	7832.8943	y_{65}^+	-0.5
7929.8943	7929.9107	$y_{66}\text{-}H_2O^+$	-2.1
7947.9212	7947.9212	y_{66}^+	0.0
8076.0105	8076.0162	y_{67}^+	-0.7
8190.0475	8190.0591	y_{68}^+	-1.4

Figure 5: CID mass spectrum of ions centred at *m/z* 1212.94 (+6 charge state), identified as cold shock proteins CspA. Fragment ions observed are shown inset.
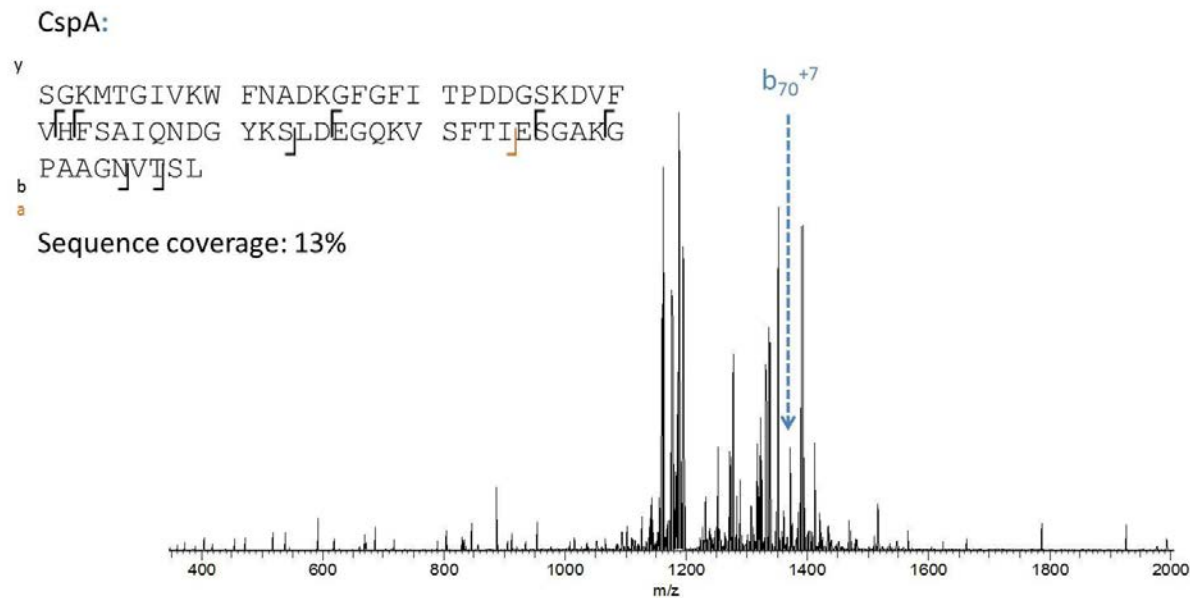

CspA:

```
y
  SGKMTGIVKW FNADKGFGFI TPDDGSKDVF
  VHFSAIQNDG YKSLDEGQKV SFTIESGAKG
b
  PAAGNVTSL
a
```

Sequence coverage: 13%

Table 6: Fragments observed following CID of +6 ions centred at m/z 1212.94 (identified as CspA).

m/z measured	*m/z* theoretical	Fragment assignment	Δppm
886.4619	886.4629	y_{10}^{+}	-1.1
1142.6161	1142.6164	y_{13}^{+}	-0.3
1165.5888	1165.6030	$y_{24}\text{-}H_2O^{+2}$	-12.2
1174.6070	1174.6083	y_{24}^{+2}	-1.1
1177.9185	1177.9145	$b_{67}\text{-}H_2O^{+6}$	3.4

1180.9910	1180.9804	$a_{54}{}^{+5}$	9.0
1185.0856	1185.0781	$b_{43}{}^{+4}$	6.3
1257.2897	1257.2900	y_{37}-$NH_3{}^{+3}$	-0.2
1302.6511	1302.6483	y_{38}-$H_2O{}^{+3}$	2.1
6850.3496	6850.3232	b_{65}-$NH_3{}^{+}$	3.9